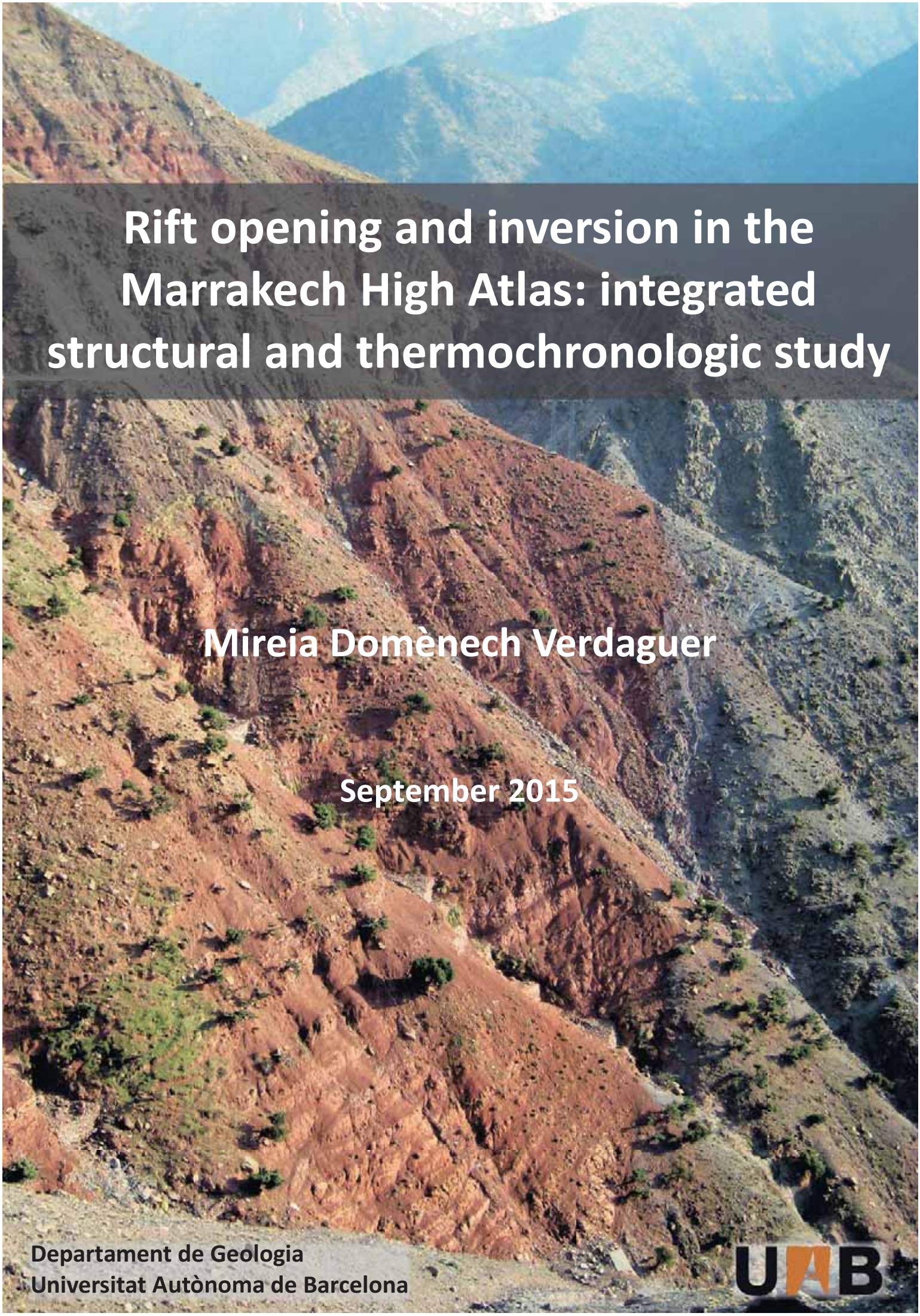

Rift opening and inversion in the Marrakech High Atlas: integrated structural and thermochronologic study

Mireia Domènech Verdaguer

September 2015

Departament de Geologia
Universitat Autònoma de Barcelona

UAB

Departament de Geologia
Universitat Autònoma de Barcelona

Rift opening and inversion in the Marrakech High Atlas: integrated structural and thermochronologic study

PhD Dissertation presented by

MIREIA DOMÈNCH VERDAGUER

In candidacy for the degree of Doctor in Geology

PhD thesis supervised by

Dr. Antonio Teixell Cácharo
Unitat de Geotectònica
Universitat Autònoma de Barcelona

September 2015

This research work is funded by a predoctoral FPU grant (AP-2009-4936) from Ministerio de Educación (España) and supported by MEC and MINECO projects CGL2014-54180-P, CGL2010-15416, CGL2007-66431-CO2-01 (TOPOMED), and Consolider-Ingenio 2010 CSD2006-00041 (TOPOIBERIA).

Als meus pares

"The earth is large and old enough to teach us modesty"

Hans Cloos (1885-1951)

Acknowledgements / Agraïments / Agradecimientos

Tot i que la realització d'una tesi doctoral és una tasca individual, seria pràcticament impossible de realitzar sense l'ajuda de tanta i tanta gent que en algun moment o altre, en major o menor mesura, han ajudat a tirar-la endavant. Arribats doncs a aquest punt, és just dedica'ls-hi unes paraules d'agraïment.

Una de les figures més determinants tant durant el procés de realització, com en el resultat final d'una tesi és el director. Jo he tingut la infinita sort de tenir un director que no només s'ha involucrat al màxim científicament, aconsellant, guiant, anant al camp, aportant idees, discutint, corregint i donant-me suport econòmic per congressos i pel camp, sinó que també m'ha donat la llibertat i confiança perquè pogués créixer i desenvolupar-me com a geòloga i s'ha preocupat en tot moment pel meu benestar tant a nivell personal com a la universitat, contribuint en gran mesura a que hagi gaudit cada dia d'aquests últims anys fent aquesta tesi. Per tot això, la meva més sentida i profunda gratitud és pel meu director de tesi, Antonio Teixell.

My sincere thanks also goes to Daniel Stockli, who gave me the opportunity to join their team for three months, and who granted me access to the laboratory and research facilities at the Jackson School of Geosciences. Also, for his valuable comments and geologic discussions, which have contributed greatly to develop Chapter 3 of this thesis. I would also like to thank Roman Kislitsyn, Spencer Seman, Josue Pujols, Mike Prior and Emily Goldstein who helped me in the lab, and Ethan Lake for his generous hospitality. All of them contributed to making my experience in Austin and in the University of Texas really nice and enriching.

I am also very grateful to Kerry Gallagher who guided me generously and with a lot of patience into the use of the QTQt software.

A Mª Luisa Arboleya por acompañarme al campo y brindarme su ayuda y discusión siempre que lo he necesitado.

Al grupo de "paleomac" de la Universidad de Zaragoza-Universidad de Burgos, especialmente a Antonio Casas y a Juanjo Villalaín, apasionados geólogos con quien tuve la suerte de compartir campo y discusiones científicas. También a Juanjo, por su hospitalidad, amabilidad y ayuda durante las 2 semanas que estuve en Burgos analizando las muestras de paleomagnetismo.

A l'Eduard Saura, que em va ajudar revisant el capítol 2 d'aquesta tesi.

A Eliseo Tesón, por su ayuda y apoyo en los inicios de esta tesis. Gracias también a ti y a Andrés Mora por la oportunidad que me brindasteis de ir a Colombia a ampliar mi formación como geóloga, y por tu hospitalidad durante las dos semanas que estuve allí.

Al Raül Mas i a l'Anna i al Mariano Medina per acompanyar-me i ajudar-me al camp.

A mis amigos Jorge Pinto y Gregoire Messager agradecerles las discusiones científicas y los ánimos que me han dado.

Al David Gómez agrair-li el seu suport i ajuda quan més ho he necessitat.

A les “secres”: Sílvia, Glòria, Tere i Sara; i als professors del departament: Gumer, Rita, Oriol, Reche i especialment a l’Esteve, Paco, Grigri, Pini, Mercè i Geneta pels ànims que m’han donat, per les calçotades-garrinades, els sopars, dinars i cafès. Gràcies al bon ambient de treball que creeu entre tots, sempre és més fàcil aixecar-se per anar a treballar.

Al Marc Viaplana, amic i company de despatx amb qui he tingut la sort de compartit llargues hores de feina i totes les alegries i penes d’aquesta tesi, i de la vida, durant els últims quatre anys. Gràcies per aguantar-me i animar-me durant tot aquest temps.

A la Lucía Struth, pels bons moments que hem viscut juntes tant a Austin com a la Universitat, per estar sempre disposada a donar-me un cop de mà quan ho he necessitat, i pel seu suport i ànims.

Al Salvador Boya, agrair-li el seu suport moral i les bones converses davant d’una cervesa filosofant sobre la vida, el món i sobre tot en general, que fan que un dia dur sempre s’acabi arreglant.

A la resta de “becarios precarios”: Isaac, Àlvar, Eudald, Jordi, Miquel, Victor, David, i molt especialment al Dídac, a la Marta i al Camilo pel bon ambient de treball, pel companyerisme constant, per les xerrades, riures i bon humor sempre presents, per les “Friday beers”, dinars, sopars, festes, cafès, etc. per tot, moltes gràcies! Sense tots vosaltres aquests anys passats a la Universitat fent aquesta tesi no haguessin estat el mateix.

A les meves amigues de tota la vida agrair’ls-hi els seus ànims. Molt especialment a la Mireia Prat, amiga amb majúscules, la qual, des de que tinc memòria, sempre ha estat allà animant-me i recolzant-me incansablement.

Als meus pares. Tot el que sóc com a persona i tot el que he fet a la meva vida, és gràcies a vosaltres. Gràcies per tots els valors que m’heu transmès i per ensenyar-me que a la vida s’ha de ser valent i confiar en un mateix per perseguir tots els teus somnis i objectius. També al meu germà Marc. Gràcies a tots tres pel vostre suport i ajuda incondicional, pels ànims constants, i per fer de casa, un refugi segur i càlid on tornar sempre. També a la resta de la meva família els seus ànims i suport, especialment a la meva padrina Montse. També agrair-li a la meva àvia Mª Teresa, per l’exemple de vida, treball i esforç que ens va donar a tots.

A tu Andreu Badia, qui m’aguanta en els bons i mals moments, qui m’anima sempre, qui veu sempre el canto positiu de tot i qui sempre veu el millor de mi. Gràcies pel teu recolzament durant tot aquest temps. Al teu costat tot és sempre molt més fàcil. També a la Pepa, els seus ànims i suport.

Index

Index

Abstract

The High Atlas of Morocco is an aborted continental rift developed during the Triassic-Jurassic and moderately inverted during the Cenozoic. The Marrakech High Atlas, with large exposures of basement and Triassic early syn-rift deposits, has been viewed as a morphologic high or a poorly subsiding domain during the Triassic-Jurassic rifting. The multidisciplinary approach presented in this thesis that integrates structural analysis and low-temperature thermochronology reveals that the Triassic-Jurassic rift was well developed in the Marrakech High Atlas (4.5-6 km thickness of Triassic-Jurassic deposits) and suggests that the Tethys and Atlantic rifts were connected in Triassic to Mid-Late Jurassic times. The main Triassic basins and basin-margin faults show a dominant dip-slip opening kinematics with strike-slip playing a minor role, at variance to models proposing a major strike-slip component, including faults belonging to the Tizi n'Test fault zone. Well-exposed fault and graben structures provide good analogues for the exploration of pre-salt systems in the subsurface. This multidisciplinary study also shows that the Marrakech High Atlas was a narrow and highly segmented orthogonal rift (sub-perpendicular to the main regional extension direction which was ~NW-SE), in contrast to the central and eastern segments of the Atlas rift which developed obliquely. This difference in orientation is attributed to the indented Ouzellarh Precambrian salient, part of the West African Craton, which deflected the general rift trend in the area evidencing the major role of inherited lithospheric anisotropies in rift direction and evolution. The Mid-Late Jurassic to Early Cretaceous zHe cooling ages obtained in certain areas indicate that rift-related subsidence in the Marrakech High Atlas finished in late Mid Jurassic times and was followed by a period of exhumation where nearly 2-3 km of rock were eroded. This, together with previous results in the Moroccan Meseta and Anti-Atlas, define a Mid-Late Jurassic to Early Cretaceous exhuming high following the orientation of the current Atlantic margin. Thermal models based on thermochronologic data indicate that Atlas orogeny in the inner parts of the High Atlas started in the Late Cretaceous, and compression-related exhumation accelerated since the Oligocene or Miocene, consistent with dated tectonics-sedimentation relationships elsewhere. Shortening appears accommodated by basement-involved large-scale folding, and by newly formed shortcut or by-pass thrusting, with rare left-lateral strike-slip indicators. Field structural evidence and thermochronology show that Triassic faults were mostly not reactivated, acting as buttresses. The Triassic-Jurassic basins reconstruction assisted by thermochronology and on the constrained tectonic structures, when compared with present-day cross-sections, suggests minimum values of total shortening in the Marrakech High Atlas of 13 to 14.2 km (21% to 17%).

Resumen

El Alto Atlas de Marruecos se formó por la inversión durante el Cenozoico de un rift continental que se formó durante el Triásico-Jurásico. El Alto Atlas de Marrakech, donde afloran principalmente materiales del basamento y del Triásico sinrift, había sido considerado como un alto o zona poco subsidente durante el rifting Triásico-Jurásico. El estudio multidisciplinario presentado en esta tesis, que integra análisis estructural y termocronología de baja temperatura, revela que el rifting Triásico-Jurásico tuvo un desarrollo completo en el Alto Atlas de Marrakech (con espesores de materiales Triásico-Jurásicos de hasta 4.5-6 km) y por tanto, sugiere que el rift del Tethys y del Atlántico estaban conectados durante el Triásico hasta el Jurásico medio-superior. El estudio de las principales cuencas Triásicas y sus fallas limitantes indican un mecanismo de apertura en extensión, siendo los movimientos direccionales menores, lo que difiere de previas interpretaciones que sugerían un modelo de apertura con movimientos direccionales importantes, incluyendo la zona de falla de Tizi n'Test. La buena exposición de las fallas y cuencas Triásicas proporciona buenos análogos de campo para la exploración en el subsuelo de sistemas extensionales de pre-sal. El análisis estructural también muestra que el rift del Alto Atlas de Marrakech fue estrecho, muy segmentado y que se desarrolló en una dirección ortogonal a la dirección de extensión regional de la época (~NW-SE), a diferencia del Alto Atlas central que desarrolló de forma oblicua. Esta diferencia en la orientación del rift la atribuyo a la indentación del macizo precámbrico del Ouzellarh (parte del Cratón Africano), que desvió la dirección general del rift evidenciando el marcado rol que ejerce la anisotropía litosférica heredada en la dirección y evolución del rift. En cuanto a los resultados de termocronología de (U-Th)He, las edades de enfriamiento de zHe del Jurásico medio-superior a Cretácico inferior obtenidas en el Alto Atlas de Marrakech indican que la subsidencia relacionada con el rift cesó en el Jurásico medio tardío, seguida por un periodo de exhumación en el que se erosionaron 2-3 km de roca. Este resultado, conjuntamente con resultados similares obtenidos por autores previos en la Meseta y el Anti-Atlas muestran una amplia área de exhumación durante esa época, siguiendo la orientación del margen Atlántico. Los modelos térmicos basados en los datos de termocronología de zHe y aHe indican que la orogenia Atlásica en las zonas internas de la cordillera empezó en el Cretácico superior. Los modelos muestran que la exhumación relacionada con la compresión se aceleró en el Oligoceno o en el Mioceno, lo cual es coherente con depósitos sinorogénicos datados anteriormente en las cuencas de antepaís periféricas. El acortamiento orogénico en el Alto Atlas de Marrakech se acomodó por pliegues de gran longitud de onda donde el basamento está involucrado, y por la creación de cabalgamientos de tipo *shortcut* o *by-pass*. Los indicadores de movimiento direccional en dichos cabalgamientos son menores. Tanto las evidencias estructurales de campo como los datos de termocronología indican que les fallas activas durante la extensión Triásico-Jurásico no fueron reactivadas en la etapa compresiva, actuando como *butresses*. La comparación entre las secciones estructurales actuales y la reconstrucción de las cuencas Triásicas-Jurásicas apoyada en la termocronología sugiere acortamientos mínimos totales para el Alto Atlas de Marrakech de entre 13 y 14.2 km (21% y 17% respectivamente).

Chapter 1

Introduction: Geologic setting and aims of this study

Chapter 1. Introduction: Geologic setting and aims of this study

1.1. Regional tectonic framework of NW Africa

The Western Mediterranean region is a complex geologic area due to its location at the boundary between the Eurasian and African tectonic plates. The plate boundary to the west of the Gulf of Cadiz is defined by a fault system that connects the Azores with Gorringe bank. To the east it is more diffusely defined by the Betics and Rift thrust belts (fig. 1.1a).

The Eurasian and African plate converge obliquely in the western Mediterranean region, at velocities of ~3 to 6 mm/a with an ESE-WNW to NW-SE approximate direction (e.g. Jimenez-Munt et al., 2001; Sella et al., 2002; McClusky et al., 2003; Serpelloni et al., 2007; de Vicente et al., 2008). Convergence took place at least from Paleocene to present times, and is responsible for the development of the main mountain systems of North Africa (Rif-Tell-Kabylias, Atlas and Anti-Atlas) (fig.1.1b).

The Rif-Tell-Kabylias is a W-E trending mountain belt located in the NW border of the African continent, from Morocco to Tunisia. The Rif, which is the westernmost segment, is connected through the Gulf of Cadiz with the Betic system in the SE of Iberia peninsula forming the Gibraltar arc (fig. 1.1b). This plate-boundary orogenic belt experienced a complex tectonic evolution. The orogen internal areas were shortened and metamorphosed between the Upper Cretaceous and the Oligocene (Saenz de Galdeano, 1992 and references therein). During the Neogene shortening processes in the external thrust belts of the system coexist with extensional processes in the internal zones and the Alboran Sea (e.g., Vera and Martín-Algarra, 2004) (fig. 1.1).

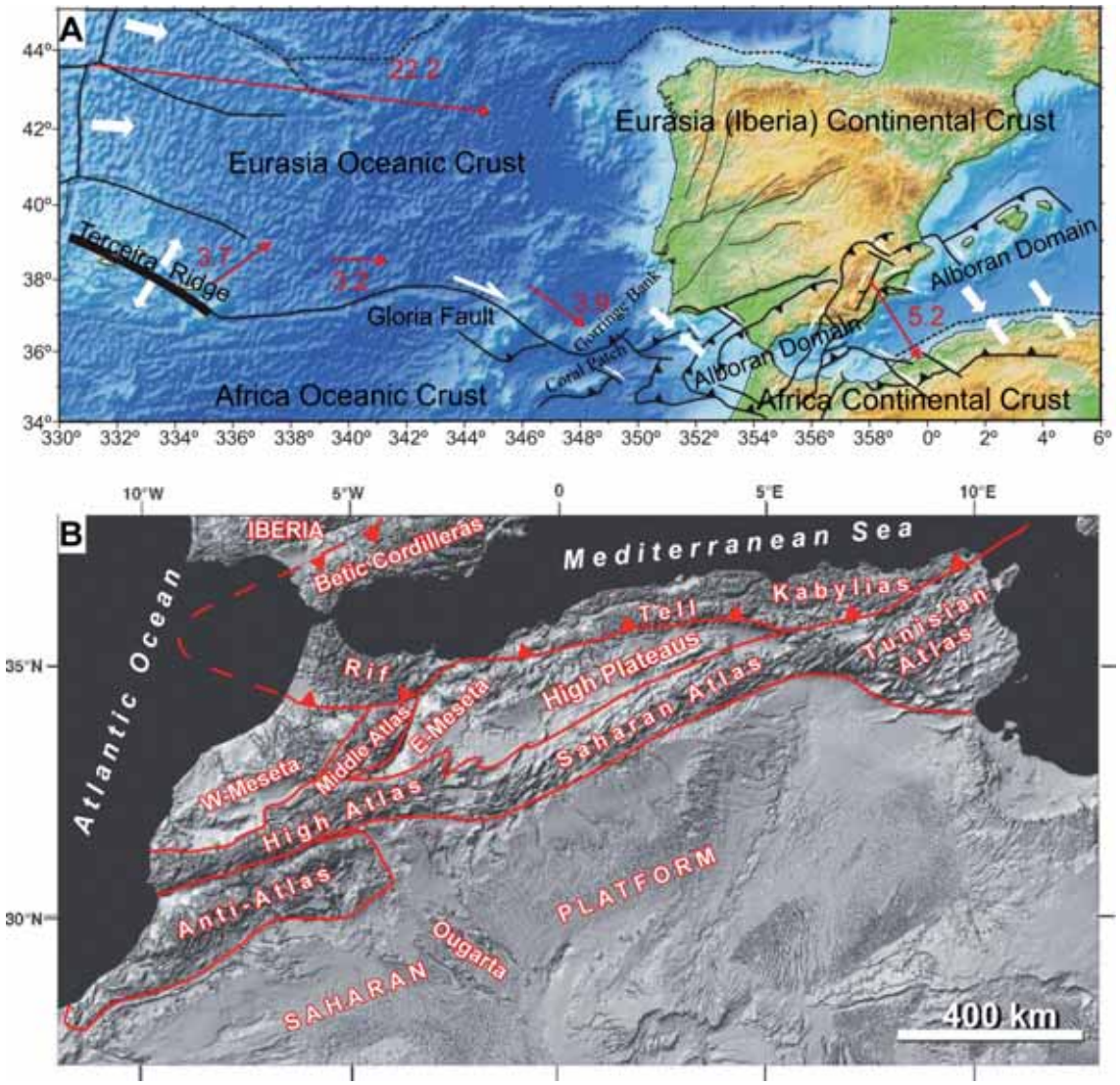

Figure 1.1. a) Main structural features of the Western Eurasia-Africa plate boundary region. Red arrows and numbers indicate local plate velocities (in mm/a) of Eurasia relative to North America and Africa (Nubia), based on model NUVEL1A (DeMets et al., 1990) (taken from de de Vicente et al., 2008). b) Map of northwestern Africa indicating the main morphotectonic units taken from Michard et al. (2008).

South of the Rift-Tell-Kabylias orogen are the High and Middle Atlas mountain belts, which are intraplate orogens resulting from the propagation of compressional stresses into the interior of the African plate (e.g. Mattauer et al., 1977) (fig. 1.1b). The High Atlas, which continues into the Saharan and Tunisian Atlas, has a WSW-ENE orientation and the system extends from Morocco to Tunisia for more than 2000 km (fig.1.1b). The Middle Atlas of Morocco has a SW-NE trend and is located between the Rif-Tell and the High Atlas. East

and West of the Middle Atlas, separating the Rift-Tell from the High Atlas there are the elevated plateaus of the Eastern and Western Mesetas (also called the Moroccan Meseta).

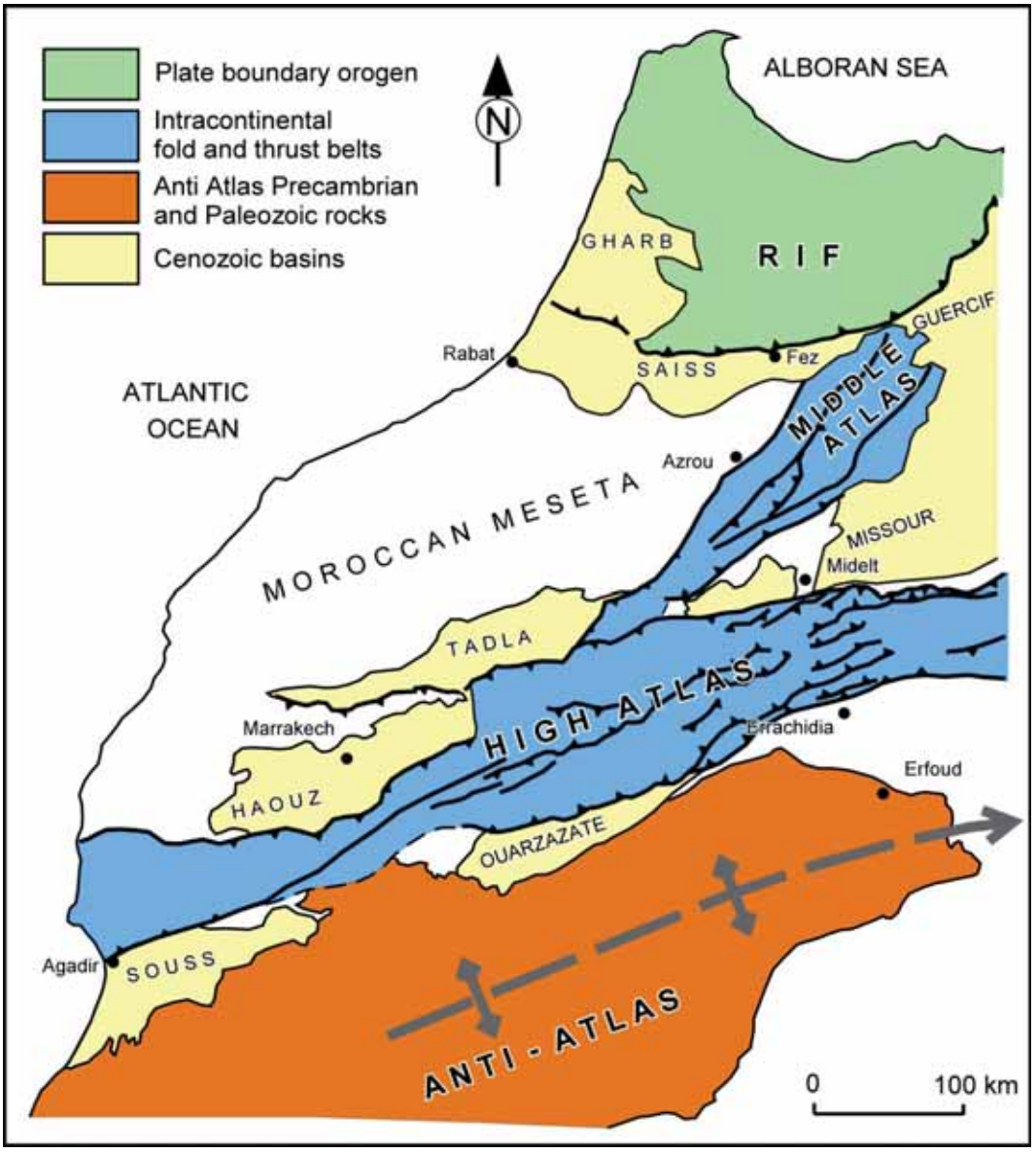

Figure 1.2. Main structural features of Morocco. Main fold-thrust belts and Cenozoic basins are showed (slightly modified from Arboleya et al., 2004).

The High and Middle Atlas derive from the Cenozoic inversion of extensional basins developed during Triassic and Jurassic rifting. These orogenic belts have experienced limited shortening. In spite of this, the High Atlas presents the highest elevations of the North of Africa, with mean elevations higher than 2000m and summits higher than 4000m. Compressional deformation is mainly thick-skinned with thin-skinned limited to

the orogen margins (Teixell et al., 2003). The main foreland basins of the Atlas are of Neogene age (Haouz-Tadla, Guercif and Missour basins to the north, Souss and Ouarzazate basins to the south). A large foredeep basin (Gharb-Saiss basin) extends south of the Rift belt (fig. 1.2).

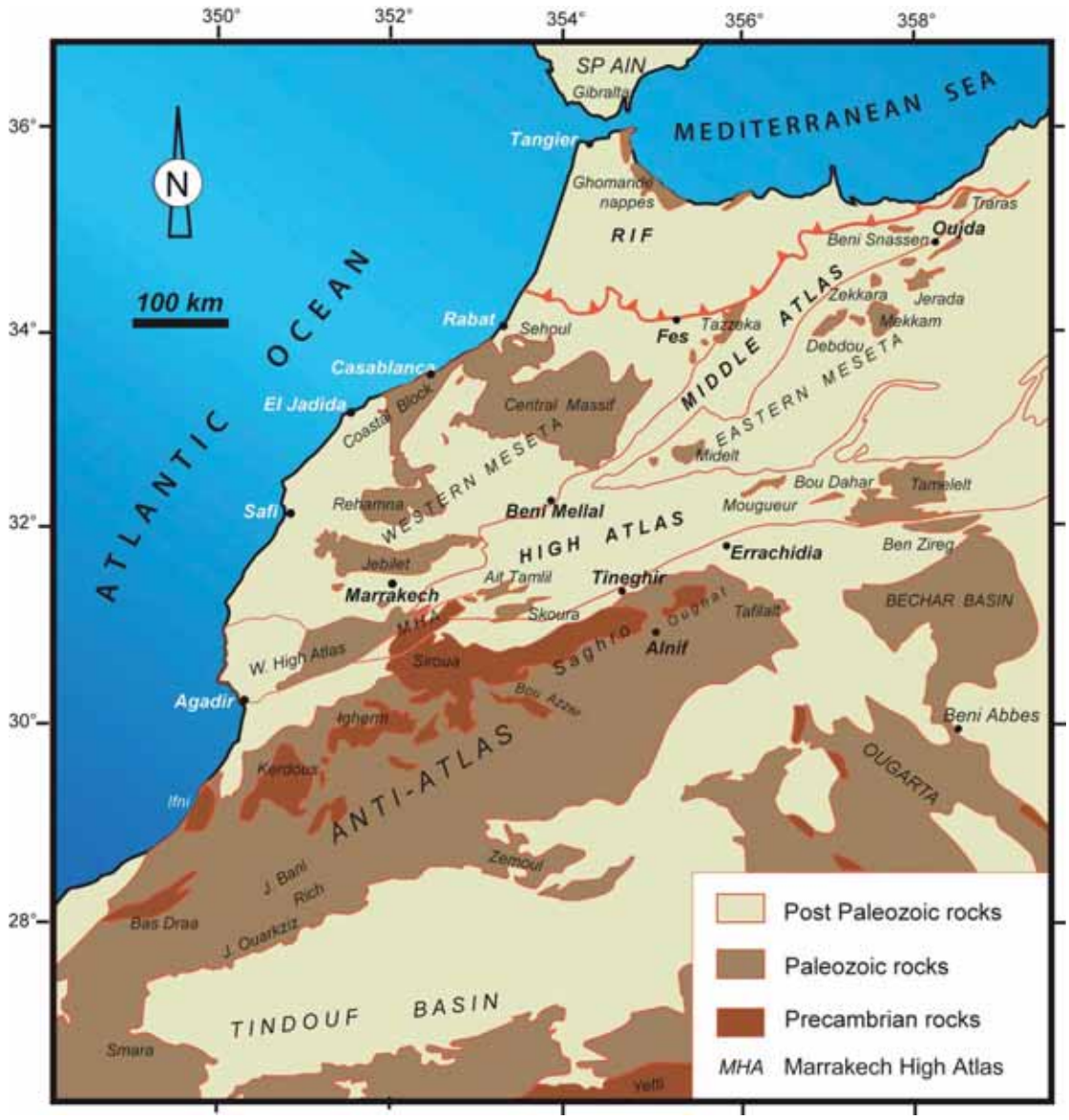

Figure 1.3. Paleozoic and Precambrian outcrops in Morocco taken from Michard et al. (2008), modified from Pique and Michard (1989).

The Anti-Atlas chain is located south of the High Atlas and formed mainly by Precambrian and Paleozoic deposits. At variance with the High and Middle Atlas, it was a relatively stable domain during the Triassic-Jurassic rifting and the later Cenozoic compression,

being then only slightly deformed with by a 100 km-scale gentle antiformal fold (which is subparallel to the High Atlas, and plunges to the east; fig.1.2) and by a few thrusts of limited displacement (Guimerà et al., 2011). The internal structure of the Paleozoic and Precambrian rocks is characterized by Variscan thick-skinned folds and thrusts with Precambrian involved (Burkhard et al., 2006; Raddi et al., 2007).

The basement is extensively exposed in Morocco (fig. 1.3) and displays superimposed compressional-extensional cycles that took place from the Precambrian to the present. These orogenic-rifting cycles are the Pan-African, Variscan-Hercynian and Alpine. Successive orogenic cycles (and the rifting that may take place prior to each orogenic episode) are superimposed in the flanks of the West African Craton (WAC), which extends over millions of square kilometers in the Sahara desert (fig.1.1b) and is composed by a crystalline basement and a sedimentary cover that spans from the Neoproterozoic to the Cenozoic without major angular unconformities (Michard, 1976). A most important outcome of the addition of superimposed orogenic-rifting cycles is that old structures and orogenic domains (which are mechanical discontinuities), often control the younger ones (as we will see in subsequent chapters).

1.2. Tectonic history of NW Africa

1.2.1 The Pan-African and Variscan orogenic domains

The Pan-African and Variscan belts formed successively during the Neoproterozoic (Nachit et al., 1996; Thomas et al., 2002, 2004; Gasquet et al., 2008 and references therein) and the Late Ordovician-Late Carboniferous (Michard, 1976; Pique and Michard, 1989; Piqué, 2001; Hoepffner et al., 2005) around the NW boundary of the Paleoproterozoic West African Craton.

Exposures of the Pan-African belt in NW Africa mainly correspond to large inliers within the NE-SW oriented Paleozoic fold belt of the Anti-Atlas (fig. 1.4). Each inlier corresponds to a structural culmination of the Variscan fold belt, but crops out frequently at elevations lower than the overlying less easily eroded Cambrian sediments, which accounts for their traditional name in french *boutonnières*. Pan-African rocks are also exposed in the High Atlas, i.e. in the Ouzellarh salient, which is a granite-rhyolite massif that connects with the Anti-Atlas (fig. 1.4).

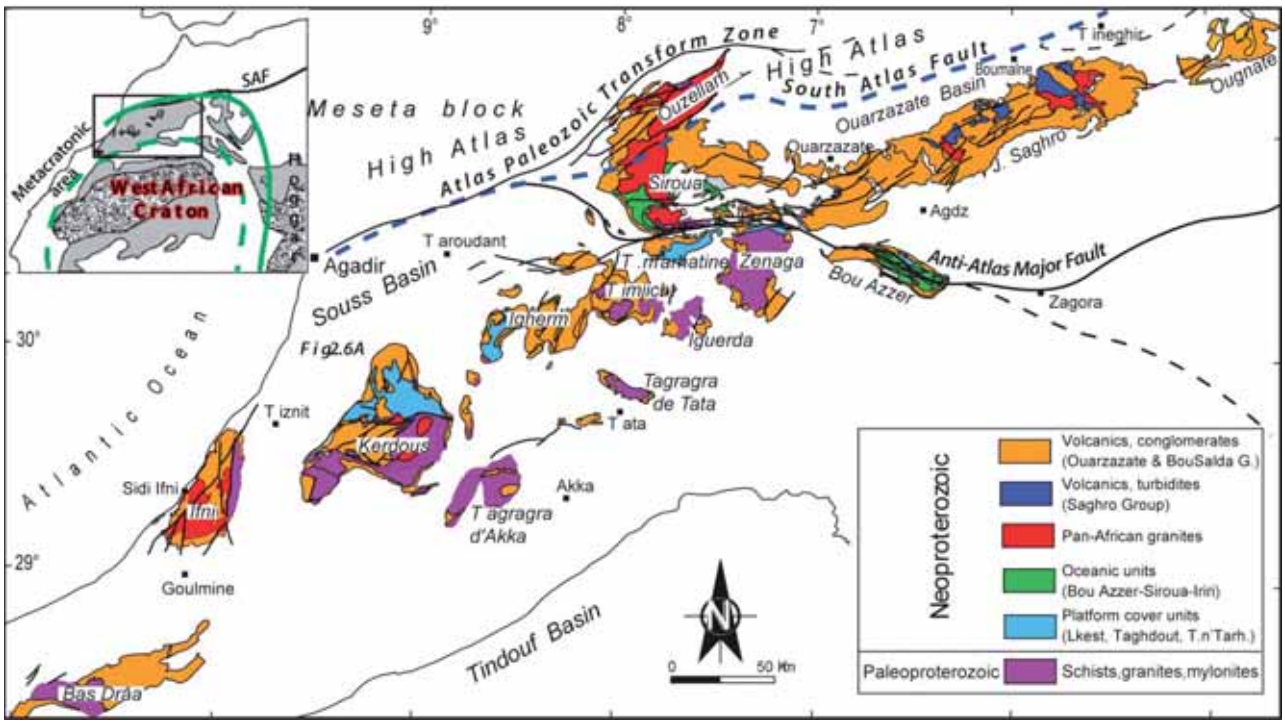

Figure 1.4. General sketch map of the Anti-Atlas Precambrian inliers taken from Gasquet et al. (2008).

In addition to the Anti-Atlas, the Variscan belt is exposed in the Western Meseta and in the High Atlas (fig. 1.3). Based on the differential characteristics of the Western Meseta-High Atlas and the Anti-Atlas, two Variscan domains were defined (Choubert and Faure-Muret, 1962; Mattauer et al., 1972; Michard, 1976; Froitzheim et al., 1988; Pique and Michard, 1989; Hoepffner et al., 2005; Michard et al., 2010):

1) The Meseta Domain, with the Western and Eastern Mesetas, the intervening Middle Atlas and most of the High Atlas to the south, except part of the High Atlas massif south of Marrakech (the Ouzellarh salient; Choubert, 1952), is characterized by detrital and carbonate rocks of Paleozoic age strongly affected by Variscan deformation. Present greenschist- to amphibolite-facies metamorphism and widespread syn- to late-orogenic magmatism. Tectonic vergence is dominantly to the WNW. The Variscan grain trends mainly NNE-SSW, markedly oblique to the post-Paleozoic structures (fig. 1.5).

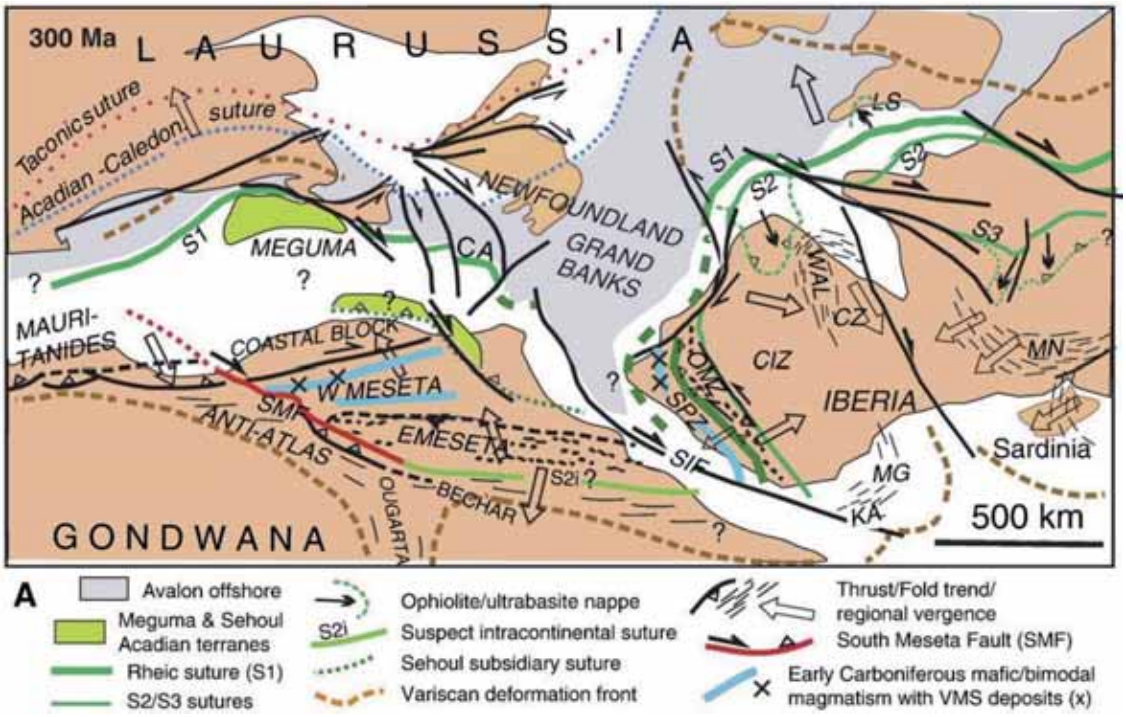

Figure 1.5. Tentative restoration of the Moroccan and Iberian Variscides in the Peri-Atlantic Variscan framework. Source map from Simancas et al. (2005) modified from Michard et al. (2010).

2) The Anti-Atlas Domain, made up of Precambrian granites and andesites/rhyolites deformed by the Pan-African orogeny and onlapped by Lower Paleozoic sedimentary rocks, was only affected by large open folds and sparse thrusts during the Variscan orogeny. It forms the foreland fold belt of the Meseta Domain, being the transitional area with the WAC. The Anti-Atlas belt connects with the Ougarta belt to the SE (Hadoum et al., 2001), both forming an arcuate chain around the WAC. Tectonic vergence is to the ESE, S and SW according to the western, central or eastern position in the arc respectively (fig. 1.5).

The southern boundary of the Meseta is poorly defined. It was first attributed by Mattauer et al. (1972) to the Tizi n'Test fault (TnTF in fig. 1.6), acting as a right-lateral strike-slip fault during the Variscan orogeny (Mattauer et al., 1972; Hoepffner et al., 2005). Pique and Michard (1989) suggest that the boundary, i.e., the Tizi n'Test fault, continues till eastern Morocco as the Eastern Meseta deformation strongly contrasts with that of the Eastern Anti-Atlas, and coined the term of "Atlas Palaeozoic Transform Zone (APTZ)" or South Meseta Fault (SMF in fig. 1.5 and 1.6) for this southern boundary fault. This SMF indents to the north in the Ouzellarh salient (fig. 1.6) (Ouanaimi and Petit, 1992). Whatever the precise trace of the Variscan boundary, we will see in the following chapters that the

rheological contrasts between the folded Paleozoic domain and the rigid Precambrian blocks such as the Ouzellarh salient played a major role on the geometry and location of the Triassic rift and the subsequent Cenozoic thrust belt.

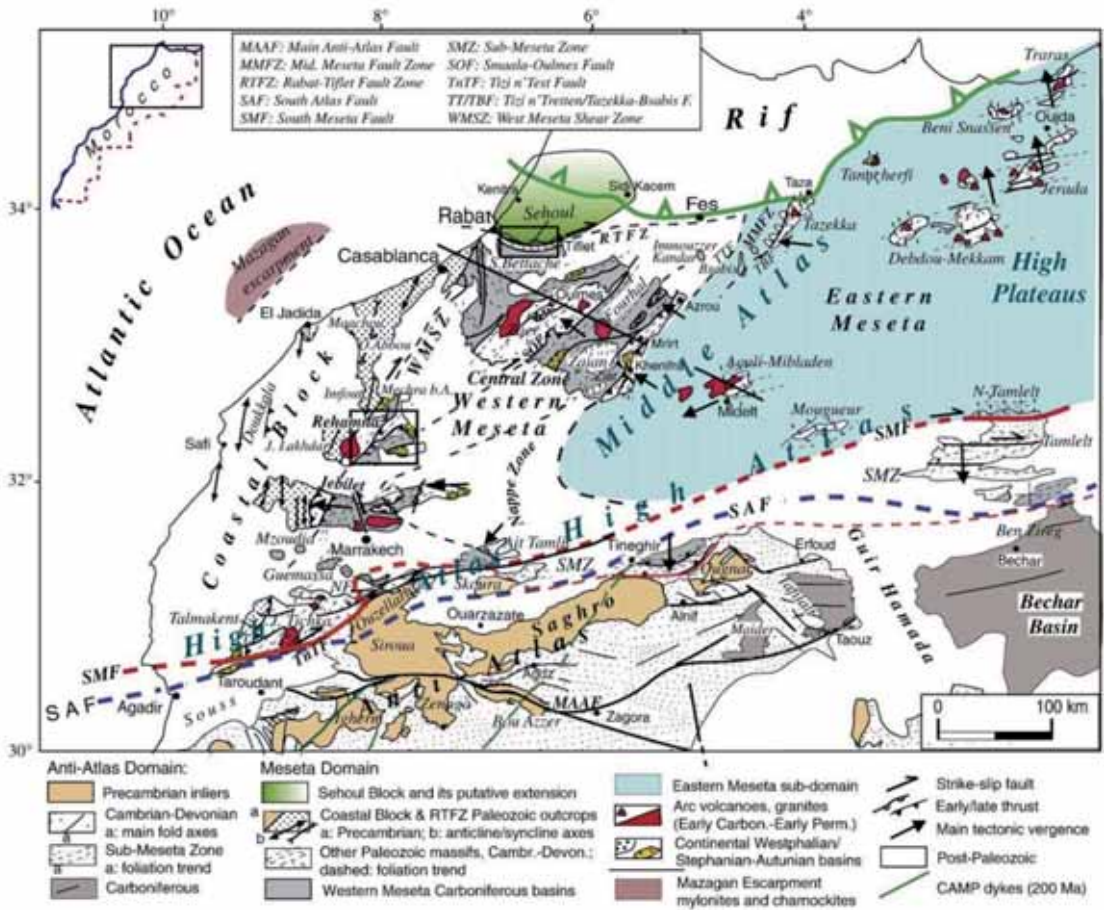

Figure 1.6. Structural map of the Variscan Domains in the Moroccan Atlas (from Michard et al., 2010 modified from Ouanaimi and Petit, 1992; Baidder et al., 2008, Soulaimani and Burkhard, 2008, Michard et al., 2008 and Tahiri et al., 2010).

1.2.2. The Triassic-Jurassic rifting and Cretaceous post-rift stage

A new tectonic regime begins with the breakup of Africa and its separation from North America in Permian times. This caused tension in the continental lithosphere and led to a well-developed rift system that propagated along the eastern North America-West Africa margin (the Atlantic rift), along the Africa-Europe margin (the Tethys rift), and in NW Africa (the High and Middle Atlas rift, hereafter called 'the Atlas rift') (e.g. Van Houten, 1977)(fig. 1.7).

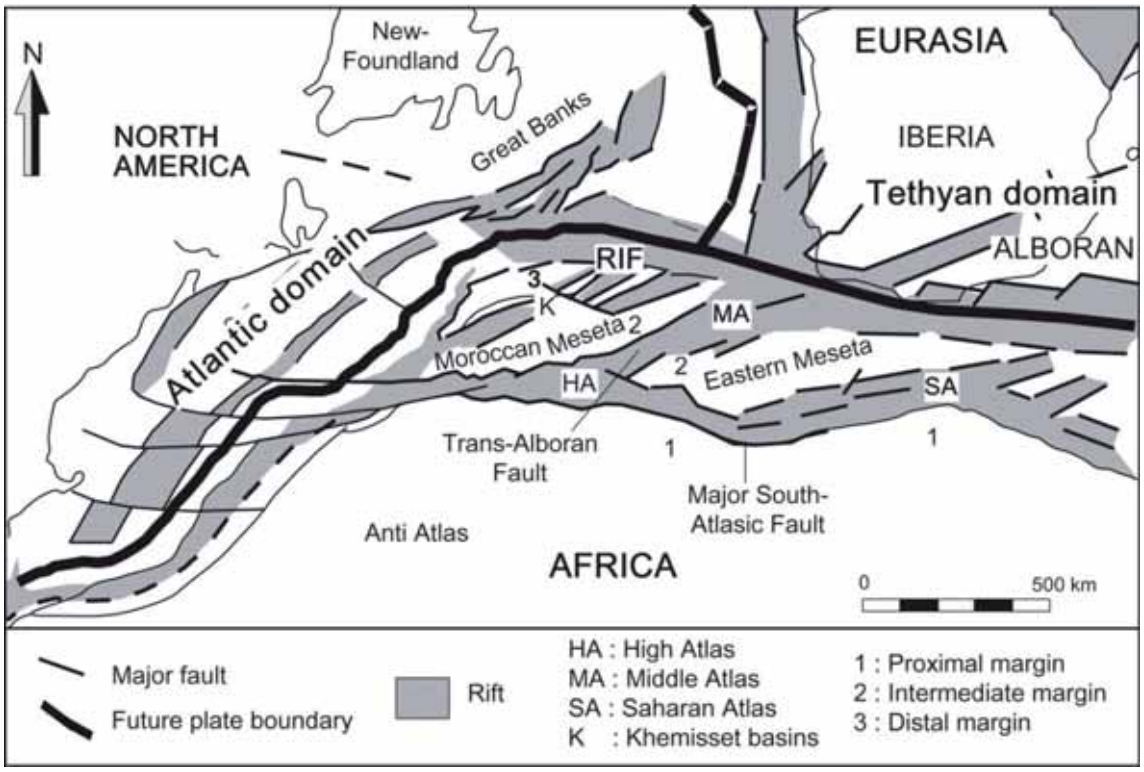

Figure 1.7. Sketchmap of the Triassic-Jurassic rifting along the northern African margin and adjacent regions (from El Harfi et al., 2006 modified from Favre, 1995; Dercourt et al., 2000). In grey it is showed the developed basins to the Jurassic. Morocco corresponds to a triple point, at the intersection of "Central Atlantic rift" (between Africa and North America) and western end termination corner of the Tethys ocean (between Africa and Eurasia).

The Atlas rift developed mainly during the Middle Triassic and the Jurassic in two main branches, one WSW-ENE (which later became the High Atlas) and other SW-NE (which later formed the Middle Atlas) (Choubert and Faure-Muret, 1962; Mattauer et al., 1977; Van Houten, 1977; Manspeizer et al., 1978; Jacobshagen et al., 1988; Laville and Piqué, 1991; Beauchamp et al., 1996; Gomez et al., 2000; Teixell et al., 2003; Arboleya et al., 2004) (fig. 1.7).

The Triassic-Jurassic rift opening in NW Africa was ruled by an extension direction oriented ~NW-SE (present-day orientations in the reference frame of the African plate; Ait Brahim et al., 2002; El Arabi et al., 2003; El Kochri and Chorowicz, 1996; Hailwood and Mitchell, 1971; Laville and Petit, 1984; Laville and Piqué, 1991; Mattauer et al., 1977; Qarbous et al., 2003). The main normal faults developed with a NE-SW direction, perpendicular to the extension direction and nearly parallel to the configuration of the actual continental margin of the NW Africa. Therefore, the Middle Atlas, with an

orientation NE-SW is considered an orthogonal rift, while the High Atlas, with an WSW-ENE direction and numerous internal oblique faults, is considered an oblique rift to the extension direction (fig. 1.8) (El Kochri and Chorowicz, 1996; Arboleya et al., 2004).

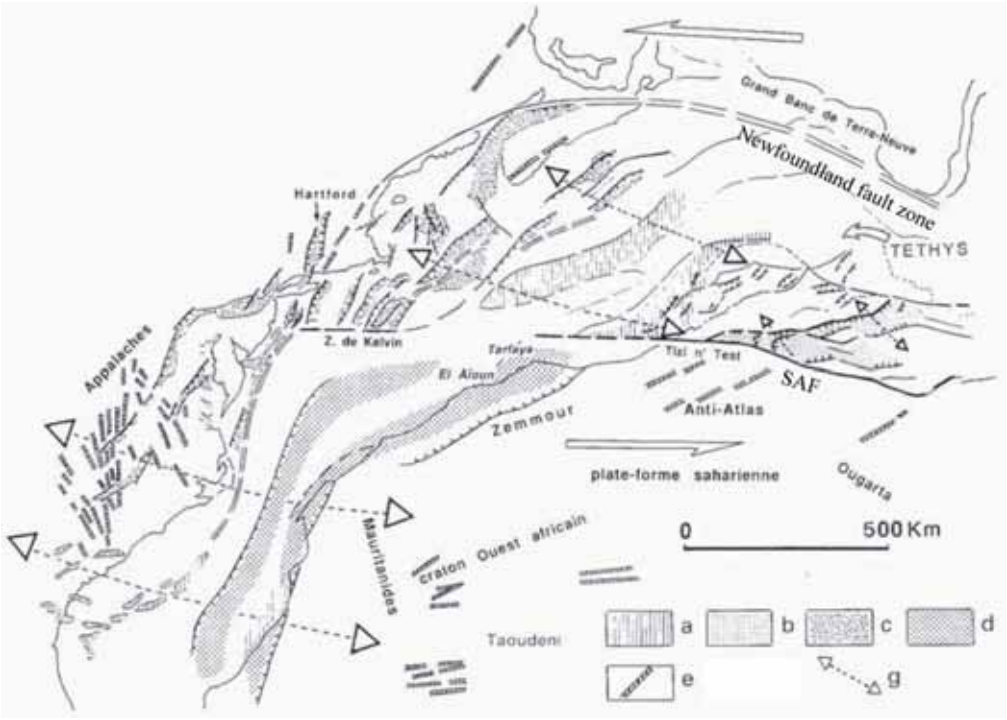

Figure 1.8. Late Triassic reconstruction of North America and Moroccan Atlantic margin (from Laville and Piqué, 1991). a: diapiric areas; b: detrital basins of the Atlas domain; c: detrital basins of the eastern coast of North America; d: Triassic basin of the Atlantic; e: tholeiitic dikes; g: Triassic extensional direction.

As for the High Atlas rifting, due to its obliquity with respect to the general extension direction, two different rifting mechanisms have been proposed by different authors. Authors advocating for strike-slip as the main tectonic regime during the Mesozoic, view the Triassic-Jurassic basins as pull-apart basins limited by major left-lateral strike-slip faults oriented NE-SW to ENE-WSW inherited from late Variscan orogeny (Mattauer et al., 1972, 1977; Proust et al., 1977; Laville and Petit, 1984; Beauchamp, 1988; Laville and Pique, 1991; Ouanaimi and Petit, 1992; Laville et al., 2004). Intra-basin faults, with NNE-SSW to NE-SW orientation are viewed as dip-slip extensional faults (Mattauer et al., 1977; Laville and Petit, 1984; Beauchamp, 1988). Laville and Pique (1991) suggested that the Triassic-Early Liassic pull-apart basins were bounded north and south by two major transform faults, the Newfoundland fault and the South Atlas fault (SAF), which comprises

the Tizi n'Test fault (fig. 1.8). On the contrary, those supporting a dominantly extensional regime, view the main basin-bounding and intra-basin faults as dominantly dip-slip structures, being the rift opened obliquely and not in a pure strike-slip stress regime (Baudon et al., 2009; El Arabi et al., 2003; El Kochri and Chorowicz, 1996; Qarbous et al., 2003; Stets and Wurster, 1982; Van Houten, 1977 El Kochri and Chorowicz, 1988; Arboleya et al. 2004).

The Triassic syn-rift deposits consist of redbeds (Mattis, 1977; Biron, 1982; Beauchamp, 1988) locally capped by basaltic flows belonging to the Central Atlantic Magmatic Province (CAMP) which are dated in the limit between the Triassic and Jurassic periods (Bertrand and Prioton, 1975; Manspeizer, 1982; Knight et al., 2004). Intervening diapiric evaporite layers are also reported but only in the Atlantic margin and in the Central High Atlas (Courel et al., 2003; Hafid et al., 2006; Saura et al., 2013; Tari and Jabour, 2013; Tari et al., 2003). These sediments present a high spatial thickness variation due to their sedimentation in compartmentalized basins during the early rifting.

Since earliest works in the Atlas, most of the Triassic-Jurassic rift paleoreconstructions distinguish two separated domains. An eastern domain connected to the Tethys rift (Central and Easterh High Atlas and Middle Atlas), and a western domain connected towards the Central Atlantic rift (Western High Atlas) (fig. 1.8). An intervening emergent (or poorly subsident) high is placed separating both domains in the present Moroccan Meseta and High Atlas south of Marrakech (so-called "Terre des Almohades", "Dorsale du Massif Hercynien Central" or West Moroccan Arch), due to the poor preservation of Triassic sediments and the absence of Jurassic carbonate deposits in the area (Choubert and Faure-Muret, 1962; Du Dresnay, 1971; Michard, 1976; Laville and Pique, 1991; Stets, 1992; Jabour et al., 2004; Laville et al., 2004; El Arabi, 2007; Frizon de Lamotte et al., 2008, 2009).

In the Atlantic domain (Western High Atlas) the end of the main rifting event is placed in the Triassic-Jurassic boundary (contemporaneously with the accretion of the Atlantic oceanic crust at about 195 Ma; e.g. Sahabi et al., 2004), and carbonate and evaporite weakly faulted sag basins developed during the Jurassic linked to thermal relaxation (Stets, 1992; Medina, 1995; Piqué and Laville, 1996; Le Roy and Piqué, 2001; Hafid et al., 2006; El Arabi, 2007). Triassic-Lower Liassic salt layers were remobilized almost immediately after deposition and breached the surface during the Middle Jurassic, suggesting that diffuse extension lasted during the entire Jurassic. Lower Cretaceous sediments lye on an almost general unconformity, with signals of erosion and a change of

sedimentary environment, dominated by siliciclastic facies (e.g. Frizon de Lamotte et al., 2008 and references therein).

In the Tethys domain (Central and Eastern High Atlas and Middle Atlas) the rifting progressed during the whole Early-Mid Jurassic. In early-mid Liassic times, tectonic subsidence caused a marine transgression in the High and Middle Atlas troughs with sedimentation of carbonates (Du Dresnay, 1971; Warme, 1988). During the Toarcian and early Dogger accelerated rift-related subsidence caused the inundation of the lower Liassic carbonate platforms and deposition of marls (Warme, 1988). In late Dogger the sedimentation changed from marine to continental with deposition of redbeds traditionally called "formation des couches rouges" (Choubert and Faure-Muret, 1962; Jenny et al., 1981; Haddoumi et al., 1998, 2002, 2008, 2010; Andreu et al., 2003; Charrière et al., 2005) which contain abundant pre-Mesozoic clasts and are occasionally interbedded (only in the Central High Atlas) with basalts. These redbeds yield ages from Bathonian to Albian in the Central High Atlas, although punctuated by frequent stratigraphic gaps (Haddoumi et al., 2002, 2008, 2010; Charrière et al., 2005). The upper deposits of this redbeds unit overflowed the Central High Atlas rift margins overlapping the basement in the northern and southern rift shoulders (Anti-Atlas and eastern Meseta area; Teixell et al., 2003). These expansive deposits are referred to as Infracenomanian Unit in the literature (Roch, 1939; Gauthier, 1960; Choubert and Faure-Muret, 1962), poorly constrained in recent works as Barremian-Aptian to Early Cenomanian (Ettachfini and Andreu, 2004; Frizon de Lamotte et al., 2009). Therefore, the Jurassic-Cretaceous boundary is placed inside this redbeds unit, which also represents the transition from a syn- to post-rift stage.

A marine transgression took place during the Cenomanian-Turonian with deposition of platform limestones and dolomites due to a marine entrance from the Atlantic. Above these carbonate deposits again redbeds were deposited which are attributed to the Senonian (Gauthier, 1960; Choubert and Faure-Muret, 1962).

1.2.3. The Atlas orogeny

The Atlas compression took place mainly and extensively in Cenozoic times (Choubert and Faure-Muret, 1962) due to the north-directed movement of the Africa plate with respect to the Eurasia plate which started in Late Cretaceous times (fig. 1.9), and which produced the inversion of the High and Middle Atlas rifts (Choubert and Faure-Muret, 1962; Mattauer et al., 1977; Frizon de Lamotte et al., 2000; Gomez et al., 2000; Piqué et al., 2002; Teixell et al., 2003; Arboleya et al., 2004). The earliest indications of folding are provided by the uppermost Cretaceous to Eocene inliers within the High Atlas or in the southern and

northern thrust fronts (occasional angular and progressive unconformities in deposits of these ages; Froitzheim et al., 1988; Herbig, 1988; Laville et al., 1977; Tesón, 2009). However, their rare occurrence suggest that this deformation was really limited and the areal distribution of subtabular limestone deposits of Paleocene to mid Eocene age still do not conform to an orogen-foreland basin system (Herbig and Trappe, 1994; Tesón and Teixell, 2008; Tesón, 2009).

As for the main thrusting episode in the Atlas, different phases from Oligocene to Pleistocene have been proposed based of syn-tectonic sediments, although there are marked discrepancies among different authors that have faced the subject (Laville et al., 1977; Fraissinet et al., 1988; Görler et al., 1988; Jacobshagen et al., 1988; Harfi et al., 1996; Frizon de Lamotte et al., 2000; Tesón et al., 2010). Field observations combined with magnestostratigraphy carried out in the Sub-Atlas thrust belt north of the Ouarzazate basin (fig. 1.9), which contain the best sedimentary record of the Atlas mountains building (e.g. Tesón and Teixell, 2008; Tesón, 2009), show that main thrusting in external fold-and-thrust belt begins during the Oligocene or early Miocene and extends up to recent times (Morel et al., 2000; Arboleya et al., 2008; Tesón and Teixell, 2008; Tesón et al., 2010). The initiation of orogeny in the High Atlas hinterland was placed in mid Eocene times (Lutetian) on the basis of the occurrence of sandstones and microconglomerates of this age, interpreted as first foreland basin deposits (Harfi et al., 1996; Frizon de Lamotte et al., 2000; Tesón and Teixell, 2008; Tesón et al., 2010) although the chronology of deformation in the internal parts of the High Atlas is little constrained. Oligocene-Miocene apatite fission track ages recorded in the High Atlas south of Marrakech (Missenard et al., 2008; Balestrieri et al., 2009; Ghorbal, 2009) and thermal modeling of AFT in the Central High Atlas (Barbero et al., 2007) are consistent with a Neogene age of main thrusting.

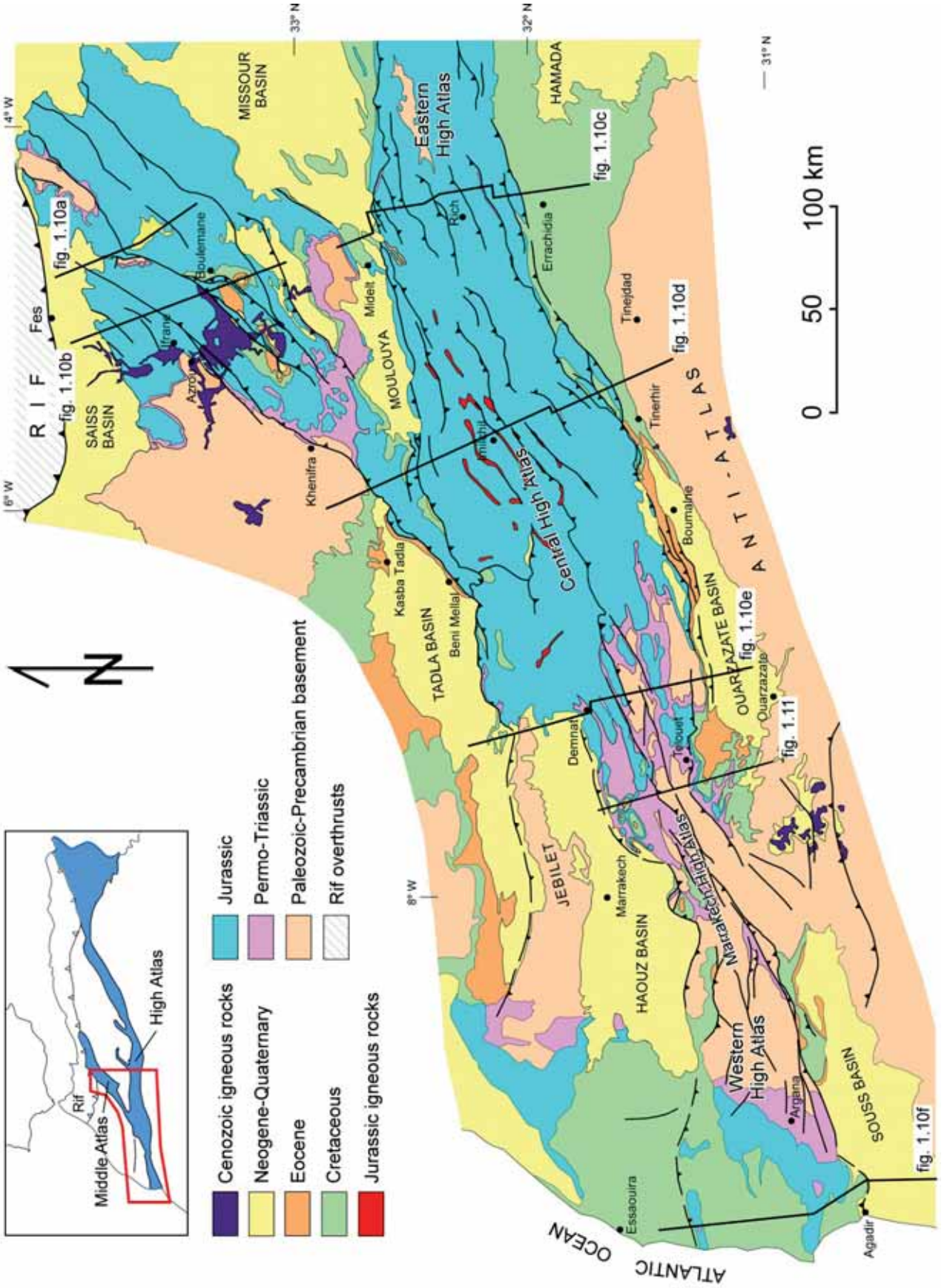

Figure 1.9. Geologic map of the Moroccan High and Middle High Atlas. Slightly modified from Teixell et al. (2007).

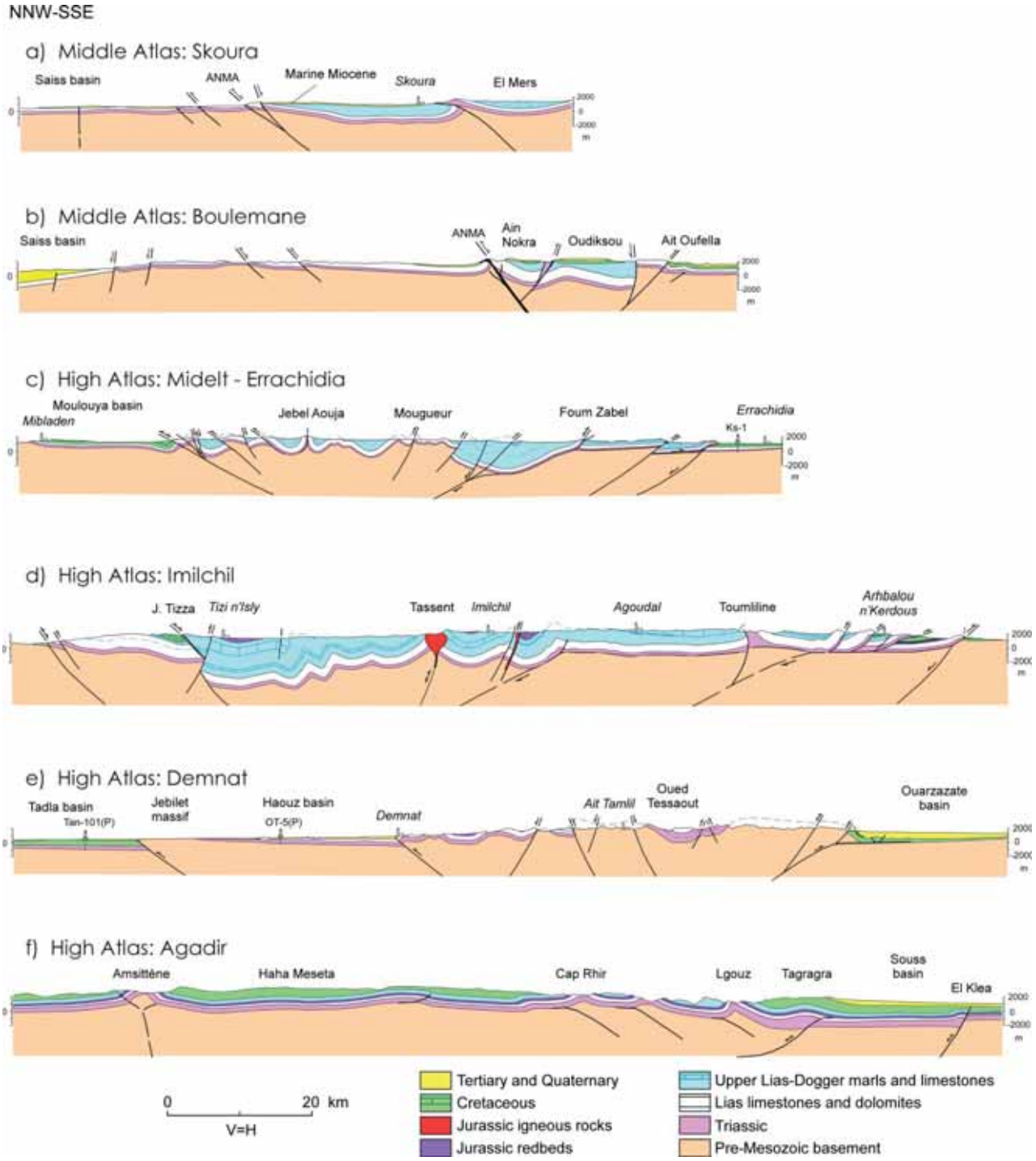

Figure 1.10. Cross-sections of the Moroccan High and Middle High Atlas (see location in fig. 1.9). Section a) from Babault et al. (2008). Section b) from Arboleya et al. (2004). Section c), d) and e) from Teixell et al. (2003). Section f) based on works from Amrhar (1995) and Frizon de Lamotte et al. (2000). Extracted from Teixell et al. (2007).

Erosional processes dominate during the Pliocene and early Quaternary in the Atlas and adjacent basins in spite of shortening is still going out at low rates as indicated by the deformed quaternary terraces (Dutour and Ferrandini, 1985; Morel et al., 1993, 2000; Sébrier et al., 2006; Arboleya et al., 2008; Pastor et al., 2013) and seismicity (Coisy and Frogneux, 1980; Medina and Cherkaoui, 1991, 1992).

The first works presenting structural cross-sections of the Atlas belts are those of Choubert and Faure-Muret (1962), Faure-Muret and Choubert (1971), Schaer (1987) and Beauchamp et al. (1999). More detailed regional cross-sections for the Central High Atlas, balanced and restored, were presented by (Teixell et al., 2003) (Midelt-Errachidia, Imilchil and Demnat sections in fig. 1.10c,d,e). Missenard et al. (2007) presented a synthetic cross-section not balanced through the High Atlas south of Marrakech (fig. 1.11) and Teixell et al. (2007) presented a series of synthetic cross-sections that includes the Western High Atlas and the Middle Atlas (fig. 1.10). These cross-sections are oriented N-S and NNW-SSE, nearly parallel to the assumed regional shortening direction (Mattauer et al., 1977; Gomez et al., 2000; Rosenbaum et al., 2002).

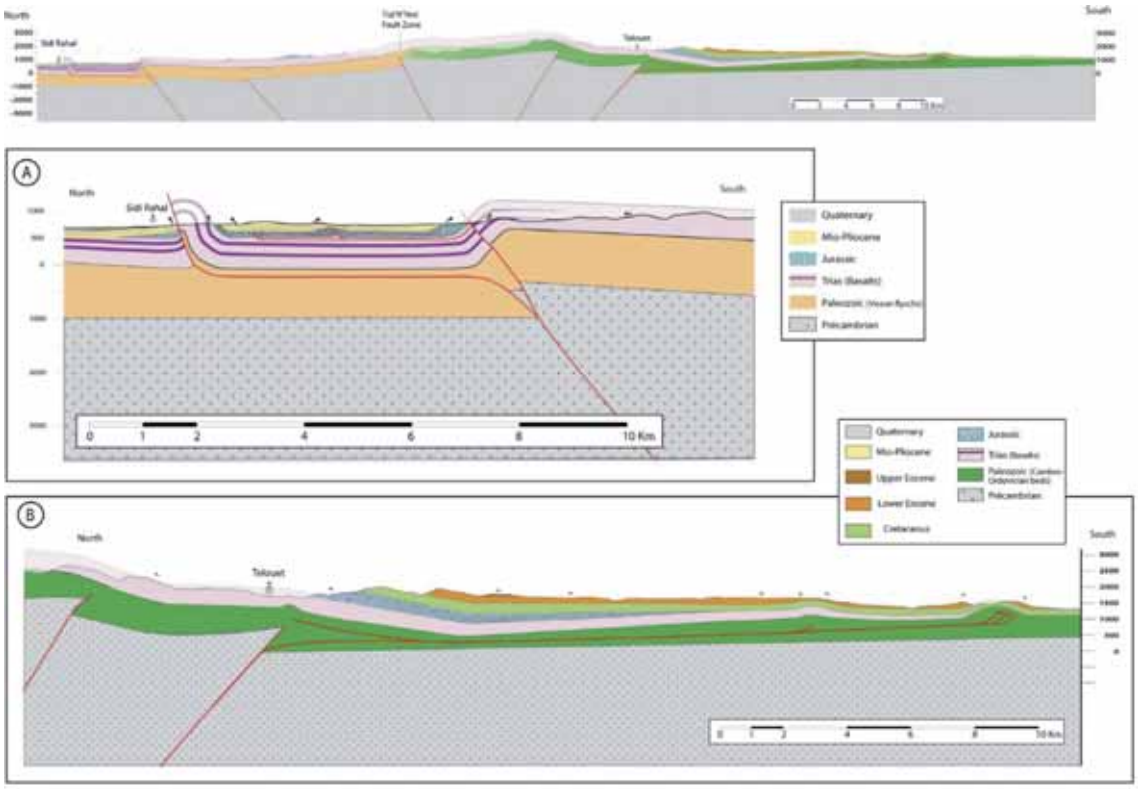

Figure 1.11. Synthetic N-S cross-section of the High Atlas south of Marrakech, from Sidi Rahal to Telouet region (see location in fig. 1.9). (a,b) Enlargement of the North and South Atlas Fronts (from Missenard et al., 2007).

The main structural features of the Atlas belts, summarized in Teixell et al. (2007), are as follows (fig. 1.10):

- Deformation is heterogeneously distributed and focused in narrow belts separated by less deformed tabular blocks.

- Most thrusts derive from the inversion of Mesozoic extensional faults, which is manifested by marked thickness changes of Mesozoic deposits across the faults.

- Basement is frequently involved in folds and faults (thick-skinned tectonics).

- Not all the folds are linked with faults, and formed as a result of buckling or diapiric processes.

- Thin-skinned compressional tectonics is focused in narrow belts south of the High Atlas. In the northern front, the basement is also involved.

- The Middle Atlas is structurally simpler than the High Atlas with more presence of little deformed tabular areas.

Some authors suggested transpressive tectonics during the inversion of the Atlas rifts (Fedan, 1988; Gomez et al., 1999). However, there are no clear evidences of strike-slip movements in thrust faults (Zouine, 1993; Teixell et al., 2003) and microtectonic data indicate a regional compressive stresses reorientation into the main faults, producing local NW-SE stresses which did not favor strike-slip movements (El Kochri and Chorowicz, 1996).

Restored cross-sections from Teixell et al. (2003) show that total orogenic shortening across the High Atlas was moderate (24% to 15%), decreasing from east to west in the Central High Atlas (fig. 1.10). For the Western High Atlas no restored cross-sections exist but shortening is supposed to be smaller (Amrhar, 1995; Frizon de Lamotte et al., 2000; Hafid et al., 2006; Missenard et al., 2007). Missenard et al. (2007) suggests 3 km of shortening (less than 4%) for the High Atlas south of Marrakech (fig. 1.11) which is not compatible with our data as few km to the east, we estimate a minimum shortening of 20 km only in the southern flank of the High Atlas (fig. 10e; Teixell et al., 2003).

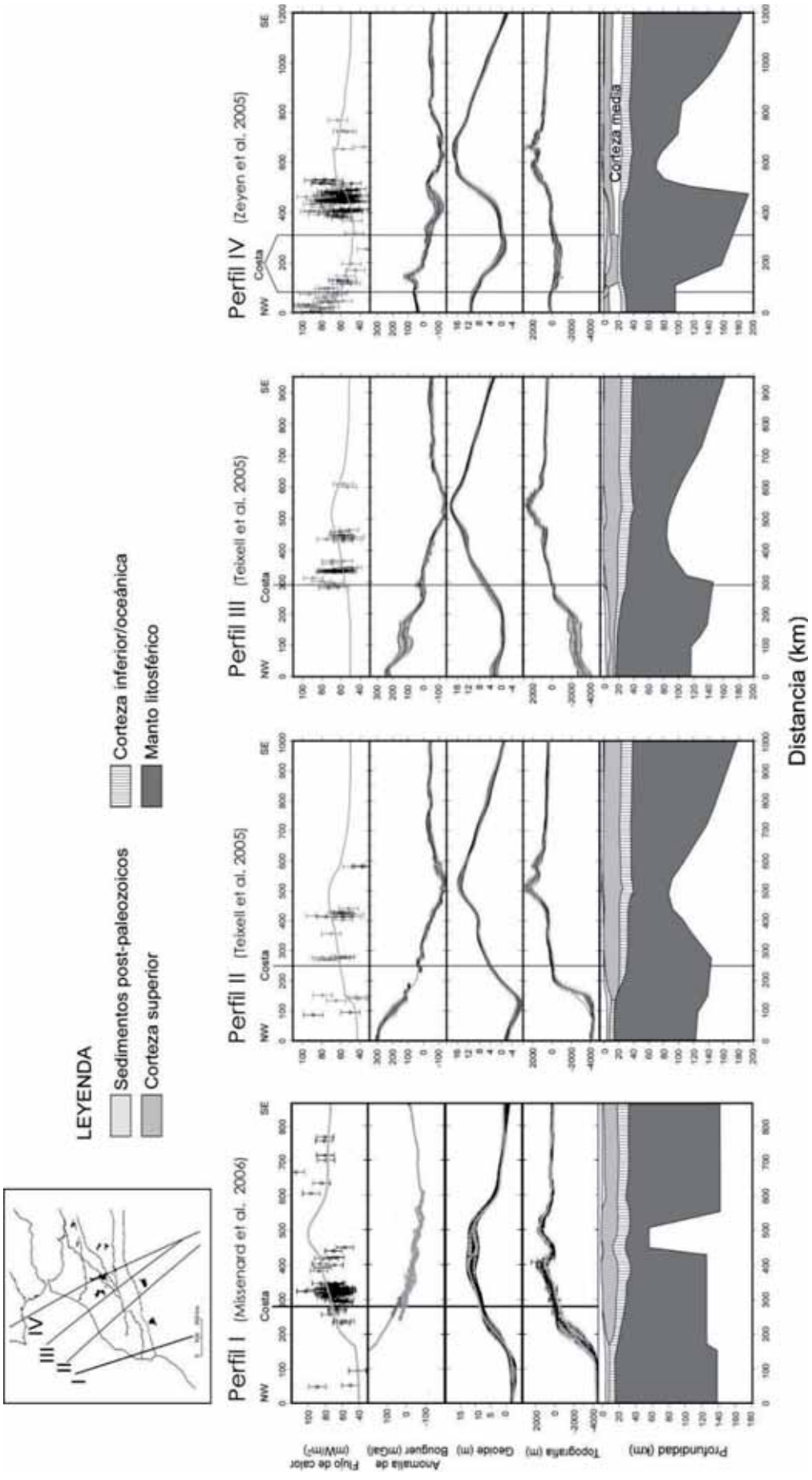

Figure 1.12. Litospheric models of the High and Middle Atlas and adjacent regions based on potential fields (redrawn from Tesón, 2009 after Teixell et al, 2005, Zeyen et al., 2005 and Missenard et al., 2006).

Teixell et al. (2003) compared the high mean elevation of the Atlas mountain belts (and also of the surrounding peripheral plateaux and plains, in which the mean elevation is above ~1200 m) and their moderate shortening and concluded that the Atlas crustal thickening is insufficient to account for the high topography, and the system is isostatically undercompensated at crustal level (Van Den Bosch, 1971; Makris et al., 1995; Ayarza et al., 2005).

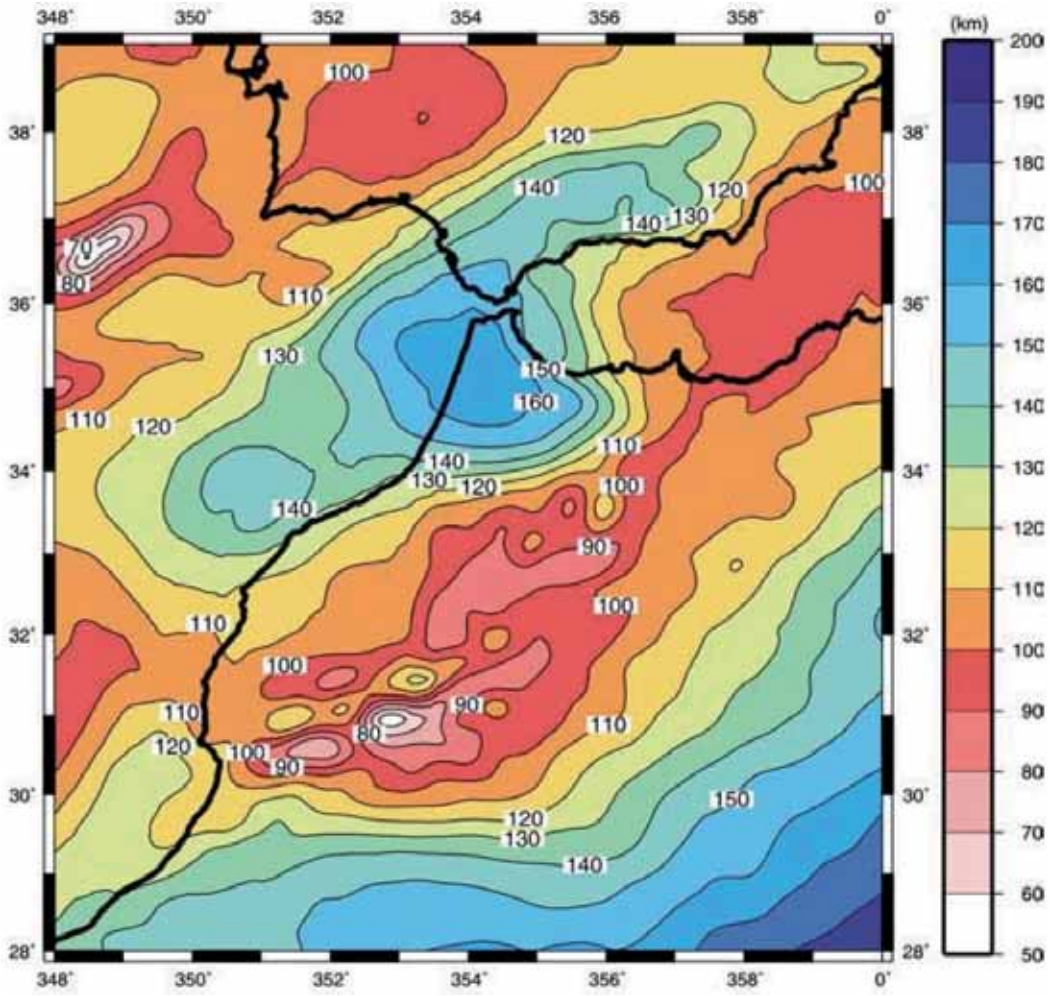

Figure 1.13. Modelling of the lithosphere base obtained using topography and geoid anomaly using 2780 kg/m^3 for crust density for the entire Moroccan Atlas domain. Note the SW-NE lithospheric thinning following the High and Middle Atlas (from Fullea et al., 2007).

Sub-crustal phenomena, such as a hot, thinned or delaminated lithosphere, have been proposed as an alternative reason for the elevated topography (Seber et al., 1996; Ramdani, 1998; Teixell et al., 2005). Potential fields modelling of the lithospheric structure, based on gravity data, geoid, topography and heat flow, argued for a thinned lithospheric mantle beneath the Atlas mountains of Morocco (from 170 km of thickness in the African craton to 80 km below the Atlas chains) (Teixell et al., 2005; Zeyen et al., 2005; Missenard et al., 2006) (fig. 1.12). A 3D geometrical modelling of the lithosphere base is presented by Fullea et al. (2007) (fig. 1.13). The mantle related uplift in the Atlas region is proposed to have started some 15 Ma ago, a timing indirectly inferred from the chronology of associated magmatic events (Teixell et al., 2005; Missenard et al., 2006). Babault et al. (2008) delayed the main phase of uplift in post-Miocene to Late Pliocene times from stratigraphic paleoelevation markers (1000 m of uplift in the past 5 Ma at *c.* 0.2 mm a^{-1}).

1.3. Aims of this study

The High Atlas has been traditionally subdivided into three differentiated segments (Michard, 1976) (fig. 1.14):

- The Eastern High Atlas, from the Ziz valley to the Saharan Atlas in Argelia. It is dominated by gently folded Jurassic rocks and is topographically lower than the Central and Western High Atlas.

- The Central High Atlas, between the Oued Ziz and the Oued Rdat. Jurassic deposits dominate and contain the highest mean elevations of the whole High Atlas. Basement outcrops only in the Mougueur, Skoura and Aït Tamlil culminations.

- The Western High Atlas, from the Atlantic coast to Oued Rdat. Basement outcrops extensively to the center and Mesozoic rocks to the west and east. Inside the western High Atlas, the High Atlas south of Marrakech (the Marrakech High Atlas or MHA), where this thesis is focused, is an area where basement is extensively exposed and that contains remnants of early syn-rift Triassic basins (red square in fig. 1.14). The highest summits of the High Atlas are located here, more than 4000 m high.

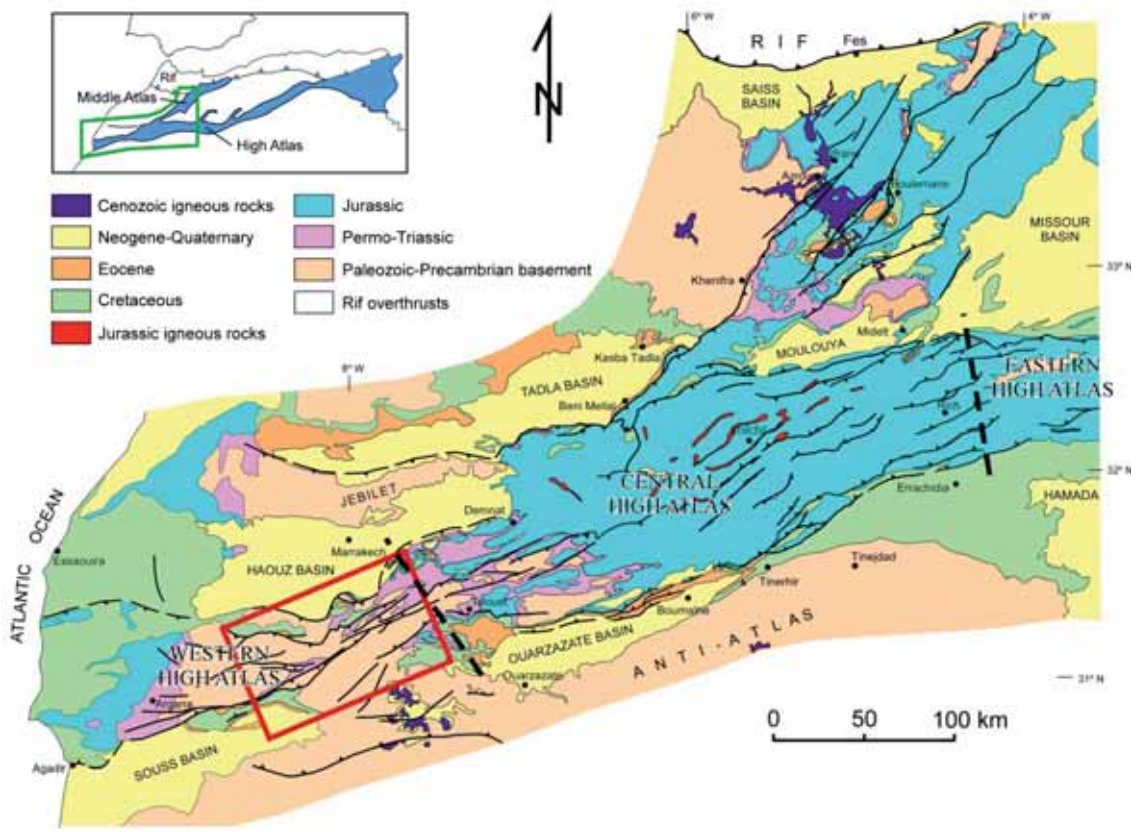

Figure 1.14. Geologic map of the High and Middle Atlas (from Teixell et al. 2007). Limits between different areas in the High Atlas defined by Michard (1976) are showed, also, the area studied in this thesis (red square).

The main objectives of this study can be grouped as follows:

- Fault kinematics and the evolution of the Triassic rift

The moderate (but unknown) shortening and the major exposures of basement and Triassic syn-rift deposits make the Marrakech High Atlas an ideal area to investigate the long-term evolution of a rift, providing the uncommon opportunity to study field analogues of pre-salt structures in early rift deposits (e.g. Karner and Gamboa, 2007) which are often obliterated due to strong inversion in field cases (e.g. Amilibia et al., 2008; Gillcrist et al., 1987; McClay et al., 1989), or poorly imaged in seismic data. At the same time, exposures in the Marrakech High Atlas permit the detailed analysis of the geometry and kinematics of superimposed extensional and compressional structures and the influence they exert over one another.

Numerous studies have been carried out concerning the Triassic rift basins of the Marrakech High Atlas, including discussions on the main opening mechanisms. Even so, the principal structural aspects are still controversial. Among these is the contrasting interpretation of the main fault kinematics during the rifting stage, viewed as dip-slip or strike-slip (see discussion in section 1.2.2) and during the Atlas orogeny. The role played by inherited basement anisotropy (i.e. Precambrian massifs and Variscan faults and folds, see section 1.2.1) in the rift development and inversion is also debated (e.g. Laville and Pique, 1991; Missenard et al., 2007).

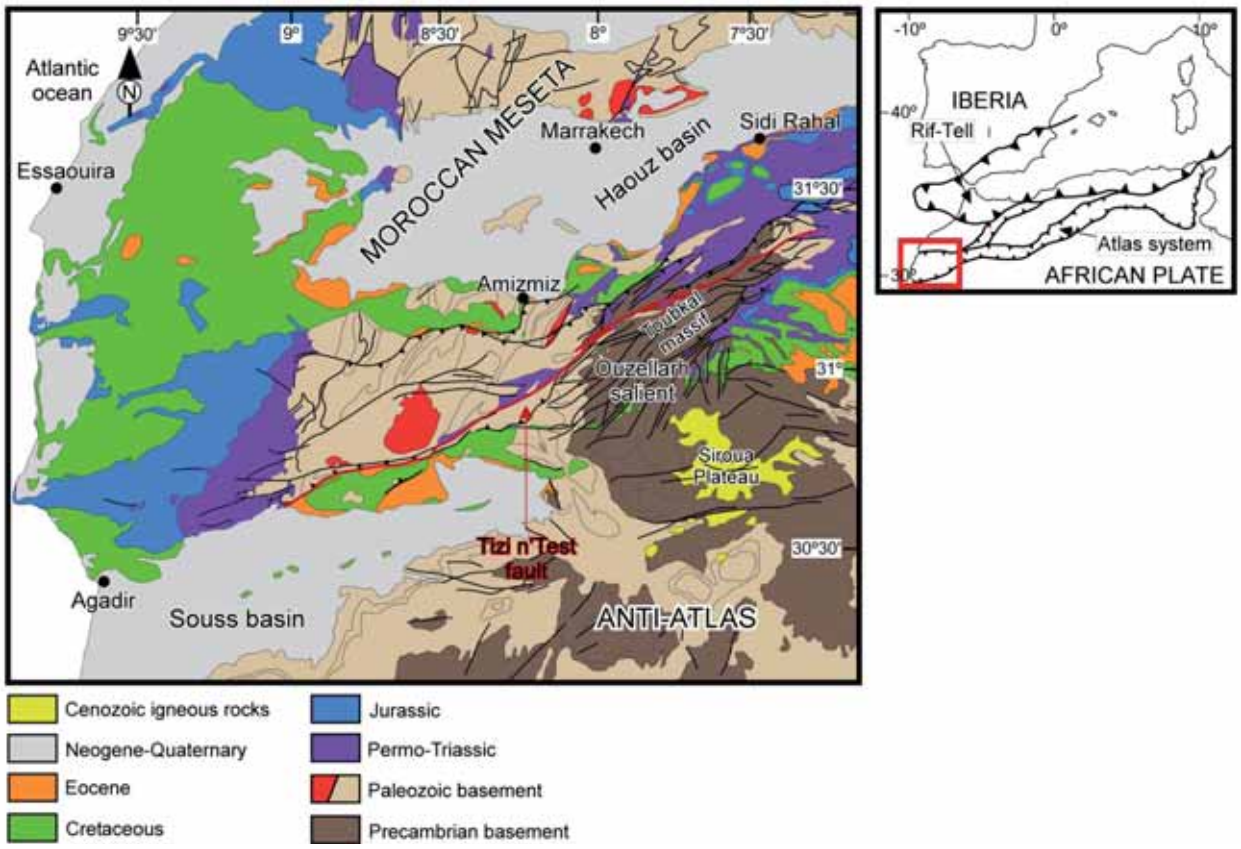

Figure 1.15. Geologic map of the western and Marrakech High Atlas (modified from Hollard, 1985).

A much debated structure is the Tizi n'Test fault, a Triassic basin-bounding fault defined as a major structure almost 280 km long (in red in fig. 1.15) inherited from at least Paleozoic times (see discussion in section 1.2.1). For some authors, the Tizi n'Test fault is interpreted during the Atlas rift as a left lateral strike-slip/transform fault with slip of tens of km (Petit, 1976; Mattauer et al., 1977; Laville and Piqué, 1991)(e.g. fig. 1.10); by others, it is viewed as a normal fault with minor strike-slip movements (Binot et al., 1986;

Qarbous et al., 2003). The polemic continues during the rift inversion stage, and the fault has been interpreted as a thrust throughout the Tertiary (Laville et al., 1977; Proust et al., 1977; Binot et al., 1986; Froitzheim et al., 1988; Qarbous et al., 2008), as a transpressive fault with a modest left strike-slip movement (Mattauer et al., 1977) or as a dextral transpressive fault still active in the Quaternary (Delcaillau et al., 2011).

With the purpose of shedding light on these controversial points, **Chapter 2** documents fault and basin geometries of Triassic basins from the Marrakech High Atlas, bordered by the Tizi n'Test fault. We have emphasized the distinction between extensional and compressional structures and between dip-slip and strike-slip kinematics. Due to the modest inversion of the rift and to the exceptional preservation of rifting structures, a new paleogeographic reconstruction of the Marrakech High Atlas to the Triassic is presented. The study examples constitute good analogues for the deep parts of the Atlas rift, buried under thick Jurassic sediments in the remainder of the Atlas mountains, and for the Triassic pre-drift basins of the Atlantic margin that are masked under salt layers in seismic data (Tari et al., 2003; Tari and Jabour, 2013) as well as, in general, for the exploration of deep rift basins. This chapter has been published in the journal Tectonophysics (Domènech et al. 2015).

- Thermochronology clues to the development and extent of the Mesozoic rift in the Marrakech High Atlas and the timing of rift inversion (Atlas orogeny)

Another matter of debate in the Marrakech High Atlas concerns the degree of development, if it ever existed, of a former Jurassic rift. The poor preservation of Triassic deposits (specially east of the Marrakech High Atlas; fig. 1.15) and the lack of massive carbonate and shale syn-rift deposits of Jurassic age (which are up to 5000 m in the Central and Eastern High Atlas; Choubert and Faure-Muret, 1962) has been attributed classically to a poor or no development of the Triassic-Jurassic rift, being the area an emergent high, separating the Tethys rift to the east from the Atlantic rift to the west (see discussion in section 1.2.2).

However, recently obtained low-temperature thermochronologic data (AFT and (U-Th)/He in apatites) in the basement rocks of the Moroccan Meseta and in the northern and southern High Atlas foothills (fig. 1.15) (Ghorbal et al., 2008; Balestrieri et al., 2009; Ghorbal, 2009; Saddiqi et al., 2009) suggest a Triassic-Jurassic moderate subsidence followed by a period of exhumation during the Mid Jurassic to the Early Cretaceous that could also explain the lack of syn-rift deposits in the Marrakech High Atlas (see paleoreconstructions in Frizon de Lamotte et al., 2008). Missenard et al. (2008) and

Balestrieri et al. (2009), based on a few AFT dates of the Marrakech High Atlas axial zone, attribute the lack of Jurassic rift deposits to erosion during the Neogene.

As for the Atlas orogenic evolution, also debated is the precise timing of the main deformation and uplift phase during the inversion of the rift, be them convergence- or mantle buoyancy-related. Different phases of deformation and mantle-driven uplift have been proposed from Oligocene to the Pleistocene (see discussion in section 1.2.3).

Being syn-orogenic deposits poorly developed or dated in the Marrakech High Atlas and peripheral basins, and as only limited thermochronologic data are available (Apatite Fission Track and (U-Th)/He ages by Balestrieri et al., 2009, Missenard et al., 2008 and Ghorbal 2009), in **Chapter 3** I present apatite and the first zircon (U-Th)/He ages and thermal models for a subset of samples collected in vertical profiles in the Marrakech High Atlas along two NNW-SSE structural transects across the range (zHe has a higher closure temperature and, in consequence, can constraint older exhumation events). The combination of the (U-Th)/He in zircons and apatites and the constrained crustal structures of the area, presented in **Chapter 2,** allow to quantify the spatial and temporal patterns of cooling in the Marrakech High Atlas from the Triassic-Jurassic rift to the present. I present two sections, restored to selected steps since the rifting, based on the zHe and aHe ages and on the thermal models.

1.4. Methodology

1.4.1. Field-based structural analysis

This thesis is based on nearly five months of field work, where the main objectives were to elaborate a detailed scale geologic and structural map and the collection of samples for thermochronologic analysis. A micro- to meso- scale structural analysis was also carried out. Cross-sections and restored cross-sections were elaborated using the 2DMove software using the built-in construction and the restoration algorithms *(fault-parallel flow* and *flexural slip unfolding)*.

1.4.2. Thermochronologic analysis and thermal modelling

Sample processing and zircon and apatite (U-Th)/He analysis was carried out at the Jackson School of Geosciences of the University of Texas-Austin under the supervision of Dr. Danniel Stockli. Thermal modelling was performed using the QTQt software of

Gallagher (2015) (see also Gallagher et al., 2009 and Gallagher, 2012 for details on the modelling technique).

Description of the (U-Th)/He dating technique

Apatite and zircon (U-Th)/He dating are well-established thermochronometric techniques that are widely employed in tectonic studies (e.g. Biswas et al., 2007; Ehlers and Farley, 2003; Macaulay et al., 2014; Stockli, 2005; Vacherat et al., 2014). (U-Th)/He dating makes use of the radioactive decay of alpha particles (α-decay) from ^{238}U, ^{235}U, ^{232}Th and ^{147}Sm leading to the production of ^{4}He nuclei (i.e., α-particles). Retention of radiogenic ^{4}He in apatite and zircon crystals is regulated by temperature (Zeitler et al., 1987; Lippolt et al., 1994; Wolf et al., 1996; Farley, 2000). The closure temperature for the He thermochronometer (Tc) in zircon is estimated of ~181ºC (Reiners, 2005; Wolfe and Stockli, 2010) while in apatite is ~70ºC (Farley, 2000), although the Tc is highly variable depending on the cooling rate, grain size, and also with radiation damage produced by α-recoil (Reiners and Farley, 2001; Reiners et al., 2002, 2004; Shuster et al., 2006; Flowers et al., 2009; Gautheron et al., 2009; Guenthner et al., 2013). Laboratory experiments and measurements from borehole data indicate that Helium is not retained in apatite at temperatures above 80-90°C and is mostly retained below 40 °C (assuming a cooling rate of 10ºC/Myr) and this defines a He partial retention zone for apatites (aPRZ) (Wolf et al., 1996, 1998; House et al., 1999; Farley, 2000; Stockli et al., 2000). Likewise, a He partial retention zone for zircon (aPRZ) is defined between ~130-200ºC (Reiners et al., 2002, 2004; Wolfe and Stockli, 2010). In addition to diffusive controls on He loss, another factor to take into account is α-ejection, due to emission from U, Th and Sm atoms near crystal edges. The measured date is corrected by a F_T factor, which is a function of the size and shape of the crystal (Farley et al., 1996; Farley, 2000; Ketcham et al., 2011).

The zHe and aHe ages for a given sample may have a high dispersion which exceeds the analytical error. This may arise from diverse factors (e.g., Brown et al., 2013; Cogné et al., 2011; Fitzgerald et al., 2006; Flowers and Kelley, 2011), which include:

1. Intra-sample grain size variation (Farley, 2000; Stockli et al., 2000; Reiners and Farley, 2001; Reiners et al., 2002, 2004). He diffusion studies of apatite have demonstrated that for the (U-Th)/He technique the effective diffusion domain is the physical grain itself and the larger the diffusion domain the higher the closure temperature. Therefore, intra-sample grain size variation in function of sample's thermal history can produce large amounts of dispersion (Reiners and Farley, 2001). In zircons, He diffusion is faster in the c-axis direction than in the c-axis orthogonal direction, and this might suggest that grain

aspect ratios may influence diffusion kinetics (Reich et al., 2007). However, Guenthner et al. (2013) suggest that this crystallographic anisotropy produces a relatively minor effect for interpreting zHe dates compared with effects of radiation damage (discussed below). The recorded grain size is used as the diffusion domain when modelling the thermal history (Gallagher et al., 2009; Gallagher, 2012, 2015).

2. Radiation damage. In apatites, the accumulation of α-recoil damage traps Helium in the crystal structure, impeding diffusion (Nasdala et al., 2004; Reiners et al., 2004; Shuster et al., 2006; Flowers et al., 2009; Gautheron et al., 2009). This is manifested by positive correlations between AHe data and eU (where eU = [U] + 0.235[Th]), since grains with higher eU usually yield older ages (because have a higher closure temperature) than grains with lower eU for the same thermal history in samples that have had a prolonged residence in the helium PRZ. Against this, Zircon He dates also show age-eU correlations related to the effect of the accumulated radiation damage on He diffusion (Reiners, 2005), but the effect is manifested as both positive and negative correlations (Guenthner et al., 2013). Low radiation damage (i.e., zircons with low eU content) causes a decrease in diffusivity because damage zones block the preferred c-axis parallel pathways producing positive age-eU correlations. As damage increases to a threshold (i.e., high eU content in zircons or "old" grains), these zones become increasingly interconnected and form fast diffusion pathways that shrink the effective diffusion domain size and produce negative age-eU correlations. This effect is quantified by radiation damage accumulation models in apatite and zircon (Flowers et al., 2009; Gautheron et al., 2009; Guenthner et al., 2013), recently incorporated in the thermal history modelling software QTQt (Gallagher, 2012, 2015).

3. U and Th zonation within crystals. If the source of α-particles is heterogeneously distributed within a crystal, then more or less ^{4}He may be ejected than expected from a uniform distribution (Farley, 2002). Even so, in apatite, for typical patterns of heterogeneity of U and Th, the dispersion from this cause is unlikely to exceed 10-15 % of the age dispersion. For practical purposes, assuming a uniform concentration of U and Th will not cause significant problems unless the heterogeneity is extreme (Farley et al., 2011; Ault and Flowers, 2012). In the zircon He system, we expect that zonation results in greater fractional date differences. Order of magnitude differences in eU zonation are not uncommon in zircons (e.g., (Reiners et al., 2004; Hourigan et al., 2005; Guenthner et al., 2013), and these can cause large discrepancies in both damage and He concentration.

4. Undetected U-Th-rich inclusions in apatite, which are not dissolved in the routine procedures producing anomalously older ages (due to the U-Th contained in the inclusions will not be measured, but the ^{4}He produced by them will be) (e.g., Farley, 2002; Lippolt et al., 1994). The careful hand picking of apatite grains excludes visible inclusions identified under high magnification polarized light microscopy. Those inclusions smaller than a few μm are unlikely to produce significant He age variation (Vermeesch et al., 2007). In zircons, due to the routine dissolution procedures, inclusions are dissolved and their U-Th content measured.

5. Helium implantation in apatites from external sources (Spiegel et al., 2009; Gautheron et al., 2012). This effect may result from high U- and Th-bearing accessory minerals like monazite or zircon being adjacent to the apatite grain, usually with low U-Th concentration (eU < 3 ppm). The effect may explain occasional individual "rogue" analyses that are much older than any other grain in the sample, sometimes even older than the crystallization age of the rock itself, which is difficult to explain by any other process.

6. Crystal breakage, which could yield either younger or older ages than the whole grain age (Brown et al., 2013).

7. Chemical influence in apatites. It is suggested that different grain Cl content could cause up to ~12-15 % dispersion of AHe ages due to changing the annealing rate of α-recoil damage. Even so, the exactly relation between He diffusion and Cl content has not yet been validated (Gautheron et al., 2013).

For samples that experienced non-simple thermal histories, prolonged residence in the PRZ or partially resetting, the reasons listed above may lead to intra-sample age dispersion exceeding 100%. Intra-sample age dispersion can be more pronounced in detrital rock samples, as different source areas may cause a high variability in the internal characteristics of the apatites and zircons. For that reason, six grains are usually analysed for detrital rocks, while only three grains are analysed for igneous rocks.

As said above, (U-Th)/He dating of the Marrakech High Atlas samples was carried out at the Jackson School of Geosciences. After routine mineral separation of zircon and apatite, euhedral crystals were handpicked based on similarity in morphology, clarity and size. Broken crystals were discarded. Apatites were examined under polarized light to exclude grains containing possible high-uranium/thorium microinclusions using customized Nikon SMZ-U/100 stereomicroscopes. Grain size was measured and recorded in order to apply a correction for α-ejection (F_T, Farley et al., 1996; Farley, 2002) and all grains were

digitally photographed. Crystals were selected with sizes of 70 to 150 μm in width to avoid high errors due to F_T corrections. Apatite and zircon single grain aliquots were placed into a platinum sleeve for thermal gas extraction. Zircons were laser heated with a 20 W Nd:YAG laser for 10 min at ~1300 ºC and repeatedly reheated to ensure complete degassing of the sample (>99%). Extracted gas was spiked with a ^{3}He tracer, cryogenically purified, and measured by isotope dilution on a quadrupole noble gas mass spectrometer. After He extraction, zircon grains were retrieved and unwrapped from Pt tubing before pressure vessel digestion procedure, including spiking with an enriched ^{230}Th, ^{235}U, ^{149}Sm and REE tracer, and subsequent two-stage dissolution using (1) a HF-HNO_3 mixture and (2) 6 N HCl. All parent nuclide concentrations were measured by isotope dilution on a Thermo Element2 HR-ICP-MS, fitted with a CETAC micro-concentric nebulizer and ESI autosampler. Apatites were heated for 5 min at ~1070 ºC and subsequently reheated to ensure complete degassing. After being unwrapped from Pt foil, apatites were spiked using an enriched ^{230}Th, ^{235}U, ^{149}Sm tracer and dissolved in HNO_3. U, Th and Sm concentrations were determined by isotope dilution HR-ICP-MS analysis using a Thermo Element2. (U-Th)/He ages of zircon and apatite grains were calculated using standard F_T corrections using morphometric analyses (Farley et al., 1996; Farley, 2002). Reported age uncertainties (2σ) reflect the reproducibility of replicate analyses of laboratory standard samples and are ~6% (2σ) for apatite and ~8% (2σ) for zircon, respectively (Farley, 2002).

Description of the QTQt software used for thermal modelling

Thermochronometric data of this study were modeled using the QTQt software (Gallagher, 2012). The QTQt software performs inverse thermal history models using the Bayesian transdimensional Markov Chain Monte Carlo (MCMC) approach described by Gallagher et al. (2009). In the MCMC approach, random time-temperature points are generated to approximate a thermal history model, and the data are let to determine the complexity of the inferred model, subject to user-defined constraints. Then, the current thermal history model is perturbed to produce a proposed model. If data fit well the proposed model, this proposed model is accepted and contributes to the overall posterior collection of models; otherwise, it is rejected. This process is repeated many times (specified by the user), updating the current model as appropriate. The choice to replace the current model with the proposed model is made in terms of the data fit (likelihood functions), but the Bayesian approach naturally favors simpler models (Gallagher et al., 2009). The output is an ensemble of models which approximates the posterior distribution of acceptable thermal history models and quantifies the probability. The maximum likelihood model is

the one that best fits the data, in spite that it can be complex as to include features that may not be justified by the data. However, the expected model, which is a weighted mean model, can contain the significant features of all the posterior models, while less constrained features can be averaged out. Measured (U-Th)/He ages are modelled by using a spherical diffusion formulation where both the alpha-ejection and diffusion during the thermal history is simulated.

In order to account for an eU-dependent diffusivity for He, the radiation damage accumulation models of Flowers et al. (2009), Gautheron et al. (2009) (for apatites) and Guenthner et al. (2013) (for zircons) are included in the QTQt software. To allow for uncertainty in the He ages observed, He data can be resampled using a normal distribution based on the observed age with a standard deviation equal to the input error. The QTQt can then use these sampled ages instead of the observed value in the likelihood function. QTQt software also allows resampling the He error which consists of introducing a scaling factor for the input error. Therefore, the data can effectively be treated as being more precise (low scaling factor) or less precise (high scaling factor), relative to the input error. QTQt software can infer the thermal history of a group of individual samples of different elevations, which are treated as a vertical profile. This approach uses the implicit assumption that all samples have experienced a similar form of thermal history, and there have been no major disruptions of this geometrical/structural relationship since the samples cooled through the zircon and apatite HePRZ. In every interation, a thermal history for the uppermost sample and the temperature offset between the uppermost and the lowermost samples are simulated, applying a linear interpolation for the T-t paths of the intermediate samples (Gallagher et al., 2009; Gallagher, 2012, 2015).

Chapter 2

The inverted Triassic rift of the Marrakech High Atlas:

a reappraisal of basin geometries and faulting histories

Chapter 2. The inverted Triassic rift of the Marrakech High Atlas: a reappraisal of basin geometries and faulting histories

2.1. Introduction

This chapter describes the geometry and kinematics of the main faults and Triassic basins of the Marrakech High Atlas. A new synthetic geological map, a series of cross-sections and a Mid Triassic paleoreconstruction are presented in this chapter, the contents of which form the body of a paper published in Tectonophysics (Domènech et al., 2015).

From a structural point of view, the Marrakech High Atlas has a general ENE-trend and can be subdivided into (1) an Axial Zone, characterized by large areas of Precambrian to Paleozoic basement exposure and numerous Triassic rift basins bounded by NE- to ENE-trending faults, and (2) the foothills, characterized by Cretaceous to Cenozoic post-rift to syn-inversion deposits, unconformable over basement or Triassic, and affected by thrust faults and folds with an E to ENE orientation (fig. 2.1).

2.2. Triassic basins in the Marrakech High Atlas

There are five main Triassic basins preserved in the High Atlas of Marrakech. From southwest to northeast they are the Tirknit, Tizi n'Test, Tizi n'Tacht-Imlil and Ourika basins (fig. 2.1b). South of the Toubkal massif, there is the Eç Çour basin (fig. 2.1a). This study focuses on the Tirknit, Tizi n'Test and Tizi n'Tacht-Imlil basins, limited to the south by the Tizi n'Test fault.

Recent accounts of the Eç Çour and Ourika basins (fig. 2.1) (El Arabi et al., 2003; Baudon et al., 2009) characterized both basins as controlled by two main fault trends: N70 and N20-45. The N70 faults controlled the basin opening and were interpreted as normal faults during the Triassic. Facies analysis of the clastic sediments suggests that these two basins were open to the east (i.e. connected to the Tethys) although separated from each other by the Ouzellarh salient. The tectonic significance of the southern border of the Ourika basin, which comprises the continuation of the Tizi n'Test fault zone, is reexamined in the present study (fig. 2.1).

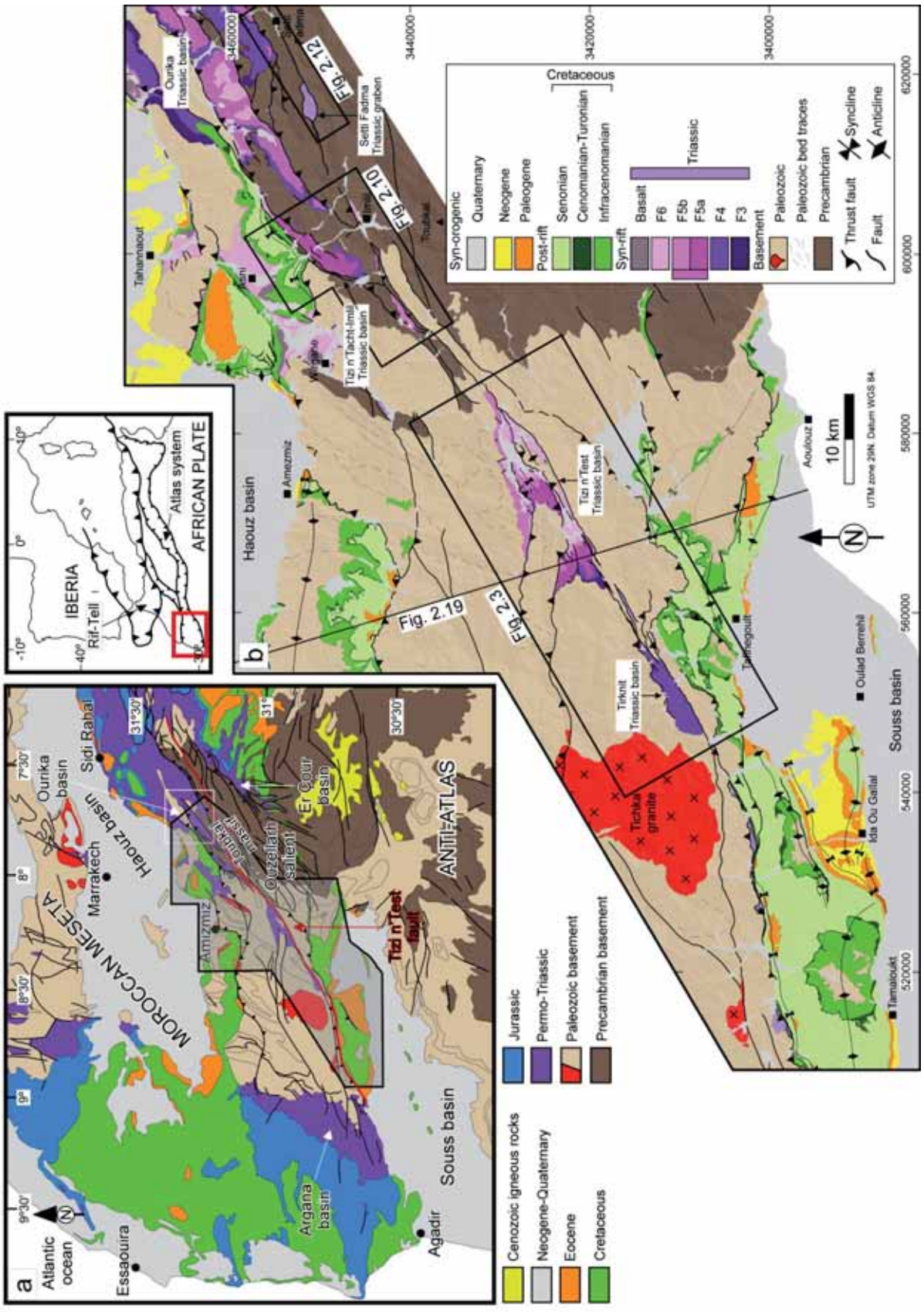

Figure 2.1. (a) Geologic map of the western and Marrakech High Atlas (modified from Hollard, 1985), showing location of the study area detailed in (b). (b) Geologic map of the Marrakech High Atlas showing the main structural elements. Squares correspond to areas described in detail in this chapter.

The Tirknit and Tizi n'Test Triassic basins (fig. 2.1b) were also the subject of previous studies (Petit and Beauchamp, 1986; Qarbous et al., 2003), where the main structural elements were identified and a series of stratigraphic units were defined. A reappraisal of the significance of these basins is presented in the following sections, together with a new detailed study of the Tizi n'Tacht-Imlil basin.

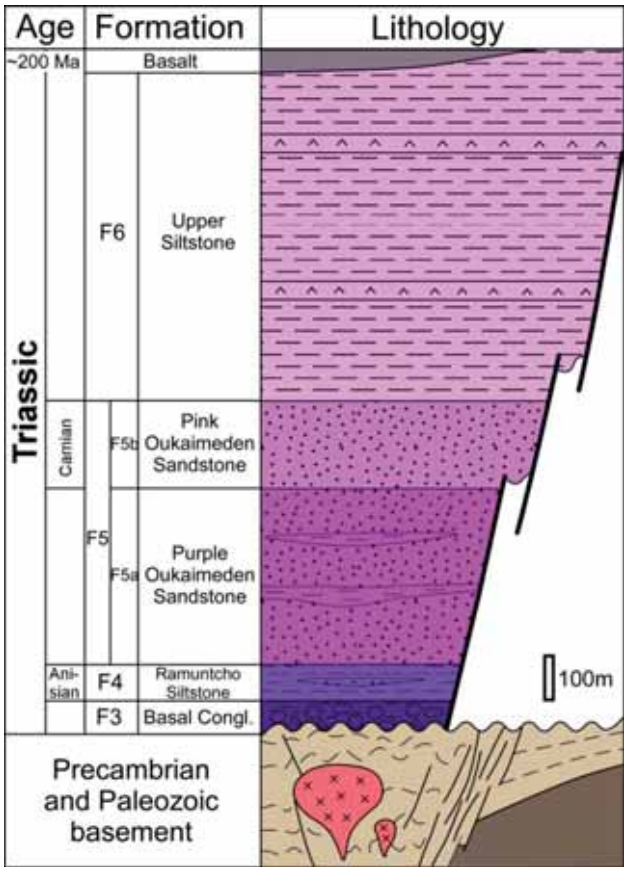

Figure 2.2. Schematic chronostratigraphic diagram showing the main stratigraphic units of the Triassic in the Marrakech High Atlas. The diagram results from a compilation of my data and data from the literature (see text for references). The thickness of the Triassic deposits represented here corresponds to the western part of the Tizi n'Test basin.

The Triassic units consist of red clastic deposits with strong thickness variations controlled by syn-sedimentary faults. Detailed stratigraphic studies were reported in previous publications (Mattis, 1977; Biron, 1982; Petit and Beauchamp, 1986; Beauchamp, 1988; Benaouiss et al., 1996; Qarbous et al., 2003). Together with the Permian, which crops out in the Argana and Ourika basins (fig. 2.1a) out of the study area, six stratigraphic units (F1 to F6) have been defined which can be correlated at the scale of the whole Marrakech High Atlas. The upper four units are Triassic in age and crop out in the study

area (fig. 2.2). From base to top, these are: (1) a Basal Conglomerate (F3), interpreted as a proximal to distal alluvial fan deposit, 10 to 100 m thick, (2) the Ramuntcho Siltstone (F4), deposited in a tidal-flat environment and 60 to 120 m thick, (3) the fluvial Oukaimeden Sandstone (F5), divided into two subunits, the F5a or Purple subunit, with siltstone intercalations and 300 to 400 m thick, and the F5b or Pink subunit, made of massive sandstones ~200 m thick, and (4) the Upper Siltstone (F6), more than 500 m thick, which contains gypsum and halite of alluvial plain to lagoonal origin, the upper limit of which is eroded. Palynological content dates the Ramuntcho Siltstone as Anisian (El Arabi et al., 2006) and the Pink Oukaimeden Sandstone as Carnian (Cousminer and Manspeizer, 1976; Biron and Courtinat, 1982). The Upper Siltstone is elsewhere overlain by tholeiitic basalts of the Central Atlantic Magmatic Province (CAMP) that yield Late Triassic to Early Liassic ages (Bertrand and Prioton, 1975; Manspeizer, 1982; Knight et al., 2004). In the study area, F3, F4 and F5a are always limited by faults while F5b and F6 are either limited by faults or lie unconformably on basement. The thicknesses reported above (also shown in fig. 2.2) correspond to the example thickness of the units in the western part of the Tizi n'Test basin (see fig. 2.3 and 2.4d). The distribution and approximate thickness variations of the different stratigraphic units are illustrated in cross sections of fig. 2.4 and 2.10.

2.3. Structural analysis of the Triassic basins

I have carried out a detailed analysis of the main structural features of three of the main Triassic basins, the Tirknit, the Tizi n'Test, and the Tizi n'Tacht-Imlil basins, and of the small Setti Fadma Triassic graben south of the Ourika basin (fig. 2.1b). The structures have been classified on the basis of their role during the Triassic rifting and the Cenozoic compression. For the sake of clarity, the main faults in the study area have been labeled by numbers. Arabic numbers indicate faults active during the rifting stage, whereas roman numbers denote faults active during the inversion (e.g. fig 2.3).

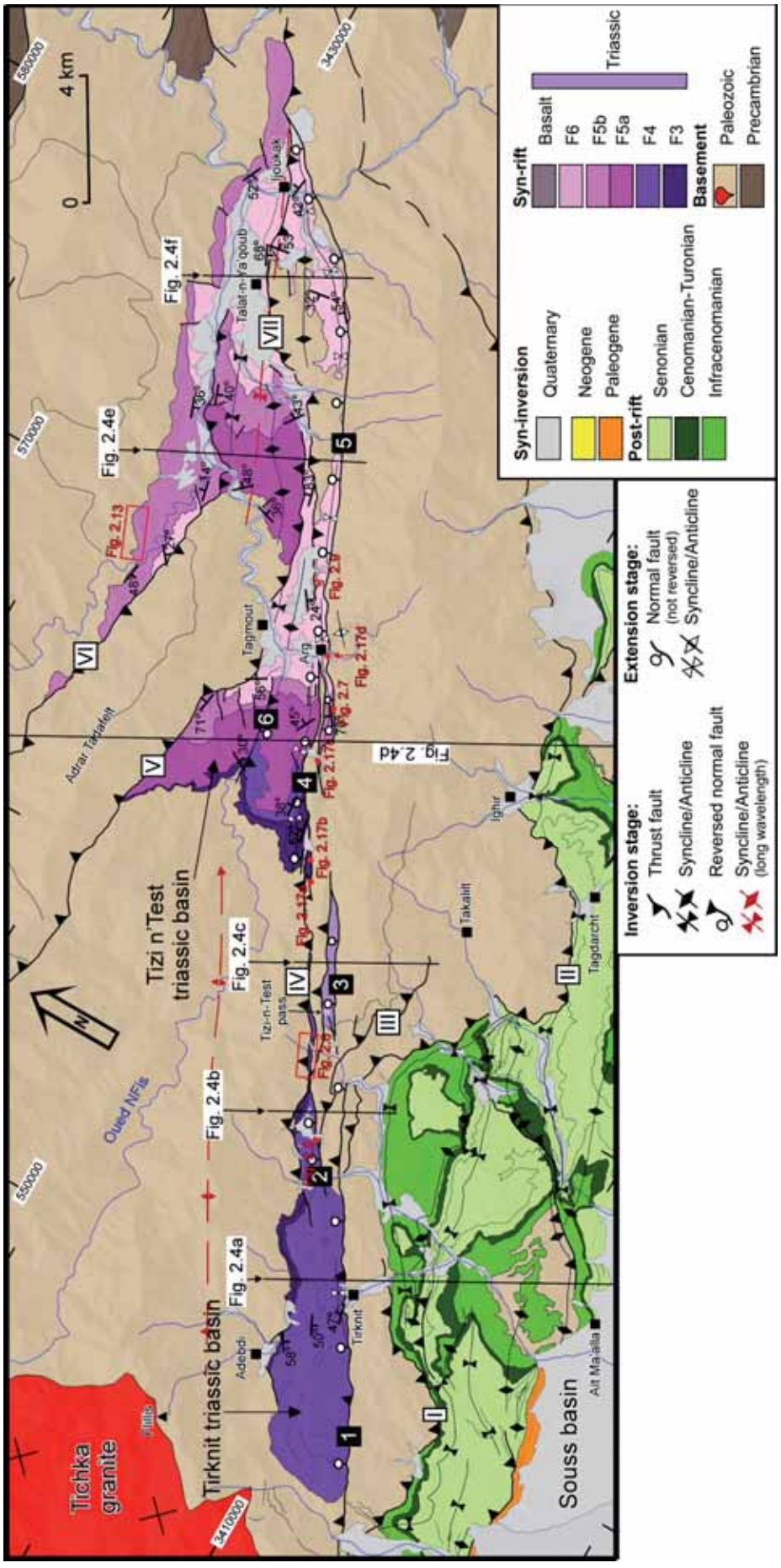

Figure 2.3. Detailed geologic map of the Tirknit-Tizi n'Test Triassic basins in the Axial Zone of the High Atlas, and of the post-rift Cretaceous-Cenozoic deposits of the Sub-Atlas zone north of the Souss basin. See Fig. 2.1(b) for location.

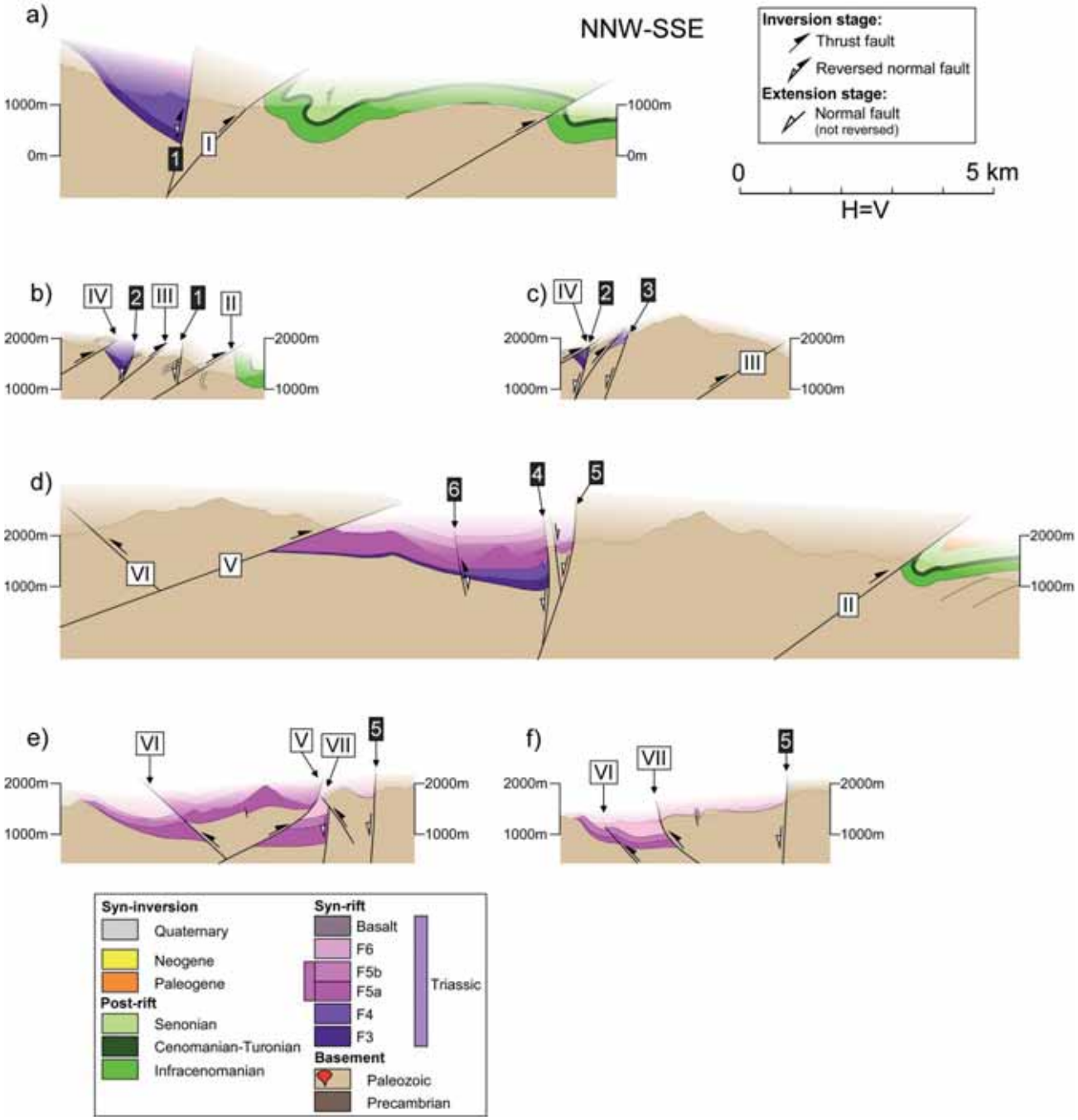

Figure 2.4. (a-f) Cross sections across the Tizi n'Test-Tirknit Triassic basins perpendicular to the NE-trending basin-boundary faults. See fig. 2.3 for location.

2.3.1. Preserved extensional structures

Tirknit and Tizi n'Test Triassic basins

The Triassic stratigraphic units (F3 to F6) of the Tirknit and Tizi n'Test basins are bounded to the south by high-angle faults belonging to the Tizi n'Test fault zone (faults 1 to 5 in fig. 2.4). Faults 1 to 5 strike N60 to N70, downthrow the NW block and dip steeply (from 70º NW to subvertical) (fig. 2.4). However, the original dip value of fault planes in the rifting stage cannot be generally determined with accuracy due to possible steepening during the compressional stage.

In the Tirknit basin, fault 1 (called Tirknit fault in Qarbous et al., 2003) was the rift border at least during sedimentation of the Basal Conglomerate (F3) and the Ramuntcho Siltstone (F4), as a few hundred meters to the south the Cretaceous post-rift deposits lie unconformably on basement (fig. 2.3 and 2.4a,b). In the Tizi n'Test basin, the F3 Triassic unit increases progressively its thickness to the south towards fault 4 and onlaps the basement to the NW defining a half-graben. The F4 unit also increases in thickness to the south, but it is limited to the NW and SE by faults 4 and 6 respectively, defining a graben (fig. 2.3 and 2.4d). The F5a subunit is bounded by fault 4 and F5b by fault 5, and both units overlaps to the NW, conforming again to a half-graben geometry (fig. 2.4d-f). Along the basin axis, units also show marked thickness variations: F3 to F5a units thin and onlap from SW to NE (i.e from the Tirknit to the Tizi n'Test basin, see fig. 2.3 and 2.4). This indicates fault propagation to the NE, and is consistent with SW directed paleocurrents (Petit and Beauchamp, 1986) suggesting a basin deepening to the SW.

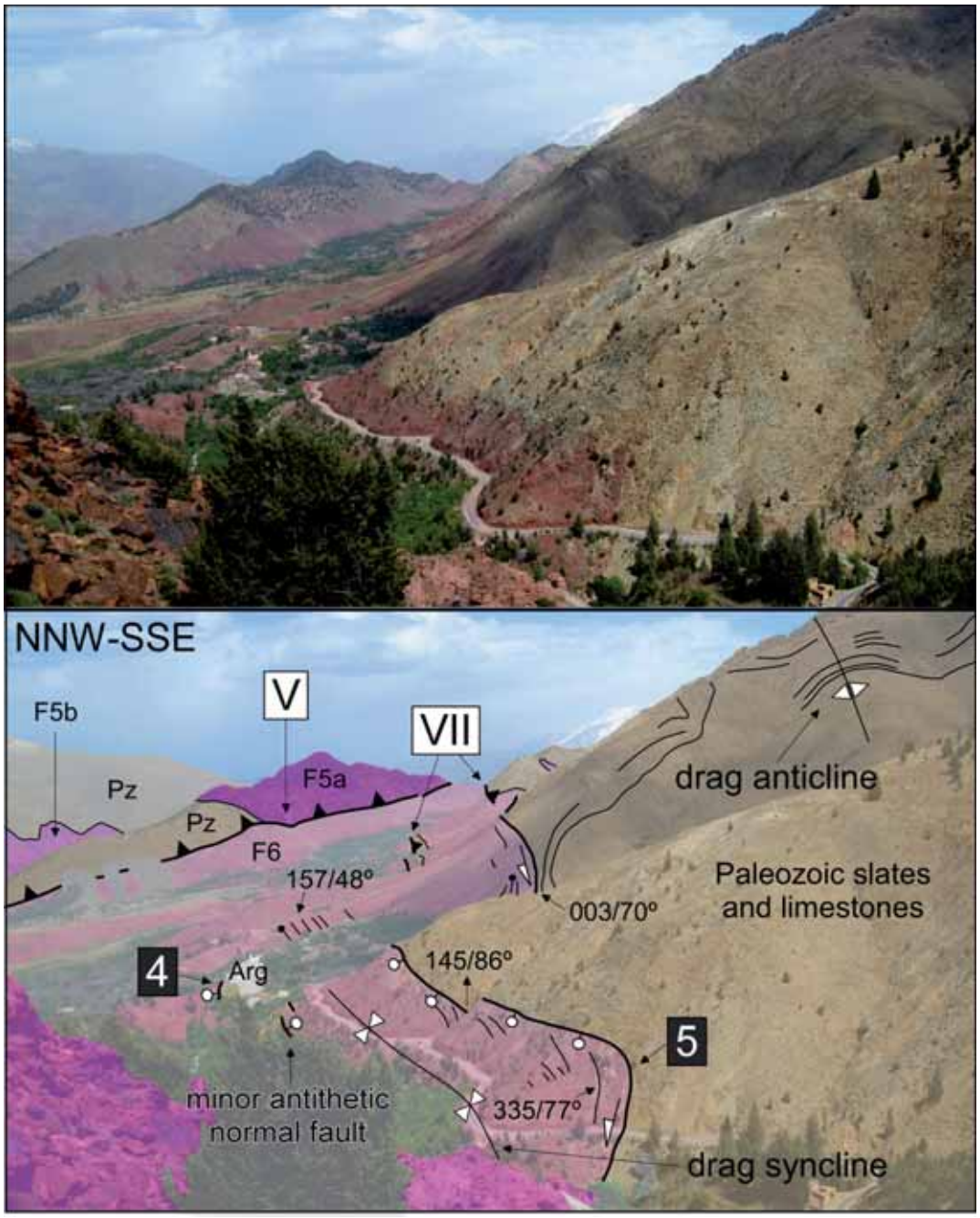

Figure 2.5. General view of the Tizi n'Test basin including the southern boundary fault. Compare with sections in fig. 2.4(d,e).

The Triassic formations located in the hanging wall of the main southern faults (faults 1 to 5 in fig. 2.3) are folded into minor synclines 0.2-1 km in wavelength (e.g. the drag folds adjacent to normal faults 4 and 5 in fig. 2.3d and to fault 5 in fig. 2.4d). Synclines are strongly asymmetric with a steeply-dipping forelimb (occasionally subparallel to the fault's strike and dip), and a gently-dipping backlimb (fig. 2.5 and 2.6). Synclinal axes run sub-parallel and close to the faults and en-echelon patterns are not observed (fig. 2.3).

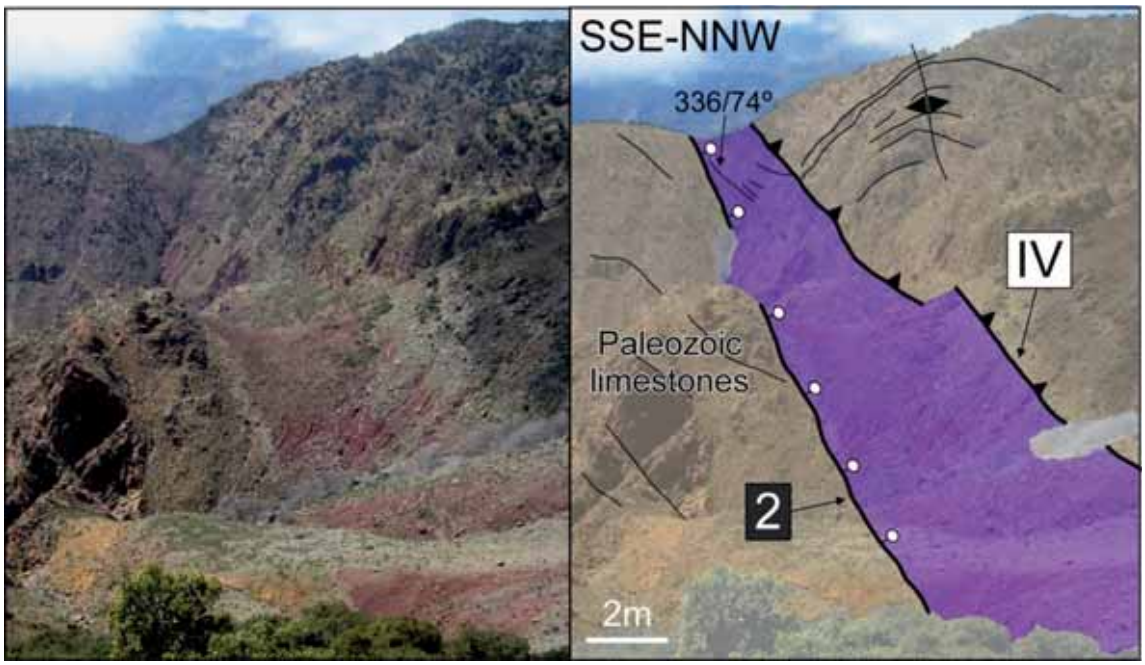

Figure 2.6. Panoramic view of normal fault 2 and its Triassic adjacent forelimb and thrust IV. Compare with sections in Fig. 2.4(b,c). See fig. 2.3 for location.

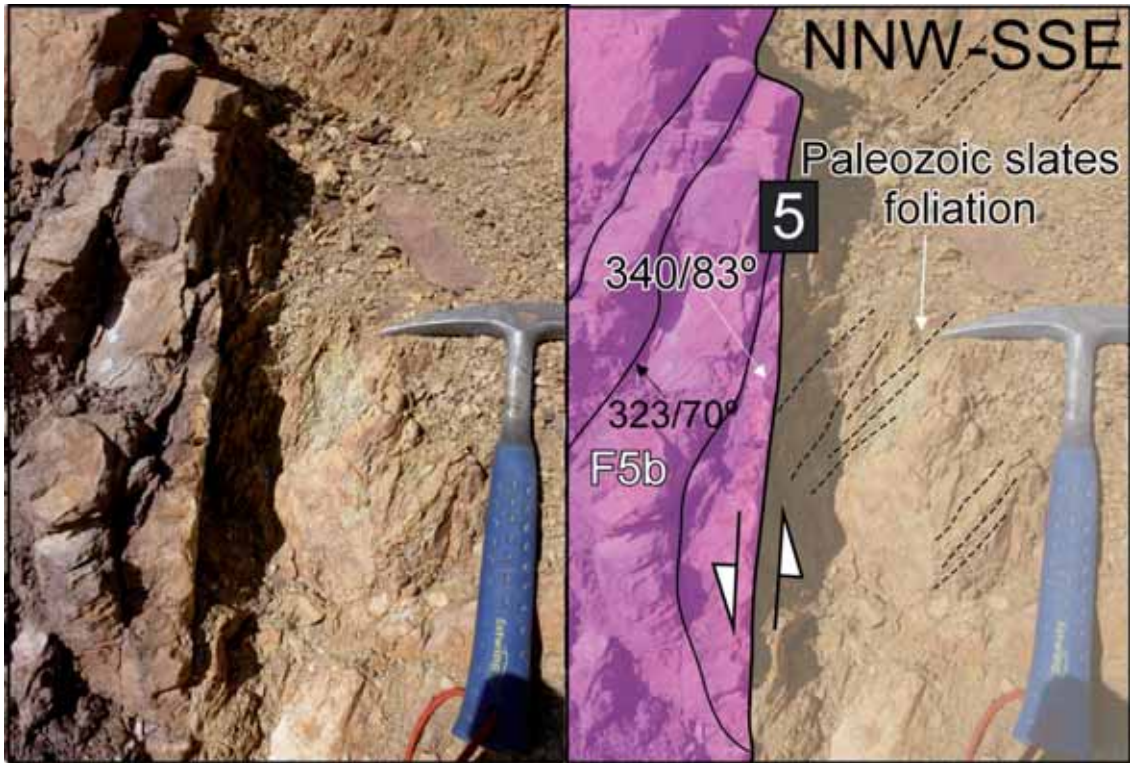

Figure 2.7. Close-up view (perpendicular to the fault dip) of fault 5, southern border of the Tizi n'Test basin. Note the foliation developed in the Paleozoic slates indicating dip-slip normal shear in this fault. See fig. 2.3 for location.

Due to their local extent they can be ascribed to drag or extensional fault-propagation folding. In line with this, a footwall anticline of ~1.8 km in wavelength is observed in the Paleozoic rocks adjacent to fault 5 (fig. 2.5) that because of its fault-parallel orientation (fig. 2.3) I ascribe to Triassic faulting. Folds in Triassic units are consistent with dip-slip extensional movement along the main faults and a minor reactivation during the compressional stage. This conclusion is reinforced by the attitude of a foliation observed in the shear zone in fault 5 and 2 (fig. 2.7 and 2.8), which is developed in Paleozoic slates and limestones, close to the fault.

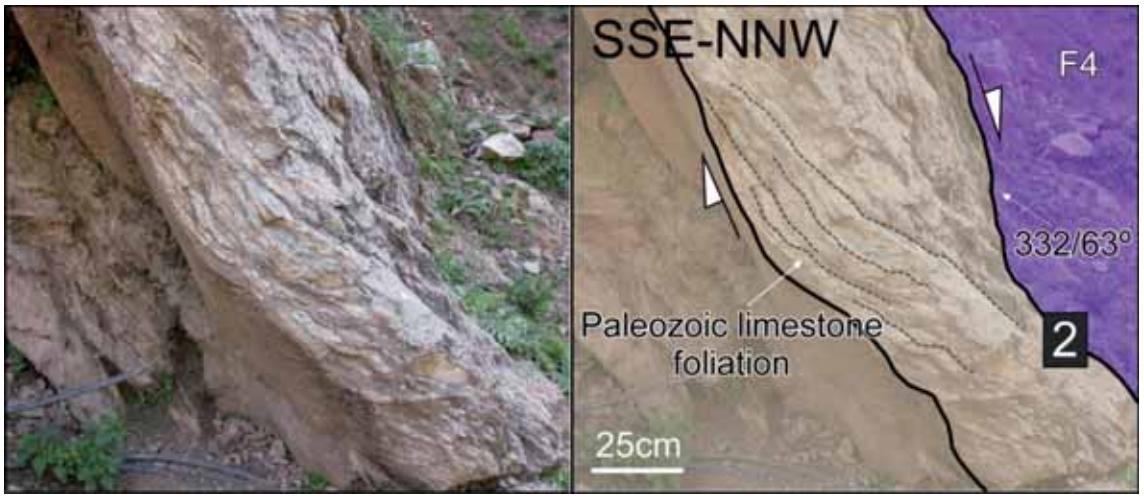

Figure 2.8. Detailed view of extensional fault zone 2, southern border of the Tirknit basin. Note the foliation developed in the Paleozoic limestone. See fig. 2.3 for location.

Therefore, faults 1 to 5 belonging to the Tizi n'Test fault zone can be interpreted as normal faults not reactivated in the later compressional stage. Qarbous et al., (2003) interpreted the drag/fault-propagation folds as formed during the compression and the faults 1 to 5 as elements of a NW-directed backthrust system, an interpretation which is not consistent with my observations since it would require these backthrust to have experienced a rotation to its current orientation, which is neither paralleled by the bedding in the adjacent fault blocks nor consistent with the potential steepening expected from the shortcut thrust II existing to the SE (fig. 2.4d-f).

These major extensional faults are linked by relay ramps (e.g. the relay between faults 1 and 2 in fig. 2.3), or by antithetic normal faults (e.g. the minor fault that links the normal faults 4 and 5, fig. 2.3,2.4d and 2.5), which are consistent with extensional faulting kinematics in Triassic times. Minor syn-sedimentary intra-basin normal faults are common in the Triassic layers (fig. 2.3 and 2.9), and were reported, in the Tizi n'Test basin, by Petit and Beauchamp (1986).

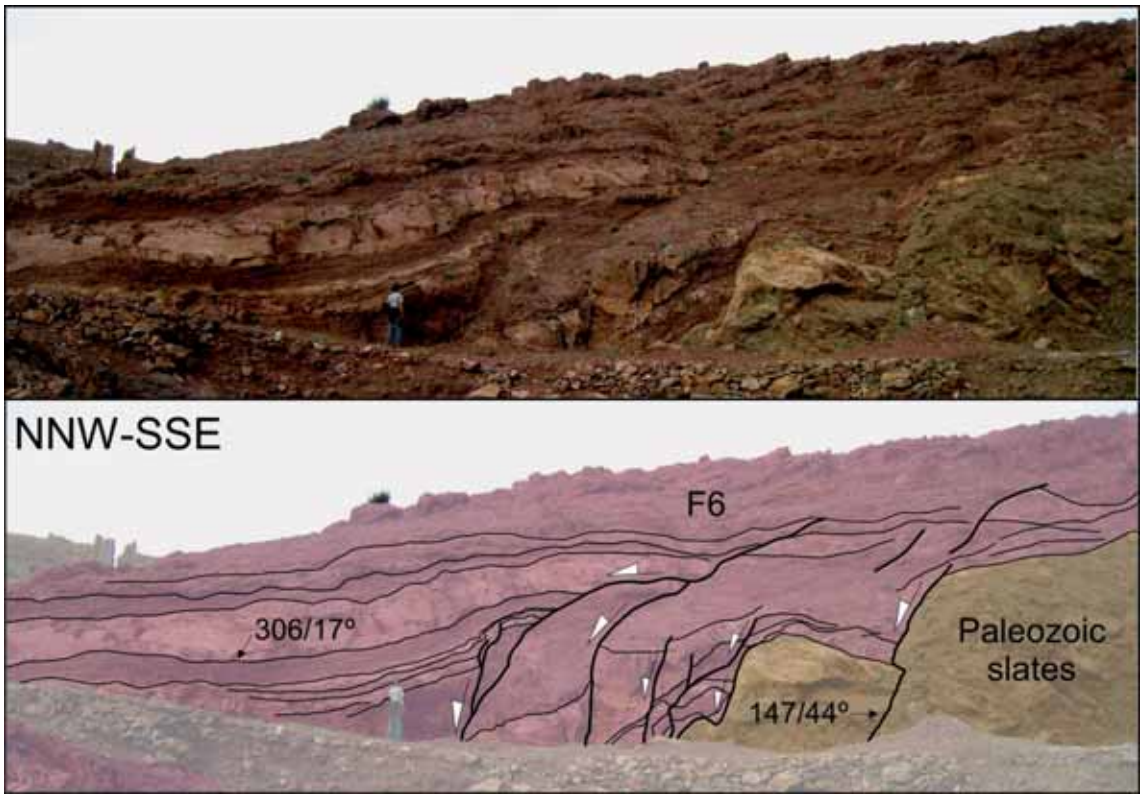

Figure 2.9. Close-up of minor normal faults affecting basement and the Upper Siltstone (F6) preserved in the hanging wall of backthrust VII. Compare with section in fig. 2.4(e,f). See fig. 2.3 for location.

Tizi n'Tacht-Imlil Triassic basin

Fault 7 forms the northern limit of the Tizi n'Tacht basin (fig. 2.10). The fault trends NE-SW and dips from 60º SE to (only locally) subvertical, and was the active rift margin during the accumulation of F4 and F5, as deduced from the rapid thickening of these units towards the fault, and also because N of fault 7, unit F6 lies unconformable on basement.

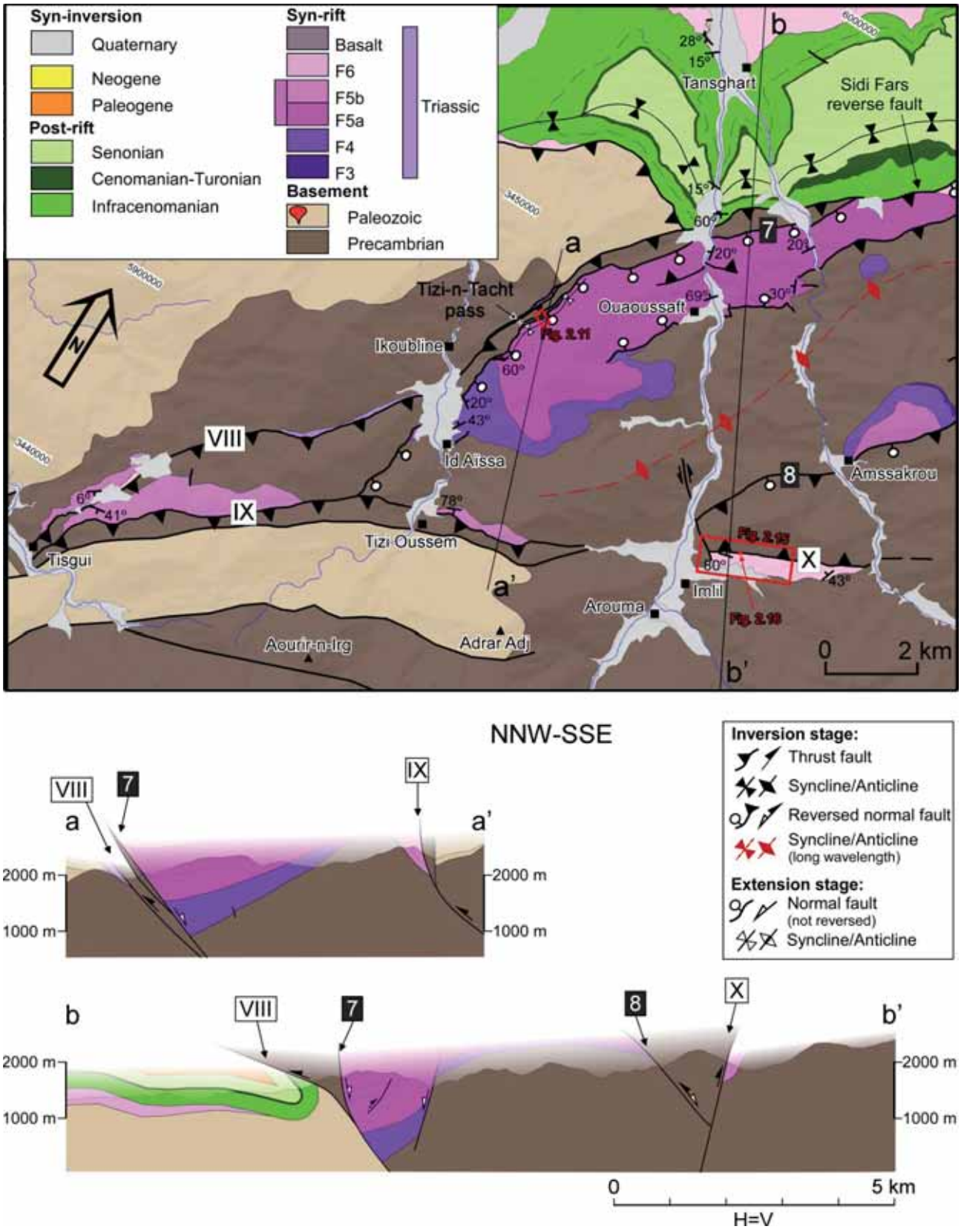

Figure 2.10. Detailed geologic map and cross sections of the Tizi n'Tacht-Imlil Triassic basin (see location in fig. 2.1).

This fault keeps its normal throw in its western segment, where extensional drag/fault-propagation folds are locally observed (fig. 2.11). To the NE, the fault merges with short-cut thrust VIII (the resultant composite fault called Sidi Fars fault in fig. 2.10), and it was thus reversed during the inversion stage.

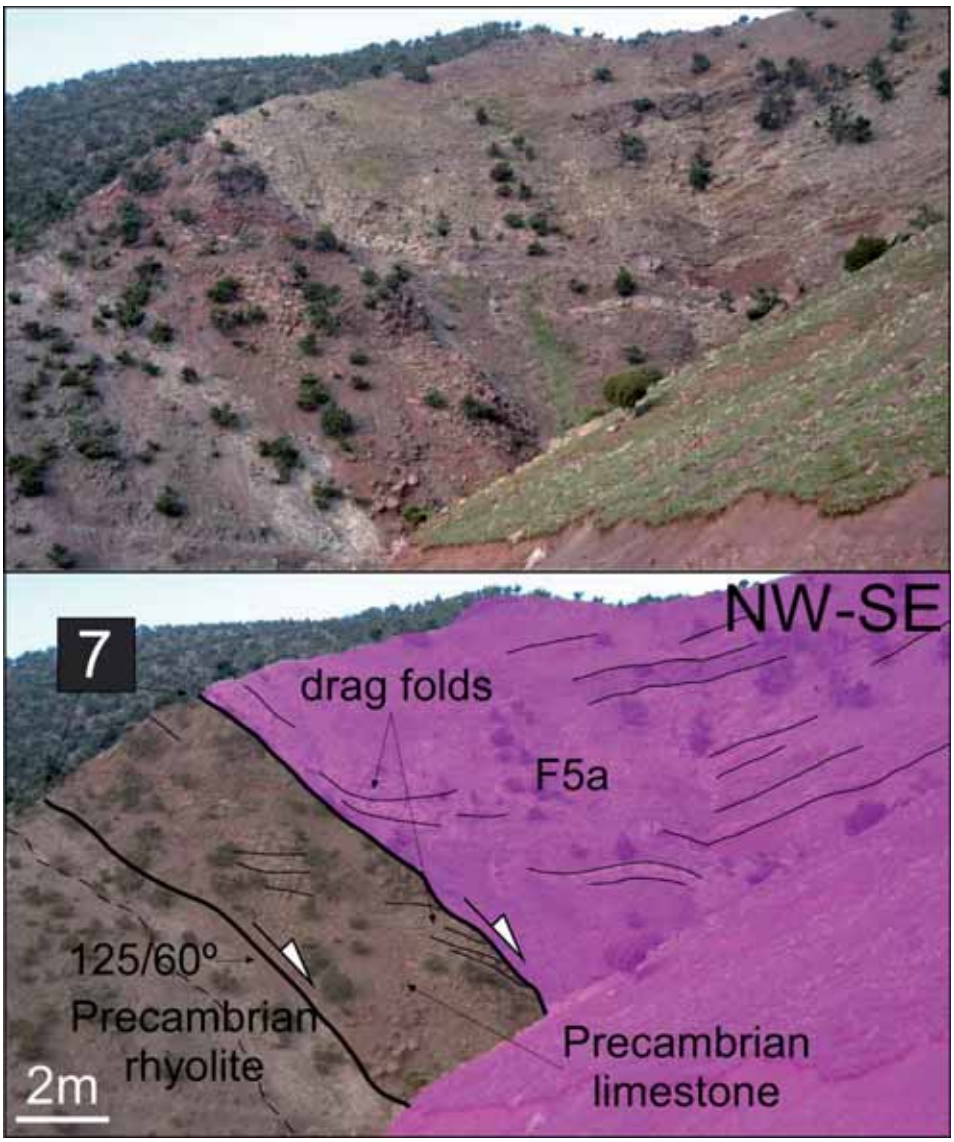

Figure 2.11. Detailed view of normal fault 7 and associated drag folds formed both in the Precambrian and in the Triassic deposits. See fig. 2.10 for location.

The Triassic infill of the Tizi n'Tacht basin thickens to the NE, and in parallel, it overlaps to the SW (e.g. F5b unit lies directly on basement in the Tisgui outcrop, see fig. 2.10). This indicates a main basin opening and increased fault throw towards the NE, in agreement with the much thicker Ourika Triassic basin found in this direction (see summary above) (Baudon et al., 2009, and references therein), where NE-directed paleocurrents were reported (Fabuel-Perez et al., 2009).

Setti Fadma Triassic graben

The small, isolated Setti Fadma Triassic graben is located south of the Ourika basin (fig. 2.1). I refer to Baudon et al. (2009) and Fabuel-Perez et al. (2009) for more information about the main Ourika basin (see a summary above). The Setti Fadma graben is limited to the south by the ENE-trending Ourika fault, labelled 9 in this study, which dips steeply (70º to 85º) to the NNW. A northern, minor fault bordering the graben and trending sub-parallel to fault 9 is dipping ~70º to the SE. Triassic beds define a syncline (fig. 2.12), strongly dragged in the proximity of faults.

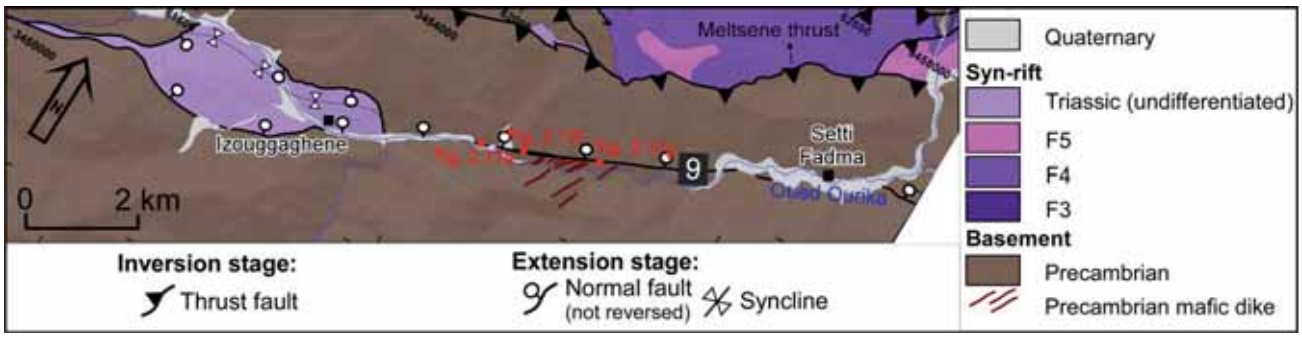

Figure 2.12. Detailed map of the Setti Fadma Triassic outcrop, southern border of the Ourika Triassic basin. See location in fig. 2.1.

The Precambrian basement is largely exposed in the area and consists of granodiorites intruded by minor mafic dykes, which are present in the footwall but not in the hanging wall of fault 9 (fig. 2.12). Dykes are NNE-SSW striking and nearly vertical, and in plan view, no progressive change on orientation into the fault 9 proximity (i.e. by shearing) is observed (fig. 2.12).

2.3.2. Compressional structures

Although the distortion of the Triassic rift structures of the Marrakech High Atlas has been relatively modest during the Atlas mountain building, a series of compressional features can be identified, consisting mainly in shortcut thrusts and large-scale folds, fault reactivation being limited.

Tizi n'Test and Tirknit basins

South of the Tizi n'Test and Tirknit basins, faults I and II (fig. 2.3) can be understood as shortcut thrusts formed in the footwall of the main extensional faults (1 to 5 faults) during the Cenozoic inversion stage. These thrusts carry basement over the Cretaceous post-rift deposits (fig.2.3 and 2.4a,d). Shortcut thrust II dips 30º-40º to the NNW. It merges with fault 1 by a lateral ramp east of Tirknit (fig. 2.3). The minor shortcut thrust I (fig. 2.3), dipping ~40º to the NNW, dies out laterally. Cretaceous and Tertiary rocks south of shortcut thrusts are affected by basement-involved WSW-ENE to E-W folds and thrusts and by minor folds linked with intra-Cretaceous decóllement levels (fig. 2.3 and 2.4a). Intra-Cretaceous folds were progressively rotated and cut by the lateral ramp of thrust II (e.g. 3 km to the SW of Takalilt, fig. 2.3), which indicates that the thrust moved at a late stage, being out-of-sequence. On the other hand, thrust II separates two distinct basement domains, with the Paleozoic strongly affected by Variscan folds, thrusts and low-grade metamorphism in the hanging wall, and the footwall only slightly affected by the Variscan orogeny (Moroccan Meseta and Anti-Atlas domains respectively, Angoud et al., 2002). These clearly differentiated pre-Triassic domains indicate that thrust II may have reactivated a Variscan structure.

The Tizi n'Test basin is partitioned by a pop-up thrust block formed by thrusts V and VI, uplifting Paleozoic rocks (fig. 2.3 and 2.4d,e). Thrust V (called Tadafelt thrust by Qarbous et al., 2003), is here interpreted as a neoformed by-pass thrust within the basin, due to its gentle dip and because the thickness of the Triassic units is similar across it, at variance with Petit and Beauchamp (1986) and Qarbous et al. (2003), who described it as a reactivated normal fault. Also the northern thrust, fault VI (called Tinmel fault by Qarbous et al., 2003), is interpreted as a neoformed thrust fault due to its orientation, parallel to thrust V, and to its gentle dip (fig. 2.4d,e). These thrusts strike E-W turning progressively into ENE-WSW close to normal fault 5, and tipping out in the Upper Siltstone (F6 in Fig. 2.3). Northwest of normal fault 5, backthrust VII also involves basement and shows a progressive dip increase towards the NE, being subvertical near Talat-n-Ya'Qoub (fig.

2.4f). I interpret backthrust VII and the map-view rotation of thrusts V and VI as produced by buttressing against the steep normal faults 4 and 5.

In addition to thrusting, the Tizi n'Test and Tirknit Triassic basins were also affected by large-scale folds which deform the basement and the Triassic cover alike, with apparently little mechanical contrast (fig. 2.3 and 2.4). These folds may indicate a component of shortening by large-scale buckling processes in the Marrakech High Atlas, not related to observable thrust faults. The Tizi n'Test basin is folded into a major synform (5-6 km in wavelength), enhancing the tilting of the northern basin border (currently dipping 30º to 60º to the SE, fig. 2.4e,f and 2.13), and possibly promoting the development of thrusts V, VI and VII as out-of-syncline thrusts in its core.

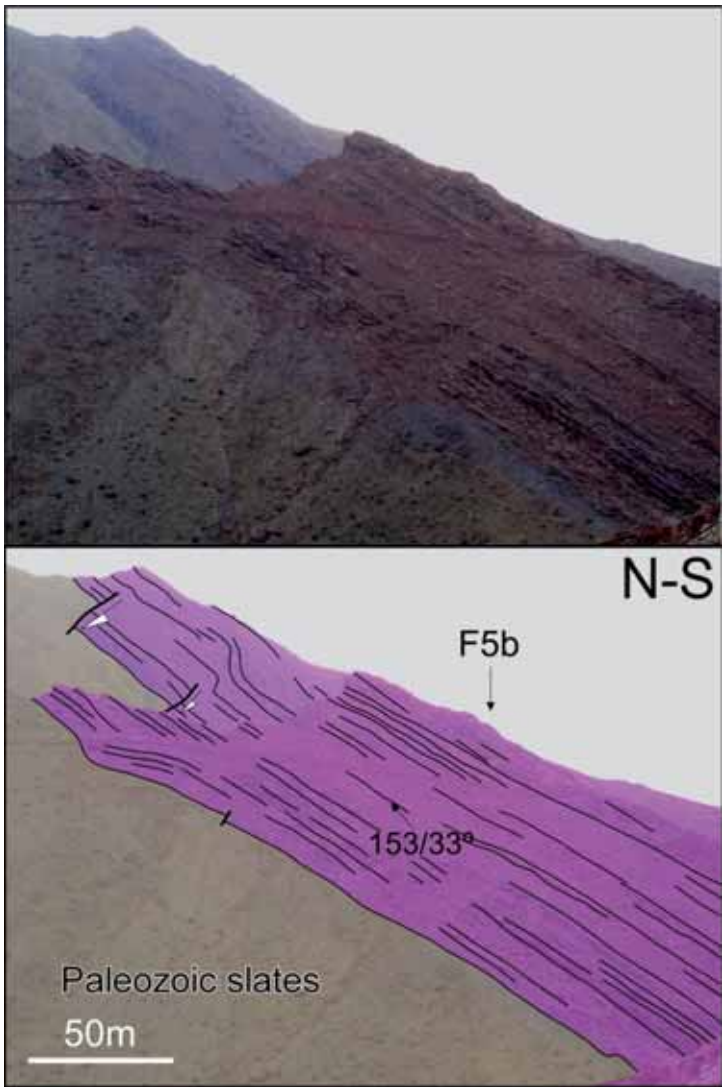

Figure 2.13. View of the erosional northern border of the Tizi n'Test Triassic basin showing the Pink Oukaimeden Sandstone (F5b) unconformable on Paleozoic slate. See fig. 2.3 for location.

This folding may be responsible of the local oversteepening of thrust VII. This deformation, together with shortcut thrusts I and II, is also responsible of the steepening of the major non-reactivated normal faults 1 to 5 to their present attitude (fig. 2.4). A correlative antiform, developed north of the Tirknit basin, tilted Triassic beds of the northern part of the basin to their current 40 to 50º dip (fig. 2.4a); the NE plunge of this antiform combined with erosion caused the SW termination of the Tizi n'Test basin exposure (fig. 2.3).

Tizi n'Tacht-Imlil basin

The Tizi n'Tacht basin and its border fault (fault 7 in fig. 2.10) were transported NW by the shortcut thrust VIII. This thrust formed in the footwall of normal fault 7 and overrides Cretaceous post-rift deposits to the north (fig. 2.10 and 2.14).

South and east of the Tizi n'Tacht area, the basin is affected by thrust IX, fault 8 and backthrust X (fig. 2.10, 2.14 and 2.15). Fault 8 (called Oukaimeden fault by Baudon et al., 2009) is interpreted as a normal fault reactivated with reverse movement (Baudon et al., 2009). Thrust IX and backthrust X are in the continuation of the Tizi n'Test fault (fig.2.1).

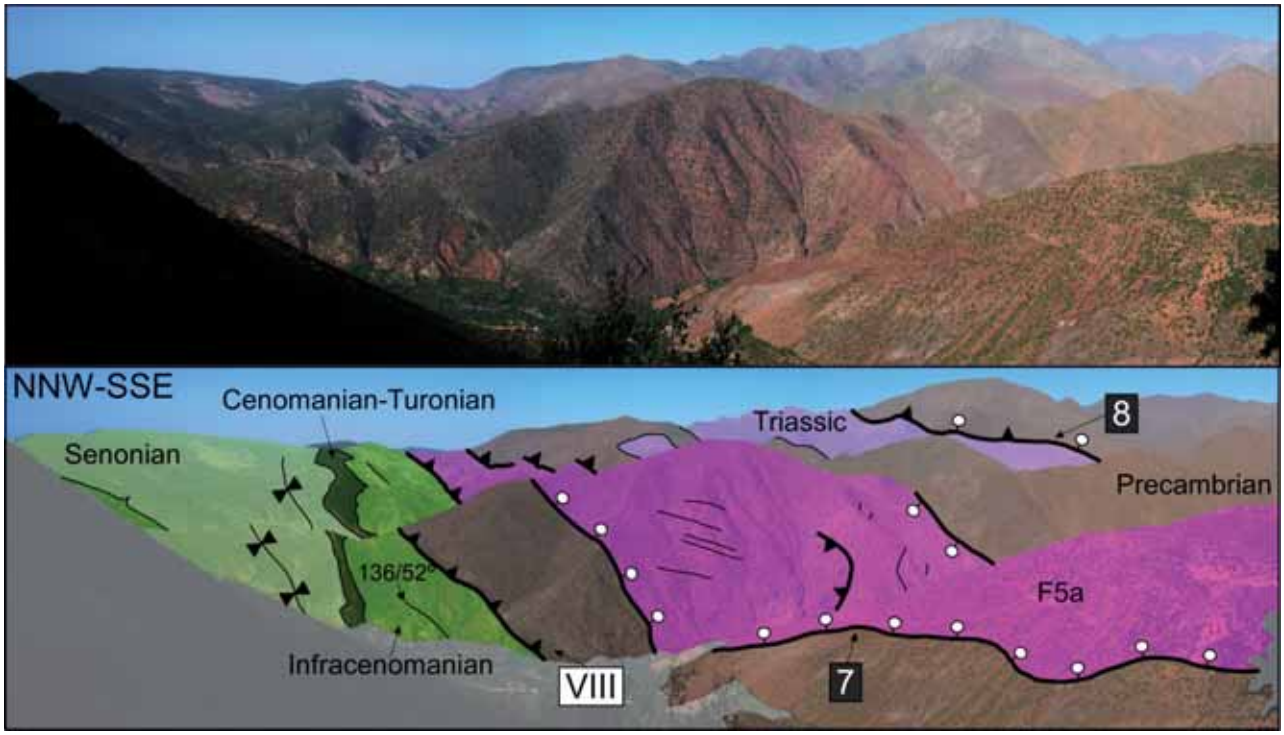

Figure 2.14. General view of the Tizi n'Tacht basin showing extensional and inversion structures. Compare with section b-b' in figure 2.10.

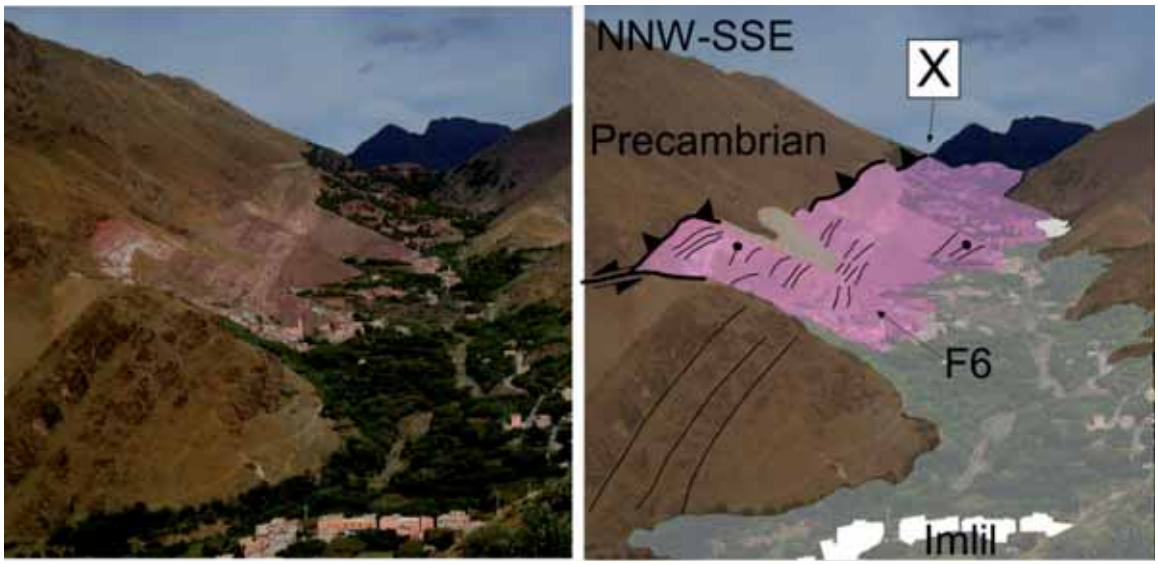

Figure 2.15. View of backthrust X. The Paleozoic block on the foreground is separated from the backthrust and the Triassic by a strike-slip cross-fault. . See fig. 2.10 for location.

Thrust IX dips gently to the SSE in the Tisgui area (fig.2.10), increasing progressively in dip (to 60-80º) to the east (section a-a' in fig. 2.10). The Triassic F5b subunit exposed in the thrust footwall lies directly on basement and is cut by the thrust in a low-angle ramp geometry (section a-a' in fig. 2.10). The X backthrust dips 70º-80º to the NW. The F6 Triassic unit is preserved in its footwall and dips steeply to the NNW, forming a footwall flat geometry (section b-b' in fig. 2.10). Due to the structural relations described, thrust IX and backthrust X cannot be considered as reactivated normal faults, but instead must have been formed during the compressional stage as new thrust faults. Both thrust faults are linked by a nearly vertical left-lateral transfer fault striking NW-SE (fig. 2.10 and 2.15) with preserved strike-slip striae on the fault plane.

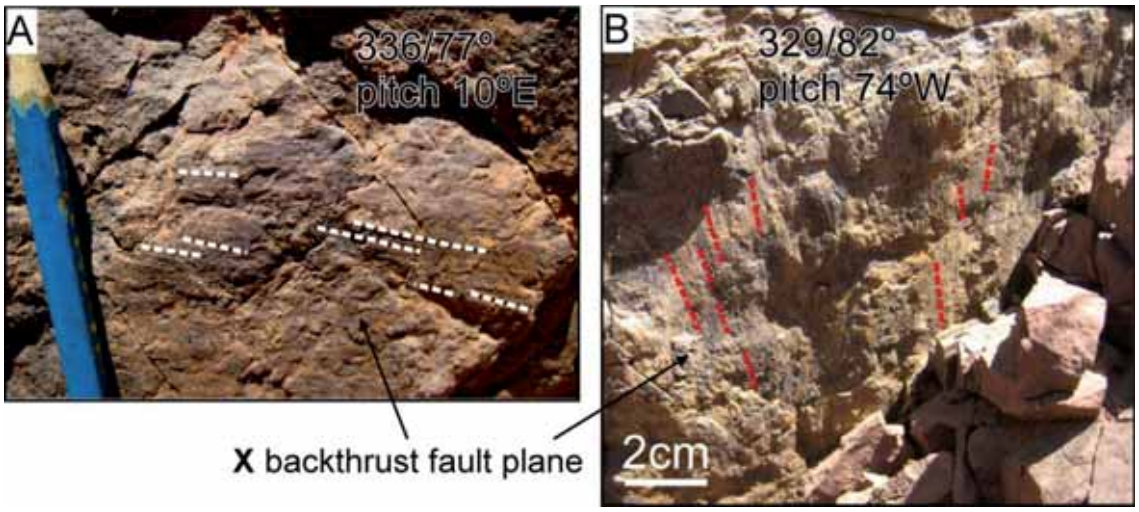

Figure 2.16. (a) Strike-slip and (b) dip-slip striae, both observed in the fault plane of backthrust X. See fig. 2.10 for location.

Backthrust X presents two distinct striae directions, one nearly vertical (fig. 2.16b) and other nearly horizontal (fig. 2.16a) with a left-lateral sense of movement. Although the amount of exposed slickensides is not enough to make a population analysis, it seems clear that backthrust X had two distinct phases of movement. In the same way, the few slickensides observed in the thrust IX indicate dip-slip, but Riedel fractures occasionally observed in the fault zone suggest a certain component of sinistral strike-slip.

A long-wavelength (~5 km) antiform affects the whole Tizi n'Tacht basin (fig. 2.10), separating the Triassic adjacent to faults IX, X and 8 from the main body of the Tizi n'Tacht basin. Again, this folding could be linked with large-scale buckling processes (not thrust-related), and could account for the present steep dip of thrusts IX and X (fig. 2.10). These thrusts may have formed as gently-dipping, later steepened enabling the strike-slip movement indicated by scarce microstructures.

2.3.3. Selective reactivation of normal faults

In the Tizi n'Test and Tirknit basins a significant normal fault reactivation with reverse movement may have occurred only in the case of fault 1 because the elevation of the lower Triassic sequences with respect to the Cretaceous layers existing to the south (fig. 2.4a) is too high to be explained by the shortcut thrust I, which has a minor displacement and limited lateral continuity (fig. 2.3). However, the amount of reverse slip cannot be precised since the upper Triassic units of the Tirknit basin have been eroded and also because part of this higher altitude could be explained by the large antiform that affects the northern Tirknit basin (fig. 2.4a). In addition, the preservation of extensional drag/fault-

propagation folds may indicate that reactivation was minor. A microstructural analysis of the fault zone was not possible as it is poorly exposed. Secondary faults within the Tizi n'Test basin such as normal fault 6 (fig. 2.3 and 2.4d) were reactivated in the compression stage. This fault, striking E-W and active during the sedimentation of the Ramuntcho Siltstone (F4) was reversed a few tens of meters and propagated into the Oukaimeden Sandstone (the thickness of this unit does not change across the fault), tipping out along strike into the Upper Siltstone unit (fig. 2.4d).

In the Tizi n'Tacht-Imlil basin, fault reactivation is observed only in faults 8 (Oukaimeden fault; Baudon et al., 2009) and Sidi Fars fault (fig. 2.10).

2.4. Microstructural analysis of fault planes

To complete the inferences from large-scale structures I undertook a kinematic analysis of the main fault zones based on slickensides (fig. 2.17). The Marrakech High Atlas has been the subject of earlier microstructural studies based on minor fault populations (Proust et al., 1977; Laville and Petit, 1984; Qarbous et al., 2003, 2008). A study by Qarbous et al. (2003) focused on fault populations within the Triassic basin fill (mainly the Oukaimeden Sandstone) indicated an intra-Triassic extensional regime. The stress fields obtained consist of a vertical maximum stress and a minimum stress oriented NW-SE to N-S (present-day orientations). The same conclusions had been earlier reported by Laville and Petit (1984), although fault plane data were not provided. Proust et al. (1977) reported conjugate NNE-SSW and NNW-SSE strike-slip faults deducing a N- to NNW-trending compressional stress of uncertain age, which could be related to the Cenozoic inversion (see also Qarbous et al., 2008).

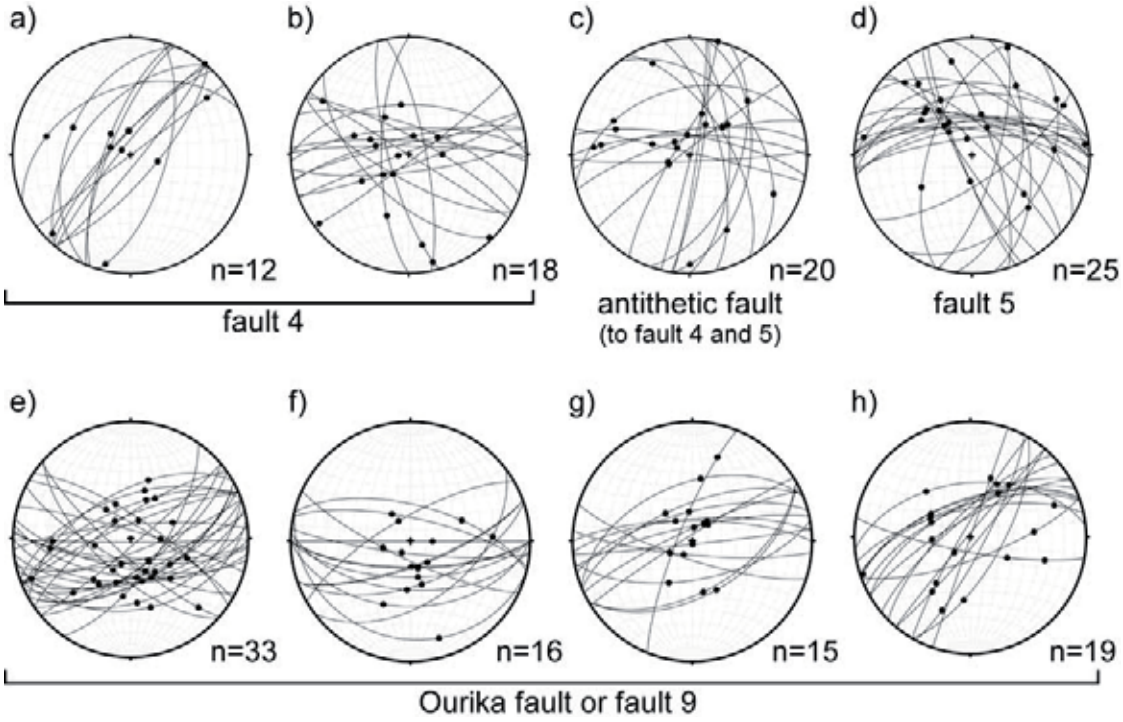

Figure 2.17. Stereographic projections showing strike, dip and striae direction of major extensional faults (faults 4, 5 and 9) at selected localities which provided a significant number of slickensides. (a-d) faults 4 and 5 southern border of the Tizi n'Test basin (see fig. 2.3 for location). (e, f) Ourika fault (fault 9), southern border of the Setti-Fadma graben (location in fig. 2.12). (h) Ourika fault (fault 9) locality at 31º 17' 38.6''N, 7º29' 47.2''W to the ENE of e,f (18 km out of the area covered in fig. 2.12).

I focused my contribution on the major Triassic faults, at selected localities which provided a significant number of striated planes. These represent 3 of the 9 numbered faults mapped in fig. 2.3, 2.10 and 2.12. The fault zones, developed in siliceous basement rocks, contain minor striated fault planes, but sense-of-shear criteria are very scarce. The majority of striae are steeply-dipping to subvertical (fig. 2.17). Of a total of 158 slickensides measured, 116 showed striae with pitch >45°. On the absence of reliable sense-of-shear indicators, I cannot ascertain whether the highly pitching striated planes formed during Triassic rifting as normal faults or during the Cenozoic inversion as thrust faults, although, as discussed above, observations point to little fault compressional reactivation at the macroscopic scale. My results show two main families of striated fault planes, a dominant one with ENE-WSW to NE-SW direction, which corresponds to the main trend of the Tizi n'Test fault zone, and a second corresponding to fault planes striking from NNE-SSW to N-S (fig. 2.17). Of those within the range of orientation of the Tizi n'Test fault zone, only 16 of them (22%) show slickenlines pitching ≤45°. I thus

conclude that the main kinematics recorded in the major fault zones of the study area is close to dip-slip, with a certain component of obliquity.

2.5. Discussion

The Triassic basins of the Marrakech High Atlas have been traditionally associated with the major Tizi n'Test fault, reported as a continuous fault dominating the rift opening and the later inversion. In this study I mapped 200 km of the 280 km long Tizi n'Test fault zone (fig 2.1). The study shows that neither the basins nor the fault are continuous throughgoing features. Instead, the fault zone is highly segmented, and faults that controlled Triassic basin opening should be regarded as forming a wide deformation band across the Marrakech High Atlas with a ENE- to NE- trend. The band consists of half-grabens in the southwest (Tirknit and Tizi n'Test basins, fig. 2.3), and a rather symmetric graben system limited by oppositely-dipping faults in the northeast (Tizi n'Tacht-Imlil and Ourika basins, fig. 2.10 and 2.12). The preservation of normal offsets and extensional minor structures indicate that during the Cenozoic inversion the main basin-bounding faults were not significantly reversed.

Of the 8 major rift faults of the study area that showed minor reactivation during the compression (faults 1 to 9 in figs. 2.3, 2.10 and 2.12; Fault 8 is not included due to their major reactivation), 7 were characterized by macrostructures (faults relays and fault-related folds), and 4 by mesostructures (3 by fault-plane populations and 1 by foliation), which indicate a dominant dip-slip movement along the main basin-bounding faults, possibly with a certain oblique-slip character. Although the absence of sense-of-shear indicators along the main rift faults is not indicative, folds and foliation observations favor a dominant extensional opening of the Triassic basins. Indeed, a number of strike-slip slickensides was observed (fig. 2.17), consistently with the observations by Proust et al. (1977) and Qarbous et al. (2008) in the Triassic basin infill, but these were attributed to horizontal compression, and are of relative minor significance in the main faults analysed here. I cannot support the common view of the Tizi n'Test fault zone as a major strike-slip/transform fault system, and the Triassic basins as formed by pull-apart mechanisms.

Diverging paleocurrents and onlap patterns observed in the Triassic deposits indicate that the Tirknit-Tizi n'Test and Tizi n'Tacht basins were separated by an intervening topographic high at the western end of the Ouzellarh salient (Toubkal massif in fig. 2.1a) at least in early and mid-rifting stages (see the overlap of Lower Triassic units to the NE and SW in Fig. 2.3 and 2.10 respectively), at variance with previous reconstructions (Laville et al., 2004; Frizon de Lamotte et al., 2009; Baudon et al., 2012) which assume a connection between the Tirknit-Tizi n'Test basins with the Tizi n'Tacht-Ourika ones.

Squeezed Triassic remnants found to the south of the Tichka granite and between the Tichka granite and the Argana basin (fig. 2.1b) suggest that the Tirknit-Tizi n'Test Triassic basins, which show paleocurrents to the SW (Petit and Beauchamp, 1986), could be connected to the Argana basin in the Atlantic margin as already proposed by (Stets, 1992). Based on these observations I present a new reconstruction of the paleogeography of the Marrakech High Atlas rift (Fig. 2.18a) in mid Triassic times (prior to the deposition of the Carnian Pink Oukaimeden sandstone, F5b).

As shown above, during the Cenozoic compression the main basin-bounding normal faults were not significantly reversed, except in local cases such as fault 1, fault 8 and the northern margin of the Ourika basin (Sidi Fars reverse fault; fig. 2.10 and 2.18b). The Atlas shortening was accommodated by newly-formed thrusts (shortcut and by-pass) and by more continuous deformation as evidenced by long-wavelength folding and steepening of normal faults by rotation. Some left-lateral slip is expected in NE- to ENE- trending faults, which were oblique to the Cenozoic compression direction, generally assumed to be close to N-S in the Atlas (Mattauer et al., 1977). The minor subpopulations of oblique- to strike-slip striated planes in the major normal faults discussed earlier (fig. 2.17) may represent this component. Evidence for a strike-slip component in the thrust faults is limited to only two near-vertical thrusts of the Tizi-n'Tacht area (thrusts IX and X, located in fig. 2.10). Again, even though a transpressive character of the thrust faults cannot be discarded, I conclude that the strike-slip component during the Cenozoic compression is minor.

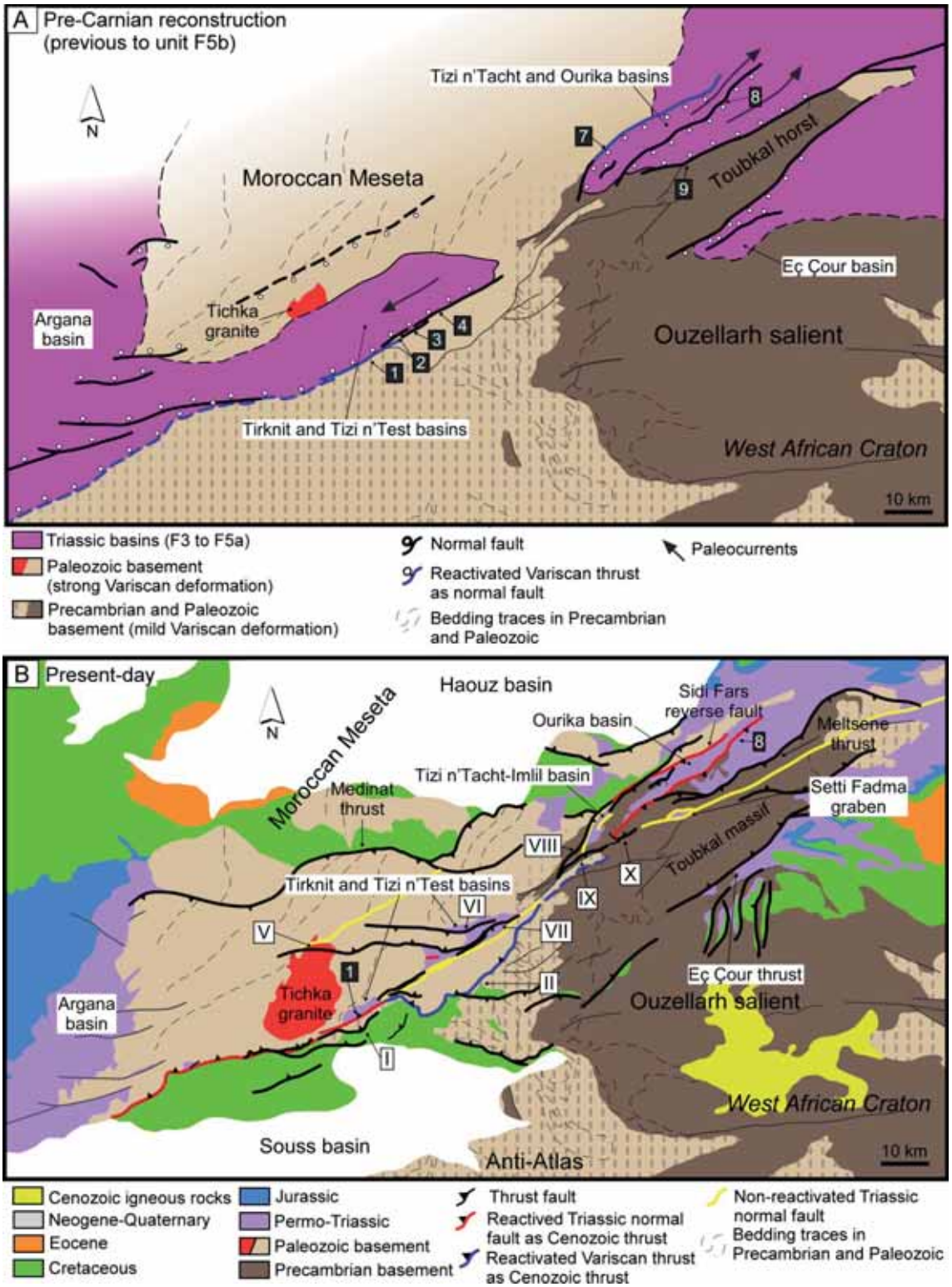

Figure 2.18. (a) Reconstruction of the Triassic basins of the Marrakech High Atlas to Mid Triassic times, previous to the sedimentation of the Carnian Pink Oukaimeden sandstone (F5b) and the Upper siltstone (F6). Paleocurrent data are from Petit and Beauchamp (1986) and Fabuel-Perez et al. (2009). (b) Present-day geologic and tectonic features after the Cenozoic inversion in the High Atlas.

Fig. 2.19 shows a present-day cross section of the Marrakech High Atlas across the Tizi n'Test basin and a tentative restoration previous to the Cenozoic orogeny (see fig. 2.1b for location). The hanging wall cutoffs of some major Cenozoic thrusts are not observed, and thus the restoration has to rely on minimum displacement estimates and contains a degree of uncertainty. Jurassic sediments are not preserved under the Cretaceous of the orogen flanks. Sediments of this age could have existed in the Axial Zone, but on the lack of data they have not been represented in the section, and the Cretaceous is drawn unconformable above the F6 Triassic unit.

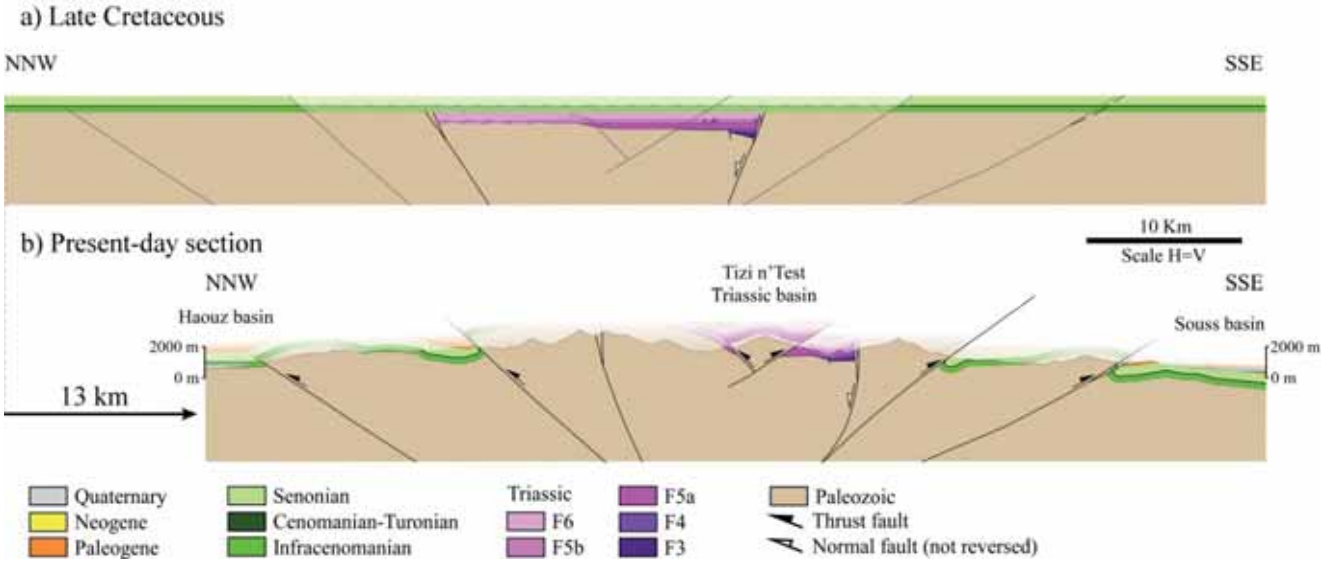

Figure 2.19. Present-day cross section of the Marrakech High Atlas (see location in fig. 2.1) and restoration to the Late Cretaceous, prior to the Atlas orogenic inversion.

A comparison between the present-day and restored sections suggests a minimum amount of total shortening of ~13 km (16%), which, in spite of the uncertainties, contrasts to the previous estimation by Missenard et al. (2007) indicating as little as 3 km of shortening in a section a few km to the east (across Sidi Rahal; see locality in fig. 2.1a). The amount of shortening here estimated is consistent with previous works in Central and Eastern High Atlas which proposed values of total shortening of 30 to 13 km, decreasing from east to west (Teixell et al., 2003).

2.5.1. Fault localization and orientation

Many previous authors assume that the major Triassic faults were inherited from Variscan structures (Proust et al., 1977; Laville and Piqué, 1991; El Arabi et al., 2003; Laville et al., 2004; Baudon et al., 2009). However, only in limited cases do the Triassic faults clearly follow Variscan structures, as for example, normal fault 1 and Sidi Fars fault (fig. 2.3 and 2.10), which mark a change in pre-Mesozoic geology (Variscan folding and metamorphism vs. mild deformation across fault 1, and Precambian vs. Carboniferous rocks across the Sidi Fars fault; fig. 2.18). As for the rest of the main basin-bordering faults, their possible inherited character cannot be ascertained, as there are no changes in pre-Triassic geology across them. At a larger scale, a major feature controlling rifting in the Marrakech High Atlas and its transition to the Central High Atlas is the Ouzellarh Precambrian salient (fig. 2.1a and 2.18). This salient, part of the West African Craton (Anti-Atlas domain), appears as a foreland uplift indented into the Variscan chain (see reconstructions in Michard et al., 2010). The Marrakech High Atlas rift is divided into three branches, the Ourika graben to the north, the Eç Çour basin to the SE and the Tizi n'Test to the SW. In between is the Toubkal horst (fig. 2.18a). The Eç Çour basin terminates to the southwest towards the Ouzellarh salient, whereas the Ourika basin borders the massif to the north and narrows dramatically to the southwest, in the Tizi n'Tacht-Imlil basin (fig. 2.18a).

The geological record of rift systems shows that continental break-up is not randomly distributed but tends to follow the trend of pre-existing weaknesses at lithospheric scale (e.g. ancient orogenic belts), avoiding stronger regions (e.g. cratons). Such lithospheric contrasts are often more influential in rift localization and orientation than the general extension direction (e.g. Corti, 2012 and references therein). The Mesozoic High Atlas rift follows a major lithospheric boundary between the Variscan chain and the West African Craton (Anti-Atlas). This boundary is still expressed today by a marked contrast in seismic velocity at the lithospheric scale (Missenard and Cadoux, 2012). This major lithospheric feature may explain the oblique rift character of the Central and Eastern High Atlas rift, with margins trending N75-N80 and internal faults oriented N55-N60, perpendicular to the inferred extension direction (El Kochri and Chorowicz, 1996; Arboleya et al., 2004). However, my paleogeographic reconstruction (fig. 2.18a) shows that the Triassic rift in the Marrakech High Atlas was narrow with margins trending NE-SW in average, that is, roughly orthogonal to the approximate NW-SE extension direction inferred for the Triassic and Jurassic (present-day orientations in the reference frame of the African plate; Hailwood and Mitchell, 1971; Mattauer et al., 1977; Laville and Petit, 1984; Laville and Piqué, 1991; El Kochri and Chorowicz, 1996; Ait Brahim et al., 2002; El Arabi et al., 2003;

Qarbous et al., 2003). The orthogonal character of this rift segment in contrast with the Central High Atlas may tell us that it roughly follows the transition zone between the Variscan chain and the West African craton, which was originally deflected due to the indentation of the Ouzellarh Precambrian salient. Moreover, temporal departures from the NW-SE prevailing extension direction during the rifting to an WNW-ESE direction as reported by Medina (1995) and Baudon et al. (2009) should not alter the dip-slip character of the main faults, as inferred today from modern oblique rift systems where measured stresses are perpendicular to the trend of the main faults irrespective of their obliquity to the regional, far-field extension (Morley, 2010) .

As for the localization of the Cenozoic contractional deformation, the Triassic faults of the Marrakech High Atlas were not the sites of major thrust reactivation, with the exception of the cases where these faults already reactivated previous Variscan faults, like fault 1 and Sidi Fars fault (fig. 2.18b). In the Tizi n'Test basin area, thrust II marks the boundary between different Variscan domains (Angoud et al., 2002). Steep Triassic normal faults acted as buttresses, and thrusts formed instead as footwall shortcuts or by-passed them (e.g. Fig. 2.5d and 2.6e). In this segment of the Atlas chain, the major Cenozoic thrusts (thrust II, Medinat thrust, south and north Atlas mountain fronts; fig. 2.18b) are out of the basin margin faults. Neither the northern nor the southern front of the Atlas coincides with Triassic rift faults in the study area (fig. 2.18). These thrust fronts trend ENE-WSW; hence, the general ENE-WSW trend of the present-day Marrakech High Atlas belt (which is oblique to the Triassic faults) results from Cenozoic thrusting. Again, a marked influence is exerted by the Ouzellarh salient, as the Eç Çour thrust and thrust II die out or bend around the massif rather than crossing it (fig. 2.18b), being the southern thrust front of the High Atlas very poorly defined in the massif itself.

2.6. Conclusions

The mild rift inversion and the erosion level of the Marrakech High Atlas, where large exposures of basement and Triassic syn-rift deposits exist, make it an ideal area to investigate the early stages of evolution of a rift and provide field analogues to pre-salt geometries in deep basins, especially for the Atlantic margins. This detailed study of the main Triassic basins and basin-margin faults of the Marrakech High Atlas shows that only a few rift faults were reactivated during the Cenozoic compressional stage, emphasizing that fault reactivation cannot be taken for granted in inverted rift systems. The location of the Triassic rift between the Moroccan Variscan chain and the West African Craton (Anti-Atlas and Ouzellarh Precambrian salient) indicates that previous lithospheric anisotropies

played a crucial role on the localization of the deformation not only during the rifting stage but also during the later inversion.

A new Middle Triassic paleogeographic reconstruction shows that the Marrakech High Atlas was a narrow rift controlled by N60-trending margin faults. Basins developed roughly orthogonal to the general extension direction (~NE-SW in the present-day reference frame of the African plate). The orthogonal character of this rift segment is interpreted as due to the indented Ouzellarh Precambrian salient, which deflected the Variscan chain and subsequently the general rift trend, at variance to the Central and Eastern High Atlas, which developed obliquely (ENE-WSW) to the general extension direction. A complex system of Triassic horsts and grabens is here described, evidencing the segmented nature of the rift. Diverging paleocurrents and onlap patterns indicate that the Tirknit-Tizi n'Test and Tizi n'Tacht-Ourika basins were separated by an intervening high at least in early- and mid-rifting stages. Preserved extensional features (e.g. fault-propagation/drag folds, minor faults, slickenslides) show a dominant dip-slip or oblique-slip opening kinematics, in contrast with models proposing a major strike-slip component into the main basin-bounding faults, including faults belonging to the Tizi n'Test fault zone (which is often viewed as a major strike-slip/transform fault).

As for the Cenozoic inversion, shortening was accommodated by basement-involved large-scale folding, and by shortcut and by-pass thrusting, with sparse evidence for left-lateral strike-slip, which could have taken place but was not a major component of the deformation. Triassic faults commonly acted as buttresses. In this segment of the High Atlas chain, the major Cenozoic thrusts are out of the basin margin faults and are associated to a modest amount of total orogenic shortening (~16%).

Chapter 3

Clues to burial and exhumation during the Atlas rifting and orogeny from apatite and zircon (U-Th)/He modelling

Chapter 3. Clues to burial and exhumation during the Atlas rifting and orogeny from apatite and zircon (U-Th)/He modelling

3.1. Introduction

In the previous chapter, a new Triassic (pre-Carnian) paleogeographic reconstruction is presented, which shows a complex system of horsts and grabens and evidences the segmented nature of the Atlas Triassic rift. However, no information can be extracted by field observations about the existence of a Jurassic rift, and the area is usually assumed to have been as a high or a poorly subsiding domain during the whole Triassic-Jurassic rifting (see discussion in section 1.2.2). Also, the timing of the Atlas orogeny and the amount of shortening is still poorly constrained in the Marrakech High Atlas, due to the scarce preservation of syn-tectonic sediments and fault cutoffs of major thrusts, as we have seen in the previous chapter. Low-temperature thermochronological methods allow reconstructing the cooling history of rocks, and therefore, may constitute a useful alternative to know and quantify past burial and exhumation events and magnitudes that are poorly constrained by the structural and sedimentary record.

In this chapter 3, I present apatite and first zircon (U-Th)/He ages and thermal models for a set of samples collected in the Marrakech High Atlas in two differentiated areas, which are already described in detail in the previous chapter. In the west, zircon (U-Th)/He ages are obtained in samples collected in the Tizi n'Test Triassic basin (see location in fig. 3.1) and its adjacent southern margin. To the east, zircon and apatite (U-Th)/He ages and thermal models are obtained in the Ourika-Tizi n'Tacht Triassic basin and Toubkal massif area (see location in fig. 3.1). The zHe and aHe ages and thermal models obtained allow reconstructing the evolution of the Marrakech High Atlas from the Triassic-Jurassic rift to present.

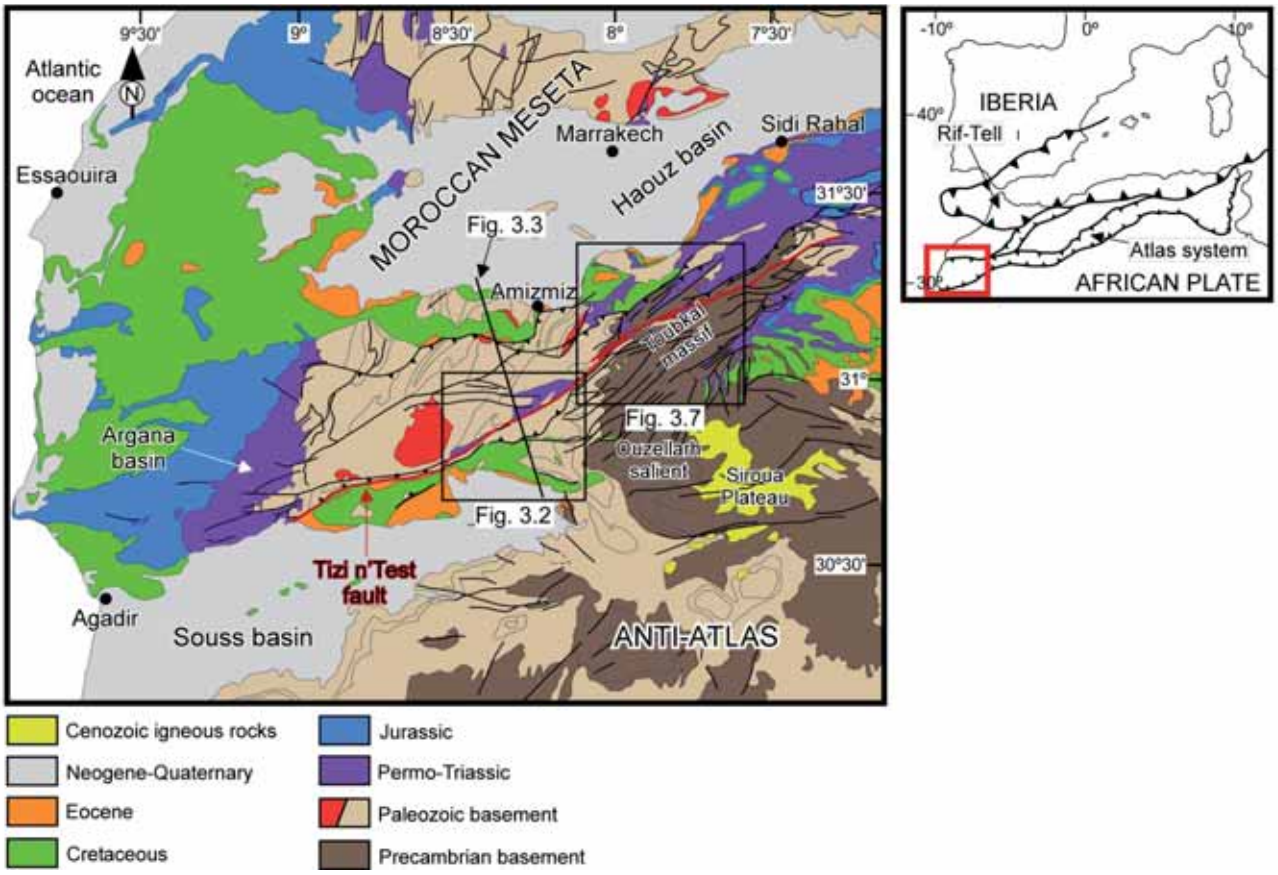

Figure 3.1. Geologic map of the western and Marrakech High Atlas (modified from Hollard, 1985). Black squares show the Tizi n'Test (west) and Ourika-Toubkal (east) areas were thermochronologic ages are obtained.

3.2. Tizi n'Test basin area

3.2.1. Sampling and thermochronologic results

In the Tizi n'Test basin area, 19 samples were collected following a NNW-SSE transect across the Triassic basin, the adjacent Paleozoic basement and in the Lower Cretaceous (the Infracenomanian Unit) and basement rocks located north-east of the Souss basin (Table 3.1; fig. 3.2). Samples are grouped in four vertical profiles (fig. 3.2 and 3.3.). The thermochronologic results obtained (zHe ages) are described in what follows for each vertical profile.

Table 3.1

Sample location in the Tizi n'Test area (WGS 84 map datum)

Sample	Longitude	Latitude	Elevation (m)	Profile	Lithologic unit	Lithology
MiHe-39T	8.2929ºW	30.9094ºN	1716	N'fis	Triassic (F5b)	Sandstone
MiHe-40T	8.2957ºW	30.9166ºN	1584	N'fis	Triassic (F5b)	Sandstone
MiHe-46T	8.3032ºW	30.9077ºN	1784	N'fis	Triassic (F5b)	Sandstone
MiHe-48T	8.3126ºW	30.9142ºN	1876	N'fis	Triassic (F5a)	Sandstone
MiHe-49T	8.3340ºW	30.8985ºN	2061	N'fis	Triassic (F3)	Conglomerate
MiHe-63T	8.2927ºW	30.9259ºN	1371	N'fis	Triassic (F5b)	Sandstone
MiHe-36T	8.2798ºW	30.8992ºN	2018	Abarnous	Cambrian	Sandstone
MiHe-38T	8.2958ºW	30.8991ºN	1806	Abarnous	Cambrian	Sandstone
MiHe-41T	8.2652ºW	30.8893ºN	2525	Abarnous	Cambrian	Grauwacke
MiHe-43T	8.2723ºW	30.8915ºN	2367	Abarnous	Cambrian	Tuff
MiHe-45T	8.2735ºW	30.8944ºN	2234	Abarnous	Cambrian	Sandstone
MiHe-56T	8.2188ºW	30.8993ºN	1685	Tama'rout	Cambrian	Grauwacke
MiHe-57T	8.2130ºW	30.8959ºN	1588	Tama'rout	Cambrian	Grauwacke
MiHe-58T	8.2228ºW	30.9106ºN	1989	Tama'rout	Cambrian	Grauwacke
MiHe-60T	8.2212ºW	30.9046ºN	1842	Tama'rout	Cambrian	Tuff
MiHe-50T	8.3005ºW	30.7762ºN	797	Al Mdad	Infracenomanian	Sandstone
MiHe-54T	8.2682ºW	30.8044ºN	855	Al Mdad	Cambrian	Sandstone
MiHe-55T	8.2637ºW	30.8475ºN	1297	Al Mdad	Infracenomanian	Sandstone
MiHe-61T	8.2090ºW	30.8671ºN	1273	Al Mdad	Infracenomanian	Sandstone

N'fis vertical profile

Six samples were collected in the Triassic deposits preserved in the Tizi n'Test Triassic basin (the N'fis vertical profile in fig. 3.2 and 3.3) between 1370 m and 2061 m of altitude. Sample MiHe-49T was collected in the F3 conglomeratic unit, poorly dated as Lower to Middle Triassic (the above F4 unit is dated as Anisian; El Arabi et al., 2006) and the other samples were collected in the F5 unit, which are mainly sandstones dated as Carnian (Cousminer and Manspeizer, 1976; Biron and Courtinat, 1982). The zircons analyzed (36 single-grain ages) yield uncorrected ages from 68.1 Ma to 361.8 Ma and σ-corrected ages (Farley et al., 1996) of 90±7 Ma to 439±35 Ma (fig. 3.4a; see details in Table 3.2) with intra-sample grain age dispersion (range of the ages divided by the mean, as used by Brown et al., 2013) from 25.2% to 158.7%. The high intra-sample age dispersion which exceed the analytical error may arise for diverse factors (e.g. grain size, zonation, radiation damage, etc.; see discussion in section 1.4.2), but the fact that some zHe ages obtained are older than their sedimentary age (i.e. 252-227 Ma) denotes that some samples were only partially reset, and therefore, they must have been heated to temperatures of 150-200°C at most (i.e. near the lower limit of the zPRZ) after Triassic sedimentation.

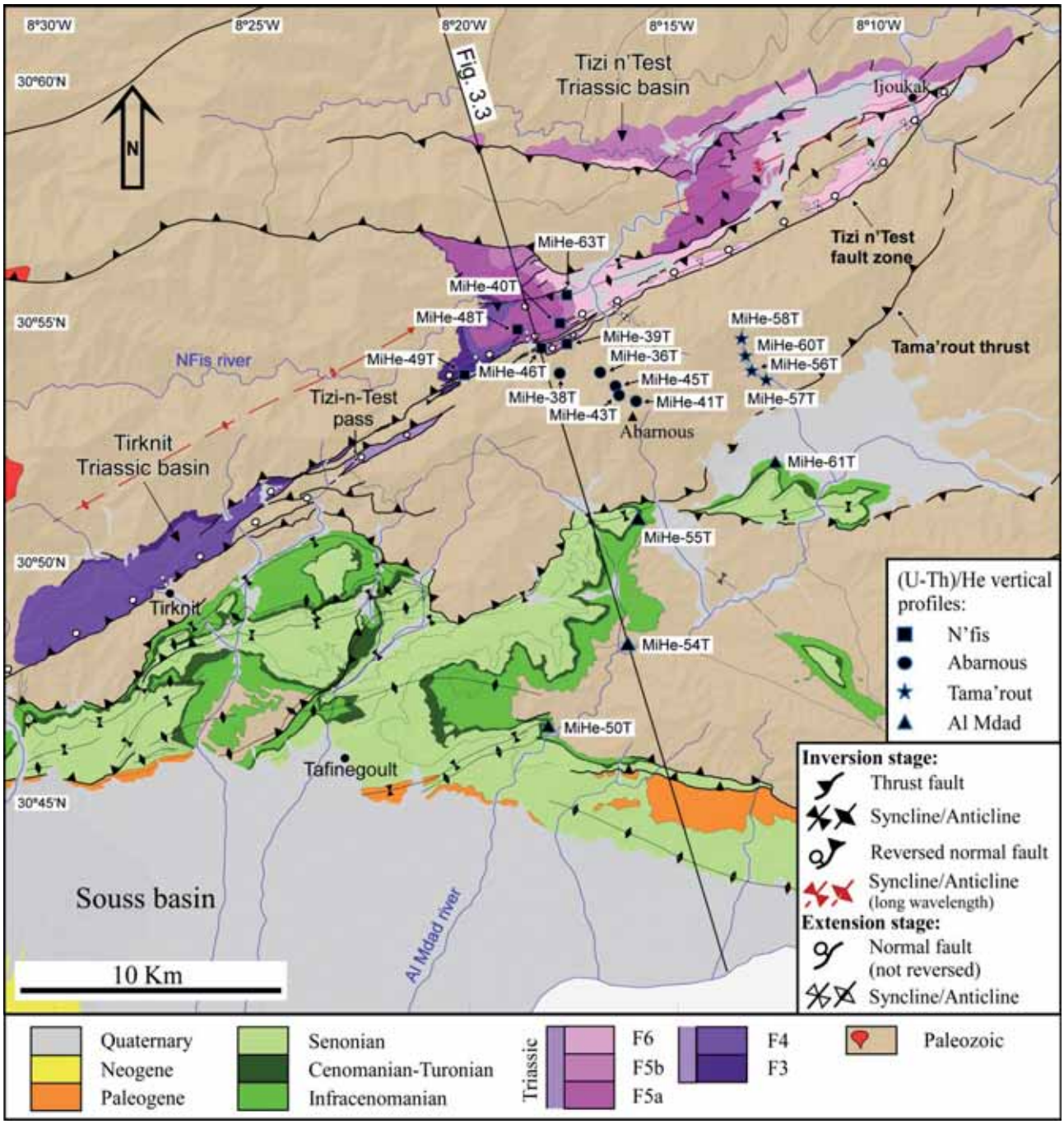

Figure 3.2. Geologic map of the Tizi n'Test area (see location in fig. 3.1) showing the main structural elements (modified from Domènech et al., 2015). Location of samples of different vertical profiles is also showed.

The zHe ages of the N'fis vertical profile are not elevation-dependent (fig. 3.4a) and show an age cluster at 155±40 Ma (4 zHe ages of 3 different samples older than 300 Ma are not accounted), which indicate that samples cooled rapidly through the zPRZ. Samples located

at stratigraphic lower position (i.e. the samples collected in the F3 Unit and in the base of the F5 subunit) are currently located at higher altitudes than the samples collected in stratigraphic higher position (fig. 3.4a). This tilting must have been produced during the Atlas orogeny, after samples crossed the zPRZ, probably due to the development of long-wavelength folds which deformed the Triassic deposits (the characteristics of this long-wavelength folds are extensively explained in Chapter 2, and their axial trace is represented in fig. 3.2). We have a good constrain of the stratigraphic position of samples in the Triassic sequence and also we have a good constrain of the thicknesses of different Triassic units; hence, samples have been projected into section of fig.3.3b at their present altitude and at their depositional initial position (fig. 3.3). As tilting of the Triassic units was produced after zHe resetting, in the following sections I will use the initial stratigraphic position of the samples (i.e. the initial vertical offset between samples) to infer amounts of cooling (an exhumation).

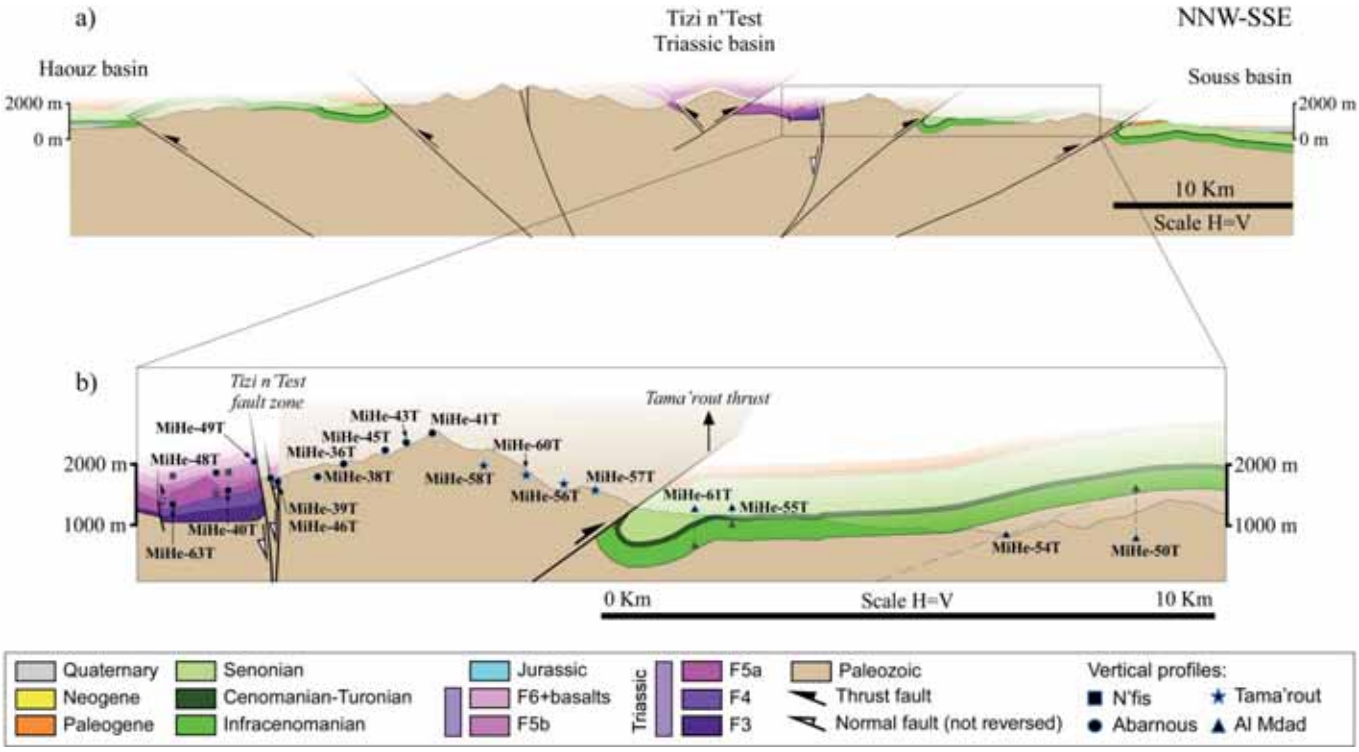

Figure 3.3. (a) General cross section from the Marrakech High Atlas across the Tizi n'Test Triassic basin (see location in fig. 3.1 and 3.2). This section was earlier presented as fig. 2.19, with a detailed location map in fig. 2.1. (b) Close-up of the basin and its margins with samples projected at their present altitude. In grey I show a projection following the stratigraphic position of the samples.

Table 3.2

Zircon (U-Th)/He data from the Tizi n'Test area

Grain Lab N°	Length (μm)	Width (μm)	Corrected age ±8% (Ma)	Uncorrected age (Ma)	U (ppm)	Th (ppm)	Sm (ppm)	^{4}He (nmol/g)	[eU]	F_T	Intra-sample dispersion (%)
Triassic samples. N'fis vertical profile											
zMiHe-39T-1	180.1	112.8	132.24±10.58	107.45	26.6	18.1	0.2	18.0	30.7	0.81	158.77
zMiHe-39T-2	193.5	115.9	439.07±35.13	361.75	172.7	77.1	46.9	384.7	190.7	0.82	
zMiHe-39T-3	228.3	106.9	113.38±9.07	92.88	137.9	22.6	0.5	72.3	143.1	0.82	
zMiHe-39T-4	171.1	101.2	214.56±17.16	170.20	77.2	77.9	0.7	89.0	95.1	0.79	
zMiHe-39T-5	213.3	107.2	208.91±16.71	169.94	109.6	58.9	0.5	114.9	123.2	0.81	
zMiHe-39T-6	158.9	101.0	122.67±9.81	96.90	111.6	101.4	1.1	71.4	135.0	0.79	
zMiHe-40T-1	152.2	82.9	151.49±12.12	115.82	171.2	29.9	2.5	112.4	178.0	0.76	25.22
zMiHe-40T-2	138.9	80.7	183.91±14.71	138.51	134.7	41.8	1.4	109.3	144.4	0.75	
zMiHe-40T-3	173.0	116.1	151.81±12.15	123.81	78.4	44.4	0.9	60.0	88.6	0.82	
zMiHe-40T-4	225.3	101.9	194.85±15.59	157.04	144.9	117.3	1.7	148.1	171.9	0.81	
zMiHe-40T-5	163.4	78.9	173.61±13.89	131.40	219.3	65.3	2.8	168.2	234.3	0.76	
zMiHe-40T-6	158.0	94.7	175.94±14.08	137.81	92.4	46.9	0.7	77.8	103.2	0.78	
zMiHe-46T-1	165.3	77.3	183.65±14.69	138.09	188.1	80.0	0.7	156.0	206.5	0.75	49.55
zMiHe-46T-2	148.8	92.3	113.34±9.07	87.76	34.0	24.2	0.5	19.0	39.6	0.77	
zMiHe-46T-3	197.3	99.1	200.33±16.03	159.48	59.5	60.7	3.0	64.4	73.5	0.80	
zMiHe-46T-4	145.2	74.6	195.97±15.68	143.87	70.7	67.3	0.9	68.0	86.2	0.73	
zMiHe-46T-5	154.4	88.9	189.39±15.15	146.11	168.3	96.6	4.3	152.4	190.5	0.77	
zMiHe-46T-6	167.4	77.4	170.76±13.66	127.58	74.9	82.7	11.4	65.7	94.0	0.75	
zMiHe-48T-1	227.7	86.6	90.03±7.20	70.44	41.3	22.7	0.4	17.8	46.6	0.78	137.13
zMiHe-48T-2	217.9	101.7	166.82±13.35	134.48	196.6	115.7	5.7	164.2	223.2	0.81	
zMiHe-48T-3	191.6	86.6	133.72±10.70	103.81	93.7	52.1	1.0	59.9	105.7	0.78	
zMiHe-48T-4	167.2	89.4	316.92±25.35	245.34	39.4	33.8	0.7	64.0	47.2	0.77	
zMiHe-48T-5	203.8	79.5	157.91±12.63	121.60	169.9	19.9	0.4	115.7	174.5	0.77	
zMiHe-48T-6	176.7	111.0	373.07±29.85	303.89	431.6	123.1	0.7	775.8	460.0	0.81	
zMiHe-49T-1	179.9	81.5	164.98±13.20	126.50	261.6	77.9	1.4	193.1	279.6	0.77	151.29
zMiHe-49T-2	217.7	101.7	231.05±18.48	187.15	189.1	44.3	0.8	204.7	199.3	0.81	
zMiHe-49T-3	209.5	72.3	206.65±16.53	154.93	297.6	99.4	2.2	271.8	320.4	0.75	
zMiHe-49T-4	229.1	81.4	148.45±11.88	114.92	327.5	117.3	3.3	222.3	354.5	0.77	
zMiHe-49T-5	158.2	109.3	403.44±32.28	325.48	59.7	21.9	0.4	117.1	64.7	0.81	
zMiHe-49T-6	136.8	86.4	89.70±7.18	68.10	59.5	42.1	0.6	25.6	69.2	0.76	
zMiHe-63T-1	167.7	91.4	149.83±11.99	117.18	241.5	86.8	1.9	167.2	261.5	0.78	51.54
zMiHe-63T-2	182.2	95.2	145.04±11.60	114.33	42.2	31.1	1.0	30.8	49.4	0.79	
zMiHe-63T-3	154.0	84.1	90.16±7.21	68.65	141.9	86.6	2.0	60.4	161.8	0.76	
zMiHe-63T-4	144.0	83.2	103.63±8.29	78.51	82.0	40.5	0.9	39.0	91.3	0.76	
zMiHe-63T-5	154.7	88.9	104.73±8.38	80.86	113.3	56.6	0.6	55.6	126.3	0.77	
zMiHe-63T-6	149.6	74.1	101.21±8.10	74.66	137.9	75.8	1.3	63.1	155.3	0.74	
Paleozoic samples (North of Tama'rout thrust). Abarnous and Tama'rout vertical profiles											
zMiHe-36T-1	198.3	98.7	217.84±17.43	174.38	120.4	45.3	0.6	125.1	130.8	0.80	12.58
zMiHe-36T-2	152.5	72.9	211.36±16.91	156.36	136.1	37.8	0.6	124.0	144.8	0.74	
zMiHe-36T-3	129.3	80.0	217.80±17.42	161.64	29.2	24.4	0.6	30.9	34.8	0.74	
zMiHe-36T-4	139.4	80.9	239.12±19.13	180.43	127.2	34.9	0.6	133.9	135.2	0.75	
zMiHe-36T-5	130.8	76.8	219.48±17.56	162.85	105.6	28.2	0.6	100.0	112.1	0.74	
zMiHe-36T-6	146.2	82.5	218.70±17.50	165.61	79.7	38.8	1.0	80.5	88.6	0.76	
zMiHe-38T-1	205.4	114.1	255.65±20.45	210.50	51.6	14.1	0.3	63.5	54.9	0.82	76.69
zMiHe-38T-2	174.4	81.9	142.26±11.38	109.01	93.2	26.5	0.8	59.0	99.3	0.77	
zMiHe-38T-3	181.0	84.8	151.88±12.15	117.55	74.5	21.5	1.1	51.0	79.5	0.77	
zMiHe-38T-4	156.6	100.1	129.25±10.34	102.30	73.4	34.0	0.6	45.3	81.2	0.79	
zMiHe-38T-5	145.1	79.9	153.94±12.32	115.91	75.5	26.8	0.6	51.6	81.7	0.75	
zMiHe-38T-6	160.8	102.2	155.83±12.47	124.23	57.2	19.4	0.5	41.8	61.7	0.80	
zMiHe-41T-1	149.1	87.6	163.17±13.05	125.59	143.9	53.0	0.5	107.1	156.1	0.77	35.96

Table 3.2. (continued)

Grain Lab N°	Length (μm)	Width (μm)	Corrected age ±8% (Ma)	Uncorrected age (Ma)	U (ppm)	Th (ppm)	Sm (ppm)	^{4}He (nmol/g)	[eU]	F_T	Intra-sample dispersion (%)
zMiHe-41T-3	160.3	78.6	153.90±12.31	116.08	143.9	52.8	0.3	98.9	156.1	0.75	
zMiHe-41T-4	146.0	93.4	160.39±12.83	125.10	261.1	75.5	0.7	190.2	278.4	0.78	
zMiHe-41T-5	115.6	71.5	111.17±8.89	80.48	561.0	78.9	0.7	253.3	579.2	0.72	
zMiHe-41T-6	155.9	63.2	134.34±10.75	95.40	158.4	54.8	0.4	88.9	171.0	0.71	
zMiHe-43T-1	194.5	98.1	156.63±12.53	125.15	112.1	38.2	0.7	82.6	120.9	0.80	25.49
zMiHe-43T-2	162.2	78.5	130.92±10.47	98.83	438.9	151.6	1.1	255.1	473.7	0.76	
zMiHe-43T-3	169.3	95.6	121.84±9.75	96.44	488.6	98.9	1.7	268.5	511.4	0.79	
zMiHe-45T-1	150.0	98.1	74.21±5.94	58.41	206.2	81.5	0.3	71.4	225.0	0.79	86.93
zMiHe-45T-2	190.4	88.8	154.74±12.38	121.07	355.3	130.4	0.8	254.7	385.4	0.78	
zMiHe-45T-3	120.9	75.1	110.38±8.83	81.09	360.1	69.8	0.8	165.8	376.2	0.74	
zMiHe-45T-4	171.8	79.6	188.77±15.10	143.63	229.0	66.2	0.7	191.9	244.2	0.76	
zMiHe-45T-5	147.5	96.4	135.49±10.84	105.37	61.4	74.7	2.0	45.3	78.6	0.78	
zMiHe-45T-6	156.7	127.2	127.07±10.17	104.59	79.8	38.0	0.9	50.5	88.6	0.82	
zMiHe-56T-1	154.4	80.8	106.60±8.53	80.83	300.5	95.3	1.7	141.7	322.4	0.76	85.70
zMiHe-56T-2*	111.1	64.3	84.73±6.78	58.92	191.1	75.2	0.6	66.7	208.4	0.70	(42.60)
zMiHe-56T-3	133.1	75.7	160.88±12.87	118.96	170.5	53.1	0.7	118.6	182.7	0.74	
zMiHe-56T-4*	115.9	63.8	66.48±5.32	46.31	130.5	47.4	0.5	35.5	141.4	0.70	
zMiHe-56T-5	134.1	73.5	116.89±9.35	85.73	472.8	168.3	1.2	238.7	511.6	0.73	
zMiHe-56T-6	106.7	60.4	125.39±10.03	85.23	198.4	77.0	0.5	100.3	216.1	0.68	
zMiHe-57T-2	206.3	100.2	164.29±13.14	132.11	154.4	55.5	0.5	120.7	167.2	0.80	29.18
zMiHe-57T-4	198.8	97.1	208.75±16.70	166.83	124.4	36.7	0.4	121.4	132.8	0.80	
zMiHe-57T-5	185.0	82.2	222.18±17.77	170.68	160.5	62.1	0.5	163.6	174.8	0.77	
zMiHe-58T-1	252.6	98.1	214.53±17.16	173.28	156.8	57.8	1.1	161.7	170.1	0.81	35.01
zMiHe-58T-2	173.4	94.4	178.90±14.31	141.23	154.0	44.5	0.3	126.9	164.3	0.79	
zMiHe-58T-3	208.1	87.8	150.99±12.08	118.27	128.8	51.9	0.7	90.9	140.8	0.78	
zMiHe-60T-3	222.5	106.6	161.21±12.90	131.53	112.6	37.7	0.3	87.2	121.3	0.82	9.48
zMiHe-60T-4	177.4	87.1	177.32±14.19	137.68	189.3	69.1	0.5	154.5	205.2	0.78	
zMiHe-60T-6	227.0	95.9	171.50±13.72	137.27	192.9	76.6	0.5	158.1	210.5	0.80	
Cretaceous (South of Tama'rout thrust). Al Mdad vertical profile											
zMiHe-50T-1	171.2	73.8	295.76±23.66	220.96	371.1	111.0	2.7	482.8	396.7	0.75	77.67
zMiHe-50T-2	179.1	101.3	153.27±12.26	122.38	19.9	11.0	0.1	15.0	22.4	0.80	
zMiHe-50T-3	159.0	104.9	273.58±21.89	219.11	21.6	7.3	0.4	28.1	23.2	0.80	
zMiHe-50T-4	171.2	104.9	351.95±28.16	282.08	76.3	49.2	0.4	136.9	87.6	0.80	
zMiHe-50T-5	142.5	87.0	252.30±20.18	193.19	97.3	43.6	2.2	114.0	107.4	0.77	
zMiHe-50T-6	178.8	85.9	207.92±16.63	161.97	197.0	19.2	1.4	178.5	201.4	0.78	
zMiHe-55T-1	172.2	70.3	252.31±20.18	184.70	281.8	202.9	1.1	333.6	328.5	0.73	20.16
zMiHe-55T-2	153.4	89.0	284.95±22.80	219.26	53.0	44.3	0.8	76.5	63.2	0.77	
zMiHe-55T-3	225.7	97.2	256.77±20.54	207.11	170.5	19.8	0.8	199.3	175.1	0.81	
zMiHe-55T-4	172.8	95.2	258.59±20.69	204.12	79.3	32.4	0.6	97.4	86.7	0.79	
zMiHe-55T-5	164.7	84.6	233.24±18.66	179.58	199.6	54.4	1.2	209.0	212.2	0.77	
zMiHe-55T-6	177.9	75.7	286.07±22.89	211.60	37.7	101.9	1.5	71.5	61.1	0.74	
zMiHe-61T-1	227.3	89.6	315.67±25.25	249.21	105.4	51.7	4.1	161.6	117.4	0.79	27.8
zMiHe-61T-2	242.5	107.1	261.02±20.88	213.82	155.3	59.9	1.2	199.0	169.1	0.82	
zMiHe-61T-3	218.5	114.7	291.15±23.29	241.49	335.7	22.7	2.1	454.1	341.0	0.83	
zMiHe-61T-5	148.8	82.9	237.99±19.04	181.61	118.7	25.3	4.2	124.0	124.5	0.76	
zMiHe-61T-6	237.2	83.6	317.09±25.37	246.62	107.3	64.8	1.8	166.6	122.2	0.78	

Table 3.2. (continued)

Grain Lab N°	Length (μm)	Width (μm)	Corrected age ±8% (Ma)	Uncorrected age (Ma)	U (ppm)	Th (ppm)	Sm (ppm)	^{4}He (nmol/g)	[eU]	F_T	Intra-sample dispersion (%)
Paleozoic (South of Tama'rout thrust). Al Mdad vertical profile											
zMiHe-54T-1	163.2	73.0	263.36±21.07	194.71	119.4	63.7	0.7	143.6	134.1	0.74	104.37
zMiHe-54T-2	141.9	73.8	353.96±28.32	259.84	190.5	127.3	5.3	316.0	219.8	0.73	(36.74)
zMiHe-54T-3	132.2	84.4	272.73±21.82	205.01	119.0	119.4	3.5	165.5	146.5	0.75	
zMiHe-54T-4*	141.1	70.8	89.69±7.18	65.30	265.4	107.3	1.9	103.0	290.1	0.73	
zMiHe-54T-5	186.5	75.0	290.53±23.24	218.95	173.6	50.2	1.6	223.2	185.2	0.75	
zMiHe-54T-6	174.8	97.0	248.92±19.91	197.31	123.4	51.3	1.3	146.7	135.2	0.79	

* Sample's grains with an (*) are not included in the interpretation. The intra-sample grain age dispersion without the discarded grains is shown in parentheses.

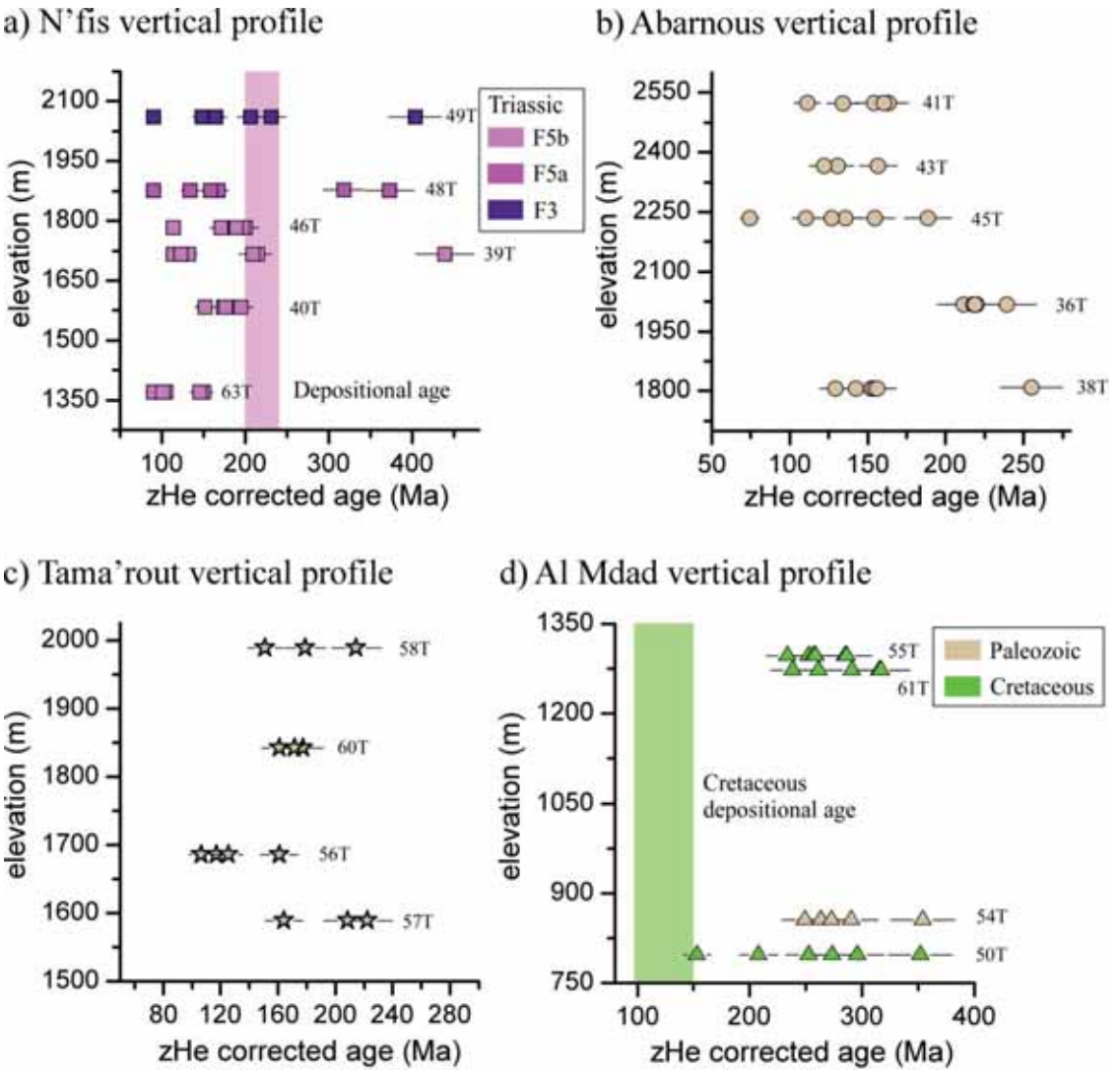

Figure 3.4. Age-elevation plots with 2σ error for the (a) N'fis, (b) Abarnous, (c) Tama'rout and (d) Al Mdad vertical profiles.

Abarnous and Tama'rout vertical profiles

Nine samples were collected in detrital and volcanic deposits (e.g., tuffs, grauwackes and sandstones) of Cambrian age (Angoud et al., 2002) to the south of the Tizi n'Test basin. They were collected in two vertical profiles (the Abarnous and Tama'rout vertical profiles in fig. 3.2 and 3.3) with difference between top and bottom samples of 719 m and 401 m respectively (Table 3.1; fig. 3.4b,c). Samples are located in a structural block between the Tizi n'Test Triassic basin and the Cretaceous-Paleozoic samples of the SubAtlas Zone adjacent to the Souss basin (fig. 3.3). This block is limited to the north by normal faults belonging to the Tizi n'Test fault zone (described in Chapter 2) and to the south by the Tama'rout thrust (fig. 3.3). The five samples (26 single-grain ages) of the Abarnous vertical profile yield uncorrected ages from 58.4 Ma to 210.5 Ma with σ-corrected ages from 74±6 Ma to 256±20 Ma (Table 3.2; fig. 3.4b) with intra-sample grain age dispersion from 12.58% to 86.93%. The four samples of the Tama'rout vertical profile yield uncorrected ages from 80.8 Ma to 173.3 Ma with σ-corrected ages from 107±9 Ma to 222±18 Ma (Table 3.2; fig. 3.4c). The aliquots MiHe-56T-2 and MiHe-56T-4 of sample MiHe-56T are not accounted due to their small width (less than 70 μm; see discussion in section 1.4.2) and their much younger age respect to the other aliquots of the same sample. Tama'rout samples present an intra-sample grain age dispersion that ranges from 9.48% to 42.60% (Table 3.2).

All the zHe ages of both vertical profiles are younger than their depositional age, which indicate that the zHe ages were fully reset at some time after their deposition. Also, both profiles show no elevation-dependent zHe ages and a similar age cluster at 163±45 Ma (Abarnous) and 166±36 Ma (Tama'rout) (fig. 3.4b,c) which indicate that samples cooled rapidly through the zPRZ. The zHe ages present a high intra-sample age dispersion which denotes that samples were in the zPRZ prior to their fast cooling in Mid Jurassic times.

Therefore, the Triassic samples of the N'fis vertical profile and the Paleozoic samples of the Abarnous and Tama'rout vertical profiles register a similar cooling history. Plotting the zHe ages of these three vertical profiles together, shows that samples rapidly cooled through the zPRZ (from temperatures near the lower limit of the zPRZ, because most zHe dates are totally reset but show high intra-sample grain age dispersion) at a cluster age of 160±41 Ma (fig. 3.5).

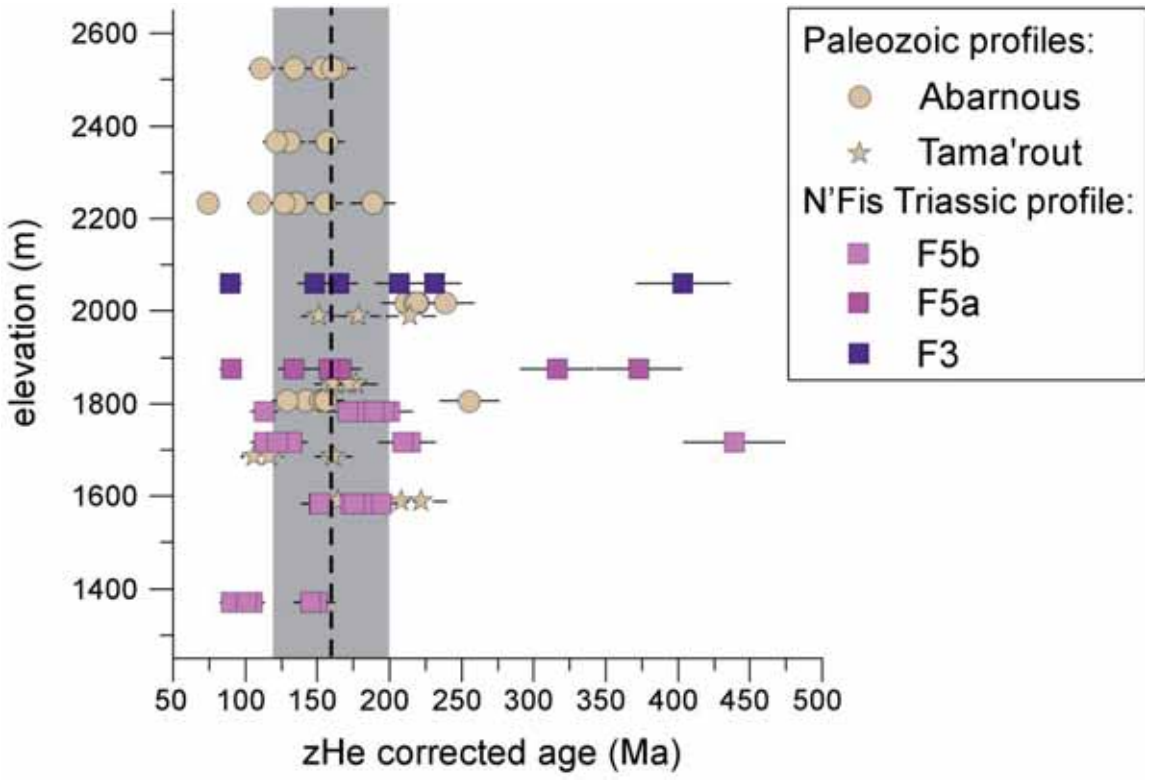

Figure 3.5. Age-elevation plot with 2σ error for the N'fis, Abarnous and Tama'rout vertical profiles showing an age cluster at 160±41 Ma.

Al Mdad vertical profile

Four samples were collected in the southern foothills of the Marrakech High Atlas. Samples MiHe-50T, MiHe-55T and MiHe-61T were collected in a poorly-sorted sandstone of the Infracenomanian Unit while sample MiHe-54T was collected in a sandstone of Early Cambrian age (Angoud et al., 2002)(fig. 3.2 and 3.3). They were collected at elevations 797 m to 1297 m (Table 3.1) and they are separated from the Paleozoic and Triassic samples to the north by the Tama'rout thrust. The Paleozoic sample yielded uncorrected ages from 194.7 Ma to 259.8 Ma with σ-corrected ages from 249±20 Ma to 354±28 Ma (fig. 3.4d), therefore, zHe ages were reset after their deposition and exhumed through the zPRZ at Carboniferous-Permian times, probably due to the Variscan orogeny. The sample remains at lower temperatures from that time to present. Samples of the Infracenomanian Unit yield uncorrected zHe ages (17 single-grain ages) from 122.4 Ma to 282.1 Ma, with σ-corrected ages from 153±12 Ma to 352±28 Ma (fig. 3.4d). All zHe ages are older than their depositional age, being not reset after their deposition, in contrast to samples of the Tizi n'Test basin. They show mainly Carboniferous to Permian zHe ages, similar to the zHe

ages of the Paleozoic sample, which denotes a near Paleozoic-Precambrian source area where zHe ages had not been reset.

3.2.2. Implications and discussion

The southern Tizi n'Test basin-border faults

Triassic and Paleozoic samples of the N'fis, Abarnous and Tama'rout profiles show similar ages, grouped at 160±41 Ma (fig. 3.5), in spite of they are located both sides of the Tizi n'Test Triassic basin-border faults. As seen and discussed in chapter 2, I interpret these southern faults belonging to the Tizi n'Test fault zone, as normal faults during the rifting stage with a limited movement during the Atlas orogeny (based on field observations and microstructure analysis). These field observations are now confirmed by thermochronology, as similar zHe ages imply that vertical movements in these faults were minor from late Mid to Late Jurassic times until the present.

The Triassic-Jurassic rift development

The partial to total reset of the zHe ages of the N'fis vertical profile, obtained in the Triassic Tizi n'Test basin, shows that samples were heated at temperatures within the zPRZ (near the lower limit) after deposition and previous to their exhumation in the Late Jurassic (age cluster 155±40 Ma). This means that assuming a minimum temperature of ~150°C (the zPRZ is ~130-200°C; see section 1.4.2) for samples located stratigraphically at higher position (i.e. samples MiHe-39T and MiHe-63T located at the top of the F5b subunit, dated as Carnian; Cousminer and Manspeizer, 1976; Biron and Courtinat, 1982), these samples had to be buried in Late Triassic and Early Jurassic times under a minimum of 3.25 km to 4.3 km of syn-rift deposits. I chose a paleogeothermal gradient of 30-40°C/km (similar to that modelled for the Ourika area, discussed in detail in following sections) and a mean surface temperature of ~20°C. This high paleogeothermal is consistent with the expected generalized upward movement of the isotherms due to the rifting and the magmatic events that took place at the limit between the Triassic-Jurassic (the CAMP event; e.g. Knight et al., 2004). The overlying F6 Triassic Unit, in spite of its upper limit is not preserved, is slightly more than 0.5 km thick in the Tizi n'Test Triassic basin, and in the Ourika basin (see location in fig. 3.1; Beauchamp, 1988; Benaouiss et al., 1996; Fabuel-Perez et al., 2009). Therefore, assuming that a maximum of 1km of Late Triassic sediments (corresponding to the F6 Unit) and that basalts were probably laid in the Tizi n'Test basin (making thus a total of ~2 km of Triassic), we need a minimum of 2.25-3.3 km of Early to Mid-Jurassic deposits to bury the F5b Triassic sample to the

estimated depth. In consequence the total amount of Triassic-Mid Jurassic syn-rift deposits accumulated in the deepest part of the Tizi n'Test basin is of 4.25-5.3 km (fig. 3.6a).

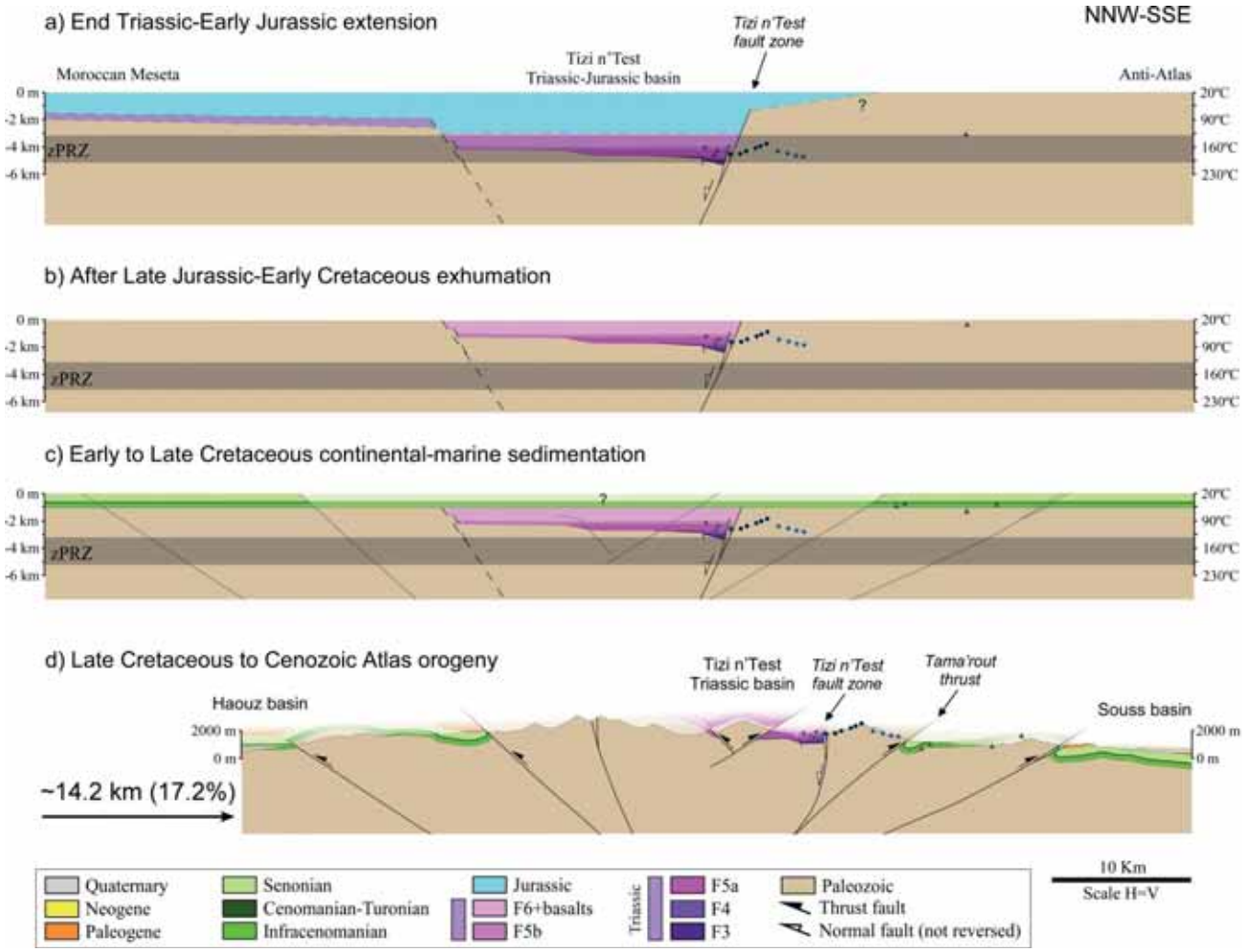

Figure 3.6. Cross-sections of the Marrakech High Atlas across the Tizi n'Test Triassic basin restored to selected steps. The location of samples at each step based on their zHe ages is also shown. (a) Restored cross-section to the end of the Triassic-Mid Jurassic extension. The southern border of the Jurassic sedimentation area cannot be precisely traced (see text for explanation). (b) After Late Jurassic-Early Cretaceous exhumation. (c) Early to Late Cretaceous continental-marine sedimentation. We assume that some sedimentation occurred also in the inner part of the Marrakech High Atlas, in spite of the fact that Cretaceous deposits are rarely preserved (see text for discussion). (d) Present-day cross-section.

The extension of the syn-rift deposits north and south of the Tizi n'Test basin is not precisely known but can be approximately assessed. The Cambrian sample of the Al Mdad vertical profile, located south of Tama'rout thrust, show Carboniferous-Permian zHe ages,

and in consequence, cannot have been buried under temperatures more than 130°C (~3km assuming a paleogeothermal gradient of 35°C/km) during the Triassic-Jurassic rift. Therefore, the maximum amount of Triassic-Jurassic sediments that could deposit south of Tama'rout thrust, if they were at all deposited, was limited. In view of the no preservation of Triassic-Jurassic elsewhere in the Anti-Atlas, I have not represented them in the restored section of fig. 3.6a. On the other hand, with the data available it cannot be ascertained whether the Triassic-Jurassic deposits extended south of the Tizi n'Test fault. This is because even though samples in the Abarnous-Tamarout block are reset, it cannot be told whether these samples were buried by Triassic-Jurassic or Paleozoic rocks (or the two; see fig. 3.6a). To the north, thermal models of AFT data obtained by previous authors in the Moroccan Meseta show a Middle Jurassic-Early Cretaceous cooling (Ghorbal et al., 2008; Saddiqi et al., 2009; Barbero et al., 2011), which is coincident with the fast cooling event registered by the zHe ages of the N'fis, Abarnous and Tama'rout samples presented in this work. As shown by these authors, the Moroccan Meseta samples are overlain by thin Triassic deposits in some localities, which means that samples were near the surface temperatures in pre-Triassic times and had to be buried to temperatures higher than 120°C to cause annealing of the apatite fission track system and reset of aHe ages during the Triassic and Early Jurassic. Assuming a paleogeothermal gradient of 30-40°C/km, this means that 2.5-3.3 km of Triassic-Early Jurassic sediments had to accumulate in the Moroccan Meseta. Therefore, the Moroccan Meseta cannot be considered as the shoulder of the Atlas rift, but instead a poorly subsiding domain during the whole rifting stage, and in consequence, a continuous Triassic-Jurassic deposition had to occur from the Tizi n'Test basin to the Moroccan Meseta. An extensional fault has been tentatively represented separating the Tizi n'Test basin from the areas to the north (fig. 3.6a), in light of a slickensided normal fault observed near a small Triassic outcrop south of Wirgane (fig. 2.1).

The Mid-Late Jurassic to Early Cretaceous cooling

ZHe ages of the N'fis, Abarnous and Tama'rout vertical profiles show that samples, located in the lower part of the zPRZ after the Triassic-Early Jurassic rifting, were rapidly exhumed through the zPRZ in late Mid to Late Jurassic times at a cluster age of 160±41 Ma. This fast cooling is also registered by the AFT ages and thermal models (also by some aHe ages) obtained by previous authors in the Moroccan Meseta (N and NW of the Tizi n'Test area) but also in the Anti-Atlas (S and SE of the Tizi n'Test area) (Ghorbal et al., 2008; Saddiqi et al., 2009; Barbero et al., 2011; Ruiz et al., 2011). Similar AFT ages were obtained by Balestrieri et al. (2009) and Bertotti and Gouiza (2012) (based on the work from

Ghorbal, 2009) for the northern and southern foothills of the Marrakech High Atlas in the Ourika area, ~42 km to the NW of the Tizi n'Test area (see location of the two areas in the fig. 3.1).

The first conclusion we can extract from the thermochronologic results presented here and from previous published data, is that the Mesozoic Atlas rift subsidence had to finish in the Marrakech High Atlas in Mid-Late Jurassic times. The second conclusion is that the end of the subsidence stage was followed by a wide upward vertical movement with exhumation during the Late Mid Jurassic-Early Cretaceous that spans from the Moroccan Meseta to the Anti-Atlas, crossing the Marrakech High Atlas, and following the orientation of the present Atlantic margin. The significance and origin of this Middle Jurassic-Early Cretaceous exhumation event will be discussed later but coincides with the intermittent sedimentation of the "formation des couches rouges" in the Central and Eastern High Atlas, which as explained in Chapter 1, is composed of sandstones and conglomerates with abundant pre-Mesozoic clasts whose source area, in view of our thermochronologic results and the previous published, could be the emergent Moroccan Meseta-Marrakech High Atlas-SW Anti-Atlas area. The upper deposits of these redbeds (referred as Infracenomanian Unit and recently dated as Barremian-Aptian to Early Cenomanian; Ettachfini and Andreu, 2004; Frizon de Lamotte et al., 2009) overflowed the Central High Atlas rift margins overlapping the basement in the rift shoulders (described in Chapter 1; Choubert and Faure-Muret, 1962; Jenny et al., 1981; Haddoumi et al., 1998, 2002, 2008, 2010; Andreu et al., 2003; Charrière et al., 2005). The Infracenomanian Unit is also preserved unconformable above the basement in the northern and southern foothills of the Marrakech High Atlas, and hence it seems that this unit post-dates the Middle Jurassic-Early Cretaceous exhumation in the Marrakech High Atlas.

Previous works in the Moroccan Meseta and the northern and southern Marrakech High Atlas foothills from Ghorbal et al. (2008), Saddiqi et al. (2009) and Bertotti and Gouiza (2012), based on the AFT dating and corresponding thermal models, show that after samples were buried in Triassic-Jurassic times to temperatures higher than 120°C they started moving upward at 170-150 Ma reaching the surface prior to 100 Ma (as samples are overlain by Early Cretaceous to Cenomano-Turonian deposits which lie unconformable above) which imply 1.5 to ~3 km of exhumation (according to the different paleogeothermal gradient chosen by different authors; Ghorbal et al., 2008; Ghorbal, 2009; Saddiqi et al., 2009; Bertotti and Gouiza, 2012). Based on the zHe of the present work, if we assume a minimum temperature for the uppermost samples of the N'fis, Abarnous and Tama'rout vertical profiles of 150-170°C (i.e. near the Tc of zHe system; Reiners, 2005;

Wolfe and Stockli, 2010), the lowest samples had to be located at temperatures of 185-200°C (considering the present vertical offset in the Paleozoic samples and the pre-tilting offset in the Triassic samples). This means a minimum amount of cooling during the Middle Jurassic to Early Cretaceous to bring samples above the zPRz (i.e. ~130°C) of 55°C to 70°C, which is translated into a minimum exhumation of 1.6-2 km (assuming a paleogeothermal gradient of 35°C/km) for the inner part of the Marrakech High Atlas in these times, in agreement with values obtained for previous authors out of the axial part Marrakech High Atlas (fig. 3.6b). If we assume that 1-1.5 km of Late Cretaceous or younger sediments (based on the thicknesses exposed in the northern and southern foothills; fig. 3.3) accumulated in the axial part of the Marrakech High Atlas, then the amount of exhumation increases to 2.6-3.5 km.

Although we could expect some post-rift thermal relaxation during this period of time, after the Mid-Late Jurassic rifting, the amount of cooling registered cannot be fully explained by a decrease in the paleogeothermal gradient, and therefore, some "real" exhumation had to operate. In addition, the modelled paleogeothermal gradients of zHe and aHe ages of vertical profiles in the Ourika area (which are presented in detail in following sections) show persistent high paleogeothermal gradients (30-40°C/km) in Late Cretaceous.

The Atlas orogeny

The amount of exhumation and the beginning of the Atlas orogeny in the Tizi n'Test area is poorly constrained by zHe dating, as all samples analyzed were out of the zPRZ in Late Jurassic to Early Cretaceous times, being the final exhumation event not registered by the data. However, some inferences can still be made. First, is that the total amount of exhumation (accounting the exhumation due to the compression and due to the mantle-related uplift, see Chapter 1 for details) in the Tizi n'Test basin and adjacent southern Paleozoic basement (north of Tama'rout thrust) had to be less than ~3km, as all samples were at temperatures lower than ~130°C in Early Cretaceous. Second, south of the Tama'rout thrust, the Paleozoic sample of the Al Mdad vertical profile, at nearly surface temperatures at the time previous to the Infracenomanian Unit sedimentation, was covered by 1-1.5 km of Cretaceous to Tertiary deposits (preserved in the SubAtlas zone of the Marrakech High Atlas above the sample; see fig. 3.2 and 3.3), implying that the total amount of Cenozoic exhumation was of ~1-1.5 km to bring that sample to surface temperatures at present time. As the Cenozoic exhumation produced by a mantle source is expected to be equal in the whole Marrakech High Atlas due to the long-wavelength

character of the uplift, the difference in exhumation of 1.5-2 km in both sites of the Tama'rout thrust from Early Cretaceous to present has to be explained by the activity of the Tama'rout thrust, providing an estimation of the vertical slip along this fault. Given the current dip (~30°C) observed for this fault, this implies a net slip of 3-4 km.

Taking into account this and the reconstruction of the Atlas rift and Middle Jurassic-Early Cretaceous exhumation presented in fig. 3.6(a,b) the restored cross section of fig. 3.6(c,d) suggests a total shortening of 14.2 km (17.2%) for the High Atlas in the Tizi n'Test transect. Minimum displacement has been assigned for thrusts in the northern foothills of the Atlas on the basis of post-Paleozoic sediments preserved.

3.3. Ourika-Toubkal area

3.3.1. Sampling and thermochronologic results

To the east of the Marrakech High Atlas, in the Ourika-Toubkal area, a suite of 24 samples was collected in rhyolitic and granitic rocks of the Precambrian basement (Table 3.3 and fig. 3.7), from which 23 zHe sample ages (65 single-grain ages) and 11 aHe sample ages (33 single-grain ages) were obtained (Table 3.4 and 3.5). Samples were taken in four vertical profiles following a NNW-SSE transect across the mountain belt (fig. 3.7 and 3.8). In what follows we describe the results for each of the four vertical profiles across the area in detail.

Table 3.3
Sample location in the Ourika-Toubkal area (WGS 84 map datum)

Sample	Longitude	Latitude	Elevation (m)	Profile	Lithologic unit	Lithology
MiHe-02	7.9237°W	31.1553°N	1608	Imlil	Neoproterozoic	Granite
MiHe-03	7.9225°W	31.1118°N	1982	Imlil	Neoproterozoic	Rhyolite
MiHe-04	7.9159°W	31.1006°N	2241	Imlil	Neoproterozoic	Rhyolite
MiHe-06	7.9044°W	31.0963°N	2587	Imlil	Neoproterozoic	Rhyolite
MiHe-08	7.8938°W	31.0985°N	2994	Imlil	Neoproterozoic	Rhyolite
MiHe-12	7.8254°W	31.1317°N	3629	Tizi n'Likemt	Neoproterozoic	Rhyolite
MiHe-15	7.8179°W	31.1219°N	2998	Tizi n'Likemt	Neoproterozoic	Granite
MiHe-17	7.8161°W	31.1092°N	2559	Tizi n'Likemt	Neoproterozoic	Granite
MiHe-19	7.8100°W	31.0589°N	3198	Tizgui	Neoproterozoic	Rhyolite
MiHe-20	7.8166°W	31.0530°W	2831	Tizgui	Neoproterozoic	Granite
MiHe-21	7.8259°W	31.0550°N	2574	Tizgui	Neoproterozoic	Granite
MiHe-23	7.8374°W	31.0463°N	2202	Tizgui	Neoproterozoic	Granite
MiHe-24	7.8476°W	31.0466°N	1989	Tizgui	Neoproterozoic	Granite
MiHe-25	7.8612°W	31.0627°N	2221	Tizgui	Neoproterozoic	Granite
MiHe-27	7.8350°W	31.0160°N	1791	Tizgui	Neoproterozoic	Granite
MiHe-28	7.6938°W	31.2177°N	1494	Ourika	Neoproterozoic	Granite
MiHe-29	7.7484°W	31.1937°N	1780	Ourika	Neoproterozoic	Granite
MiHe-30	7.7738°W	31.1980°N	2038	Ourika	Neoproterozoic	Granite
MiHe-31	7.7893°W	31.1965°N	2204	Ourika	Neoproterozoic	Granite
MiHe-32	7.7961°W	31.1985°N	2401	Ourika	Neoproterozoic	Granite
MiHe-33	7.7951°W	31.2041°N	2595	Ourika	Neoproterozoic	Granite
MiHe-34	7.7919°W	31.2078°N	2818	Ourika	Neoproterozoic	Granite
MiHe-35	7.8029°W	31.2088°N	3029	Ourika	Neoproterozoic	Granite

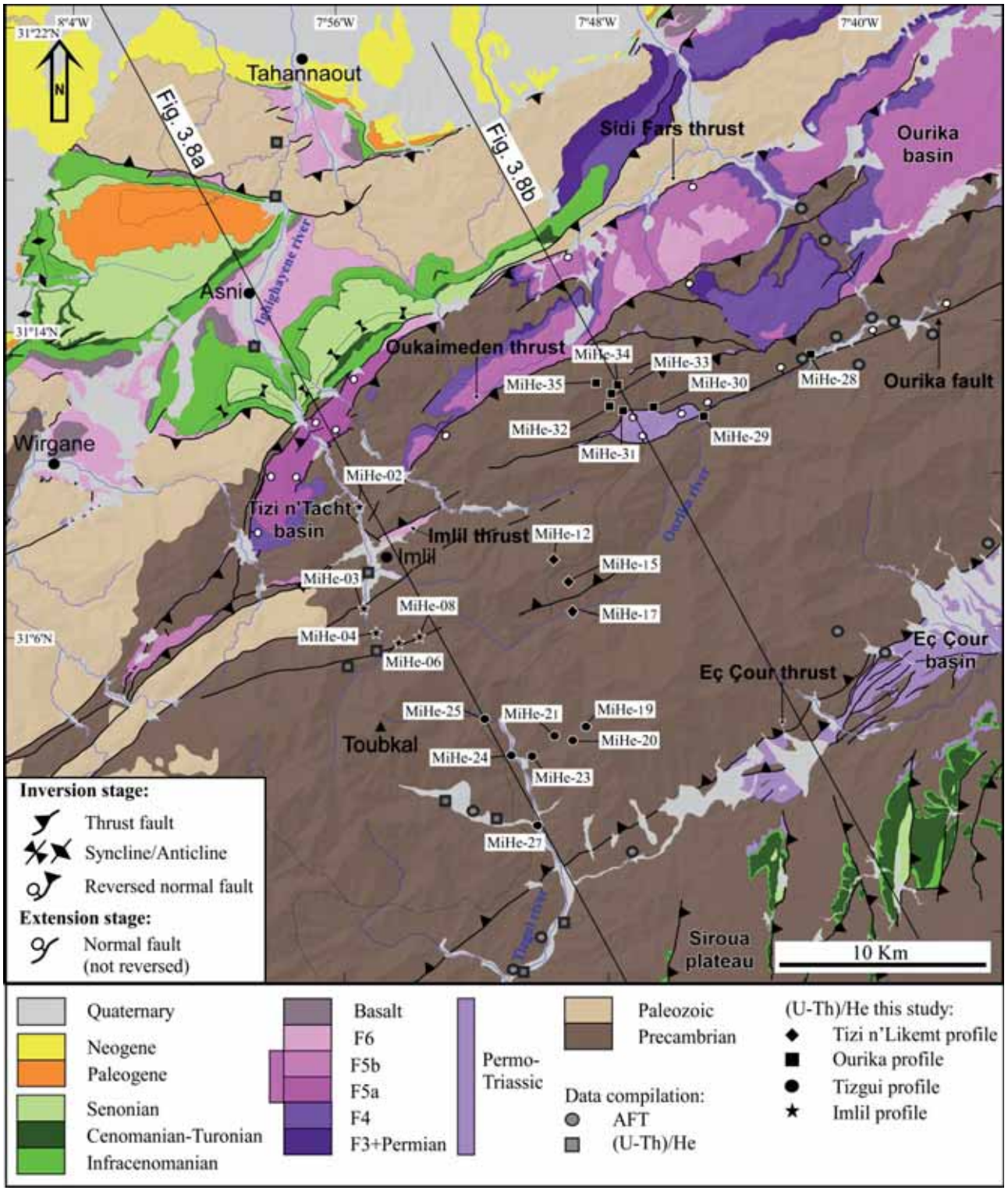

Figure 3.7. Geologic map of the Ourika-Toubkal area (see location in fig. 3.1) showing the main structural elements (modified from Domènech et al., 2015). Location of samples of the four vertical profiles is also shown. The location of low-temperature data previously published (AFT and (U-Th)/He in apatites) is shown on the map by grey circles and squares (after Missenard et al., 2008; Balestrieri et al., 2009; Ghorbal, 2009).

Table 3.4

Zircon (U-Th)/He data from the Ourika area

Grain Lab N°	Length (μm)	Width (μm)	Corrected age ±8% (Ma)	Uncorrected age (Ma)	U (ppm)	Th (ppm)	Sm (ppm)	^{4}He (nmol/g)	[eU]	F_T	Intra-sample dispersion (%)
Imlil vertical profile											
zMiHe-02-2	226.7	111.8	111.63±8.93	91.84	140.7	50.4	0.6	76.1	152.3	0.82	16.57
zMiHe-02-3	212.7	106.7	131.80±10.54	107.57	185.3	36.3	0.3	113.5	193.7	0.82	
zMiHe-03-1	273.5	90.2	123.18±9.86	98.31	308.6	74.0	1.5	174.3	325.6	0.80	16.20
zMiHe-03-2	271.3	97.8	110.02±8.80	89.20	325.1	74.2	2.8	166.0	342.2	0.81	
zMiHe-03-3	217.9	87.6	104.93±8.39	82.50	211.0	53.1	1.1	100.2	223.3	0.79	
zMiHe-04-1	253.7	121.7	127.70±10.22	106.87	110.5	43.2	0.5	70.2	120.4	0.84	168.53
zMiHe-04-4*	233.6	92.5	469.09±37.53	395.44	48.4	2.8	381.4	109.5	50.9	0.80	(39.37)
zMiHe-04-3	212.6	89.2	85.69±6.85	67.36	131.7	57.2	0.5	53.0	144.8	0.79	
zMiHe-06-2*	112.2	77.4	178.90±14.31	132.06	180.9	17.1	2.2	133.3	184.9	0.74	100.36
zMiHe-06-3*	115.0	63.6	59.34±4.75	41.51	207.2	35.4	0.2	48.4	215.3	0.70	
zMiHe-08-1*	109.4	59.0	249.69±19.98	168.13	298.5	172.1	1.7	312.0	338.1	0.67	212.08
zMiHe-08-2*	108.2	73.6	43.73±3.50	31.25	156.2	146.2	0.9	32.2	189.8	0.72	
zMiHe-08-3*	84.3	66.0	24.76±1.98	16.92	172.2	49.5	0.2	16.8	183.6	0.68	
Tizi n'Likemt vertical profile											
zMiHe-12-1	197.9	101.9	63.75±5.10	51.19	121.5	64.3	0.4	37.9	136.3	0.80	231.62
zMiHe-12-2*	189.2	100.0	708.74±56.70	569.01	82.9	48.3	1.9	304.3	94.0	0.80	(0.56)
zMiHe-12-3	178.3	86.3	63.39±5.07	48.91	146.8	99.3	0.5	45.1	169.7	0.77	
zMiHe-15-1	197.4	116.0	52.13±4.17	42.89	326.7	104.1	0.2	81.5	350.6	0.82	79.37
zMiHe-15-2	185.1	94.0	47.98±3.84	37.74	365.8	264.3	0.7	87.4	426.7	0.79	
zMiHe-15-3	183.8	139.1	20.28±1.62	17.03	82.9	39.7	0.6	8.5	92.0	0.84	
zMiHe-17-1	188.5	105.2	135.32±10.83	109.49	297.9	70.4	0.6	187.5	314.1	0.81	41.99
zMiHe-17-2	121.1	69.2	98.44±7.88	70.77	487.6	102.4	2.2	196.5	511.2	0.72	
zMiHe-17-3	106.8	82.9	90.01±7.20	66.93	660.9	157.0	0.6	253.3	697.0	0.74	
Tizgui vertical profile											
zMiHe-19-1	221.9	83.6	322±25.76	251.15	286.7	72.8	1.9	420.9	303.4	0.78	7.74
zMiHe-19-2	182.3	99.0	305.74±24.46	244.13	129.2	46.0	1.6	188.4	139.8	0.80	
zMiHe-19-3	175.5	90.6	298.10±23.85	233.51	91.1	30.5	0.4	126.3	98.1	0.78	
zMiHe-20-1	133.5	81.4	273.72±21.90	206.01	133.8	43.4	0.5	163.0	143.8	0.75	70.10
zMiHe-20-3	177.4	96.9	131.64±10.53	104.48	196.0	64.3	1.9	120.1	210.8	0.79	
zMiHe-21-1	221.7	69.6	265.55±21.24	197.71	137.3	42.1	0.9	159.7	146.9	0.74	46.33
zMiHe-21-2	197.0	73.7	305.87±24.47	229.99	173.9	53.7	0.8	236.2	186.3	0.75	
zMiHe-21-3	201.1	112.7	188.50±15.08	154.83	166.0	37.9	0.5	148.1	174.8	0.82	
zMiHe-23-1	126.5	76.1	152.96±12.24	112.79	381.6	123.3	0.9	252.2	410.0	0.74	36.07
zMiHe-23-2	138.9	94.6	197.27±15.78	154.05	223.5	44.5	0.9	197.0	233.8	0.78	
zMiHe-23-4	160.1	94.0	221.73±17.74	174.13	238.5	72.4	0.6	243.7	255.2	0.79	
zMiHe-24-1	156.0	105.9	132.42±10.59	106.13	116.7	32.6	0.4	71.8	124.2	0.80	43.79
zMiHe-24-2	140.6	90.2	121.30±9.70	93.80	223.0	52.6	0.5	120.0	235.1	0.77	
zMiHe-24-3	162.4	74.9	185.39±14.83	138.39	418.4	143.8	1.1	341.7	451.5	0.75	
zMiHe-25-1	187.3	133.0	199.87±16.00	167.51	101.1	29.9	0.5	99.1	108.0	0.84	7.84
zMiHe-25-2	206.1	107.6	215.57±17.25	175.69	134.0	42.6	0.5	138.6	143.8	0.82	
zMiHe-25-3	193.1	116.3	199.51±15.96	164.30	68.4	17.7	0.2	65.3	72.5	0.82	
zMiHe-27-1	190.2	113.6	280.66±22.45	230.27	145.0	35.7	0.7	194.4	153.2	0.82	19.26
zMiHe-27-2	159.4	86.3	234.86±18.79	181.34	140.8	36.5	0.9	148.5	149.2	0.77	
zMiHe-27-3	214.4	114.1	286.35±22.91	236.22	151.2	43.9	0.7	210.2	161.3	0.82	
Ourika vertical profile											
zMiHe-28-1	184.6	106.6	35.03±2.80	28.40	384.8	62.9	0.4	61.4	399.3	0.81	32.89
zMiHe-28-2	177.9	94.6	49.22±3.94	38.96	196.9	40.2	0.5	43.5	206.2	0.79	
zMiHe-28-3	186.2	83.7	45.21±3.62	35.00	307.3	55.8	0.5	60.7	320.2	0.77	

Table 3.4 (continued)

Grain Lab N°	Length (μm)	Width (μm)	Corrected age ±2σ (Ma)	Uncorrected age (Ma)	U (ppm)	Th (ppm)	Sm (ppm)	^{4}He (nmol/g)	[eU]	F_T	Intra-sample dispersion (%)
zMiHe-29-1	197.1	92.9	63.78±5.10	50.54	286.1	68.3	0.6	82.7	301.8	0.79	38.63
zMiHe-29-2	187.7	99.5	61.84±4.95	49.52	250.2	61.8	0.6	71.0	264.4	0.80	
zMiHe-29-3	189.3	85.4	42.18±3.37	32.80	492.9	107.3	0.7	91.9	517.6	0.78	
zMiHe-30-1	166.6	99.3	46.40±3.71	36.88	192.8	57.3	0.3	41.2	206.0	0.80	20.54
zMiHe-30-2	100.9	159.2	56.80±4.54	45.20	102.8	25.6	0.4	26.6	108.8	0.80	
zMiHe-30-3	217.5	116.6	48.65±3.89	40.19	116.7	47.1	0.5	27.8	127.5	0.83	
zMiHe-31-1	211.2	98.2	66.07±5.29	53.01	82.5	25.4	0.6	25.4	88.3	0.80	25.22
zMiHe-31-2	199.6	81.1	76.52±6.12	58.87	105.6	34.1	4.0	36.3	113.5	0.77	
zMiHe-31-3	222.9	113.2	59.53±4.76	49.07	88.4	25.9	0.5	25.1	94.3	0.82	
zMiHe-32-1	238.3	102.2	67.04±5.36	54.43	92.4	30.8	0.6	29.4	99.5	0.81	24.16
zMiHe-32-2	180.7	102.1	52.59±4.21	42.18	56.3	18.0	0.4	13.8	60.5	0.80	
zMiHe-33-1	201.6	111.3	64.15±5.13	52.51	104.1	29.6	0.4	31.6	110.9	0.82	54.16
zMiHe-33-2	190.3	90.2	92.12±7.37	72.47	175.6	38.6	0.5	72.6	184.5	0.79	
zMiHe-33-3	186.2	108.6	54.14±4.33	44.02	257.7	55.7	0.4	64.5	270.5	0.81	
zMiHe-34-1	195.6	114.4	151.79±12.14	124.72	79.3	21.0	0.3	57.3	84.1	0.82	85.31
zMiHe-34-2	171.4	85.3	113.22±9.06	87.52	152.2	38.8	0.7	76.7	161.1	0.77	
zMiHe-34-3	215.5	90.9	59.51±4.76	47.17	467.6	90.5	0.9	124.9	488.5	0.79	
zMiHe-35-1	186.1	109.6	112.71±9.02	91.65	78.2	25.7	0.4	42.0	84.1	0.81	47.76
zMiHe-35-2	199.9	114.8	156.11±12.49	128.43	88.4	24.5	0.3	65.9	94.0	0.82	
zMiHe-35-3	177.8	110.9	97.75±7.82	79.50	102.6	29.8	0.8	47.3	109.5	0.81	

* Sample's grains with an (*) are not included in the interpretation. The intra-sample grain age dispersion without the discarded grains is shown in parentheses.

Table 3.5

Apatite (U-Th)/He data from Ourika area

Grain Lab N°	Length (μm)	Width (μm)	Corrected age ±6% (Ma)	Uncorrected age (Ma)	U (ppm)	Th (ppm)	Sm (ppm)	^{4}He (nmol/g)	[eU]	F_T	Intra-sample dispersion (%)
Imlil vertical profile											
MiHe-02-1	121.7	84.3	3.96±0.24	2.600	9.2	13.5	44.6	0.175	12.5	0.64	58.19
MiHe-02-2	149.2	86.4	4.91±0.29	3.310	11.1	11.9	32.2	0.250	14.0	0.67	
MiHe-02-3	134.7	73.5	7.05±0.42	4.410	9.0	16.7	48.4	0.310	13.1	0.61	
Tizgui vertical profile											
MiHe-21-1*	227.3	117.4	9.12±0.55	7.530	1.3	0.7	19.0	0.059	1.5	0.76	98.72
MiHe-21-2*	165.3	97.9	2.89±0.17	2.040	6.4	9.8	20.8	0.096	8.7	0.70	
MiHe-21-3*	155.3	90.2	6.93±0.42	4.770	29.1	15.4	30.2	0.845	32.8	0.68	
MiHe-24-1	150.4	68.8	9.25±0.56	5.670	13.8	22.0	52.6	0.582	19.1	0.60	30.70
MiHe-24-2	101.5	75.2	12.47±0.75	7.550	23.3	43.4	73.6	1.371	33.6	0.60	
MiHe-24-3	94.5	73.4	9.73±0.58	5.890	6.4	5.6	24.5	0.246	7.8	0.59	
MiHe-27-1	119.7	97.1	5.59±0.34	3.840	7.6	12.2	35.6	0.219	10.6	0.67	48.42
MiHe-27-2	121.7	72.3	6.22±0.37	3.810	3.0	5.0	12.2	0.087	4.2	0.60	
MiHe-27-3	122.1	89.0	8.94±0.54	6.080	5.3	10.1	46.1	0.253	7.8	0.65	
Ourika vertical profile											
MiHe-28-1	102.4	79.7	3.06±0.18	1.910	106.3	60.2	28.0	1.248	120.3	0.63	40.02
MiHe-28-2	102.2	84.4	2.62±0.16	1.670	26.5	17.3	9.8	0.277	30.5	0.64	
MiHe-28-3	83.3	82.7	2.03±0.12	1.240	43.5	23.0	11.5	0.331	48.9	0.62	
MiHe-29-1	153.0	86.1	6.14±0.37	4.100	35.6	44.6	55.5	1.025	46.1	0.66	74.36
MiHe-29-2	127.2	77.0	8.48±0.51	5.350	28.0	32.4	52.5	1.031	35.7	0.63	
MiHe-29-3	160.1	74.5	3.89±0.23	2.460	24.8	33.2	43.3	0.436	32.7	0.63	
MiHe-31-1	119.4	73.7	4.40±0.26	2.700	64.1	47.1	31.7	1.101	75.1	0.62	77.56
MiHe-31-2	133.2	76.2	9.05±0.54	5.660	63.7	75.4	23.7	2.495	81.1	0.63	
MiHe-31-3	253.1	102.6	4.53±0.27	3.290	6.6	11.3	4.1	0.164	9.2	0.73	
MiHe-32-1	128.3	93.7	7.55±0.45	5.090	68.5	72.1	20.0	2.355	85.2	0.67	37.56
MiHe-32-2	125.1	75.1	7.30±0.44	4.520	82.4	79.8	24.8	2.476	100.9	0.62	
MiHe-32-3	149.0	84.1	10.47±0.63	6.880	70.8	91.9	22.8	3.441	92.1	0.66	
MiHe-33-1	125.4	63.0	8.94±0.54	5.130	101.4	75.6	38.8	3.310	119.0	0.57	18.64
MiHe-33-2	115.3	69.9	7.46±0.45	4.450	101.6	81.4	37.5	2.909	120.5	0.60	
MiHe-33-3	111.9	80.2	7.50±0.45	4.750	63.5	42.1	31.2	1.888	73.4	0.63	
MiHe-34-1	110.4	73.8	10.16±0.61	6.190	30.0	38.6	59.9	1.310	39.2	0.60	11.36
MiHe-34-2	113.4	75.3	11.37±0.68	7.020	40.2	35.1	35.9	1.839	48.4	0.62	
MiHe-34-3	144.1	67.1	10.34±0.62	6.180	77.9	86.7	53.0	3.284	98.1	0.60	
MiHe-35-1	155.9	73.0	11.31±0.68	7.110	70.8	60.2	34.8	3.265	84.8	0.63	19.10
MiHe-35-2	107.8	63.9	9.32±0.56	5.280	65.2	59.7	50.9	2.262	79.2	0.57	
MiHe-35-3	90.1	70.2	10.63±0.64	6.180	84.2	58.0	56.9	3.269	97.8	0.58	

* Sample's grains with an (*) are not included in the interpretation.

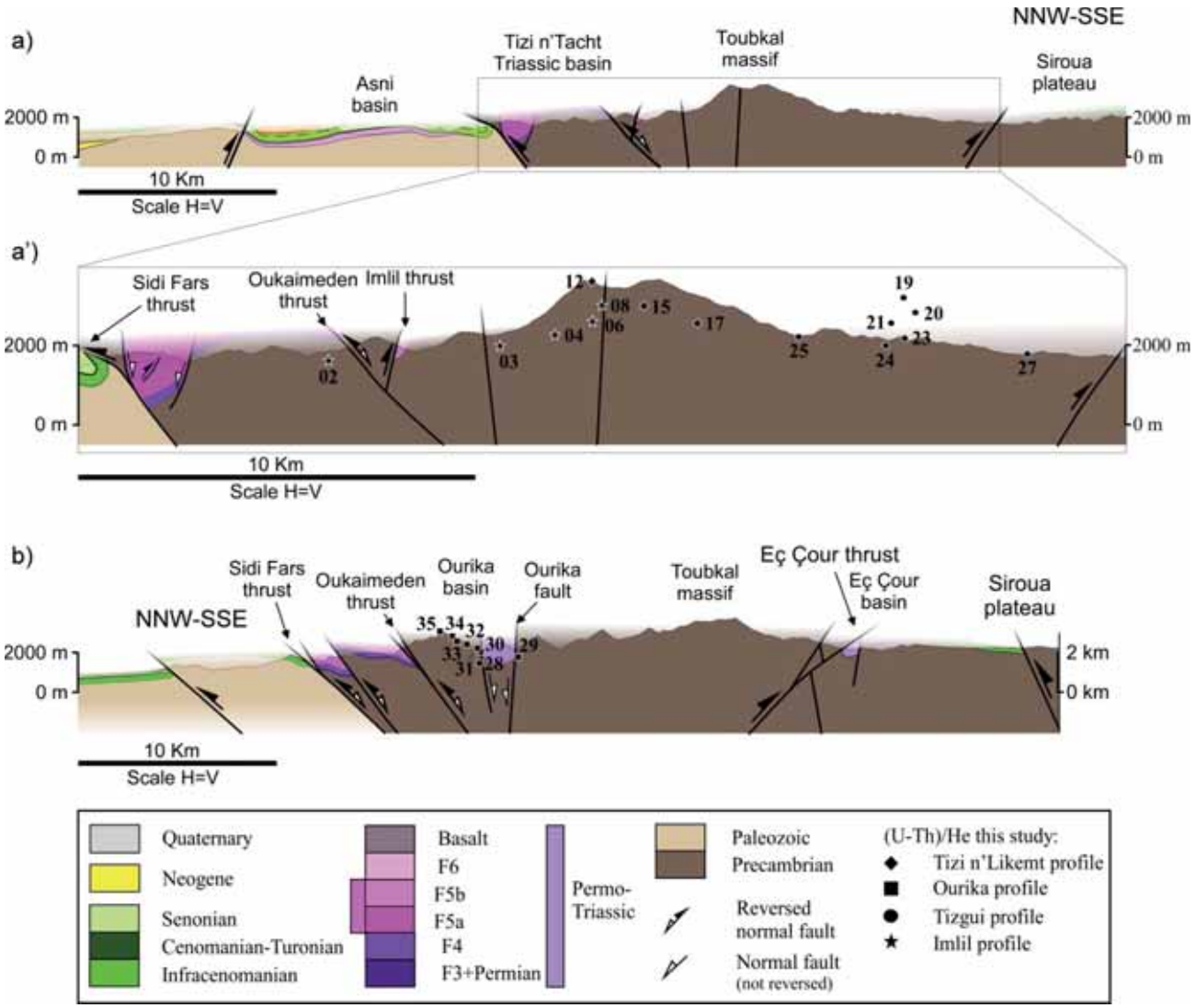

Figure 3.8. (a) General cross section of the Marrakech High Atlas across the Tizi n' Tacht Triassic basin (which is the western continuation of the Ourika basin) and Toubkal massif (see location in fig. 3.7). (a') Close-up of the Axial zone with the Imlil (stars), Tizi n'Likemt (diamonds) and Tizgui (circles) samples projected. (b) General cross section from the Marrakech High Atlas across the Ourika and Eç Çour Triassic basins with the Ourika samples projected (squares; see location in fig. 3.7). The southern part of the cross section is modified from El Arabi et al. (2003).

Ourika vertical profile

Samples of the Ourika profile are located in the Ourika river thalweg and hillslope, in the eastern part of the study area (black squares in fig. 3.7 and 3.8b). A set of 8 samples (MiHe-28 to Mihe-35) was collected from a Neoproterozoic granitic rock (Assarag Suite; U-Pb zircon age of 614-575 Ma; Thomas et al., 2002). The vertical profile has over ~1500 m of local relief. The eight samples yield zHe (23 single-grain) ages from 28.44 Ma to 128.50

Ma, with σ-corrected ages from 35.01±2.8 Ma to 156.11±12.5 Ma, and intra-sample grain age dispersion from 20.54% to 85.31% (Table 3.4 and fig. 3.9a). Seven samples provide suitable apatites to be analyzed and yield aHe (21 single-grain) ages from 1.25 Ma to 7.10 Ma, with σ-corrected ages from 2.03±0.12 Ma to 11.37±0.68 Ma, and intra-sample grain age dispersion from 11.36% to 77.56% (Table 3.5 and fig. 3.9a). The Precambrian samples are located north of the Ourika Triassic basin and adjacent to the Triassic detrital deposits (fig. 3.7), and therefore, they should be near surface temperatures (probably due to the high exhumation produced by the Variscan orogeny in Carboniferous times) previous to the Triassic rifting and Ourika basin development. Plotted aHe and zHe ages in fig. 3.9a show positive age-elevation relationships. The bottom samples show σ-corrected zHe ages from 35.01±2.8 Ma to 92.12±7.4 Ma ages with intra-sample dispersions from 20.5% to 38.6%, while the two upper samples present σ-corrected zHe ages from 59.51±4.8 Ma to 156.11±12.5 Ma with intra-sample dispersion from 47.8% to 85.3%. The high intra-sample age dispersion may be indicative that the upper samples have been buried to temperatures in the zPRZ being not completely reset or have remained in the zPRZ for a long period of time as the helium diffusion in the PRZ is highly dependent on the crystal characteristics or imperfections (i.e. zonation of zircons, radiation damage, size, etc.; see discussion in section 1.4.2) producing high intra-sample age dispersion. Sample MiHe-29 was collected south of the Ourika fault while other samples in the profile were collected north (fig. 3.7 and 3.8b). The Ourika fault is classically attributed to be part of the Tizi n'Test fault zone (e.g., Proust et al., 1977) and from structural criteria it is recently interpreted as a normal fault active during the rifting stage but not reactivated in Cenozoic times (Domènech et al. 2015; Chapter 2). The positive age-elevation relationship in the aHe and zHe ages presented here show (fig. 3.9a) that no major vertical displacement exists in the Ourika fault almost from Late Cretaceous times to present. Previous AFT ages obtained in the area (Missenard et al., 2008; see location of samples in fig.3.7), which yielded ages from 11.5±0.6Ma to 16.9±0.7 Ma (fig. 3.9a), also show little differential ages across the fault, and therefore, it seems that vertical displacement across the fault were minor in Cenozoic times. Therefore, samples of the Ourika vertical profile are considered as belonging to the same structural block since the closure of the zircon (U-Th)/He system to the present, and their zHe and aHe ages are modelled together.

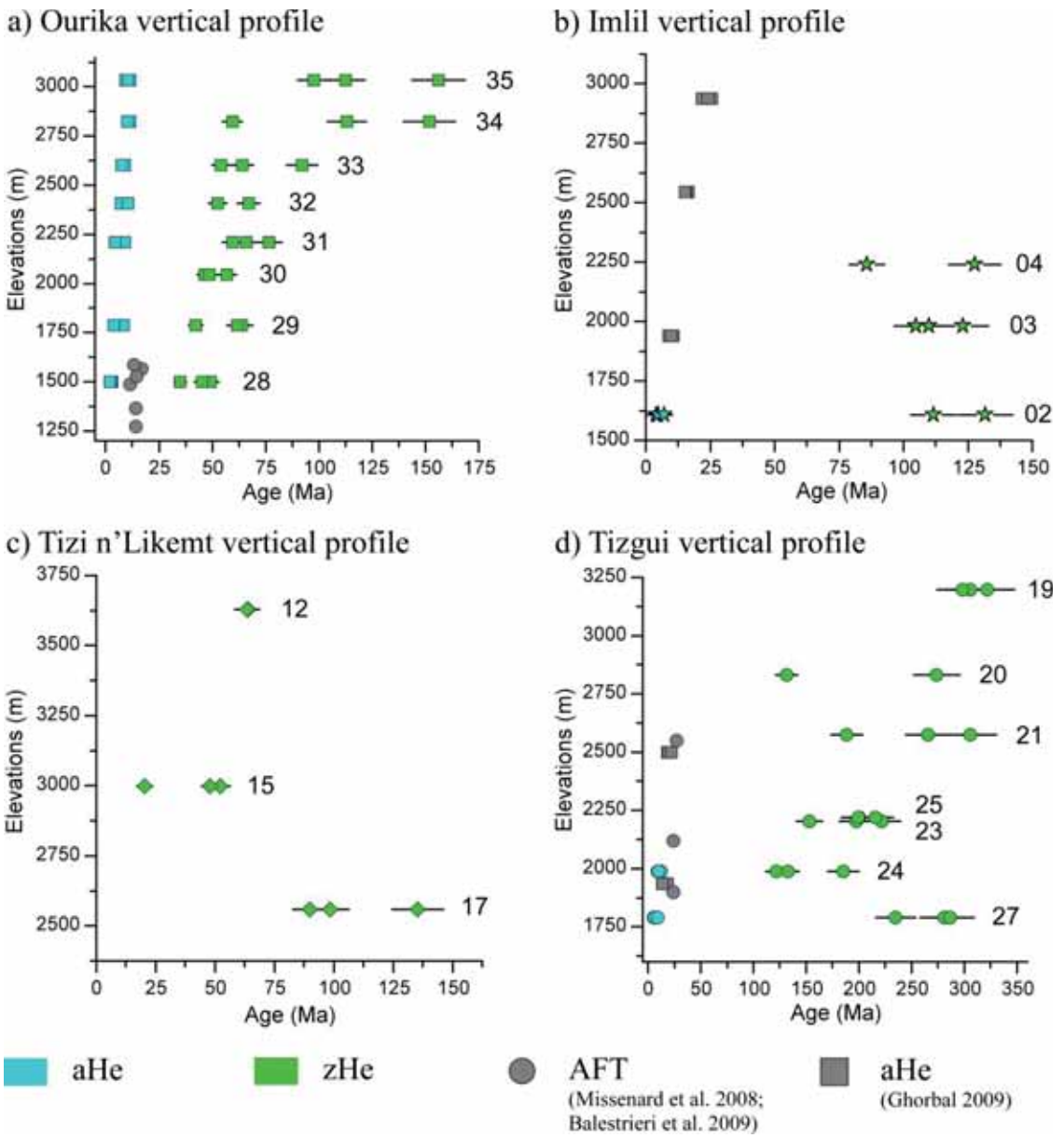

Figure 3.9. Age-elevation plots with 2σ error for the (a) Ourika, (b) Imlil, (c) Tizi n'Likemt and (d) Tizgui vertical profiles. Samples of Missenard et al. (2008), Balestrieri et al. (2009) and Ghorbal (2009) used in the thermal modelling are also plotted.

Imlil vertical profile

Samples of the Imlil vertical profile (MiHe-02 to MiHe-08) were collected in the Ighighayene river thalweg and slope in the in the proximities of the Imlil town and the Toubkal massif, between 1608 m and 2994 m of altitude (Table 3.3 and fig. 3.7). Sample MiHe-02 was collected in a granite of the Assarag Suite and it is located 300 m below Triassic unconformable deposits (F4 unit, Anisian in age; El Arabi et al., 2006) which crop

out to the NW (fig. 3.7 and 3.8a). The other samples, MiHe-03 to MiHe-08, are rhyolites belonging to the Ouarzazate Group (U-Pb zircon age of 575 to 560 Ma; Thomas et al., 2002). Aliquot zMiHe-04-4 of sample MiHe-04 has been excluded from the interpretation due to its old age that is not easily explainable when compared with other grains in the sample. Samples MiHe-06 and MiHe-08 have been also excluded from the interpretation due to their small crystal sizes (most smaller than 70 μm, and all smaller than 80 μm), their poor crystal clarity and their high intra-sample dispersion (100% and 212% respectively) not explainable by their eU content, grain size, zonation, etc. (Table 3.4). Better zircon crystals from these samples could not be obtained due to their scarcity in the rhyolitic rock.

The three samples suitable for interpretation in the Imlil vertical profile (seven zircon aliquots) yield zHe ages from 67.42 Ma to 107.63 Ma with σ-corrected ages from 85.69±6.86 Ma to 131.80±10.54 Ma. Intra-sample grain age dispersion ranges from 16.20% to 39.37%. Only sample MiHe-02 provided apatites to be analyzed (three aliquots), and yield aHe ages from 2.55 Ma to 4.31 Ma and σ-corrected ages from 3.96±0.24 to 7.05±0.42 (Table 3.4 and fig. 3.9b). Intra-sample grain age dispersion is 58.19%. Previous (U-Th)/He ages in apatites (3 samples) obtained by Ghorbal (2009) near the MiHe-03 and MiHe-04 show ages from 6.5 Ma to 15.4 Ma with σ-corrected ages from 8.9±0.4 Ma to 25.6±1.5 Ma (see location in fig. 3.7; fig. 3.9b). Sample MiHe-02 is separated from samples MiHe-03, MiHe-04 and the samples of Ghorbal (2009) by the Oukaimeden and Imlil thrusts (fig. 3.7 and 3.8a). Some intra-Precambrian faults are additionally identified between sample MiHe-02 and MiHe-03-MiHe-04, and between the lower and two upper samples of Ghorbal (2009). The zHe ages of samples MiHe-02, MiHe-03 and MiHe-04 are not elevation dependent and show similar ages ranging from 85 Ma to 130 Ma (fig. 3.9b) which means that samples were out of the zPRZ during the Atlas orogeny and bear no memory of the associated cooling event. Due to the movement of the Oukaimeden and Imlil thrusts after the closure of the zircon (U-Th)/He system, samples cannot be ascribed to belong to the same structural block (which means that vertical offset between samples could change from their closure time to present due to thrusting) and in consequence, the zHe ages of samples are not modeled. However, the samples with apatite fit a straight positive age-elevation relationship for aHe, which suggests that displacement along the Oukaimeden and Imlil thrusts in the Imlil valley is really small (ranging in the range of error of the aHe ages), at least since the late Oligocene (past 25 Ma). Hence, samples are considered to belong to the same structural block (from Oligocene to present) and can be modelled together.

Tizi n'Likemt vertical profile

The three samples of the Tizi n'Likemt vertical profile (samples MiHe-12 to MiHe-17) are located in the highest part of the Ourika river (i.e., near the headwater) from the thalweg of the river to the Tizi n'Likemt mountaint pass (diamonds in fig. 3.7 and 3.8a). Samples were picked between 2559 to 3629 m of altitude and correspond to ryholites (the MiHe-12) and granites of Neoproterozoic age (Assarag Suite and Ouarzazate Group; Thomas et al., 2002). Aliquot zMiHe-12-2 has been excluded from the interpretation due to its old age (older than its U-Pb age of ~614-560 Ma; Thomas et al., 2002). The (U-Th)/He ages suitable for interpretation were obtained only for zircons (8 single-grain ages), and range from 17.05 Ma to 109.56 Ma with σ-corrected ages from 20.28±1.62 Ma to 135.32±10.83 Ma (Table 3.4 and 3.9c). The intra-sample grain age dispersion ranges from 0.56% to 79.37%. Samples MiHe-12 and MiHe-15, in spite of their higher altitude, show younger ages which may indicative of they belong to a different structural block respect to the sample MiHe-17. Therefore, they may have undergone a different thermal history which cannot be constrained with the structural and geologic information available and they are not modelled as a group.

Tizgui vertical profile

The seven samples of the Tizgui vertical profile (samples MiHe-19 to MiHe-27) are located in the southern slopes of the Marrakech High Atlas, in the hanging wall of the Eç Çour thrust (black circles in fig. 3.7 and 3.8a). The Eç Çour thrust forms the southern Atlas front and it was identified by El Arabi et al. (2003) as a south-dipping normal fault which suffered a progressive inversion of its dip to the north during the compression stage. Due to its present gentle northward dip, I reinterpret it as a neoformed by-pass thrust, which cuts the oppositely-dipping former normal fault. Seven samples were collected in 1407m of difference in elevation in the valley floor and slopes of the Tizgui River (Table 3.3 and fig. 3.7). They correspond to a rhyolite of the Ouarzazate Group (sample MiHe-19) and granites of the Assarag Suite (Thomas et al., 2002 and references therein). The seven samples yield zHe ages (20 single-grain) from 93.86 Ma to 251.06 Ma with σ-corrected ages from 121.3±9.7 Ma to 322±25.8 Ma and intra-sample grain age dispersion from 7.74% to 70.10% (Table 3.4 and fig. 3.9d). Only three samples contained apatites, and within them, the apatites of sample MiHe-21 have been excluded in the interpretation due to very low eU content in one crystal (the MiHe-21-1; see Table 3.5) and because all aliquots present visible microfractures which could lead to helium loss. Also because this sample shows a high intra-sample dispersion (82.4%) which may not be attributed to

differences in intra-sample grain size or eU content. Therefore, only samples MiHe-24 and MiHe-27 were suitable for interpretation and yielded aHe ages (6 single-grain) from 7.45 Ma to 3.75 Ma with σ-corrected ages from 5.59±0.34 Ma to 12.47±0.75 Ma (Table 3.5 and 3.9d). The intra-sample grain age dispersion ranged from 30.70% to 48.42%. Three AFT ages previously obtained in the hanging wall of the Eç Çour thrust by Balestrieri et al. (2009) and Missenard et al. (2008) range from 24±2 Ma to 26.9±2.6 Ma. The aHe ages obtained by Ghorbal (2009) in two samples yield ages from 13.7±1.2 Ma to 22.4±1.2 Ma (see location in fig. 3.7; fig. 3.9d). In the elevation-age plot of fig. 3.9d it is observed that aHe shows a positive age-elevation relationship (included aHe ages from Ghorbal, 2009). ZHe ages show also a positive age-elevation relationship except from the bottom sample (the MiHe-27). Therefore, the aHe and zHe ages of the Tizgui vertical profile (included samples from Ghorbal, 2009) are considered to belong to same structural block and modelled together except sample MiHe-27.

3.3.2. Inverse thermal modeling

In accordance with the results described above, I have performed an inverse thermal modelling of the zHe and aHe ages of the Tizgui and Ourika vertical profiles. In the Imlil vertical profile, thermal modelling has been attempted only for the aHe data. Inverse thermal modeling has been performed using the QTQt software, as explained in section 1.4.2. As model set-up, all models were forced to end at surface temperature (20±5 °C) at 0 Ma. As some of the observed intra-sample age dispersion cannot be explained by grain size or radiation damage (see discussion in section 1.4.2), we took into account some uncertainty in the He ages observed. Therefore, a serial of trial runs were performed using the He ages observed and the He ages resampled (see details in section 1.4.2) in an effort to validate the robustness of the thermal models. In all models, the radiation damage accumulation model for apatites of Flowers et al. (2009) is incorporated. As the radiation damage accumulation model for zircons of Guenthner et al. (2013) is recently implemented in QTQt software and not extensively tested, thermal models are run with and without the zircon radiation damage model. In all the thermal models we allowed the temperature difference between bottom and top samples to vary from the equivalent geothermal gradient of 10 to 50°C/km and forced to be now at the surface. In some thermal models, the temperature difference between samples is fixed to be the same over time and in others it is allowed to vary over time. We assumed that the geothermal gradient was linear in the shallow levels of the crust, and as explained earlier, we assume that the zHe and aHe of different vertical profiles modelled belong to the same structural block so that the vertical offset between samples is the same over time. This means that in

fact, any modelled change in the temperature difference between bottom and top samples is translated into changes of the paleogeothermal gradient. Models were run for 300.000 iterations in total. The resulting set of thermal models with all these variables considered are shown in the Appendix. Representative thermal models are shown in fig. 3.10,3.11 and 3.12.

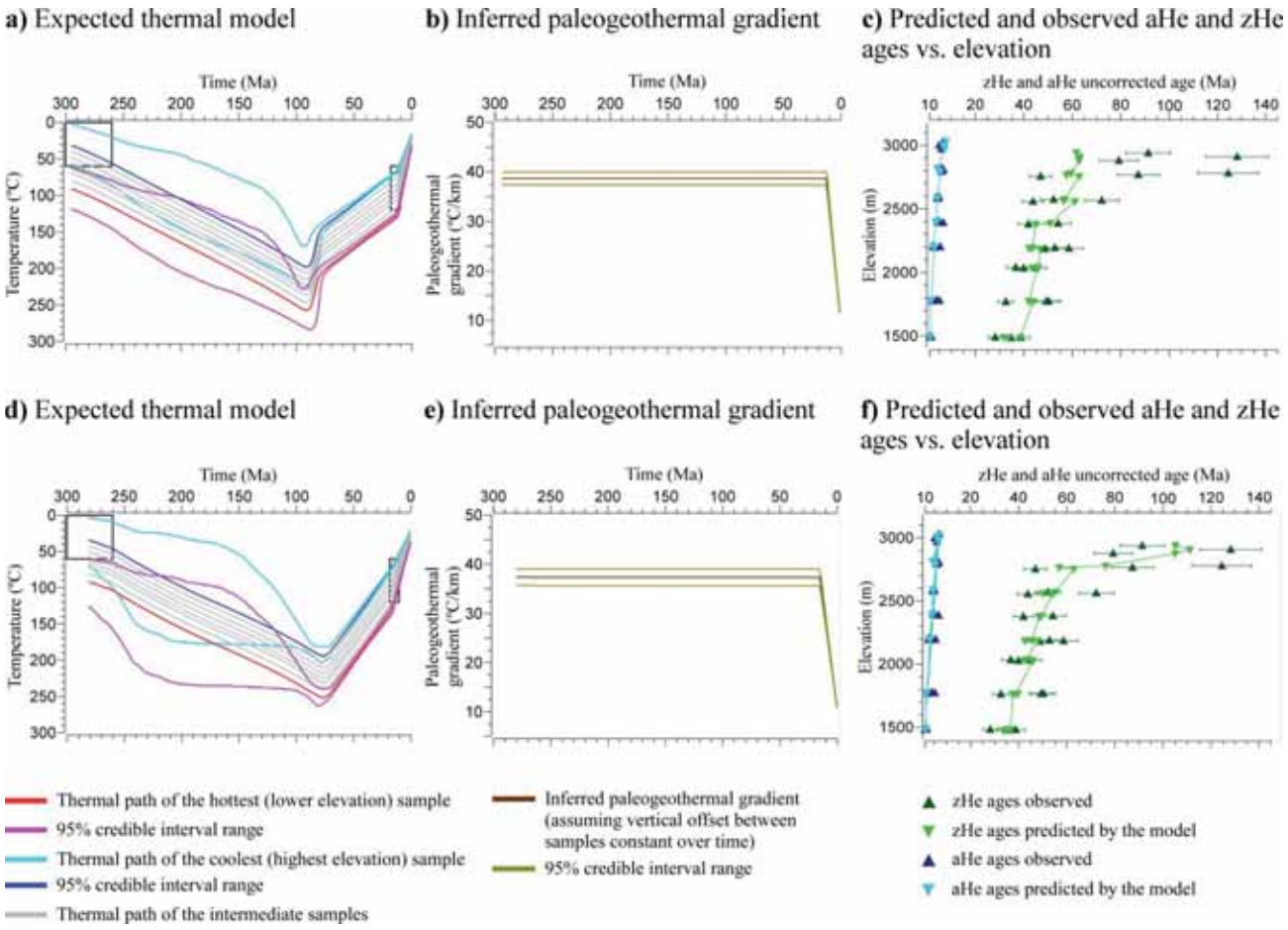

Figure 3.10. Inverse thermal modeling results of the vertical profile in the Ourika valley (see location in fig. 3.7). The temperature between top and bottom samples is allowed to vary between the equivalent geothermal gradient of 10-50°C/km but is fixed over time. He data are resampled using a normal distribution based on the observed age with a standard deviation equal to the input error. (a,b,c) Modelling with radiation damage accumulation model in zircons of Guenthner et al. (2013) included. (d,e,f) No radiation damage accumulation model in zircons used. Standard values of E_a and D_0 follow Ketcham et al. (2011). For visualization purposes, the elevation of the aliquots with the same altitude in (c) and (f) is slightly modified by the software.

Ourika vertical profile thermal model

Two representative models of the Ourika vertical profile (the expected model) are shown in fig. 3.10a,d. As samples are located adjacent to Triassic deposits (also Triassic deposits lie unconformable above the basement few km to the east of samples, see fig. 3.7) they were forced to be near surface temperatures during the Permian. To account for the AFT ages available from the area (see fig. 3.7 for approximate location) (Missenard et al., 2008), we constrained the thermal histories to pass through 60-120°C (which corresponds to the Apatite Fission Track Partial Annealing zone, the aPAZ; Gleadow and Fitzgerald, 1987) at 10-18 Ma.

The zHe and aHe ages observed are well predicted in all the thermal models performed (fig. 3.10c,f and Appendix). The big picture extracted from the models (fig. 3.10a,d and in Appendix) is that the thermal history is well constrained from Late Cretaceous (~100 Ma) to present times, and that a priori no reliable information can be extracted from the Ourika vertical profile before this time due to high uncertainties in the modeled t-T path. Thermal models show that basement rocks, at surface temperatures prior to the Triassic-Jurassic rifting, were reheated, reached temperatures of 190°C to 250°C (for the top and bottom samples respectively) at 75-85 Ma. Since 75-85 Ma (Santonian-Campanian) the samples cooled, being at surface temperatures at present times. While the thermal models where the zircon radiation damage accumulation model of Guenthner et al. (2013) is included show a first fast cooling from 85 to 70 Ma followed by a period of slower cooling from 70 Ma to 10-20 Ma (fig. 3.10a and Appendix), the thermal models where radiation damage model is not included show a continuous cooling from 75-85 Ma to 17 Ma (fig. 3.10d and Appendix) and the upper samples are better predicted (fig. 3.10f and Appendix). All thermal models run show an increase in cooling rate from 20-10 Ma to present times (fig. 3.10a,d and Appendix). Therefore, we can conclude that cooling started in the Santonian-Campanian times with a mean cooling rate of 1.5-2°C/Ma (taking into account only the thermal models were the zircon radiation damage model is not included) from 75-85 Ma to 20-10 Ma (Miocene) when cooling is accelerated to bring the samples to surface temperatures at a rate of 3.5°C/Ma to 6.5°C/Ma for the top and bottom samples respectively (a variation due to the creation of surface relief).

The paleogeothermal gradient is inferred from the temperature difference between top and bottom samples and by the vertical offset between them (assuming no major disruptions of this geometrical/structural relationship; fig. 3.10b,e and in Appendix). The inferred paleogeothermal gradient shows different evolution when it is allowed to vary

over time (Appendix), which suggests that the zHe and aHe ages modeled have not enough precision to accurately model the gradient changes over time or that little variations in the vertical offset between samples occurred. In any case, all models show high paleogeothermal gradients (from 30°C/km to more than 40°C/km) from the Late Cretaceous to the present (when samples are forced to be at surface temperatures with a difference in temperature between top and bottom samples not larger than ~15°C).

Therefore, assuming a mean geothermal gradient of ~35°C/km invariant along time, this represents that samples were exhumed at a mean rate of 0.04-0.06 mm/a from Santonian-Campanian to Miocene and at a rate of 0.1-0.2 mm/a for the top and bottom samples respectively, from that time to present. The amounts of exhumation are discussed in section 3.3.3.

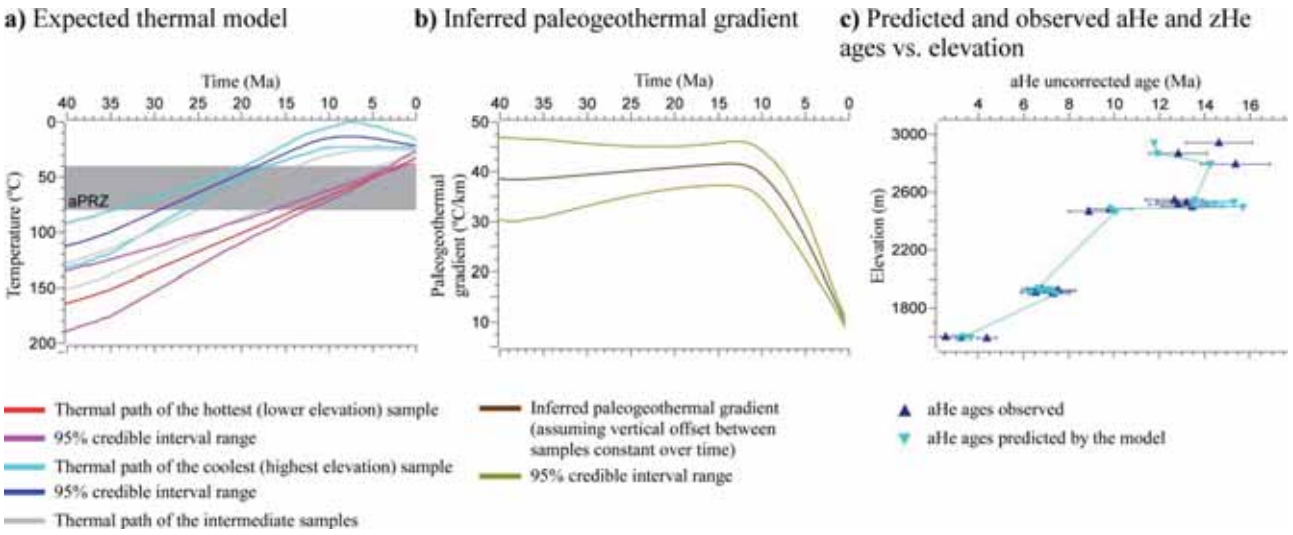

Figure 3.11. Inverse thermal modeling results of the vertical profile in the Imlil valley (only aHe data; see location in fig. 3.7). The temperature between top and bottom samples is allowed to vary over time between the equivalent geothermal gradient of 10-50°C/km. For visualization purposes, the elevation of the aliquots with the same altitude in (c) and (f) is slightly modified by the software.

Imlil vertical profile thermal model

Thermal models for this profile are run only with aHe data (samples from Ghorbal, 2009 included; fig. 3.9c). All thermal models performed are similar and the aHe ages observed are well predicted (fig. 3.11c and Appendix). The thermal models where the offset is fixed

over time show an acceleration of cooling at 15 Ma (Appendix), therefore, due to the lower closure temperature of the apatite (U-Th)/He thermochronometer and the effect of surface temperature and topography in the geotherms near the surface (e.g. Braun, 2002), this enhanced in cooling could be an artefact of the thermal model because when the gradient is allowed to vary over time, thermal models show a progressive cooling from 25 to 10 Ma at rates of ~3°C/Ma. Since 10 Ma (Tortonian) ago, while the top sample (near the mountain summits) remains at surface temperature, the bottom sample continues exhuming at similar rates (~3°C/Ma) (fig. 3.11a). This is due to the creation of topographic relief.

The inferred paleogeothermal gradients for the Imlil aHe models are always high (from 30 to 50°C/km) in spite of high uncertainties. Assuming a mean geothermal gradient of 35°C/km, the samples exhumed at rates of ~0.09 mm/a from Late Oligocene to Tortonian.

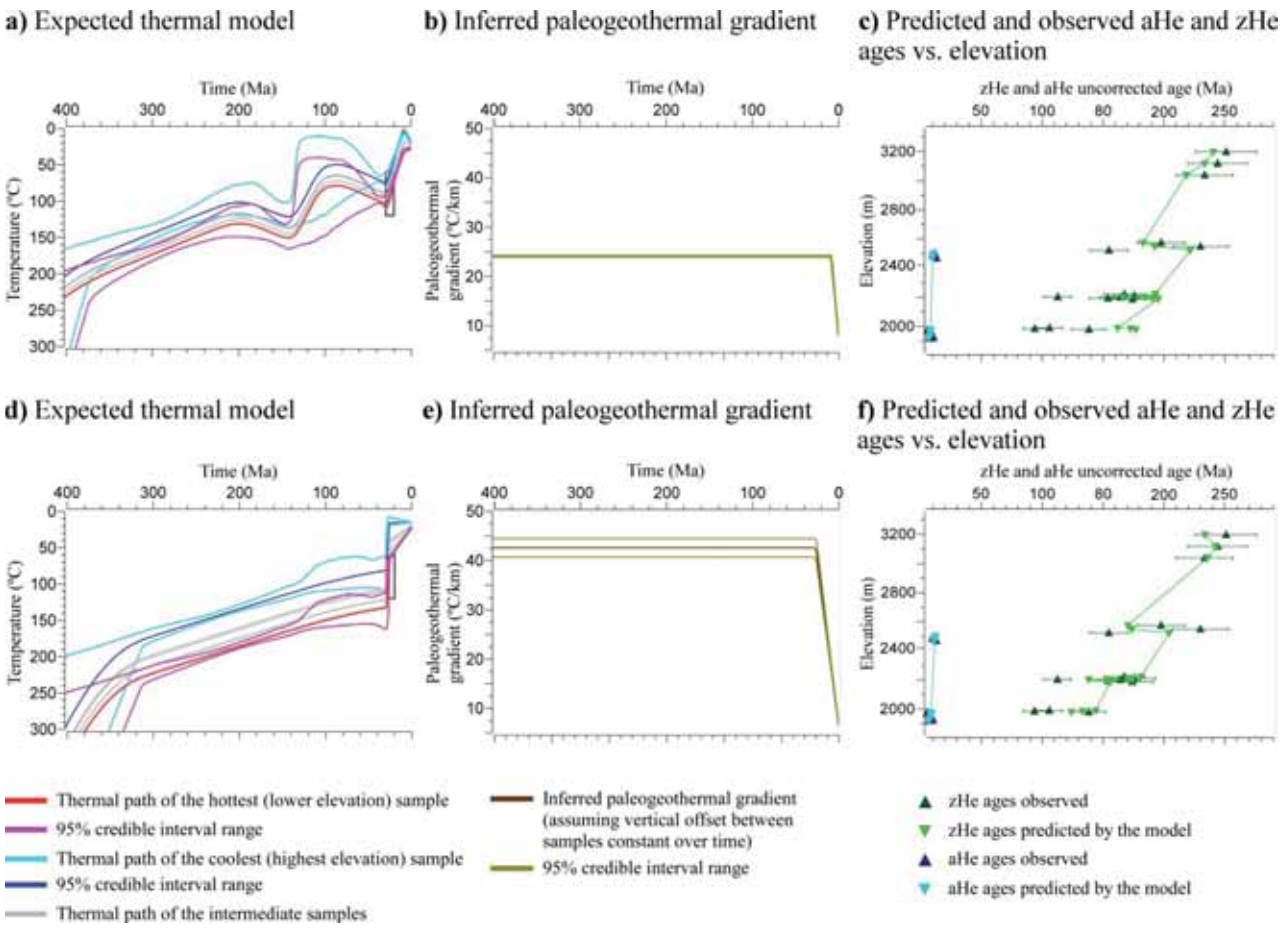

Figure 3.12. Inverse thermal modeling results of the vertical profile in the Tizgui valley (see location in fig. 3.7). The temperature difference between top and bottom samples is allowed to vary between the equivalent geothermal gradient of 10-50°C/km but is fixed over time. He ages are not

resampled. (a,b,c) Modelling with radiation damage accumulation model in zircons of Guenthner et al. (2013) included. (d,e,f) No radiation damage accumulation model in zircons used. Standard values of E_a and D_0 follow Ketcham et al. (2011). For visualization purposes, the elevation of the aliquots with the same altitude in (c) and (f) is slightly modified by the software.

Tizgui vertical profile thermal model

Two representative models of the Tizgui vertical profile (the expected model) are shown in fig. 3.12a,d. AHe ages in two samples from Ghorbal (2009) (fig. 3.9d.; location in fig. 3.7) have been included in the thermal modeling and sample MiHe-27 has been excluded (see above). Also, sample MiHe-20 was excluded from the thermal modelling because only two intra-sample ages could be obtained and they present a dispersion higher than 100% that cannot be accounted by differences in eU content or grain size. To respect the AFT data published (fig. 3.9d; Missenard et al., 2008; Balestrieri et al., 2009), we constrained the thermal histories to pass through the aPAZ from 20 to 30 Ma (central ages with 1σ error accounted).

The zHe and aHe ages observed are well predicted in all thermal models (fig. 3.6c,f and Appendix). Thermal paths modeled show that samples cooled slowly from ~320-300 Ma to 140-125 Ma (from Carboniferous to Early Cretaceous times) at mean rates of ~0.25-0.35°C/Ma and remained at temperatures lower than ~130°C from Early Cretaceous to present times. Some of thermal models (fig. 3.12a and Appendix) show an acceleration of cooling that started at 140-160Ma. However, the high uncertainties observed in the modeled cooling history for the period of time that goes from 160 Ma to ~30 Ma means that, in fact, the cooling history for this period of time cannot be safely constrained in the Tisgui profile. The thermal model is again well constrained from ~30 Ma to present by the aHe data. Some of thermal models show a fast cooling at 30 Ma to 25 Ma at mean rates of ~12-13°C/km (fig. 3.12d and Appendix), followed by a period of slower cooling. Other thermal models show a more moderate cooling from 30 Ma to 10 Ma at rates of ~3.5°C/Ma. The last 10 Ma of the thermal model are not constrained and the cooling rates observed in the thermal models are largely due to the imposed surface temperature and the topography (fig. 3.12a and Appendix).

The inferred paleogeothermal gradient in different model runs show varying evolution and high uncertainty when it is allowed to vary over time (Appendix), but in general it is high. When we fix the model to have the same temperature difference between top and bottom samples over time (which is equivalent to impose the same geothermal gradient for the whole time), the models where the zircon damage of Guenthner et al. (2013) is

included show an inferred paleogeothermal gradient of ~25°C (fig. 3.12b and Appendix), and when the damage model is not included, the inferred paleogeothermal gradient is 40-45°C/km (fig. 3.12e and Appendix). As most of the thermal models run show high paleogeothermal gradients (30 to 40°C/km), and in order to enable comparison of the exhumation rates of the Tizgui vertical profile with the models of the other vertical profiles, we selected the same 35°C/km paleogeothermal gradient invariant over time.

Therefore, the Tizgui vertical profile shows a constant exhumation rate of 0.007-0.01 mm/a from late Carboniferous to Early Cretaceous times, followed by a period of time not registered in the aHe and zHe data (125-30 Ma), and by a last period of faster exhumation from Early Oligocene to Tortonian with exhumation rates of 0.35 mm/a to 0.1 mm/a depending on the thermal path modeled.

3.3.3. Implications and discussion

The Ourika fault

Modelling of the Ourika vertical profile (fig. 3.10), where all zHe and aHe ages at both sides of the Ourika fault can be well predicted (also with AFT ages by Missenard et al. 2008 included in the thermal model), denotes that the fault (part of the Tizi n'Test fault zone), which extends by more than 26 km to the NE of the area represented in fig. 3.7, experienced no major vertical movements from Late Cretaceous to present times, i.e. during the Atlas orogeny. This thermochornologic result confirms the previous field observations and microstructural analysis carried out in the Ourika fault (Chapter 2) which suggested that the fault was active as normal fault during the rifting stage with limited moment during the orogeny.

The Triassic-Jurassic rift and Mid Jurassic-Early Cretaceous exhumation

Thermal modelling of the Tizgui vertical profile (fig. 3.6) shows that rocks were progressively cooled from Carboniferous to Lower Cretaceous times at rates of 0.007-0.01 mm/a, which implies that during the Triassic, but also during the Jurassic rift the area was an exhuming high, namely a horst. This result confirms by thermochornology the previous paleoreconstructions based on sedimentary inferences (Chapter 2; Stets, 1992; El Arabi et al., 2003; Frizon de Lamotte et al., 2009; Domènech et al., 2015) which suggested an interhigh/horst in the present Toubkal massif separating the northern (i.e. the Ourika-Tizi n'Tacht basins) and southern (i.e. the Eç Çour basin) Triassic rift basins (fig. 3.1; see also the Triassic paleoreconstruction in fig. 2.18). The older zHe ages observed in the sample

MiHe-27 (fig. 3.9d), separated ~3km (to the south) from the other samples of the same vertical profile and not included in the thermal model could be produced by differential exhumation rates in the Toubkal horst during the extension or by an undetected fault.

The zHe ages of the Imlil vertical profile (samples MiHe-02 to MiHe-04 in fig. 3.9b) but also the zHe ages of sample MiHe-17 of the Tizi n'Likemt vertical profile (fig. 3.9c), located to the NNW of the Tizgui vertical profile (fig. 3.7 and 3.8) show mainly Early Cretaceous ages invariant with altitude which means that samples where at temperatures higher than ~200°C after the Triassic-Jurassic rift and previous to their Early Cretaceous fast cooling. Sample MiHe-02 (see location in fig. 3.7) is currently located in the footwall of the Oukaimeden reversed normal fault and 300 below the F4 Triassic unit, which lies unconformable on basement in the preserved Tizi n'Tacht Triassic basin. This implies that this sample had to be near surface temperatures in Permian times, being later heated to a minimum of 200°C. This means that more than 4.8 km of Triassic-Jurassic syn-rift sediments had to cover this sample (assuming a paleogeothermal gradient of 35°C/km), which means that assuming 2 km of Triassic (based on the thickness of the lower deposits which are preserved in the Ourika Triassic basin, and assuming a maximum of 1 km for the top F6 Unit and basalts; Beauchamp, 1988; Benaouiss et al., 1996; Fabuel-Perez et al., 2009), more than 2.8 km of Jurassic sedimentary rocks accumulated in the Tizi n'Tacht basin, in the footwall of the Oukaimeden normal fault. I have no stratigraphic reference to constrain the position of samples MiHe-03, MiHe-04 and MiHe-17 during the Triassic-Jurassic rift prior to their Early Cretaceous cooling as none of these samples are overlain by Triassic deposits and they are separated from sample MiHe-02 by intra-Paleozoic faults and Cenozoic thrusts. In any case, all samples were cooled in Early Cretaceous across the zPRZ (from 200°C to ~130°C), which implies a total amount of exhumation in Early Cretaceous of minimum ~2km (assuming a paleogeothermal gradient of 35°C/km).

The significance of these Early Cretaceous zHe ages is comparable to those obtained for the samples of the Tizi n'Test basin area analyzed above, which showed a fast Mid-Late Jurassic exhumation. This event is also detected with AFT ages and thermal models obtained in the northern and southern foothills (north and south of the Sidi Fars and Eç Çour thrust respectively in fig. 3.7), as well as in the Moroccan Meseta and SW of the Anti-Atlas (Ghorbal et al., 2008; Balestrieri et al., 2009; Ghorbal, 2009; Saddiqi et al., 2009; Barbero et al., 2011; Ruiz et al., 2011; Bertotti and Gouiza, 2012). The minimum of ~2km of exhumation evidenced by samples MiHe-02 to MiHe-04 and MiHe-17 is also similar to the values calculated by previous authors and from the zHe ages of the Tizi n'Test basin (see discussion above).

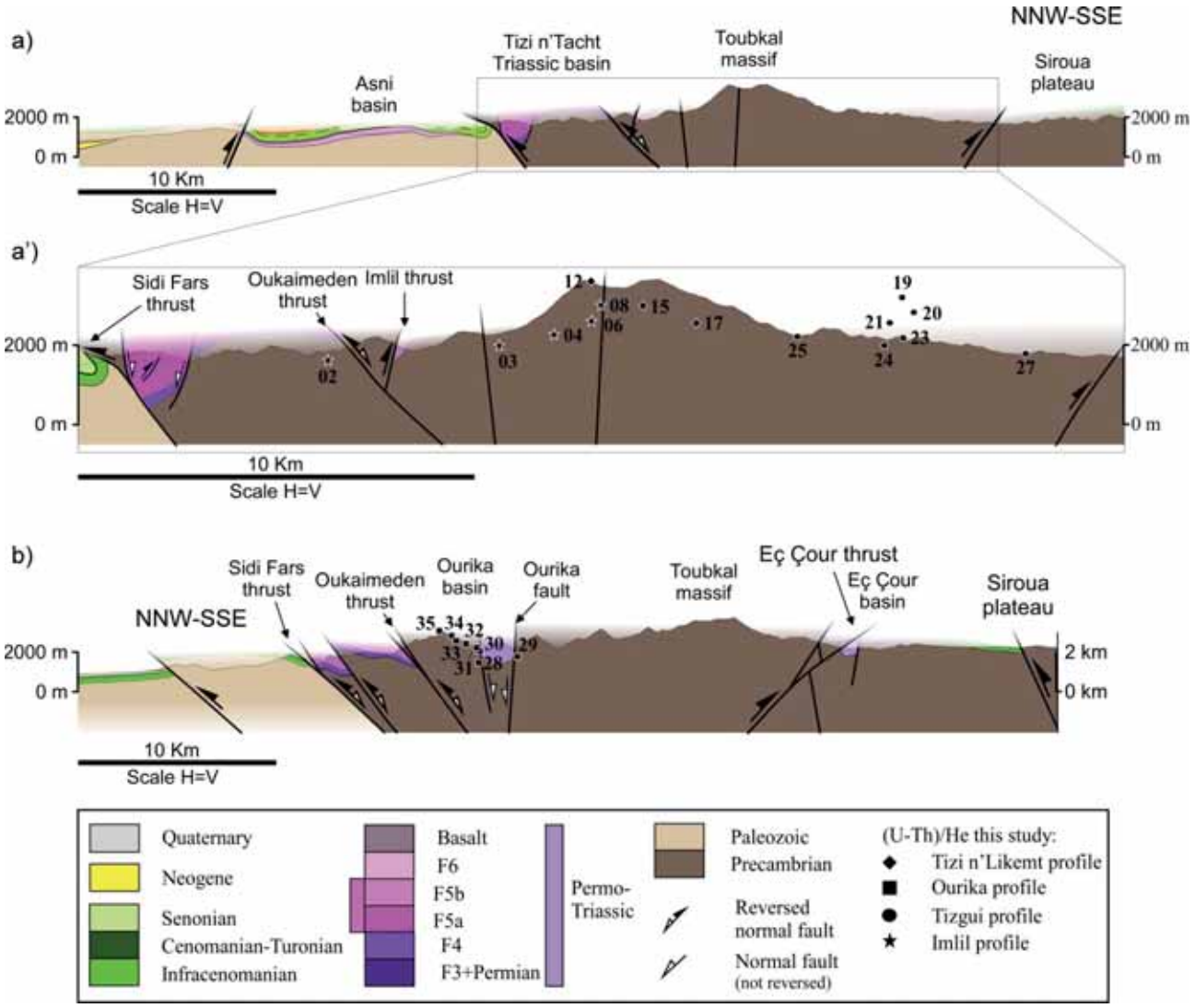

Figure 3.13. Post-rift to present reconstructed cross-section for the Marrakech High Atlas across the Ourika Triassic basin and Toubkal horst in selected steps. In black it is showed the location of samples at any stage based on their zHe ages and the Ourika vertical profile thermal models (see location in fig. 3.7).

Combining the results of the thermal model of the Tizgui vertical profile (evidencing a horst structure) and the zHe ages obtained for the Imlil vertical profile (and also the zHe ages of the Tizi n'Test area and the AFT of the previous authors) with the thermal model obtained in the Ourika vertical profile, a stepwise restoration of the Ourika area from the Triassic-Jurassic extension to the present-day is presented in fig. 3. 13. Sample MiHe-02 is projected in this restoration as it directly constrains the amount of the Triassic-Jurassic that deposited (more than 4.8 km) in the footwall of the Oukaimeden reversed fault, as

explained above (see location of sample in fig. 3.13a). The modelling of the Ourika vertical profile (which is located in the hanging wall of the Oukaimeden reversed normal fault) and the high dispersion of the upper samples, indicates that the top samples were located near the lower limit of the zPRZ, which means that they were buried to a depth of ~4.5-5 km assuming a paleogeothermal gradient of 35°C/km, prior to their exhumation starting at 85-75 Ma (Santonian-Campanian) (fig. 3.13c). We also know that these samples had to be located near surface temperatures prior to the Triassic-Jurassic rifting. This implies that the Ourika samples were buried in Triassic-Jurassic times, exhumed in Middle Jurassic-Early Cretaceous (2-3 km), and probably reburied under thin Late Cretaceous deposits (no more than ~500 m, as seen in the preserved record of the northern and southern foothills, fig. 3.8) being located at 4-5-5 km in the Santonian-Campanian.

Therefore, it is necessary that samples were covered under more than 6 km (for the top sample) syn-rift Triassic-Jurassic deposits to keep them 4.5-5 km deep after the Mid Jurassic to Cretaceous exhumation and burial events (see the position of samples in each step at fig. 3.13). This implies that assuming a maximum thickness for the Triassic deposits of 2km (see above), more than 4 km of Jurassic sediments accumulated in the Oukaimeden hanging wall as represented in fig. 3.13a. Furthermore, in this reconstruction (fig. 3.13a) the southern border between the Ourika basin and the Toubkal horst (represented by the Tizgui thermal model) is well defined in the Ourika basin and represented by the Ourika fault (interpreted as a normal fault during the extension based on field evidence and microstructural analysis; see Chapter 2).

The Atlas orogeny

In the northern flank of the Marrakech High Atlas, the modeling of the Ourika vertical profile (fig. 3.10) shows unequivocally a relatively fast cooling event starting in the Santonian-Campanian, providing the first thermochronologic evidences in the High Atlas for a Late Cretaceous initiation of the Atlas orogenic-driven exhumation. The modeled thermal path and paleogeothermal gradient indicate that samples were exhumed from the Santonian-Campanian to the Burdigalian-Tortonian (constrained by the zHe ages) at rates of 0.04-0.06 mm/a, which implies nearly 3-3.25 km of total exhumation for this period of time. From the Burdigalian-Tortonian to the present (constrained by the aHe ages), samples were exhumed at higher rates of 0.1-0.2 mm/a for the top and bottom samples respectively, with a total amounts of exhumation of 1.5 km for the top sample and 3 km for the bottom one (due to topographic relief).

The thermal model of aHe ages in the Imlil vertical profile shows that samples were exhumed from Late Oligocene to present times at rates of ~0.09 mm/a with total amount of exhumation of ~1km for the top sample and 2.25 km for the bottom one. Exhumation prior to Late Oligocene cannot be constrained as zHe ages of the Imlil vertical profile crossed the zPRZ in the Early Cretaceous and remained at lower temperature since then. Taking into account that samples were less than ~3 km deep after their Early Cretaceous exhumation (equivalent to less than ~130°C for the bottom sample, the upper limit of the zPRZ), and that 1km to 2.25 km of exhumation was produced from the Late Oligocene to the present, the amount of exhumation from the beginning of Atlas orogeny to the Late Oligocene must have been very limited, i.e. less than 1 km.

In the Tizi n'Likemt vertical profile (note that the main drainage divide of the Atlas mountain belt is located between this vertical profile and the Tizgui one; fig. 3.7), which was not modelled, the two upper samples yielded Paleocene to Early Eocene ages (fig. 3.9c), but the lower sample has older age, which we interpret as indicating the existence of a thrust in between. This thrust was not mapped before and is shown tentatively in the map of fig. 3.7. The early Paleogene ages in this vertical profile indicate that samples were reset from temperatures under the zPRZ before that time, and suffered an amount of exhumation of more than 5 km since then.

In the southern flank of the High Atlas, modeling of the Tizgui vertical profile indicates that samples were at depths of 3.14 km and 2 km for the bottom and top samples respectively in Early Cretaceous times (as the bottom sample had to be located at less than ~130°C). The aHe ages show that samples were exhumed a total amount of ~1.9 km to 3.1 km for the top and bottom samples from Early Oligocene to present. This implies that the exhumation at time prior to Early Oligocene was nearly zero.

The total amounts of exhumation estimated from the northern and southern flanks of the Marrakech High Atlas across the Ourika Triassic basin and Toubkal massif have major implications on the Atlas orogenic development and indicate that while the northern thrust faults start to move since the Late Cretaceous or early Paleogene, the southern Eç Çour thrust was not active before the Early Oligocene, which implies that early shortening was mainly focused in the northern flank. From the Oligocene-Miocene to the present, I deduce a generalized exhumation in the northern and southern flanks with similar total amounts of exhumation, attesting a joint movement of the northern and southern thrust systems. However, the total amount of exhumation from Oligocene to recent times cannot

be fully ascribed to thrust-related uplift, because a mantle-sourced component to uplift may have operated in the past 15 Ma (Teixell et al., 2005; Missenard et al., 2006).

Based on the pre-orogenic restored cross-section of fig. 3.13c (which relies on the zHe and aHe ages obtained in the present work) and the present-day cross-section (fig. 3.8 and fig. 3.13d), the total amount of shortening at this transect of the High Atlas mountains is of ~13 km (21%). For the southern and northern thrust faults (fig. 3.13d), whose hanging wall cutoffs cannot be constrained by thermochronologic ages, the restoration relies on minimum displacement estimates.

The beginning of the Atlas orogeny, constrained by the Ourika thermal model at the Santonian-Campanian (fig. 3.10), coincides with the sedimentation of the so-called Senonian Unit, which consists of terrestrial to restricted marine redbeds (Gauthier, 1960; Ambroggi, 1963). This unit records a slow marine transgression (from the west) that occurred after a rapid regression produced at the end of the Turonian (after the deposition of the Cenomano-Turonian limestone) (Gauthier, 1960; Choubert and Faure-Muret, 1962; Ambroggi, 1963). Local evidences of growth strata in Senonian deposits and a clear unconformity of the overlying Eocene strata has been reported in the High and Middle Atlas (Laville et al., 1977; Froitzheim et al., 1988; Herbig, 1988). However, these features are scarce and only locally recognized, and no major foreland basins developed at this stage. In my point of view, this is not incompatible with the results presented here. The slow exhumation rate of 0.04-0.06 mm/a obtained for the Ourika thermal model from late Cretaceous to Miocene makes viable the coexistence of exhumation in the inner parts of the belt, probably in a few emergent structures, within a broad continental-marine shelf, with no major foredeep development. Similar late Turonian to early Eocene AFT ages we obtained in the Central High Atlas Axial zone (Barbero et al., 2007). These authors attributed these AFT ages to post-rift/post-magmatic cooling, because they lie within a continuous cooling path since the Late Jurassic, that may well be partially due to the Atlas orogeny since the latest Cretaceous.

As explained above, thermal paths obtained by modelling the aHe data in the Tizgui, Imlil and Ourika vertical profiles (including the AFT and (U-Th)/He ages of previous authors; Missenard et al., 2008; Balestrieri et al., 2009; Ghorbal, 2009) (fig. 3.10,3.11 and 3.12), suggest an acceleration of exhumation since the Early Oligocene at Tizgui, the Late Oligocene at Imlil, and Burdigalian-Tortonian at Ourika. This result is consistent with structural geology and recent magnetostratigraphy of the tectono-sedimentary record in

the northern Ouarzazate basin external thrust belt, in foreland basin deposits (Tesón and Teixell, 2008; Tesón et al., 2010).

3.4. Synthesis of the new insights on burial and exhumation history of the Marrakech High Atlas from the rifting stage to the present

The zHe and aHe ages and thermal models obtained for the Marrakech High Atlas reveal that more than 4.8 km (up to 6 km) of Triassic-Jurassic syn-rift sediments deposited in the present-day Ourika basin area. To the west, in the Tizi n'Test Triassic basin area, the amount of Triassic-Jurassic syn-rift deposition is similarly estimated to be have been more than 4.5 km. Assuming that the maximum thickness of the Triassic redbeds was of 2km (in spite of the thickness of the Triassic deposits is highly variable between and inside basin, as explained in Chapter 2) the thickness of Jurassic rocks is of 2.5 to 4 km from west to east (fig. 3.6a and 3.13a). These findings constitute, in fact, the first reliable estimations of the total syn-rift sediment thickness in the Marrakech High Atlas, as all low-temperature thermochornologic dates (Fission tracks and (U-Th)/He in apatites) obtained previously in the Marrakech High Atlas yielded Tertiary ages (Missenard et al., 2008; Balestrieri et al., 2009; Ghorbal, 2009), and therefore, bear no memory of the Mesozoic vertical movements. The Triassic-Jurassic thicknesses presented in this work for the Marrakech High Atlas are comparable to the thickness of the Central High Atlas (where more than 5 km of Jurassic were locally deposited; Choubert and Faure-Muret, 1962), demonstrates that a continuous rift had to develop from the Central and Marrakech High Atlas to the Western High Atlas. That is to say that the rift was fully developed in the Marrakech High Atlas and a connection between the Atlantic and Tethys rifts had to exist, which is at variance to previous reconstructions which show the Marrakech High Atlas as a morphologic high or a poorly subsiding domain during the Triassic-Jurassic rifting (Choubert and Faure-Muret, 1962; Du Dresnay, 1971; Michard, 1976; Stets, 1992; Jabour et al., 2004; Laville et al., 2004; El Arabi, 2007; Frizon de Lamotte et al., 2008, 2009; Baudon et al., 2012). The complex system of horsts and grabens during the Triassic, evidenced by the structural field study presented in Chapter 2 (see fig. 2.18) is confirmed by my thermochronologic results, which show that the present Toubkal massif was an exhuming horst during the whole rifting stage, separating the northern and southern Ourika and Eç Çour basins (fig. 3.13a). The reconstructed cross section in fig. 3.13a also show major thickness differences in syn-rift deposits between the Ourika basin and the Eç Çour basin, which was a poorly subsiding basin compared with the Ourika. The horst-graben geometry and the fully developed Ourika basin respect to the Eç Çour one evidences, as I discussed in Chapter 2, that the main Mesozoic rift through followed the transition zone between the Variscan

chain and the West African Craton (respectively, the Moroccan Meseta and Anti-Atlas domains; see also Chapter 1) which is deflected due to the indentation of the Ouzellarh Precambrian salient in the Marrakech High Atlas.

ZHe ages obtained in the Tizi n'Test basin area and also a few zHe ages in the Ourika area evidence that the subsidence stage ended in the Marrakech High Atlas in late Mid-Upper Jurassic and was followed by a period of at least 2 km of exhumation from late Mid-Upper Jurassic to Early Cretaceous times. We have seen that this period of exhumation (with similar amounts of exhumation) is also recorded by AFT ages in the northern and southern Marrakech High Atlas, in the Moroccan Meseta and in the SW of the Anti-Atlas (Ghorbal et al., 2008; Balestrieri et al., 2009; Ghorbal, 2009; Saddiqi et al., 2009; Barbero et al., 2011; Ruiz et al., 2011; Bertotti and Gouiza, 2012), thus defining a N-S oriented wide region of km-scale upward vertical movement from the Moroccan Meseta to the Anti-Atlas (considered stable domains since the Atlas orogeny), crossing the Marrakech High Atlas, and parallel to the trend of the Atlantic margin.

The origin of this Late Jurassic-Early Cretaceous exhumation is not fully understood and is still under debate. Bertotti and Gouiza (2012) attributed it to a E-W shortening superimposed on the thermal subsidence of the Atlantic margin, based on the observation of a few syn-sedimentary structures (m-scale folds and minor thrusts) in the Middle Jurassic to Lower Cretaceous formations of the Eassouira-Agadir basin (see location in fig. 3.1). No E-W trending compressional structures are observed in the Marrakech High Atlas and elsewhere, and the minor m-scale folds and thrusts observed in the Eassouira and Agadir basins could be caused by passive diapirism, as proposed by Hafid et al. (2006). Salt-related structures are also identified in the Central High Atlas and in the Atlantic margin (Courel et al., 2003; Tari et al., 2003; Hafid et al., 2006; Saura et al., 2013; Tari and Jabour, 2013). In contrast, Frizon de Lamotte et al. (2009) suggest a thermal doming cause for the uplift, based on the magmatic activity in the Central High Atlas during the late Mid Jurassic-Early Cretaceous and on paleogeographic reconstructions for the Late Jurassic. In fact, coinciding with the dated period of exhumation, the whole Atlas region was submitted to decelerated subsidence or even emersion which result in redbeds sedimentation ("couches rouges") and frequent stratigraphic gaps until the eastern High Atlas (Haddoumi et al., 2002, 2008, 2010; Charrière et al., 2005; Medina et al., 2015). Frizon de Lamotte et al. (2009) described these features as reflecting the expansion of a so-called West Moroccan Arch of uplift which occupied much of present-day Morocco during the Late Jurassic and Early Cretaceous. The generalized high paleogeothermal gradient deduced from my thermal modelling since Late Permian times defines an

anomalously hot condition persistent through time, which could favour a thermal doming interpretation. We should note that this broad uplift feature consists of a western part with effective uplift and exhumation (the Marrakech High Atlas and adjoining areas in the Moroccan Meseta and Anti-Atlas) and an eastern part with decelerated subsidence or sedimentary interruptions without major erosional incision (the Central and Eastern High Atlas). The thermal doming interpretation has the disadvantage that the magmatism is not observed precisely in the uplifting domain, i.e. the Marrakech High Atlas, a fact that was attributed to imprecise lithospheric reasons by Frizon de Lamotte et al. (2009), but could well be due to the nature of the host rocks, i.e. the Jurassic-Cretaceous magmatic bodies rather emplace at shallow depths in the Jurassic sedimentary pile and leave little trace in the Paleozoic basement (as also does the end-Triassic magmatism).

To account for the lateral change between exhumation in the west and decelerated or interrupted subsidence in the east, I suggest that the exhuming area may be affected by a superimposed shoulder effect of the Atlantic rift, i.e. a combination of enhanced convective thinning of the lithosphere and flexural uplift. This explanation is not devoid of problems as the chronology proposed for the Atlantic rift by some authors is that it ended in the Early Jurassic (Stets, 1992; Medina, 1995; Piqué and Laville, 1996; Le Roy and Piqué, 2001; Tari et al., 2003; Hafid et al., 2006; El Arabi, 2007; Tari and Jabour, 2013) synchronously with the accretion of the Atlantic Ocean at about 195 Ma (e.g. Sahabi et al., 2004; Schettino and Turco, 2009).

As long as Frizon de Lamotte et al. (2009) consider that the Late Jurassic-Early Cretaceous is essentially a post-rift episode, others describe it as in full rifting (Bensalah et al., 2013)(see discussion in Michard et al., 2013). Recently Medina et al. (2015) describe that epoch as a failed rift with differential stretching between crust and mantle leading to uplift. While the beginning of effective post-rift thermal subsidence in the Atlas region can be unequivocally placed in the Early Cretaceous (Barremian-Aptain) by the expansive sedimentation in the Anti-Atlas and Meseta domains, the timing of the structural transition between rift extension and post-rift quiescence in the Atlas is not straightforward, as it appears contaminated by superimposed processes that mask subsidence. Late Jurassic zHe ages at both sides of the Tizi n´Test fault indicate that fault was inactive at least since that time (fig. 3.5). A completely satisfactory explanation for the Late Jurassic-Early Cretaceous event is still to be found.

As for the Cenozoic rift inversion, thermal models show that inversion in the Marrakech High Atlas started in Late Cretaceous times with low rates of exhumation. This exhumation

is accelerated from the Oligocene (or Miocene locally) in relation to thrusting, with a possible component of mantle origin since 15 Ma. The restored cross-sections presented in fig. 3.6 and 3.13 show minimum amounts of orogenic shortening of 13 to 14.2 km (21% to 17%) from east to west in the Marrakech High Atlas. This is in contrast with the 3 km (~4%) shortening estimated by Missenard et al. (2007), although it is consistent with the values obtained in the Central High Atlas of 30 to 13 km (24 to 15%; Teixell et al., 2003). The restored section of the Ourika-Toubkal transect shows a predominant N-vergence of the main thrusts, which is in agreement with the higher magnitude of total exhumation for the northern flank of the Marrakech High Atlas with respect to the southern one. This compressional geometry could be, again, influenced by the Variscan inherited rheological domains and the Triassic rift configuration. The Ouzellarh Precambrian salient could act as a backstop to the south of the High Atlas belt, producing the propagation of the deformation to the north of it. Therefore, the fact that the highest summits of the High Atlas are located in the Toubkal massif (>4000m) can be explained as reflecting the inherited rifting structure. The restored section of the Tizi n'Test basin shows a net slip for the southern Tama'rout thrust of 3-4 km and a no predominant vergence of the main thrusts.

Thermochronologic ages obtained both sides of the southern-limiting faults of the Tizi n'Test basin and in the Ourika fault, which together represent more than 90 km of the 280 km long Tizi n'Test fault zone (fig. 3.1) show that vertical movements in this fault zone during the inversion stage were minor and corroborate the conclusions presented in Chapter 2, extracted from structural field observations and microstructural analysis. This argues against all previous interpretations that suggested that the fault was a thrust throughout the Tertiary (Laville et al., 1977; Proust et al., 1977; Binot et al., 1986; Froitzheim et al., 1988; Qarbous et al., 2008), a transpressive fault with a modest left strike-slip movement (Mattauer et al., 1977) or as a dextral transpressive fault still active in the Quaternary (Delcaillau et al., 2011).

3.5. Conclusions

New apatite and the first zircon (U-Th)/He dates have been obtained from basement and Triassic rocks of the Marrakech High Atlas in eight vertical profiles following two NNW-SSE transects across the mountain belt, separated 50-60 km from each other. The zHe and aHe ages and thermal paths obtained from the modelling of the vertical profiles reveal a horst-graben geometry during the Triassic-Jurassic rift in the present Toubkal massif and Ourika Triassic basin (adjacent to the Toubkal massif to the north). They also show that

the Triassic-Jurassic rift was well developed in the Marrakech High Atlas with accumulation of more than 4.5-6 km of Triassic-Jurassic syn-rift deposits. This is the first reliable estimation of the total amount of syn-rift sediment thickness in the Marrakech High Atlas, and suggests that the Tethys and Atlantic rifts were connected in Triassic to late Mid to Upper Jurassic times.

The late Mid-Upper Jurassic to Early Cretaceous zHe cooling ages obtained in the Tizi n'Test and Ourika-Toubkal areas indicate that the Marrakech High Atlas rift-related subsidence finished in late Mid to Upper Jurassic times and it was followed by a period of exhumation. These zHe ages are in agreement with previously published AFT ages in the Moroccan Meseta, the Anti-Atlas and also in foothills of the Marrakech High Atlas, and together define a Mid to Late Jurassic-Early Cretaceous exhuming high following the orientation of the current Atlantic margin.

Thermal modeling also reveals a local moderate cooling event starting in the Santonian-Campanian, which I view as providing the first thermochronologic clue for a Late Cretaceous initiation of the Atlas orogeny in the inner parts of the High Atlas. Exhumation is accelerated in thermal paths since the Oligocene or Miocene, which is consistent with dated tectonics-sedimentation relationships in the northern Ouarzazate basin external thrust belt.

Based on the Triassic-Jurassic Tizi n'Test and Ourika basin reconstruction assisted by thermochronology and on the constrained tectonic structures of the area, a restoration of the present-day cross-section to the onset of the Atlas orogeny is presented, suggesting minimum values of total shortening in the Marrakech High Atlas of 13 to 14.2 km (21% to 17%).

Chapter 4

Conclusions

Chapter 4. Conclusions

Using a multidisciplinary approach that integrates structural analysis and thermochronology, this thesis presents new results on the geodynamics of the Marrakech High Atlas Triassic-Jurassic rift and its inversion, which are summarized in what follows.

4.1. The Triassic-Jurassic Marrakech High Atlas rift

- The detailed field-based structural study of the main Triassic basins and basin-margin faults shows that the Marrakech High Atlas was a narrow rift system controlled by N60-trending margin-faults defining basins which are roughly orthogonal to the general extension direction (~NE-SW in the present-day reference frame of the African plate).
- The orientation of the High Atlas rift follows in general the border of the Variscan Chain. While this determines that the central and eastern segments formed as oblique rifts oriented ~ENE-WSW, the rift in the Marrakech segment trends ~NE due to the indentation of the rigid block of the Ouzellarh Precambrian salient, which originally deflected the Variscan chain.
- A complex system of Triassic horsts and grabens is described, evidencing the segmented nature of the rift. Diverging paleocurrents and onlap patterns indicate that the Tirknit-Tizi n'Test and Tizi n'Tacht-Ourika basins were separated by an intervening high at least in early- and mid-rifting stages (Mid Triassic times). Also, a horst-graben geometry is evidenced by zHe ages and thermal models in the present Toubkal massif and Ourika Triassic basin, which extended for the whole Triassic-Jurassic rift. Well-exposed fault and graben structures provide good analogues for the exploration of pre-salt systems in the subsurface.
- Preserved extensional features (e.g. fault-propagation/drag folds, minor faults, slickenslides) show a dominant dip-slip or oblique-slip opening kinematics, in contrast with models proposing a major strike-slip component for the main basin-bounding faults, including faults belonging to the Tizi n'Test fault zone (which is often viewed as a major strike-slip/transform fault).
- ZHe dating and thermal modeling indicates that more than 4.5-6 km of Triassic to Mid-Late Jurassic deposits accumulated in the Tizi n'Test and Tizi n'Tacht-Ourika basins. Assuming a maximum thickness for the Triassic redbeds and basalts of 2 km, from 2.5 km to more than 4 km of Jurassic syn-rift rocks were deposited in the basins. This result evidences that the Triassic-Jurassic rift was well developed in the Marrakech

High Atlas and suggests that the Tethys and Atlantic rifts were connected in Triassic to Mid-Late Jurassic times.

4.2. The Mid-Late Jurassic to Early Cretaceous exhumation

- Mid-Late Jurassic to Early Cretaceous zHe cooling ages obtained in the Tizi n'Test and Ourika-Toubkal areas indicate that the rift-related subsidence in the Marrakech High Atlas segment finished in late Mid Jurassic times and was followed by a period of exhumation where 2-3 km of rock were eroded. These zHe cooling ages are in agreement with previously published AFT ages in the Moroccan Meseta, the Anti-Atlas and also in foothills of the Marrakech High Atlas, and together define a Mid-Late Jurassic to Early Cretaceous exhuming high following the orientation of the current Atlantic margin.
- Similar Mid-Late Jurassic zHe cooling ages across the Tizi n'Test fault zone, in the southern margin of the Tizi n'Test Triassic basin, indicate that this fault zone experienced limited vertical movements after rifting.

4.3. The Atlas orogeny

- Orogenic shortening in the Marrakech High Atlas is accommodated by basement-involved large-scale folding, and by shortcut and by-pass thrusting, with sparse evidence for left-lateral strike-slip, which may have taken place but was not a major component of the deformation.
- Based on structural observations and thermochronology, most rift faults, including faults belonging to the Tizi n'Test fault zone, were not reactivated during the orogenic compressional stage, acting then as buttresses.
- Thermal models based on zHe reveal a localized, moderate cooling event starting in the Santonian-Campanian in the Ourika area, which is viewed as providing the first thermochronologic clue for a Late Cretaceous initiation of the Atlas orogenic-driven exhumation in the inner parts of the High Atlas.
- On the basis of aHe data, orogenic-driven cooling is accelerated in thermal paths since the Oligocene or Miocene, which is consistent with dated tectonics-sedimentation relationships in the northern Ouarzazate basin external thrust belt.
- Present-day geological cross-sections across the Marrakech High Atlas are restored to pre-orogenic states (rift and post-rift) with the assistance of thermochronological data. Minimum values of total shortening in this segment of the High Atlas are of 13 km to 14.2 km (21% to 17%).

Chapter 5

References

Chapter 5. References

Ait Brahim, L., Chotin, P., Hinaj, S., Abdelouafi, A., El Adraoui, A., Nakcha, C., Dhont, D., Charroud, M., Sossey Alaoui, F., Amrhar, M., Bouaza, A., Tabyaoui, H., Chaouni, A., 2002. Paleostress evolution in the Moroccan African margin from Triassic to Present. Tectonophysics 357, 187–205. doi:10.1016/S0040-1951(02)00368-2

Ambroggi, R., 1963. Étude géologique du versant méridional du Haut Atlas Occidental et de La Plaine du Souss. Notes et mémoires du Service Géologique 157, 321 pp.

Amilibia, A., Sàbat, F., McClay, K.R., Muñoz, J.A., Roca, E., Chong, G., 2008. The role of inherited tectono-sedimentary architecture in the development of the central Andean mountain belt: Insights from the Cordillera de Domeyko. Journal of Structural Geology 30, 1520–1539. doi:10.1016/j.jsg.2008.08.005

Amrhar, M., 1995. Tectonique et inversions géodynamiques post rift dans le Haut Atlas occidental. Structures, inestabilités tectoniques et magmatismes liés à l'ouverture de l'Atlantique central et la collision Afrique-Europe. Universite Cadi Ayyad, Marrakech, 253 pp.

Andreu, B., Colin, J.P., Haddoumi, H., Charrière, A., 2003. Les Ostracodes des "Couches rouges" du synclinal d'Aït Attab, Haut Atlas Central, Maroc: systématique, biostratigraphie, paléoécologie, paléobiogéographie. Revue de Micropaléontologie 46, 193–216.

Angoud, M., Atik, M., Benchra, M., Cherifi, A., Daimi, A., Driouiche, H., El Houari, N., El Khlifi, A., El Maoukour, A., El Mouatani, A., Essafi, M., Labriki, M., Mimet, A., Yahyaoui, L., 2002. Carte géologique du Maroc, scale 1:50.000, sheet NH-29-XXIII-1c: Tafingoult. Editions du Service Géologique du Maroc. Notes et Mémoires 444.

Arboleya, M.-L., Babault, J., Owen, L.A., Teixell, A., Finkel, R.C., 2008. Timing and nature of Quaternary fluvial incision in the Ouarzazate foreland basin , Morocco. Journal of the Geological Society of London 165, 1059–1073.

Arboleya, M.L., Teixell, A., Charroud, M., Julivert, M., 2004. A structural transect through the High and Middle Atlas of Morocco. Journal of African Earth Sciences 39, 319–327.

Ault, A.K., Flowers, R.M., 2012. Is apatite U-Th zonation information necessary for accurate interpretation of apatite (U-Th)/He thermochronometry data?. Geochimica et Cosmochimica Acta 79, 60–78.

Ayarza, P., Alvarez-Lobato, F., Teixell, A., Arboleya, M.L., Tesón, E., Julivert, M., Charroud, M., 2005. Crustal structure under the central High Atlas Mountains (Morocco) from geological and gravity data. Tectonophysics 400, 67–84.

Babault, J., Teixell, A., Arboleya, M.L., Charroud, M., 2008. A Late Cenozoic age for long-wavelength surface uplift of the Atlas Mountains of Morocco. Terra Nova 20, 102–107.

Balestrieri, M.L., Moratti, G., Bigazzi, G., Algouti, A., 2009. Neogene exhumation of the Marrakech High Atlas (Morocco) recorded by apatite fission-track analysis. Terra Nova 21, 75–82. doi:10.1111/j.1365-3121.2008.00857.x

Barbero, L., Jabaloy, A., Gómez-Ortiz, D., Pérez-Peña, J. V., Rodríguez-Peces, M.J., Tejero, R., Estupiñán, J., Azdimousa, A., Vázquez, M., Asebriy, L., 2011. Evidence for surface uplift of the Atlas Mountains and the surrounding peripheral plateaux: Combining apatite fission-track results and geomorphic indicators in the Western Moroccan Meseta (coastal Variscan Paleozoic basement). Tectonophysics 502, 90–104. doi:10.1016/j.tecto.2010.01.005

Barbero, L., Teixell, A., Arboleya, M.L., del Río, P., Reiners, P.W., Bougadir, B., 2007. Jurassic-to-present thermal history of the central High Atlas (Morocco) assessed by low-temperature thermochronology. Terra Nova 19, 58–64. doi:10.1111/j.1365-3121.2006.00715.x

Baudon, C., Fabuel-Perez, I., Redfern, J., 2009. Structural style and evolution of a Late Triassic rift basin in the Central High Atlas, Morocco: controls on sediment deposition. Geological Journal 44, 677–691. doi:10.1002/gj.1197

Baudon, C., Redfern, J., Van Den Driessche, J., 2012. Permo-Triassic structural evolution of the Argana Valley, impact of the Atlantic rifting in the High Atlas, Morocco. Journal of African Earth Sciences 65, 91–104. doi:10.1016/j.jafrearsci.2012.02.002

Beauchamp, J., 1988. Triassic sedimentation and rifting in the High Atlas (Morocco), in: Manspeizer, W. (Ed.), Triassic-Jurassic Rifting. Developments in Geotectonics 22. Elsevier, pp. 477–497.

Beauchamp, W., Allmendinger, R., Barazangi, M., 1999. Inversion tectonics and the evolution of the High Atlas Mountains, Morocco, based on a geological-geophysical transect. Tectonics 18, 163–184.

Beauchamp, W., Barazangi, M., Demnati, A., El Alji, M., 1996. Intracontinental Rifting and Inversion: Missour Basin and Atlas Mountains, Morocco. AAPG Bulletin 80, 1459–1482.

Benaouiss, N., Courel, L., Beauchamp, J., 1996. Rift-controlled fluvial/tidal transitional series in the Oukaïmeden Sandstones, High Atlas of Marrakesh (Morocco). Sedimentary Geology 107, 21–36.

Bensalah, M.K., Youbi, N., Mata, J., Madeira, J., Martins, L., El Hachimi, H., Bertrand, H., Marzoli, A., Bellieni, G., Doblas, M., Font, E., Medina, F., Mahmoudi, A., Beraâouz, E.H., Miranda, R., Verati, C., De Min, A., Ben Abbou, M., Zayane, R., 2013. The Jurassic-Cretaceous basaltic magmatism of the Oued El-Abid syncline (High Atlas, Morocco): Physical volcanology, geochemistry and geodynamic implications. Journal of African Earth Sciences 81, 60–81. doi:10.1016/j.jafrearsci.2013.01.004

Bertotti, G., Gouiza, M., 2012. Post-rift vertical movements and horizontal deformations in the eastern margin of the Central Atlantic: Middle Jurassic to Early Cretaceous evolution of Morocco. International Journal of Earth Sciences 101, 2151–2165. doi:10.1007/s00531-012-0773-4

Bertrand, H., Prioton, J.M., 1975. Les dolérites marocaines et l'ouverture de l'Atlantique; étude pétrologique et géochimique. PhD thesis, Univ. Claude Bernard, Lyon (321 pp.).

Binot, F., Dresen, G., Stets, J., Wurster, P., 1986. Die Tizi-n' Test-Verwerfungszone im Hohen Atlas (Marokko). Geologische Rundschau 75, 647–664.

Biron, P., Courtinat, B., 1982. Contribution palynologique a la connaissance du Trias du Haut-Atlas de Marrakech, Maroc. Geobios 15, 231–235.

Biron, P.E., 1982. Le Permo-Trias de la région de l'Ourika (Haut Atlas de Marrakech, Maroc). Thèse de 3e cycle. Institut Dolomieu, Grenoble (170 pp.).

Biswas, S., Coutand, I., Grujic, D., Hager, C., Stöckli, D., Grasemann, B., 2007. Exhumation and uplift of the Shillong plateau and its influence on the eastern Himalayas: New constraints from apatite and zircon (U-Th-[Sm])/He and apatite fission track analyses. Tectonics 26. doi:10.1029/2007TC002125

Braun, J., 2002. Quantifying the effect of recent relief changes on age–elevation relationships. Earth and Planetary Science Letters 200, 331–343.

Brown, R.W., Beucher, R., Roper, S., Persano, C., Stuart, F., Fitzgerald, P., 2013. Natural age dispersion arising from the analysis of broken crystals. Part I: Theoretical basis and implications for the apatite (U–Th)/He thermochronometer. Geochimica et Cosmochimica Acta 122, 478–497. doi:10.1016/j.gca.2013.05.041

Burkhard, M., Caritg, S., Helg, U., Robert-Charrue, C., Soulaimani, A., 2006. Tectonics of the Anti-Atlas of Morocco. Comptes Rendus Geoscience 338.

Charrière, A., Haddoumi, H., Mojon, P.-O., 2005. Découverte de Jurassique supérieur et d'un niveau marin du Barrémien dans les "couches rouges" continentales du Haut Atlas central marocain: implications paléogéographiques et structurales. Comptes Rendus Palevol 4, 385–394.

Choubert, G., 1952. Histoire géologique du domaine de l'Anti-Atlas. Notes et Mémoires du Service géologique du Maroc 100, (196 pp).

Choubert, G., Faure-Muret, A., 1962. Évolution du Domaine Atlasique Marocain depuis les temps paléozoïques. Livre à la mémoire du Professeur Paul Fallot - Soc. Geol. France 1, pp. 447–527.

Cogné, N., Gallagher, K., Cobbold, P.R., 2011. Post-rift reactivation of the onshore margin of southeast Brazil: Evidence from apatite (U–Th)/He and fission-track data. Earth and Planetary Science Letters 309, 118–130. doi:10.1016/j.epsl.2011.06.025

Coisy, P., Frogneux, M., 1980. Un etude de microsismicité. La région de Tillouguire (Haut Atlas de Beni Mellal). Mines, Géologie et Energie 45, 93–102.

Corti, G., 2012. Evolution and characteristics of continental rifting: Analog modeling-inspired view and comparison with examples from the East African Rift System. Tectonophysics 522-523, 1–33. doi:10.1016/j.tecto.2011.06.010

Courel, L., Aït Salem, H., Benaouiss, N., Et-Touhami, M., Fekirine, B., Oujidi, M., Soussi, M., Tourani, A., 2003. Mid-Triassic to Early Liassic clastic/evaporitic deposits over the Maghreb Platform. Palaeogeography, Palaeoclimatology, Palaeoecology 196, 157–176. doi:10.1016/S0031-0182(03)00317-1

Cousminer, H.L., Manspeizer, W., 1976. Triassic pollen date Moroccan High Atlas and the incipient rifting of the pangea as middle Carnian. Science 191, 943–945.

De Vicente, G., Cloetingh, S., Muñoz-Martín, A., Olaiz, A., Stich, D., Vegas, R., Galindo-Zaldívar, J., Fernández-Lozano, J., 2008. Inversion of moment tensor focal mechanisms for active stresses around the microcontinent Iberia: Tectonic implications. Tectonics 27, 1–22. doi:10.1029/2006TC002093

Delcaillau, B., Amrhar, M., Namous, M., Laville, E., Pedoja, K., Dugué, O., 2011. Transpressional tectonics in the Marrakech High Atlas: Insight by the geomorphic evolution of drainage basins. Geomorphology 134, 344–362. doi:10.1016/j.geomorph.2011.07.010

DeMets, C., Gordon, G., Argus, D.F., Stein, S., 1990. Current plate motion. Geophysical Journal International 101, 425–478.

Domènech, M., Teixell, A., Babault, J., Arboleya, M.-L., 2015. The inverted Triassic rift of the Marrakech High Atlas: A reappraisal of basin geometries and faulting histories. Tectonophysics. doi:10.1016/j.tecto.2015.03.017

Du Dresnay, R., 1971. Extension et développement des phénomènes récifaux Jurassiques dans le domaine Atlasique Marocain, particulièrement au Lias moyen. Bulletin de la Société Géologique de France 13, 46–56.

Dutour, A., Ferrandini, J., 1985. Nouvelles observations néotectoniques dans le Haut Atlas de Marrakech et le Haouz central (Maroc). Apports sur l'évolution récente d'un segment du bati atlasique. Revue de Géologie Dynamique et de Géographie Physique 26, 285–297.

Ehlers, T., Farley, K., 2003. Apatite (U–Th)/He thermochronometry: methods and applications to problems in tectonic and surface processes. Earth and Planetary Science Letters 206.

El Arabi, E.H., 2007. La série permienne et triasique du rift haut-atlasique: nouvelles datations; évolution tectonosédimentaire. Univ. Hassan II Casablanca, 225 pp.

El Arabi, E.H., Diez, J.B., Broutin, J., Essamoud, R., 2006. Première caractérisation palynologique du Trias moyen dans le Haut Atlas ; implications pour l'initiation du rifting téthysien au Maroc. Comptes Rendus Geoscience 338, 641–649. doi:10.1016/j.crte.2006.04.001

El Arabi, H., Ferrandini, J., Essamoud, R., 2003. Triassic stratigraphy and structural evolution of a rift basin: the Eç Çour basin, High atlas of Marrakech, Morocco. Journal of African Earth Sciences 36, 29–39. doi:10.1016/S0899-5362(03)00020-4

El Harfi, A., Guiraud, M., Lang, J., 2006. Deep-rooted "thick skinned" model for the High Atlas Mountains (Morocco). Implications for the structural inheritance of the southern Tethys passive margin. Journal of Structural Geology 28, 1958–1976. doi:10.1016/j.jsg.2006.08.011

El Kochri, A., Chorowicz, J., 1996. Oblique extension in the Jurassic trough of the central and eastern High Atlas. Journal of Canadian Earth Sciences 33, 84–92.

Ettachfini, E.M., Andreu, B., 2004. The Cenomanian and Turonian of the Precambrian Platform. Cretaceous Research 25, 277–302.

Fabuel-Perez, I., Redfern, J., Hodgetts, D., 2009. Sedimentology of an intra-montane rift-controlled fluvial dominated succession: The Upper Triassic Oukaimeden Sandstone Formation, Central High Atlas, Morocco. Sedimentary Geology 218, 103–140. doi:10.1016/j.sedgeo.2009.04.006

Farley, K.A., 2000. Helium diffusion from apatite: General behavior as illustrated by Durango fluorapatite. Journal of Geophysical Research 105, 2903–2914.

Farley, K.A., 2002. (U-Th)/He Dating: Techniques, Calibrations, and Applications. Reviews in Mineralogy and Geochemistry 47, 819–844. doi:10.2138/rmg.2002.47.18

Farley, K.A., Shuster, D.L., Ketcham, R.A., 2011. U and Th zonation in apatite observed by laser ablation ICPMS, and implications for the (U-Th)/He system. Geochimica et Cosmochimica Acta 75, 4515–4530.

Farley, K.A., Wolf, R.A., Silver, L.T., 1996. The effects of long alpha-stopping distances on (U-Th)/He ages. Geochimica et Cosmochimica Acta 60, 4223–4229.

Faure-Muret, A., Choubert, G., 1971. Le Marroc. Domaine rifain et atlasique, in: Tectonique de l'Afrique, Sciences de La Terre 6. UNESCO. pp. 17–46.

Fedan, B., 1988. Evolution géodynamique d'un bassin intraplaque sur décrochements (Moyen Atlas, Maroc) durant le Méso-Cenozoique. Université Mohammed V, Rabat, 141 pp.

Fitzgerald, P.G., Baldwin, S.L., Webb, L.E., O'Sullivan, P.B., 2006. Interpretation of (U-Th)/He single grain ages from slowly cooled crustal terranes: A case study from the Transantarctic Mountains of southern Victoria Land. Chemical Geology 225, 91–120. doi:10.1016/j.chemgeo.2005.09.001

Flowers, R.M., Kelley, S.A., 2011. Interpreting data dispersion and " inverted" dates in apatite (U-Th)/He and fission-track datasets: An example from the US midcontinent. Geochimica et Cosmochimica Acta 75, 5169–5186. doi:10.1016/j.gca.2011.06.016

Flowers, R.M., Ketcham, R.A., Shuster, D.L., Farley, K.A., 2009. Apatite (U–Th)/He thermochronometry using a radiation damage accumulation and annealing model. Geochimica et Cosmochimica Acta 73, 2347–2365. doi:10.1016/j.gca.2009.01.015

Fraissinet, C., Zouine, E.M., Morel, J.L., Poisson, A., Andrieux, J., Faure-Muret, A., 1988. Structural evolution of the southern and northern Central High Atlas in Paleogene and Mio-Pliocene times, in: Jacobshagen, V. (Ed.), The Atlas System of Morocco. Springer-Verlag, Berlin, pp. 273–291.

Frizon de Lamotte, D., Leturmy, P., Missenard, Y., Khomsi, S., Ruiz, G., Saddiqi, O., Guillocheau, F., Michard, A., 2009. Mesozoic and Cenozoic vertical movements in the Atlas system (Algeria, Morocco, Tunisia): an overview. Tectonophysics 475, 9–28. doi:10.1016/j.tecto.2008.10.024

Frizon de Lamotte, D., Saint Bezar, B., Bracène, R., 2000. The two main steps of the Atlas building and geodynamics of the western Mediterranean. Tectonics 19, 740–761.

Frizon de Lamotte, D., Zizi, M., Missenard, Y., Hafid, M., El Azzouzi, M., Maury, R.C., Charrière, A., Taki, M., Benami, M., Michard, A., 2008. The Atlas System, in: Michard, A., Saddiqi, O., Chalouan, A., Frizon de Lamotte, D. (Eds.), Continental Evolution: The

Geology of Morocco. Notes in Earth Sciences. Springer-Verlag Berlin Heidelberg, pp. 133–202.

Froitzheim, N., Stets, J., Wurster, P., 1988. Aspects of Western High Atlas tectonics, in: Jacobshagen, V.H. (Ed.), The Atlas System of Morocco. Springer-Verlag, Berlin, pp. 219–244.

Fullea, J., Fernandez, M., Zeyen, H., Verges, J., 2007. A rapid method to map the crustal and lithospheric thickness using elevation, geoid anomaly and thermal analysis; application to the Gibraltar Arc system, Atlas Mountains and adjacent zones. Tectonophysics 430, 97–117.

Gallagher, K., 2012. Transdimensional inverse thermal history modeling for quantitative thermochronology. Journal of Geophysical Research 117, B02408. doi:10.1029/2011JB008825

Gallagher, K., 2015. QTQt v 5.3.0 User Guide.

Gallagher, K., Charvin, K., Nielsen, S., Sambridge, M., Stephenson, J., 2009. Markov chain Monte Carlo (MCMC) sampling methods to determine optimal models, model resolution and model choice for Earth Science problems. Marine and Petroleum Geology 26, 525–535. doi:10.1016/j.marpetgeo.2009.01.003

Gasquet, D., Ennih, N., Liégeois, J.-P., Soulaimani, A., Michard, A., 2008. The Pan-African Belt, in: Michard, A., Saddiqi, O., Chalouan, A., Frizon de Lamotte, D. (Eds.), Continental Evolution: The Geology of Morocco. Lecture Notes in Earth Sciences. Springer-Verlag Berlin Heidelberg, pp. 33–64.

Gautheron, C., Barbarand, J., Ketcham, R.A., Tassan-Got, L., Van der Beek, P., Pagel, M., Pinna-Jamme, R., Couffignal, F., Fialin, M., 2013. Chemical influence on alpha-recoil damage annealing in apatite: Implications for (U-Th)/He dating. Chemical Geology 351, 257–267.

Gautheron, C., Tassan-Got, L., Barbarand, J., Pagel, M., 2009. Effect of alpha-damage annealing on apatite (U–Th)/He thermochronology. Chemical Geology 266, 157–170. doi:10.1016/j.chemgeo.2009.06.001

Gautheron, C., Tassan-Got, L., Ketcham, R.A., Dobson, K.J., 2012. Accounting for long alpha-particle stopping distances in (U-Th-Sm)/He geochronology: 3D modeling of

diffusion, zoning, implantation, and abrasion. Geochimica et Cosmochimica Acta 96, 44–56.

Gauthier, H., 1960. Contribution a l'etude geologique des formations post-liasiques des bassins du Dades et du haut Todra (Maroc meridional). Notes et Memoires du Service Geologique (Rabat) 119, 1–137.

Ghorbal, B., 2009. Mesozoic to Quaternary Thermo-tectonic evolution of Morocco (NW Africa). Vrije Universiteit Amsterdam, 226 pp.

Ghorbal, B., Bertotti, G., Foeken, J., Andriessen, P., 2008. Unexpected Jurassic to Neogene vertical movements in "stable" parts of NW Africa revealed by low temperature geochronology. Terra Nova 20, 355–363. doi:10.1111/j.1365-3121.2008.00828.x

Gillcrist, R.M.P., Coward, J.L., Mugnier, X., 1987. Structural inversion and its controls: examples from the Alpine foreland and the French Alps. Geodinamica Acta 1, 5–34.

Gleadow, A.J.W., Fitzgerald, P.G., 1987. Uplift history and structure of the Transantarctic Mountains: new evidence from fission track dating of basement apatites in the Dry Valleys area, southern Victoria Land. Earth and Planetary Science Letters 82, 1–14.

Gomez, F., Barazangi, M., Beauchamp, W., Demnati, A., 1999. Evolution of the Atlas Mountains (Morocco) and adjacent sedimentary basins; implications for hydrocarbons. AAPG Bulletin 83, 1314–1315.

Gomez, F., Beauchamp, W., Barazangi, M., 2000. Role of the Atlas Mountains (northwest Africa) within the African-Eurasian plate-boundary zone. Geology 28, 775–778.

Görler, K., Helmdach, F.-F., Gaemers, P., Heissig, K., Hinsch, W., Mädler, K., Schwarzhans, W., Zucht, M., 1988. The uplift of the central High Atlas as deduced from Neogene continental sediments of the Ouarzazate province, Morocco, in: Jacobshagen, V. (Ed.), The Atlas System of Morocco. Springer-Verlag, Berlin, pp. 361–404.

Guenthner, W.R., Reiners, P.W., Ketcham, R.A., Nasdala, L., Giester, G., 2013. Helium diffusion in natural zircon: Radiation damage, anisotropy, and the interpretation of zircon (U-Th)/He thermochronology. American Journal of Science 313, 145–198. doi:10.2475/03.2013.01

Guimerà, J., Arboleya, M.L., Teixell, A., 2011. Structural control on present-day topography of a basement massif: The central and Eastern anti-atlas (Morocco). Geologica Acta 9, 55–65. doi:10.1344/105.000001643

Haddoum, H., Guiraud, R., Moussine-Pouchkine, A., 2001. Hercynian compressional deformations of the Ahnet-Mouydir Basin, Algerian Saharan Platform: far-field stress effects of the Late Palaeozoic orogeny. Terra Nova 13, 220–226.

Haddoumi, H., Aiméras, Y., Bodergat, A.-M., Charrière, A., Mangold, C., Benshili, K., 1998. Ages et environnements des couches rouges d'Anoual (Jurassique moyen et Cretace inferieur, Haut-Atlas oriental, Maroc). Comptes Rendus de l'Academie des Sciences, Serie II. Sciences de la Terre et des Planetes 327, 127–133.

Haddoumi, H., Charrière, A., Andreu, B., Mojon, P.-O., 2008. Les dépôts continentaux du Jurassique moyen au Crétacé inférieur dans le Haut Atlas oriental (Maroc): paléoenvironments successifs et signification paléogéographique. Carnets de Géologie/Notebooks on Geology Article 20.

Haddoumi, H., Charriere, A., Feist, M., Andreu, B., 2002. Nouvelles datations (Hauterivien superieur-Barremien inferieur) dans les "Couches rouges" continentales du Haut Atlas central marocain; consequences sur l'age du magmatisme et des structurations mesozoiques de la chaine Atlasique. Comptes Rendus Palevol 1, 259–266.

Haddoumi, H., Charrière, A., Mojon, P.-O., 2010. Stratigraphie et sédimentologie des "Couches rouges" continentales du Jurassique-Crétacé du Haut Atlas central (Maroc): implications paléogéographiques et géodynamiques. Geobios 43, 433–451.

Hafid, M., Zizi, M., Bally, A.W., Ait Salem, A., 2006. Structural styles of the western onshore and offshore termination of the High Atlas, Morocco. Comptes Rendus Geoscience Geoscience 338, 50–64.

Hailwood, E.A., Mitchell, J.C., 1971. Paleomagnetic and radiometric dating results from Jurassic in south Morocco. Geophys. J. R. Astron. Soc. 24, 351–364.

Harfi, A. El, Lang, J., Salomon, J., 1996. Le remplissage continental cenozoique du bassin d'avant-pays de Ouarzazate. Implications sur l'evolution geodynamique du Haut-Atlas Central (Maroc). Comptes Rendus de l'Académie des Sciences - Series II: Sciences de la Terre et des Planetes 323, 623–630.

Herbig, H.G., 1988. Synsedimentary tectonics in the Northern Middle Atlas (Morocco) during the Late Cretaceous and Tertiary, in: Jacobshagen, V. (Ed.), The Atlas System of Morocco. Springer-Verlag, Berlin, pp. 321–337.

Herbig, H.G., Trappe, J., 1994. Stratigraphy of the Sub-atlas Group (Maastrichtian-Middle Eocene, Morocco). Newsletters on Stratigraphy 30, 125–165.

Hoepffner, C., Soulaimani, A., Piqué, A., 2005. The Moroccan Hercynides. Journal of African Earth Sciences 43, 144–165.

Hollard, H., 1985. Carte géologique du Maroc-Echelle: 1/1.000.000. Ed. Service Géologique du Maroc, Rabat.

Hourigan, J.K., Reiners, P.W., Brandon, M.T., 2005. U-Th zonation-dependent alpha-ejection in (U-Th)/He chronometry. Geochimica et Cosmochimica Acta 69, 3349–3365.

House, M.A., Farley, K.A., Kohn, B.P., 1999. An empirical test of helium diffusion in apatite: borehole data from the Otway basin, Australia. Earth and Planetary Science Letters 170, 463–474. doi:10.1016/S0012-821X(99)00120-X

Jabour, H., Dakki, M., Nahim, M., Charrat, F., El Alji, M., Hssain, M., Oumalch, F., El Abibi, R., 2004. The Jurassic depositional system of Morocco, geology and play concepts. MAPG Memoirs 1, 5–39.

Jacobshagen, V., Brede, R., Hauptmann, M., Heinitz, W., 1988. Structure and post-Palaeozoic evolution of the central High Atlas, in: Jacobshagen, V. (Ed.), The Atlas System of Morocco. Springer-Verlag, Berlin, pp. 245–271.

Jenny, J., Le Marrec, A., Monbaron, M., 1981. Les couches rouges du Jurassique moyen du Haut Atlas central (Maroc); Correlations lithostratigraphiques, elements de datations et cadre tectono-sedimentaire. Bulletin de la Société géologique de France 23, 627–640.

Jimenez-Munt, I., Fernandez, M., Torne, M., Bird, P., 2001. The transition from linear to diffuse plate boundary in the Azores-Gibraltar region; results from a thin-sheet model. Earth and Planetary Science Letters 192, 175–189.

Karner, G.D., Gambôa, L.A.P., 2007. Timing and origin of the South Atlantic pre-salt sag basins and their capping evaporites. Geological Society, London, Special Publications 285, 15–35. doi:10.1144/SP285.2

Ketcham, R. a., Gautheron, C., Tassan-Got, L., 2011. Accounting for long alpha-particle stopping distances in (U–Th–Sm)/He geochronology: Refinement of the baseline case. Geochimica et Cosmochimica Acta 75, 7779–7791. doi:10.1016/j.gca.2011.10.011

Knight, K.B., Nomade, S., Renne, P.R., Marzoli, A., Bertrand, H., Youbi, N., 2004. The Central Atlantic magmatic province at the Triassic-Jurassic boundary: paleomagnetic and Ar-Ar evidence from Morocco for brief, episodic volcanism. Earth and Planetary Science Letters 228, 143–160.

Laville, E., Lesage, J.-L., Seguret, M., 1977. Géométrie, cinématique (dynamique) de la tectonique atlasique sur le versant sud du Haut Atlas marocain. Aperçu sur les tectoniques hercyniennes et tardi-hercyniennes. Bulletin de la Société Géologique de France (7), t.XIX, 527–539.

Laville, E., Petit, J.-P., 1984. Role of synsedimentary strike-slip faults in the formation of Moroccan Triassic basins. Geology 12, 424–427.

Laville, E., Piqué, A., 1991. La distension crustale atlantique et atlasique au Maroc au début du Mésozoïque: le rejeu des structures hercyniennes. Bull. Soc. Géol. France t. 162, n°, 1161–1171.

Laville, E., Piqué, A., Amrhar, M., Charroud, M., 2004. A restatement of the Mesozoic Atlasic Rifting (Morocco). Journal of African Earth Sciences 38, 145–153.

Le Roy, P., Piqué, A., 2001. Triassic-Liassic Western Moroccan synrift basins in relation to the Central Atlantic opening. Marine Geology 172, 359–381.

Lippolt, H.J., Leitz, M., Wernicke, R.S., Hagedorn, B., 1994. (U+Th)/He dating of apatite: experience with samples from different geochemical environments. Chemical Geology 112, 179–191.

Macaulay, E.A., Sobel, E.R., Mikolaichuk, A., Kohn, B., Stuart, F.M., 2014. Cenozoic deformation and exhumation history of the Central Kyrgyz Tien Shan. Tectonics 33, 135–165. doi:10.1002/2013TC003376

Makris, J., Demnati, A., Klussmann, J., 1995. Deep seismic soundings in Morocco and a crust and upper mantle model deduced from seismic and gravity data. Annales Geophysicae 3, 369–380.

Manspeizer, W., 1982. Triassic-Liassic basins and climate of the Atlantic passive margins. Geologische Rundschau 71, 895–917.

Manspeizer, W., Puffer, J.H., Cousminer, H.L., 1978. Separation of Morocco and eastern North America: a Triassic-Liassic stratigraphic record. GSA Bulletin 89, 901–920.

Mattauer, M., Proust, F., Tapponnier, P., 1972. Major Strike-slip Fault of Late Hercynian Age in Morocco. Nature 237, 63–72.

Mattauer, M., Tapponnier, P., Proust, F., 1977. Sur les mécanismes de formation des chaînes intracontinentales. L'exemple des chaînes atlasiques du Maroc. Bulletin de la Société Géologique de France 7 (t. XI), 521–526.

Mattis, A.F., 1977. Nonmarine Triassic sedimentation, central High Atlas Mountains, Morocco. Journal of Sedimentary Research 47, 107–119.

McClay, K.R., Insley, M.W., Anderton, R., 1989. Inversion of the Kechika Trough, Northeastern British Columbia, Canada. Geological Society, London, Special Publications. doi:10.1144/GSL.SP.1989.044.01.14

McClusky, S., Reilinger, R., Mahmoud, S., Ben Sari, D., Tealeb, A., 2003. GPS constraints on Africa (Nubia) and Arabia plate motions. Geophysical Journal International 155, 126–138.

Medina, F., 1995. Syn- and postrift evolution of the El Jadida-Agadir basin (Morocco): constraints for the rifting model of the Central Atlantic. Can. J. Earth Sci. 32, 1273–1291.

Medina, F., Cherkaoui, T.-E., 1991. Focal mechanisms of the Atlas earthquakes and tectonic implications. Geologische Rundschau 80, 639–648.

Medina, F., Cherkaoui, T.-E., 1992. Mecanismes au foyer des seismes du Maroc et des regions voisines (1959-1986); consequences tectoniques. Eclogae geologicae Helvetiae 85, 433–457.

Medina, F., Youbi, N., Bensalah, M.K., 2015. Thermo-tectonic Evolution of the Central High Atlas during the Mesozoic. 77th EAGE Conference and Exhibition. doi:10.3997/2214-4609.201413285

Michard, A., 1976. Eléments de géologie marocaine. Notes et Mémoires du Service géologique du Maroc 252, 1–408.

Michard, A., Frizon de Lamotte, D., Saddiqi, O., Chalouan, A., 2008. An outline of the geology of Morocco, in: Michard, A., Saddiqi, O., Chalouan, A., Frizon de Lamotte, D. (Eds.), Continental Evolution: The Geology of Morocco. Lecture Notes in Earth Sciences. Springer-Verlag Berlin Heidelberg, pp. 1–31.

Michard, A., Hoepffner, A., Soulaimani, A., Baidder, L., 2008. The Variscan Belt, in: Michard, A., Saddiqi, O., Chalouan, A., Frizon de Lamotte, D. (Eds.), Continental Evolution: The Geology of Morocco. Notes in Earth Sciences. Springer-Verlag Berlin Heidelberg, pp. 65–132.

Michard, A., Lamotte, D.F. De, Hafid, M., Charrière, A., Haddoumi, H., Ibouh, H., 2013. Comment on "The Jurassic-Cretaceous basaltic magmatism of the Oued El-Abid syncline (High Atlas, Morocco): Physical volcanology, geochemistry and geodynamic implications" by Bensalah et al., J. Afr. Earth Sci. 81 (2013) 60-81. Journal of African Earth Sciences 88, 101–105. doi:10.1016/j.jafrearsci.2013.08.009

Michard, A., Soulaimani, A., Hoepffner, C., Ouanaimi, H., Baidder, L., Rjimati, E.C., Saddiqi, O., 2010. The South-Western Branch of the Variscan Belt: Evidence from Morocco. Tectonophysics 492, 1-24. doi:10.1016/j.tecto.2010.05.021

Missenard, Y., Cadoux, A., 2012. Can Moroccan Atlas lithospheric thinning and volcanism be induced by Edge-Driven Convection? Terra Nova 24, 27–33. doi:10.1111/j.1365-3121.2011.01033.x

Missenard, Y., Saddiqi, O., Barbarand, J., Leturmy, P., Ruiz, G., El Haimer, F.-Z., Frizon de Lamotte, D., 2008. Cenozoic denudation in the Marrakech High Atlas, Morocco: insight from apatite fission-track thermochronology. Terra Nova 20, 221–228. doi:10.1111/j.1365-3121.2008.00810.x

Missenard, Y., Taki, Z., Frizon de Lamotte, D., Benammi, M., Hafid, M., Leturmy, P., Sébrier, M., 2007. Tectonic styles in the Marrakesh High Atlas (Morocco): the role of heritage

and mechanical stratigraphy. Journal of African Earth Sciences 48, 247–266. doi:10.1016/j.jafrearsci.2007.03.007

Missenard, Y., Zeyen, H., Frizon de Lamotte, D., Leturmy, P., Petit, C., Sébrier, M., Saddiqi, O., 2006. Crustal versus asthenospheric origin of relief of the Atlas Mountains of Morocco. Journal of Geophysical Research 111, B03401. doi:10.1029/2005JB003708

Morel, J., Zouine, E.-M., Andrieux, J., Faure-Muret, A., 2000. Déformations néogènes et quaternaires de la bordure nord haut atlasique (Maroc): rôle du socle et conséquences structurales. Journal of African Earth Sciences 30, 119–131.

Morel, J.L., Zouine, M., Poisson, A., 1993. Relations entre la subsidence des bassins moulouyens et la creation des reliefs atlasiques (Maroc); un exemple d'inversion tectonique depuis le Neogene. Bulletin de la Société Géologique de France 164, 79–91.

Morley, C.K., 2010. Stress re-orientation along zones of weak fabrics in rifts: An explanation for pure extension in "oblique" rift segments? Earth and Planetary Science Letters 297, 667–673. doi:10.1016/j.epsl.2010.07.022

Nachit, H., Barbey, P., Pons, J., Burg, J.P., 1996. L'Eburnéen existe-il dans l'Anti-Atlas occidental marocain? L'exemple du massif du Kerdous. C.R. Acad. Sci. Paris 322, 677–683.

Nasdala, L., Hanchar, J.M., Kronz, A., Whitehouse, M.J., 2004. Long-term stability of alpha particle damage in natural zircon. Chemical Geology 220, 83–103.

Ouanaimi, H., Petit, J., 1992. La Limite sud de la chaine hercynienne dans le Haut Atlas marocain; reconstitution d'un saillant non deforme. Bulletin de la Société Géologique de France 163, 63–72.

Pastor, A., Teixell, A., Arboleya, M.-L., 2013. Rates of Quaternary deformation in the Ouarzazate Basin (Southern Atlas Front, Morocco). Annals of Geophysics 55.

Petit, J.P., 1976. La zone de décrochement de Tizi n'Test (Maroc) et son fonctionnement depuis le Carbonifère. Thèse de 3ème cycle. Université des Sciences et Techniques du Languedoc, Montpellier.

Petit, J.P., Beauchamp, J., 1986. Synsedimentary faulting and palaeocurrent patterns in the Triassic sandstones of the High Atlas (Morocco). Sedimentology 33, 817–829.

Piqué, A., 2001. Geology of Northwest Africa. Berlin-Stuttgart, Gebrueder Borntraeger Verlagsbuchhandlung, 324 pp.

Piqué, A., Laville, E., 1996. The central Atlantic rifting: Reactivation of Palaeozoic structures? Journal of Geodynamics 21, 235–255.

Pique, A., Michard, A., 1989. Moroccan Hercynides; a synopsis. The Paleozoic sedimentary and tectonic evolution at the northern margin of West Africa. American Journal of Science 289, 286–330.

Piqué, A., Tricart, P., Guiraud, R., Laville, E., Bouaziz, S., Amrhar, M., Ouali, R.A., 2002. The Mesozoic-Cenozoic Atlas belt (North Africa): an overview. Geodinamica Acta 15, 185–208. doi:10.1080/09853111.2002.10510752

Proust, F., Petit, J.P., Tapponnier, P., 1977. L'accident du Tizi n'Text et le rôle des décrochements dans la tectonique du Haut Atlas occidental (Maroc). Bulletin de la Société Géologique de France 7, (t. XI), 541–551.

Qarbous, A., Medina, F., Hoepffner, C., 2003. Le bassin de Tizi n'Test (Haut Atlas, Maroc): exemple d'évolution d'un segment oblique au rift de l'Atlantique central au Trias. Can. J. Earth Sci. 40, 949–964. doi:10.1139/E03-029

Qarbous, A., Medina, F., Hoepffner, C., 2008. Tectonique cassante et état de contrainte dans le bassin de Tizi n'Test (Haut Atlas, Maroc) au cours de l'inversion tertiaire. Estudios Geológicos 64, 17–30.

Raddi, Y., Baidder, L., Michard, A., Tahiri, M., 2007. Variscan deformation at the northern border of the West African Craton, eastern Anti-Atlas, Morocco: compression of a mosaic of tilted blocks. Bulletin de la Société Géologique de France 178, 343–352.

Ramdani, F., 1998. Geodynamic implications of intermediate-depth earthquakes and volcanism in the intraplate Atlas Mountains (Morocco). Physics of the Earth and Planetary Interiors 108, 245–260.

Reich, M., Ewing, R.C., Ehlers, T.A., Becker, U., 2007. Low-temperature anisotropic diffusion of helium in zircon: Implications for zircon (U–Th)/He thermochronometry. Geochimica et Cosmochimica Acta 71, 3119–3130. doi:10.1016/j.gca.2007.03.033

Reiners, P.W., 2005. Zircon (U-Th)/He Thermochronometry, in: Reiners, P.W., Ehlers, T.A. (Eds.), Low-Temperature Thermochronology: Techniques, Interpretations, and Applications: Reviews in Mineralogy and Geochemistry, 58. pp. 151–179. doi:10.2138/rmg.2005.58.6

Reiners, P.W., Farley, K.A., 2001. Influence of crystal size on apatite (U–Th)/He thermochronology: an example from the Bighorn Mountains, Wyoming. Earth and Planetary Science Letters 188, 413–420.

Reiners, P.W., Farley, K.A., Hickes, H.J., 2002. He diffusion and (U–Th)/He thermochronometry of zircon: initial results from Fish Canyon Tuff and Gold Butte. Tectonophysics 349, 297–308. doi:10.1016/S0040-1951(02)00058-6

Reiners, P.W., Spell, T.L., Nicolescu, S., Zanetti, K.A., 2004. Zircon (U-Th)/He thermochronometry: He diffusion and comparisons with 40Ar/39Ar dating. Geochimica et Cosmochimica Acta 68, 1857–1887. doi:10.1016/j.gca.2003.10.021

Roch, E., 1939. Description géologique des montagnes a l'Est de Marrakech. Notes et Mémoires du Service géologique du Maroc 80, 1–438.

Rosenbaum, G., Lister, G.S., Duboz, C., 2002. Relative motions of Africa, iberia and Europe during Alpine Orogeny. Tectonophysics 359, 117–129.

Ruiz, G.M.H., Sebti, S., Negro, F., Saddiqi, O., Frizon De Lamotte, D., Stockli, D., Foeken, J., Stuart, F., Barbarand, J., Schaer, J.P., 2011. From central Atlantic continental rift to Neogene uplift - western Anti-Atlas (Morocco). Terra Nova 23, 35–41. doi:10.1111/j.1365-3121.2010.00980.x

Saddiqi, O., El Haimer, F.Z., Michard, A., Barbarand, J., Ruiz, G.M.H., Mansour, E.M., Leturmy, P., Frizon de Lamotte, D., 2009. Apatite fission-track analyses on basement granites from south-western Meseta, Morocco: Paleogeographic implications and interpretation of AFT age discrepancies. Tectonophysics 475, 29–37. doi:10.1016/j.tecto.2009.01.007

Saenz de Galdeano, C., 1992. Algunos problemas geológicos de la cordillera Bética y del Rift. Física de la Tierra; Editorial complutense (Madrid) 4, 11–40.

Sahabi, M., Aslanian, D., Olivet, J.-L., 2004. Un nouveau point de départ pour l'histoire de l'Atlantique central. Comptes Rendus Geoscience 336, 1041–1052.

Saura, E., Verges, J., Martin-Martin, J.D., Messager, G., Moragas, M., Razin, P., Grelaud, C., Joussiaume, R., Malaval, M., Homke, S., Hunt, D.W., 2013. Syn- to post-rift diapirism and minibasins of the Central High Atlas (Morocco): the changing face of a mountain belt. Journal of the Geological Society 171, 97–105. doi:10.1144/jgs2013-079

Schaer, J.-P., 1987. Evolution and structure of the High Atlas of Morocco. The anatomy of mountain ranges. Princeton Univ. Press, Princeton, NJ 107–127.

Schettino, A., Turco, E., 2009. Breakup of Pangaea and plate kinematics of the central Atlantic and Atlas regions. Geophysical Journal International 178, 1078–1097. doi:10.1111/j.1365-246X.2009.04186.x

Seber, D., Barazangi, M., Tadili, B.A., Ramdani, M., Ibenbrahim, A., Ben Sari, D., 1996. Three dimensional upper mantle structure beneath the intraplate Atlas and interplate Rif mountains of Morocco. Journal of Geophysical Research 101, 3125–3138.

Sébrier, M., Siame, L., Zouine, E.M., Winter, T., Missenard, Y., Leturmy, P., 2006. Active tectonics in the Moroccan High Atlas. Comptes Rendus Geoscience 338, 65–79.

Sella, G.F., Dixon, T.H., Mao, A., 2002. REVEL; a model for recent plate velocities from space geodesy. Journal of Geophysical Research 107.

Serpelloni, E., Vannucci, G., Pondrelli, S., Argnani, A., Casula, G., Anzidei, M., Baldi, P., Gasperini, P., 2007. Kinematics of the western Africa-Eurasia plate boundary from focal mechanisms and GPS data. Geophysical Journal International 169, 1180–1200.

Shuster, D.L., Flowers, R.M., Farley, K.A., 2006. The influence of natural radiation damage on helium diffusion kinetics in apatite. Earth and Planetary Science Letters 249, 148–161. doi:10.1016/j.epsl.2006.07.028

Simancas, J.F., Tahiri, A., Azor, A., Lodeiro, F.G., Martínez Poyatos, D.J., El Hadi, H., 2005. The tectonic frame of the Variscan-Alleghanian orogen in Southern Europe and Northern Africa. Tectonophysics 398, 181–198.

Spiegel, C., Kohn, B., Belton, D., Berner, Z., Gleadow, A., 2009. Apatite (U-Th-Sm)/He thermochronology of rapidly cooled samples: the effect of He implantation. Earth and Planetary Science Letters 285, 105–114.

Stets, J., 1992. Mid-Jurassic events in the Western High Atlas (Morocco). Geologische Rundschau 81, 69–84. doi:10.1007/BF01764540

Stets, J., Wurster, P., 1982. Atlas and Atlantic-Structural Relations, in: von Rad, V., Sarnthein, M., Seibold, E., Hinz, K. (Eds.), Geology of the Northwest African Continental Margin. Springer-Verlag, Berlin, Heidelberg, pp. 69–85.

Stockli, D.F., 2005. Application of Low-Temperature Thermochronometry to Extensional Tectonic Settings, in: Reiners, P.W., Ehlers, T.A. (Eds.), Low-Temperature Thermochronology: Techniques, Interpretations, and Applications: Reviews in Mineralogy and Geochemistry, 58. pp. 411–448. doi:10.2138/rmg.2005.58.16

Stockli, D.F., Farley, K.A., Dumitru, T.A., 2000. Calibration of the apatite (U-Th)/He thermochronometer on anexhumed fault block, White Mountains, California. Geology 28, 983–986. doi:10.1130/0091-7613(2000)28<983:COTAHT>2.0.CO;2

Tari, G., Jabour, H., 2013. Salt tectonics in the Atlantic margin of Morocco. Geological Society, London, Special Publications 369, 337–353.

Tari, G., Molnar, J., Ashton, P., 2003. Examples of salt tectonics from West Africa: a comparative approach. Geological Society, London, Special Publications 207, 85–104. doi:10.1144/gsl.sp.2003.207.5

Tari, G., Molnar, J., Ashton, P., Hedley, R., 2000. Salt tectonics in the Atlantic margin of Morocco. The Leading Edge October.

Teixell, A., Arboleya, M.L., Julivert, M., 2003. Tectonic shortening and topography in the central High Atlas (Morocco). Tectonics 22, 1051. doi:10.1029/2002TC001460

Teixell, A., Ayarza, P., Tesón, E., Babault, J., Alvarez-Lobato, F., Charroud, M., Julivert, M., Barbero, L., Amrhar, M., Arboleya, M.L., 2007. Geodinámica de las cordilleras del Alto y Medio Atlas: Síntesis de los conocimientos actuales. Revista de la Sociedad Geológica de España 20, 119–135.

Teixell, A., Ayarza, P., Zeyen, H., Fernandez, M., Arboleya, M.-L., 2005. Effects of mantle upwelling in a compressional setting: the Atlas Mountains of Morocco. Terra Nova 17, 456–461. doi:10.1111/j.1365-3121.2005.00633.x

Tesón, E., 2009. Estructura y cronología de la deformación en el borde sur del Alto Atlas de Marruecos a partir del registro tectono-sedimentario de la cuenca de antepaís de Ouarzazate. Universitat Autònoma de Barcelona, 217 pp, Barcelona.

Tesón, E., Pueyo, E.L., Teixell, A., Barnolas, A., Agustí, J., Furió, M., 2010. Magnetostratigraphy of the Ouarzazate Basin: Implications for the timing of deformation and mountain building in the High Atlas Mountains of Morocco. Geodinamica Acta 23, 151–165. doi:10.3166/ga.23.151-165

Tesón, E., Teixell, A., 2008. Sequence of thrusting and syntectonic sedimentation in the eastern Sub-Atlas thrust belt (Dadès and Mgoun valleys, Morocco). International Journal of Earth Sciences 97, 103–113. doi:10.1007/s00531-006-0151-1

Thomas, R., Chevallier, L., Gresse, P., Harmer, R.E., Eglington, B.M., Armstrong, R.A., de Beer, C.H., Martini, J.E.J., Kock, G.S., Macey, P.H., Ingram, B.A., 2002. Precambrian evolution of the Sirwa window, Anti-Atlas orogen, Morocco. Precambrian Research 118, 1–57.

Thomas, R.J., Fekkak, A., Ennih, N., Errami, E., Loughlin, S.C., Gresse, P.G., Chevallier, L.P., Liégeois, J.P., 2004. A new lithostratigraphic framework for the Anti-Atlas Orogen, Morocco. Journal of African Earth Sciences 39, 217–226. doi:10.1016/j.jafrearsci.2004.07.046

Vacherat, A., Mouthereau, F., Pik, R., Bernet, M., Gautheron, C., 2014. Thermal imprint of rift-related processes in orogens as recorded in the Pyrenees. Earth and Planetary Science Letters 16, 4302. doi:10.1016/j.epsl.2014.10.014

Van Den Bosch, J.W.., 1971. Carte gravimetrique du Maroc, scale 1:500.000. Editions du Service Géologique du Maroc. Notes et Mémoires 234.

Van Houten, F.B., 1977. Triassic-Liassic deposits of Morocco and eastern North America: comparison. AAPG Bulletin 61, 79–99.

Vera, J.A., Martín-Algarra, A., 2004. Cordillera Bética y Baleares, in: Vera, J.A. (Ed.), Geología de España. Sociedad Geológica de España, pp. 347–350.

Vermeesch, P., Seward, D., Latkoczy, C., Wipf, M., Günther, D., Baur, H., 2007. Alpha emitting mineral inclusions in apatite, their effect on (U-Th)/He ages, and how to reduce it. Geochimica et Cosmochimica Acta 71, 1737–1746.

Warme, J.E., 1988. Jurassic carbonate facies of the central and eastern High Atlas Rift, Morocco. Lecture Notes in Earth Sciences 15, 169–199.

Wolf, R.A., Farley, K.A., Kass, D.M., 1998. Modeling of the temperature sensitivity of the apatite (U-Th)/He thermochronometer. Chemical Geology 148, 105–114.

Wolf, R.A., Farley, K.A., Silver, L.T., 1996. Helium diffusion and low-temperature thermochronometry of apatite. Geochimica et Cosmochimica Acta 60, 4231–4240.

Wolfe, M.R., Stockli, D.F., 2010. Zircon (U–Th)/He thermochronometry in the KTB drill hole, Germany, and its implications for bulk He diffusion kinetics in zircon. Earth and Planetary Science Letters 295, 69–82. doi:10.1016/j.epsl.2010.03.025

Zeitler, P.K., Herczig, A.L., McDougall, I., Honda, M., 1987. U-Th-He dating of apatite: a potential thermochronometer. Geochimica et Cosmochimica Acta 51, 2865–2868.

Zeyen, H., Ayarza, P., Fernàndez, M., Rimi, A., 2005. Lithospheric structure under the western African-European plate boundary: A transect across the Atlas Mountains and the Gulf of Cadiz. Tectonics 24. doi:10.1029/2004TC001639

Zouine, E.M., 1993. Géodynamique récente du Haut Atlas. Evolution de sa bordure septentrionale et du Moyen Atlas sud-occidental au cours du Cenozoïque. Université Mohammed V, Rabat, 303 pp.

Appendix

Complete series of model runs with QTQt software for the Ourika, Tizgui and Imlil vertical profiles

Ourika vertical profile thermal models

A. Expected thermal models with radiation damage accumulation model in zircons of Guenthner et al. (2013) included. The temperature between top and bottom samples is allowed to vary between the equivalent paleogeothermal gradient of 10-50ºC/km but it is fixed over time.

A.1. Modelling of the aHe and zHe ages observed.

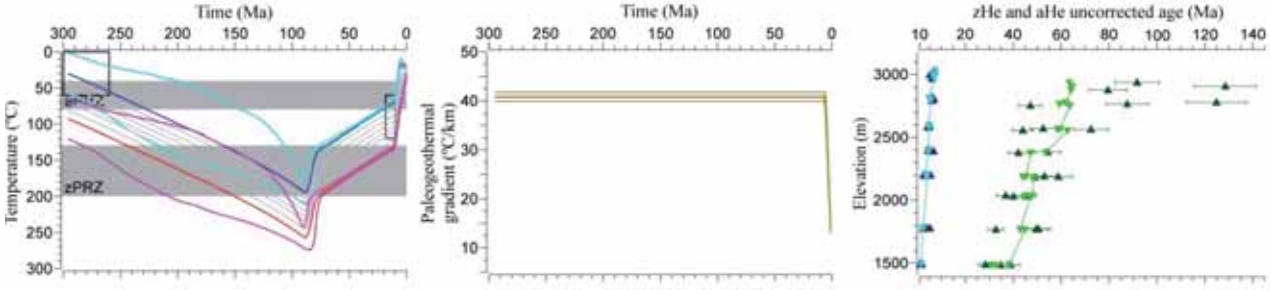

A.2. Modelling of the aHe and zHe with ages resampled.

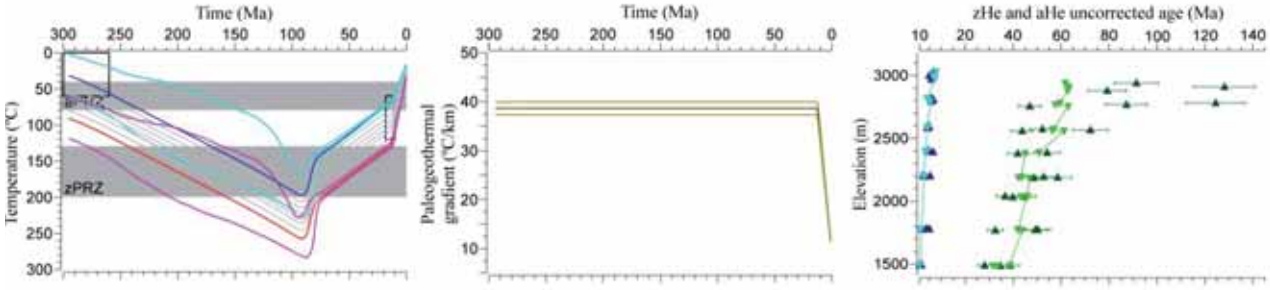

B. Expected thermal models with radiation damage accumulation model in zircons of Guenthner et al. (2013) included. The temperature between top and bottom samples is allowed to vary between the equivalent paleogeothermal gradient of 10-50ºC/km and it is allowed to vary over time.

B.1. Modelling of the aHe and zHe ages observed.

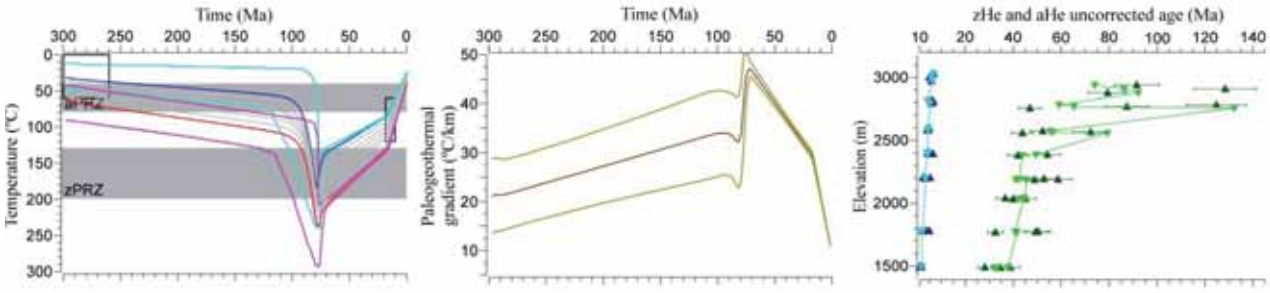

B.2. Modelling of the aHe and zHe with age resampled.

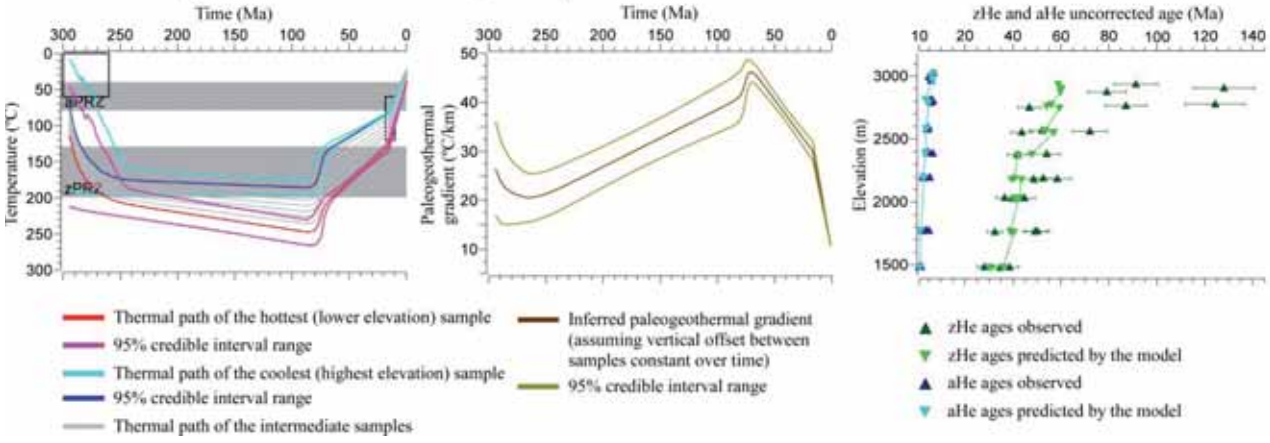

C. Expected thermal models with no radiation damage accumulation model included in zircons. Standard values of E_a and D_o (Ketcham et al. 2011). The temperature between top and bottom samples is allowed to vary between the equivalent paleogeothermal gradient of 10-50ºC/km but it is fixed over time.

C.1. Modelling of the aHe and zHe ages observed.

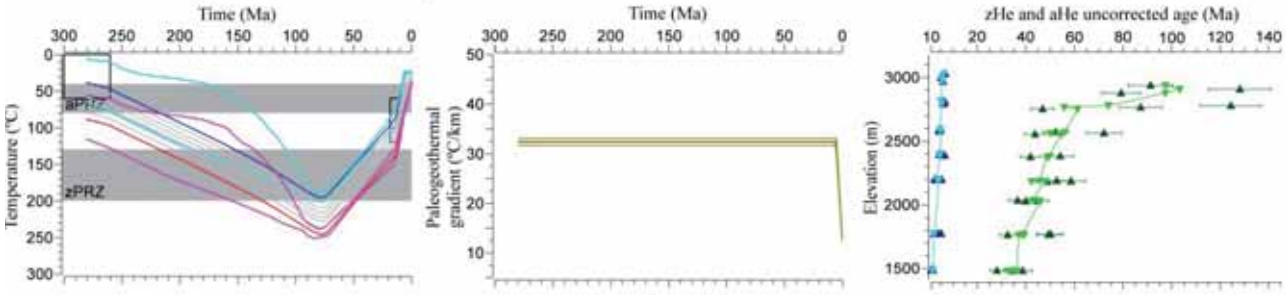

C.2. Modelling of the aHe and zHe with ages resampled.

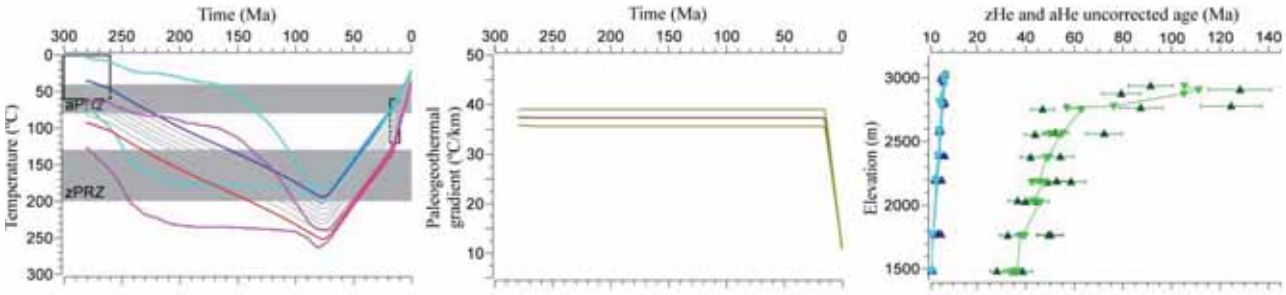

D. Expected thermal models with no radiation damage accumulation model included in zircons. Standard values of E_a and D_o (Ketcham et al. 2011). The temperature between top and bottom samples is allowed to vary between the equivalent paleogeothermal gradient of 10-50ºC/km and it is allowed to vary over time.

D.1. Modelling of the aHe and zHe ages observed.

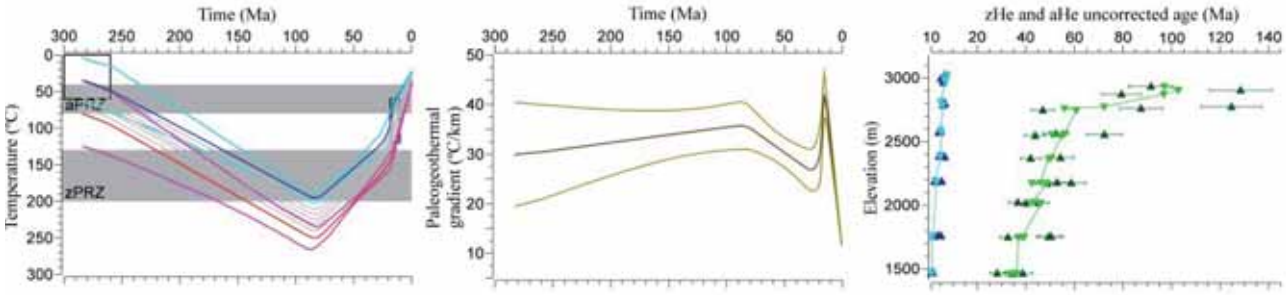

D.2. Modelling of the aHe and zHe with age resampled.

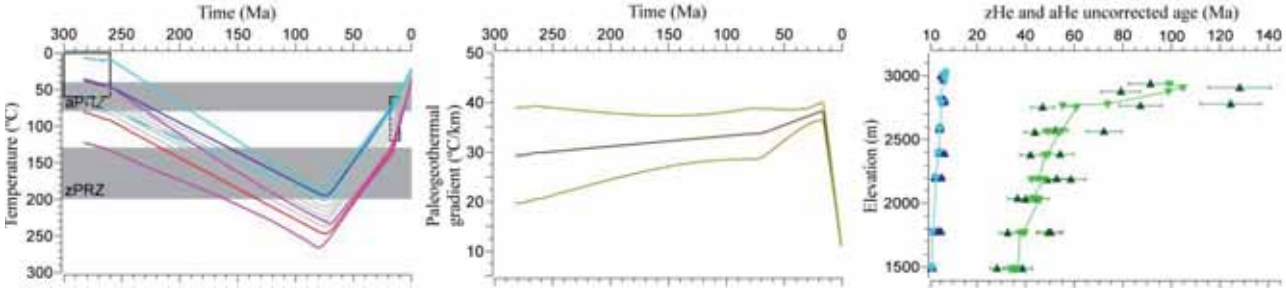

Imlil vertical profile thermal models

I. Expected thermal models. The temperature between top and bottom samples is allowed to vary between the equivalent paleogeothermal gradient of 10-50ºC/km but it is fixed over time.

I.1. Modelling of the aHe ages observed.

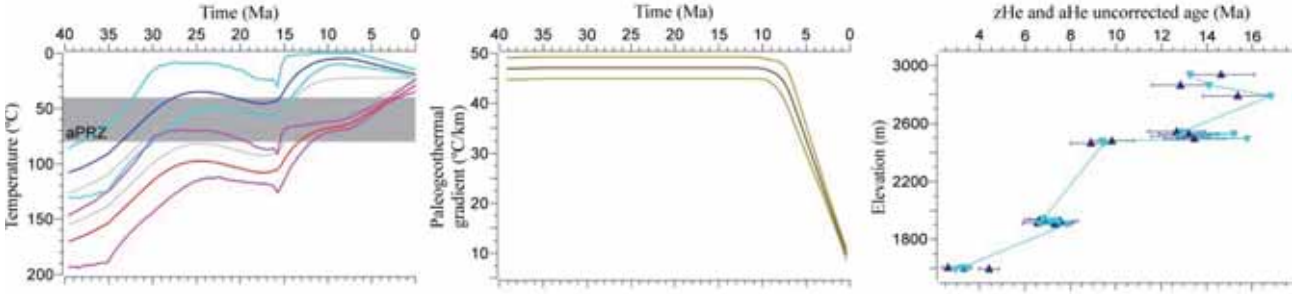

I.2. Modelling of the aHe with ages resampled.

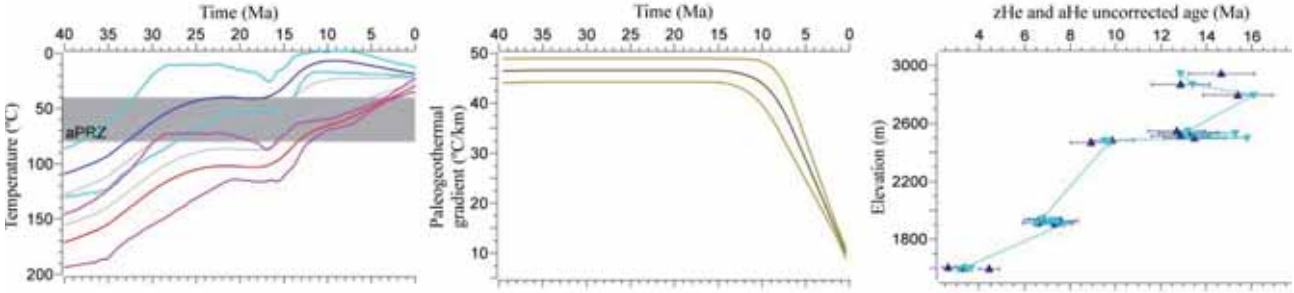

J. Expected thermal models. The temperature between top and bottom samples is allowed to vary between the equivalent paleogeothermal gradient of 10-50ºC/km and it is allowed to vary over time.

J.1. Modelling of the aHe ages observed.

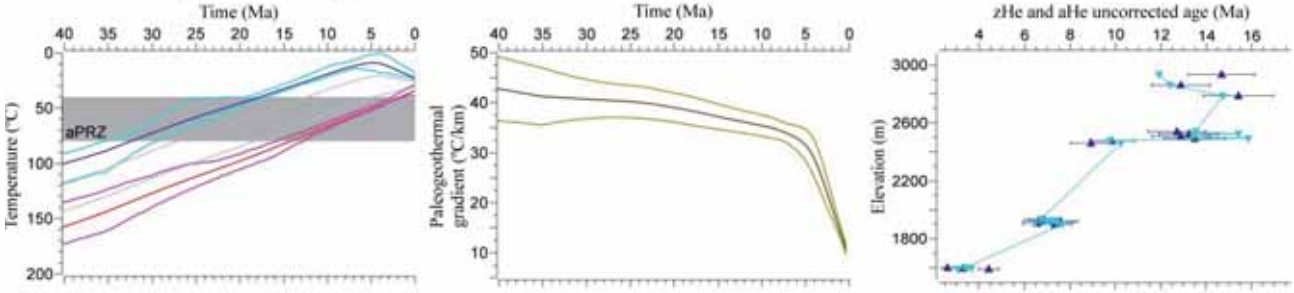

J.2. Modelling of the aHe with age resampled.

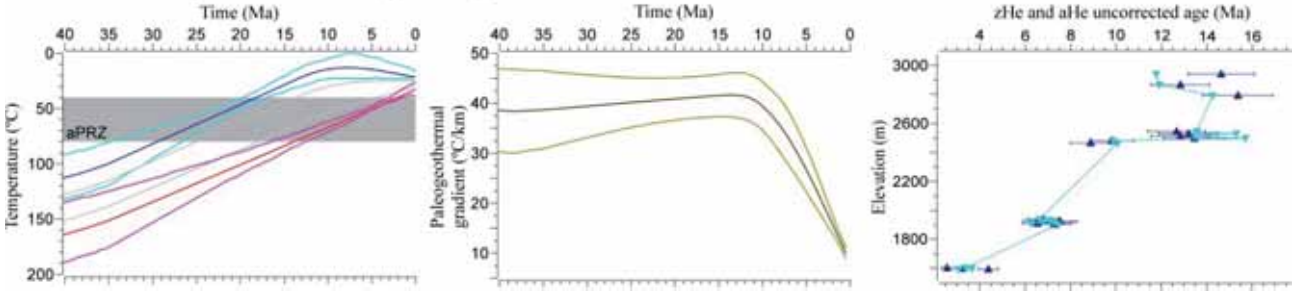

Tizgui vertical profile thermal models

E. Expected thermal models with radiation damage accumulation model in zircons of Guenthner et al. (2013) included. The temperature between top and bottom samples is allowed to vary between the equivalent paleogeothermal gradient of 10-50ºC/km but it is fixed over time.

E.1. Modelling of the aHe and zHe ages observed.

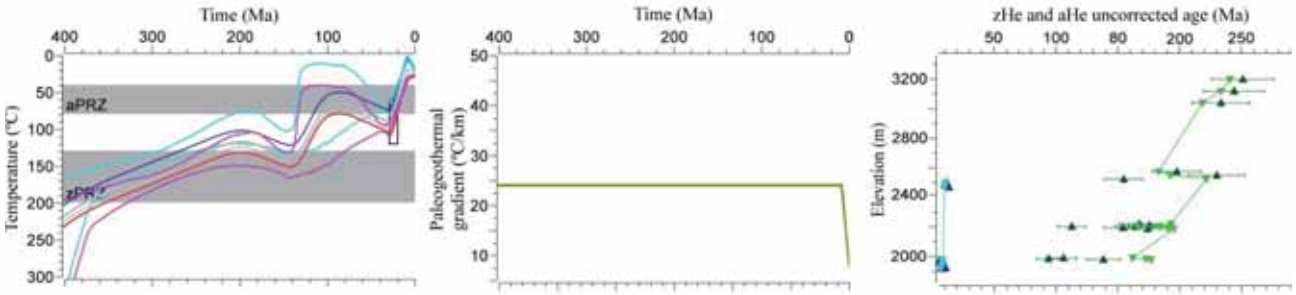

E.2. Modelling of the aHe and zHe with ages resampled.

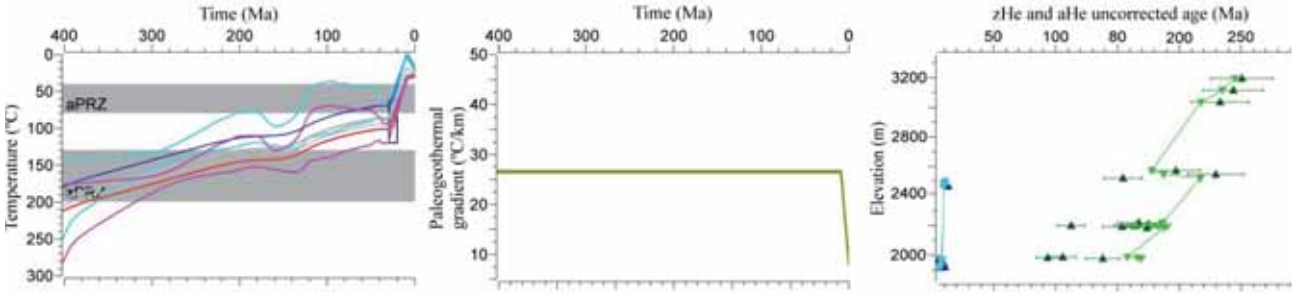

F. Expected thermal models with radiation damage accumulation model in zircons of Guenthner et al. (2013) included. The temperature between top and bottom samples is allowed to vary between the equivalent paleogeothermal gradient of 10-50ºC/km and it is allowed to vary over time.

F.1. Modelling of the aHe and zHe ages observed.

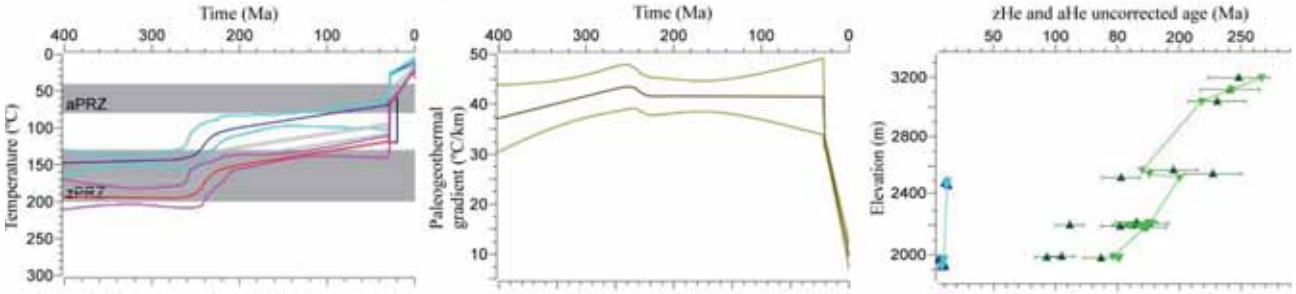

F.2. Modelling of the aHe and zHe with age resampled.

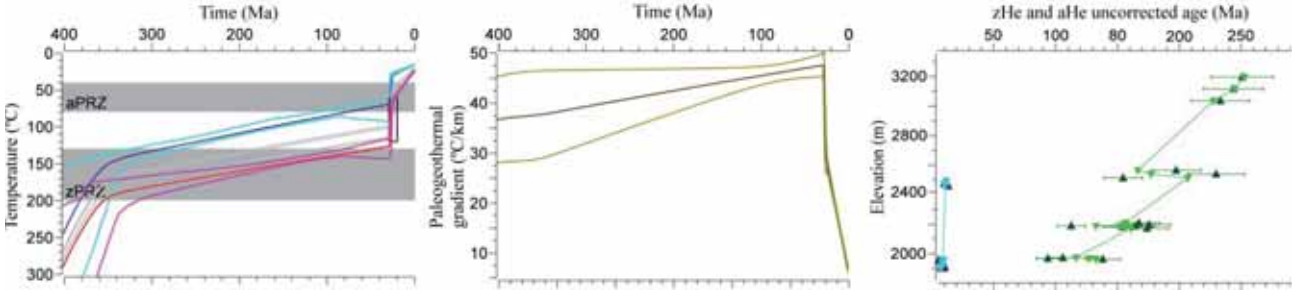

G. Expected thermal models with no radiation damage accumulation model included in zircons. Standard values of E_a and D_o (Ketcham et al. 2011). The temperature between top and bottom samples is allowed to vary between the equivalent paleogeothermal gradient of 10-50ºC/km but it is fixed over time.

G.1. Modelling of the aHe and zHe ages observed.

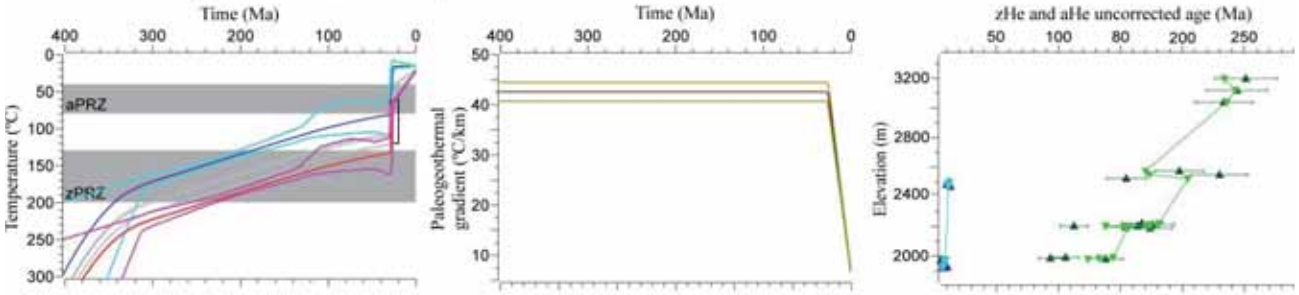

G.2. Modelling of the aHe and zHe with ages resampled.

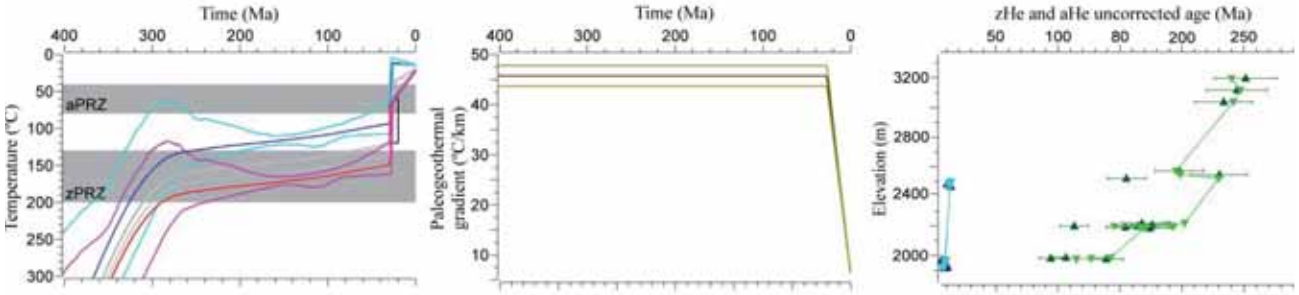

H. Expected thermal models with no radiation damage accumulation model included in zircons. Standard values of E_a and D_o (Ketcham et al. 2011). The temperature between top and bottom samples is allowed to vary between the equivalent paleogeothermal gradient of 10-50ºC/km and it is allowed to vary over time.

H.1. Modelling of the aHe and zHe ages observed.

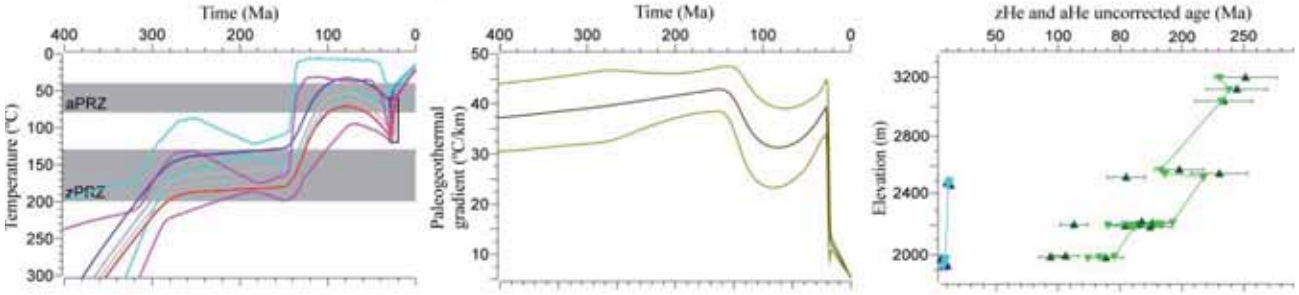

H.2. Modelling of the aHe and zHe with age resampled.